UNIVERSITAT
ROVIRA I VIRGILI

ESCOLA TÈCNICA SUPERIOR D'ENGINYERIA QUÍMICA
DEPARTAMENT D'ENGINYERIA QUÍMICA

Experimental and Numerical Investigation of the Flow in a Toroidal Cavity

By

Mohammad Y. S. Al-Shannag

A Dissertation Submitted to the DEPARTAMENT D'ENGINYERIA QUÍMICA DE LA UNIVERSITAT ROVIRA I VIRGILI in Partial Fulfillment of the Requirements for the Degree of Doctor of Philosophy in Chemical Engineering.

Tarragona, June, 2002

DEDICATION

To my parents, sisters, and brothers.

ACKNOWLEDGMENT

I would like to thank the Departament d’Enginyeria Química de la Universitat Rovira i Virgili who gave me the opportunity for realizing this investigation.

I wish to acknowledge with deep gratitude the encouragement and guidance of my supervisors Prof. Francesc Giralt and Dr. Joan Herrero, who made themselves available on a continuos basis for performing this work.

I am very grateful to Prof. Joseph A. C. Humphrey for his help, kindness, and the many stimulating discussions I had with him when I was at Mechanical and Aerospace Engineering Department, University of Virginia. I thank also Dr. Donald Jordan and Mr. Bouvard Hosticka for their help in building up the toroidal cavity apparatus at the Aerospace Research Laboratory, University of Virginia.

I would like to thank all my professors, colleagues, and friends at Universitat Rovira i Virgili, who helped me in one way or another to finish this work. Special thanks go to Dr. Alex Arenas, Mr. Mohamed Debbat, Dr. Abdelali El Aroudi, Mr. Zaid Al-Anber, and Mr. Amgad Moussa.

My parents, sisters, brothers, nieces, and nephews are always a constant source of endearment, support, and encouragement. I should thank every one of them.

Above all, I thank Allah, the almighty, for his help, care, and protection.

TABLE OF CONTENTS

LIST OF FIGURES

LIST OF TABLES

NOMENCLATURE

a	Constant, Eq. (3.1) [-]
A	Gap width, see Fig. 3.6 [mm]
b	Constant, Eq. (3.1) [mm]
C	Constant, (Eq. 2.4) [m^2/s]
C_P	Fluid heat capacity, [J/(kg. ^oC]
d	Feeding tube diameter, see Fig. 1.3 [mm]
D	Toroid square cross-section dimension, see Fig. 1.3 [mm]
D_E	Dimensionless dissipation of the fluctuating kinetic energy, Eq. (4.1) [-]
D_w	Dimensionless dissipation of the fluctuating vorticity, Eq. (4.2) [-]
E	Dimensionless specific kinetic energy [-]
F	Oscillation frequency [Hz]
G	Görtler number, Eq. (2.36) [-]
h	Width of the channel, see Fig. 1.3 [mm]
k	Fluid thermal conductivity [W/(m. ^oC)]
l	Angle, see Fig. 3.4 [rad]
N	Refraction index [-]
Nu	Nusselt number, Eq. (2.45) [-]
p	Dimensionless pressure [-]
P	Dimensionless mean pressure [-]
P	Dimensionless production of energy, Eq. (4.1) [-]
P_1	Dimensionless production of fluctuating vorticity, Eq. (4.2) [-]
P_2	Dimensionless production of fluctuating vorticity, Eq. (4.2) [-]
Pe	Peclet number (Pe = ReSc) [-]
Pr	Prandtl number, Eq. (2.38) [-]
r	Radial coordinate [mm]
R	Dimensionless radial coordinate, Eq. (2.8) [-]
R_i	Toroid inner radius, see Figs. 1.1(b) and 1.3 [mm]
R_o	Toroid outer radius, see Figs. 1.1(b) and 1.3 [mm]
R_2	Radius of the disks, see Fig. 3.6 [mm]
Re	Reynolds number, Eq. (2.16) [-]
R_c	Toroid radius of curvature [mm]
s	Dimensionless rate of fluctuating strain [-]
S	Dimensionless rate of mean strain [-]
t	time [s]
t_i	Initial time used for averaging $\boldsymbol{u}$, ***?*** , and p [s]
t_f	Final time used for averaging $\boldsymbol{u}$, ***?*** , and p [s]
T	Temperature [^oC]
thick	Thickness of Plexiglas cover of the cavity [mm]
$\boldsymbol{u}$	Dimensionless velocity vector [-]
$\boldsymbol{U}$	Dimensionless mean velocity [-]
U_{average}	Channel-width average velocity [m/s]
U_{tube}	Radially-averaged axial velocity in the inlet tube [m/s]
x	Horizontal distance [mm]
z	Axial coordinate [mm]
Z	Dimensionless axial coordinate, Eq. (2.8) [-]

Greek Letters:

δ	Curvature ratio ($\delta = D/R_c$) [-]
δ_m	Momentum boundary layer thickness [m]
θ	Circumferential coordinate [rad]
θ_{max}	Angel of the circumferential sector [rad]
Γ	Circulation, Eq. (2.35) [m^2/s]
$\Re$	Radius of curvature of the streamlines [m]
κ	Wavenumber [-]
l	Wavelength [m]
γ	Gap-to-width ratio ($\gamma = h/D$) [-]
m	Fluid viscosity [kg/m s]
ν	Fluid kinematic viscosity [m^2/s]
$\hbar$	Local heat transfer coefficient [$W/(m^2.\ ^oC)$]
r	Fluid density [kg/m^3]
τ	Dimensionless time, Eq. (2.8) [-]
Φ	Discriminant, Eq. (2.34) [$1/s^2$]
ψ	Dimensionless stream function, Eq. (2.9) [-]
w	Dimensionless vorticity vector [-]
W	Dimensionless mean vorticity vector [-]
Π	Dimensionless helicity ($\Pi = \boldsymbol{u}.\ w$) [-]
Ξ	Angular velocity of the disks and hub, see Fig. 3.6 [rpm]
Λ	Period of oscillation [s]

Subscripts

i, j, k	Indices denote components of a vector along the coordinate directions

Superscripts

′	Time-fluctuating quantity
″	Circumferentially-fluctuating quantity
*	Dimensionless quantity

Miscellaneous

^	Dimensional quantity
‾	Time-, circumferentially- or surface-averaged quantity.

Mathematical Symbols:

∇	Gradient
Δ	Difference
∇^2	Laplacian

Acronyms:

CUTEFLOWS	Computing Unsteady Three-dimensional Elliptic Flows
DNS	Direct Numerical Simulations
LDC	Lid-driven cavity
PIV	Particle Image Velocimetry
QUICK	Quadratic Upstream Interpolation for Convective Kinematics
SIMPLE	Semi-Implicit Method for Pressure-Linked Equations

ABSTRACT

Experimental and Numerical Investigation of the Flow in a Toroidal Cavity

By

Mohammad Yousuf Suliman Al-Shannag

Supervisor: Professor Francesc Giralt i Prat
Co-supervisor: Dr. Joan Herrero i Sabartés

The shear-driven incompressible flow in a toroidal cavity of square cross-section (DxD) and radius of curvature R_c has been studied both experimentally and numerically. The flow has been realized in two toroidal cavities driven by an external channel flow adjacent to the top flat lid of the toroid (open-cavity flow configuration). The first toroidal cavity has been designed and constructed for a curvature ratio ($\delta = D/R_c$) of about $\delta = 0.51$ (D = 100.0 mm and $R_c = 195.0$ mm). In addition, the toroid test section, previously, designed by Cushner (2001), for $\delta = 0.25$ ($D = 50.0$ mm and $R_c = 200.0$ mm) has been used to construct the second facility.

The Particle Image Velocimetry (PIV) technique and a Rheoscopic fluid have been used to visualize the motion of liquid water at certain vertical and horizontal planes of the flow domain. Numerical solutions have been obtained by integrating the incompressible time-dependent Navier-Stokes equations using a fourth-order accurate code. In addition to the open-cavity flow arrangement, the toroidal cavity driven by sliding the top flat wall, Lid-driven cavity (LDC) problem, has been considered in the calculations.

The flow visualization experiments have captured the three-dimensional periodic structures of Taylor-Görtler vortices (TGV) at Reynolds number of about

Re = 1000. Three-dimensional calculations of idealized LDC and open-cavity flow arrangement have resulted in steady two-dimensional flow solutions for small Reynolds numbers. When Reynolds number is sufficiently increased, the two-dimensional flow becomes unstable to different centrifugal-type of modes depending on curvature of the toroid. Steady modes of short wavelength render the LDC flow, driven by sliding the top wall radially outward, three-dimensional in a slightly curved enclosure ($\delta \leq 0.125$). When the motion is induced by sliding the top wall radially inward, the same type of mode has been obtained regardless of the δ value. The dominant modes become time-periodic and of longer wavelength for both open-cavity flow (δ = 0.25 and 0.51) and idealized LDC flow (sliding wall radially outward with δ = 0.25) cases. From the Eulerian viewpoint, the dynamic flow behavior is characterized by periodic alternation in the sense of rotation of the TGV. In contrast, for a strongly curved enclosure ($\delta \geq 0.51$) with an outwardly sliding lid, the modes are stationary and of very long wavelength.

Heat transport accompanying both 2D and 3D LDC flows has been investigated numerically. The transfer rates have been calculated for a range of Reynolds numbers and curvature ratios. A comparison between the 2D and 3D numerical results demonstrates the importance role of Taylor-Görtler vortices in improving the heat transfer processes. While, for $\delta = 0.125$, the heat transfer rate increases slightly when the 2D flow becomes three-dimensional, a drastic increase in the heat transfer has been noticed for $\delta = 1.0$. Thus, Taylor-Görtler modes of longer wavelength favor the mixing process largely.

Calculations of the kinetic energy and vorticity budgets have demonstrated that the first active modes are caused mainly by stretching/tilting of vorticity fluctuations and through an energy exchange between the fluctuating and the mean vorticity fields.

1. INTRODUCTION

Shear-driven cavity flows in which fluid motion is induced by a parallel shear action concern a wide range of industrial, biological, and environmental applications. The problem of flow of burned and unburned fluids in the combustion chambers is approximated by motion in a channel with a cavity to investigate the stability of flame (Sand, 1991). Many manufacturing devices, such as flexible blade coaters and short-dwell coaters (Aidun et al., 1991), used to produce high quality papers and photographic films, and continuos drying chambers (Alleborn et al., 1999), have shear flow phenomena. The present class of flows finds applications in the mixing processes of biological suspensions and blending of viscous fluid, where the thermal energy and molecular species transfer are greatly enhanced (Miles et al., 1995, Jana et al, 1994, Ottino, 1989). In botany, the plant nutrient vessels are modeled as axisymmetric vessels with periodically distributed cavities in order to study the transport phenomena of physiological liquids (Jeje and Zimmerman, 1979). In the environment, shear-driven cavity flows can provide a good test bed to study the waterborne pollutant creation in large lakes or ponds (Cuesta et al., 1999).

Many shear-driven cavity flow problems of complicated geometry are simplified by a well-known version called lid-driven cavity (LDC). Usually, it consists of a rectangular enclosure where the fluid motion is induced by sliding one or more distinct solid walls. The shape of the cavity and the way of creating the motion depend on the purpose of the study. The problem of incompressible fluid flow in rectangular parallelepiped enclosures, which is driven by sliding one solid wall has been widely studied over the past three decades in numerous research centers (see the sketch in Fig. 1.1a). Many engineering situations have flow regimes similar to the rectangular LDC hydrodynamics, such as the flow over cavities on the surfaces of aircrafts or on the walls of heat exchangers (Prasad and Koseff, 1989). Indeed, the simple domain and the easily posed boundary conditions have made this type of shear-driven flow an attractive benchmark for Navier-Stokes solvers. Furthermore, this flow arrangement offers the opportunity to better understand many fundamental problems in fluid mechanics. Several phenomena typical of incompressible flows occur in LDC such as: separation of streamlines (corner eddies and primary eddy), corner singularities, local features of centrifugal instability such as Taylor-Görtler-like vortices (TGV), complex and chaotic mixing motions, transition, and turbulence. It can be said that the LDC flow problem is very rich in its physics. Most of the previous studies have been conducted on LDC flows in a rectangular geometry.

The toroidal cavity shown in Fig. 1.1(b) represents a generalized configuration for the shear-driven cavity flow problems (Phinney and Humphrey, 1996; Sudarsan et al., 1998). Since the end-walls of the parallelepiped are absent in the toroidal geometry, this permits the experimental and the numerical realization of the axisymmetric flow at low Reynolds numbers and the investigation of the first transition, solely due to centrifugal instability. The literature review will show that few studies have investigated the shear-driven cavity flow in this geometrical configuration. Thus, the attention of this investigation has focused on the LDC flows with the toroidal geometry shown in Figs. 1.1b and 1.3.

1.1 Literature review

A review of the literature reveals that many numerical studies have used direct numerical simulation (DNS) or a linear stability analysis to investigate the two-and three-dimensional characteristics of LDC flows. In contrast, few experiments of the LDC flow problem appear in the literature. Some of the numerical investigations reported a qualitative agreement with the experiments. However, most of these studies correspond to three-dimensional (3D) flow calculations and have failed to obtain a clear picture of the flow behavior because of the high cost of the computations.

1.1.1 Two-dimensional rectangular LDC flows

The steady two-dimensional rectangular LDC flow (see Fig. 1.1a) has been calculated by many different numerical techniques (Burggraf, 1966; Pan and Acrivos, 1967; Benjamin and Denny, 1979; Ghia et al., 1982; Schreiber and Keller, 1983; Prasad and Koseff, 1989; Luchini, 1991; Nishida and Satufoka, 1992). These studies have found that the flow structure is characterized by a primary large eddy and that secondary vortices form near the lower corners; see Fig. 1.2(a). Steady flow solutions have been reported for Reynolds number up to approximately Re = 10000. Benjamin and Denny (1979) have found that when the Reynolds number is increased beyond about Re = 1200, an additional secondary eddy appears at the upper upstream corner. Ghia et al. (1982) have obtained highly accurate solutions using the coupled strongly implicit and multigrid methods with a grid as fine as (257x257). At Re = 7500 and 10000, Ghia et al. (1982) have reported the appearance of two tertiary vortices in the corner regions.

Time dependent two-dimensional rectangular LDC flow has been computed by several investigators including Goodrich et al., 1990; Shen, 1991; and Poliashenko and Aidun, 1995. In a rectangular LDC of unit height-to-width ratio (aspect ratio), Shen (1991) has found that the flow is periodic in time (which indicates Hopf bifurcation) for $10000<Re\leq15000$. At Re = 15500, the flow loses time periodicity and

becomes quasi-periodic. When the aspect ratio of the cavity is equal to 2:1, Goodrich et al. (1990) have noticed persistent time oscillation of the 2D flow at Re = 10000. Poliashenko and Aidun (1995) have calculated the sequence of transitions from steady state to chaotic flow in the plane LDC of aspect ratios 0.8,1.0, and 1.5. They have showed that, depending on the cavity aspect ratio, the first transition from steady flow to a time periodic flow could be through a supercritical or a subcritical Hopf bifurcation.

1.1.2 Three-dimensional rectangular LDC flows

Koseff and coworkers (Rhee et al., 1984, Koseff and Street, 1984a, b, c; Koseff et al., 1983, 1985; Freitas et al., 1995; Prasad et al., 1988; Prasad and Koseff, 1989) have studied both experimentally and numerically the three-dimensional flow in the LDC for Reynolds numbers in the range 1000<Re<10000. Koseff and Street (1984) have visualized the main circulation cell and the three-dimensional structures, such as corner vortices in the end-wall region and longitudinal Taylor-Görtler-like vortices (see Fig. 1.2). The flow field has been visualized using the thymol-blue technique and by means of a rheoscopic liquid illuminated by laser-light sheets. Quantitative velocity profiles have been measured using a two-component laser-Doppler anemometer. The gross flow characteristics are in a qualitative agreement with the previous two-dimensional calculations. By varying the span-to-width aspect ratio (SAR), Koseff and Street (1984) have noticed that the size of the downstream secondary eddy (DSE) increases as Re increases from 1000 to 10000 for a SAR of 3:1, while for SAR's of 1:1 and 2:1 the DSE reduces in size when Re>2000. Before the appearance of turbulence, at $Re \approx 6000$, they have observed TGV that form between the primary circulating cell and the DSE one (see Fig. 1.2b). Another feature of the three-dimensionality of the flow is the corner vortex. The existence of this vortex is attributed to the adjustment of the shear and pressure forces to the no-slip condition imposed at the end-walls.

Freitas and Street (1988) have simulated numerically the three-dimensional flows in a 150 mm by 150 mm by 450 mm cavity (SAR of 3:1) at Re = 3200. They have included in their numerical simulations the effect of end-walls viscous damping, which results in a pressure-driven secondary flow. The TGV predicted by their numerical simulation posses wavelengths in the range 30-50 mm and time scales between 40 and 140 s.

Aidun et al. (1991) have visualized experimentally the flow in a cavity of square-cross section (50.8 mm by 50.8 mm), with a SAR of 3:1, over a range of Re from 100 to 2000. Their cavity has allowed some through-flow due to fluid losses from the downstream corner of the moving lid. They have found that the flow becomes time-periodic at Re = 825. The critical period of oscillation is about $\Lambda = 3.0$ s and it decreases by about 20% at Re = 1000. Time-periodic spiral-shaped vortices appear to travel from the symmetry plane to the end-walls. For Re>1900, six pairs of TGV are produced in the form of mushroom-shaped structures. The flow visualizations show that these structures are irregularly spaced and nonuniform in size. By increasing Re, their size shrinks but their number remains unchanged. When Re is suddenly decreased from Re = 2000 (unsteady state) to Re<500, Aidun et al. have identified a steady three-dimensional vortex flow which fills the whole cavity.

Jordan and Ragab (1994) have used both direct numerical simulation (DNS) and large eddy simulation (LES) methodologies to predict the unsteady and turbulent flow characteristics at Re = 5000 and 10000. Their cavity had square-cross section with a SAR of 1.5:1. Their DNS results at Re = 5000, show an unsteady 3D laminar flow which is characterized by nine pairs of TGV spanning the cavity bottom and by 3D corner vortices owing to the end-walls effect. The Taylor-Görtler vortices change rapidly in size and they meander only locally. Using LES at Re = 10000, Jordan and Ragab have found a distortion of the TGV and an irregular development of the DSE because of the random combined effects of the main circulation cell, TGV, and the 3D corner vortices. The quantitative measurements done by Benson and Aidun (1992) in the same apparatus using wall-mounted hot-film probes have confirmed the existence of the unstable mode in the LDC flow problem of Aidun et al. (1991).

Other studies have used linear stability methods to analyze the onset of instability in the rectangular LDC flows. These studies have imposed periodic boundary conditions in the spanwise direction in order to investigate centrifugal instability, the responsible for the generation of TGV cleanly. Ramanan and Homsy (1994) have computed first the 2D base flows over a range of Reynolds numbers. Then, they have perturbed these mean flows with three-dimensional disturbances. They have observed that the mean flow losses stability due to a long wavelength steady mode at a critical Reynolds number of Re = 594. A second unstable mode, with wavelength close to the cavity width, is found at Re = 730. Ding and Kawahara (1998) have investigated the linear stability of the same LDC flow by means of the mixed finite element method. They have noticed that the three-dimensionality in the flow appears at a critical Reynolds number of 920, with an unsteady mode of wavenumber $\kappa = 7.4$.

Recently, Albensoeder et al. (2001a) have carried out linear stability analyses with shorter wavelength modes for rectangular cavities of different aspect ratios. They have found that the first instability in the square LDC flow is characterized by a steady mode with a critical Reynolds number, Re = 786 and a critical wavenumber

$\kappa = 15.4$. They have calculated the energy-transfer rates from the base flow to the critical perturbation mode and they have concluded that the physical instability mechanism responsible for the formation of the steady three-dimensional vortex flow is due to a centrifugal process. They have found that the critical Taylor-Görtler mode receives most of its energy from a banana-shaped region near the upstream wall. It is therefore clear that Ramanan and Homsy (1994) and Ding and Kawahara (1998) have missed this steady mode since the true critical wave number is out of the boundary of their linear stability analyses. Albensoeder et al. (2001a) have confirmed experimentally the steady mode in a square cavity with a large span-to-width aspect ratio (SAR of 6.55:1). Their linear stability analyses have predicted a three-dimensional steady mode with a long wavelength for deep cavities. For shallow cavities, the mode is unsteady with very short wavelength. The unsteady mode consists of three-dimensional short waves propagating in the spanwise direction of the cavity.

Other studies have investigated both laminar and turbulent flows characteristics in the LDC problem. Leriche and Gavrilakis (1999) have simulated directly the flow in a lid-driven cubical cavity at a Reynolds number above 10000. They have reported an unsteady laminar flow within the cavity for Re between 10000 and 18000. Deshpande and Milton (1998) have investigated the Kolmogorov scales in a cubical cavity by means of DNS. They have found that a value of 0.01 times the size of the cubical cavity is a good representative value for the Kolmogorov length scales at Re = 10000. A review of the lid-driven cavity flow problem is given by Shankar and Deshpande (2000).

Kuhlmann and coworkers (Kuhlmann et al., 1997, 1998; Albensoeder et al., 2001b; Blohm and Kuhlmann, 2002) have investigated both numerically and experimentally the incompressible vortex flows in two-sided lid-driven cavities in a set of recent studies. In these studies, two opposite walls of the cavity move steadily in parallel or anti-parallel directions with the same velocity value and some cases with different velocities. They have reviewed some interesting topics in the LDC flow problem such as non-uniqueness of the basic two–dimensional flow and the elliptic instability, which destabilizes the basic flow through steady or unsteady three-dimensional modes.

1.1.3 Toroidal lid-driven cavity flows

In parallelepiped lid-driven cavity, the centrifugal forces driving the TGV in the bulk of the flow differ in magnitude from the pressure forces driving 3D corner vortices near end-walls. Non-linear interaction between the forces of the two types can affect the critical values that characterize the Taylor-Görtler mode. Hence, the presence of end-walls in the parallelepiped lid-driven cavity prevented many researchers to capture the correct mode in their experiments or numerical simulations.

Phinney and Humphrey (1996) have proposed curving the finite parallelepiped LDC upon itself such that the two end-walls will merge to form a toroid of rectangular cross-section as shown in Fig. 1.1b. In this way, the pressure gradient induced near the end-walls is removed. The motion in the toroid is characterized by the Reynolds number, the aspect ratio, and curvature ratio ($\delta = D/R_c$); where D is the width of the toroid cross-section, $R_c = (R_i + R_o)/2$ is the toroid radius of curvature.

In the study of Phinney and Humphrey (1996), the motion within the toroid is generated by imposing a constant radial velocity at the top flat wall. Steady axisymmetric calculations are performed for values of the Reynolds number equal to

2400, 3200, and 4000 and values of δ ranging from $5.0\text{x}10^{-6}$ to 1.0. For values of the curvature ratio below $\delta = 0.05$, the typical two-dimensional gross flow pattern of the rectangular cavity is reproduced. At a given value of the Reynolds number, a critical curvature ratio is found above which the primary circulating cell has migrated toward the upper downstream corner. Humphrey and Phinney have specified the transition boundary for migration of the primary vortex by the relation: $\delta_{cr}^{1/4} = 3.58\,\mathrm{Re}^{-1/5}$.

Cushner (2000) has realized experimentally the shear-driven flow of liquid water in a toroid of square-cross section and of a curvature ratio ($\delta = 0.25$); $D = 50.0$ mm and $R_c = 200$ mm. As shown in Fig. 1.3, the motion within the cavity is induced by an stream of the same fluid that expands radially outward through the external channel located between the bottom of the lid and the top of inner-radius and the outer-radius walls of the cavity. Another new parameter, gap-to-width ratio ($\gamma = h/D$) is specified to characterize the fluid motion, where h is the gap width of the external channel. Reynolds number has been defined as $\mathrm{Re} = U_h D/\nu$, where U_h is the channel-width average velocity at the inlet section shown in Fig 1.3. For $\mathrm{Re} = 5000$ and $\gamma = 0.015$, Cushner has reported the presence of Taylor-Görtler vortices with a wavenumber $\kappa = 13.0$, approximately.

Spassov (2001) has used both linear analysis and numerical simulation to study the stability of the lid-driven incompressible flows in toroidal cavities of square-cross section and five different curvature ratios, namely, $\delta = 0$ (parallelepiped), 0.125, 0.25, 0.5, and 1. The fluid motion within the toroid was induced by sliding the upper flat wall radially outward. The radial velocity along the upper flat wall is inversely proportional to the radial distance. For small curvatures, $\delta \leq 0.125$, the steady three-dimensional mode of the straight LDC flow predicted by Albensoeder et al. (2001a) has been reproduced. Spassov (2001) has reported two other types of modes. For $\delta = 0.25$, the mode is unsteady and its wavelength is twice the wavelength of the modes corresponding to the small curvatures. For larger curvature $\delta \geq 0.5$, a steady type of modes with wavelength five times longer than the wavelength at smaller curvatures has been obtained. Furthermore, Spassov (2001) has found that the critical modes at $\delta = 0.125$ and 0.25 draw their energy from a region near the dividing streamlines between the primary vortex and the upstream secondary eddy. For $\delta \geq 0.5$, this region is located between the primary vortex and the downstream secondary eddy.

1.2 Objectives of this study

The aim of the present study is to identify, numerically and experimentally, the structure and the dynamics of the isothermal flow of liquid water and its mixing process within toroidal cavities of different curvature ratios. This will be achieved through the following specific objectives:

(a) Design and construction of a shear-driven cavity apparatus which has a toroid of square-cross section (D = 100.0 mm) and radius of curvature (R_c = 195.0 mm). This toroidal cavity is characterized by curvature ratio of about $\delta = D/R_c = 0.51$. Another toroidal cavity apparatus with $\delta = 0.25$ will be built as a part of the present investigation using the toroid, previously, designed by Cushner (2000), with square-cross section ($D = 50.0$ mm) and radius of curvature (R_c = 200.0 mm).

(b) Measurement of the velocity field at given planes of the toroidal cavity with $\delta = 0.51$, gap-to-width ratio ($\gamma = h/D = 0.04$), and Reynolds number of about 1000. Furthermore, a possible three-dimensional flow structures will be visualized under these operating conditions in the toroidal cavity with $\delta = 0.25$.

(c) Unsteady two- and three-dimensional calculations will be performed for the toroidal geometry of both LDC flow and open-cavity flow arrangements, sketched in Figs. 1.1(b) and 1.3, respectively, using a fourth-order finite difference discretization algorithm. The numerical results will be compared with the corresponding experimental results.

(d) Calculation of the kinetic energy and vorticity budgets to provide an insight into the instability mechanism that originates the three-dimensional vortex flows in the toroidal cavity.

(e) Assessment of the effect of Taylor-Görtler vortices on the mixing process within the toroidal cavity. The calculated heat transfer rates of the axisymmetric flows will be compared with the corresponding rates of the three-dimensional flows.

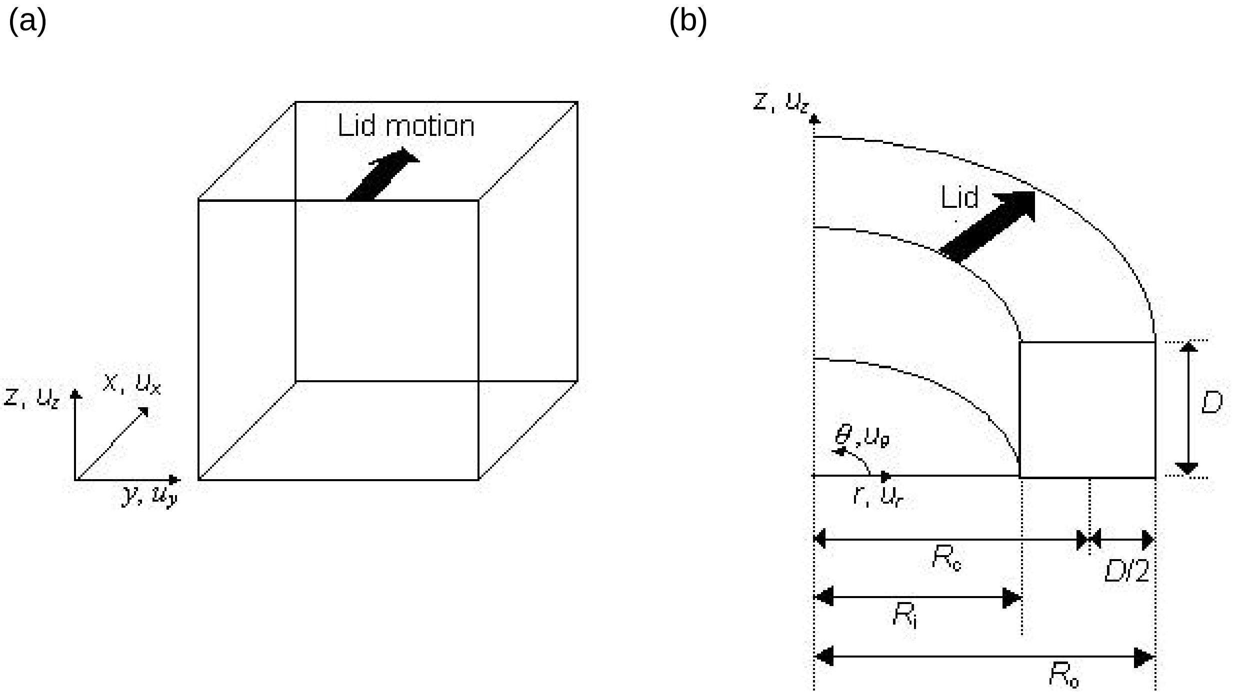

Figure 1.1. Schematic of lid-driven cavity (LDC) flow. (a) Coordinate system and view of the overall flow field in rectangular LDC; (b) Coordinate system of toroidal LDC flows for one-quarter of the toroid.

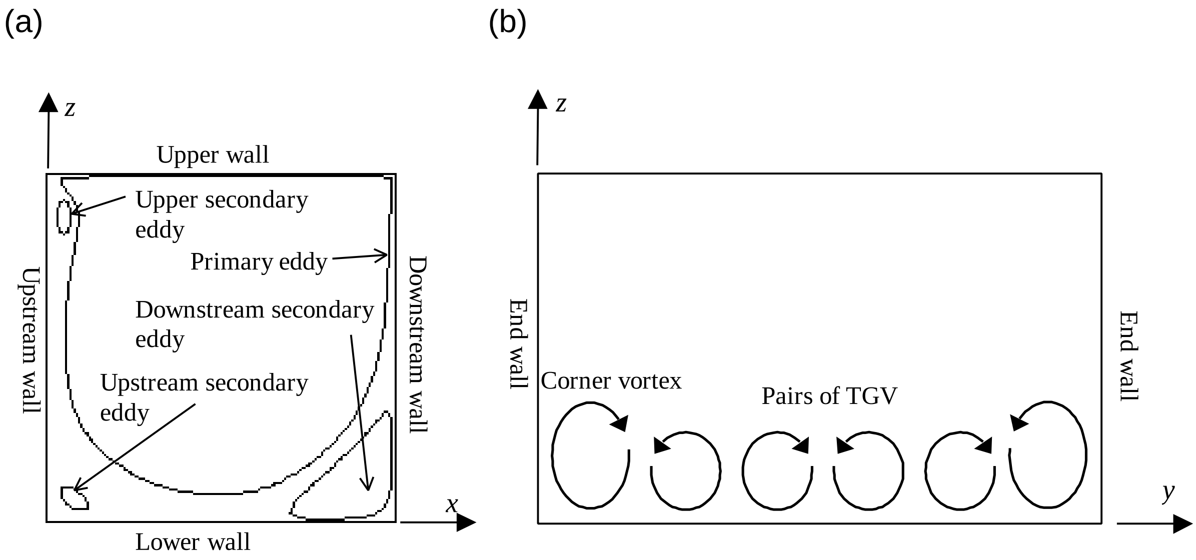

Figure 1.2. Overall view of the rectangular LDC flow.(a) Sketch of the basic features in the 2D flow problem; (b) Sketch of the TGV and corner vortices in 3D flow problem.

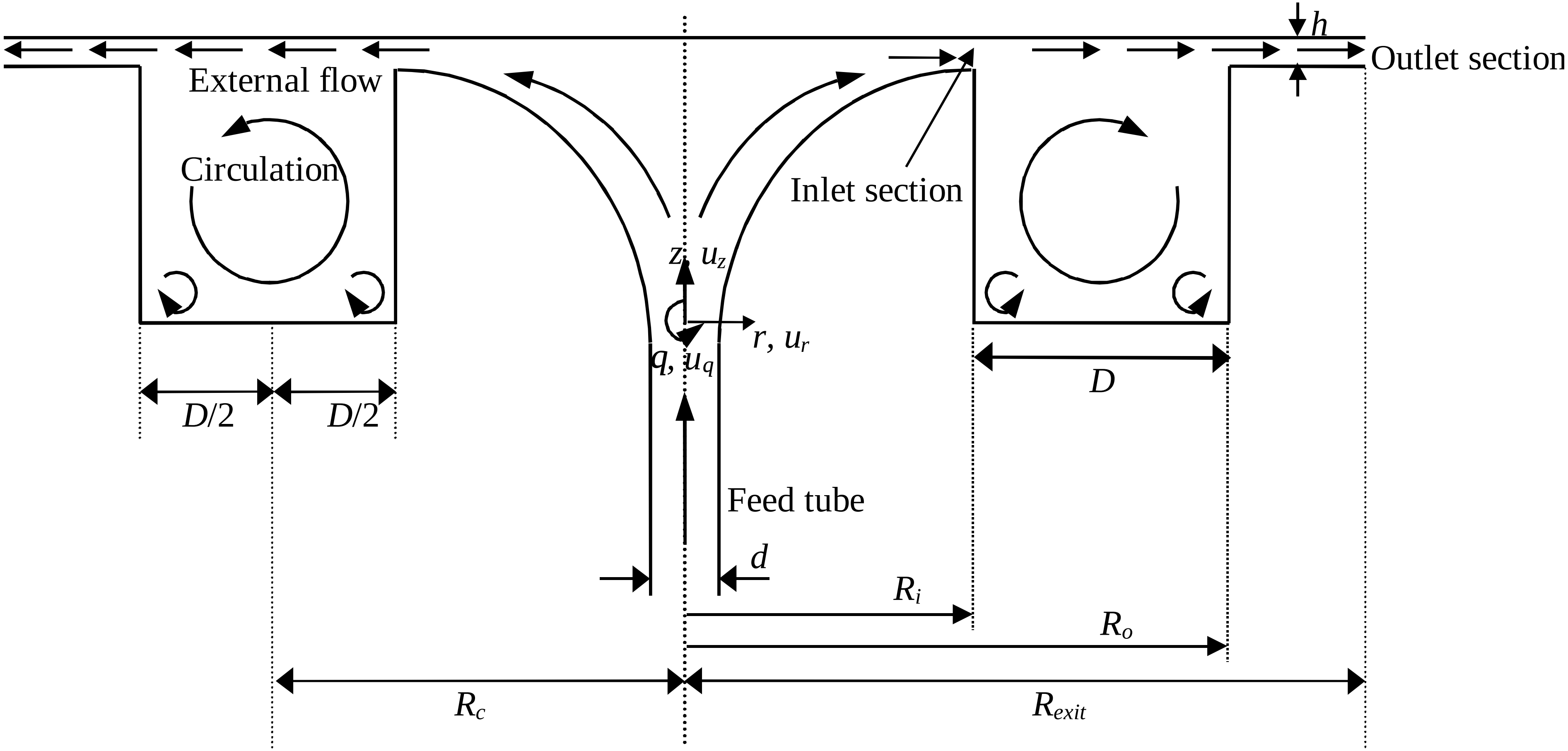

Figure 1.3. Front view of the open-cavity with a toroidal geometry. The circulation of the fluid is induced by the shearing action of the external channel flow.

2. THEORY

2.1 Equations of motion

The present investigation presumes an incompressible flow of constant properties, Newtonian fluid. Hence, the continuity equation and the Navier-Stokes equation can be described in general vectorial form as:

Continuity equation:

$$\nabla \cdot \hat{\boldsymbol{u}} = 0 \tag{2.1}$$

Navier-Stokes equation:

$$\frac{\partial \hat{\boldsymbol{u}}}{\partial t} + (\hat{\boldsymbol{u}} \cdot \nabla)\hat{\boldsymbol{u}} = -\frac{1}{\rho}\nabla \hat{p} + \nu \nabla^2 \hat{\boldsymbol{u}} \tag{2.2}$$

where $\hat{\boldsymbol{u}}$ is the velocity vector, *t* is time, $\hat{p}$ is the dynamic pressure, , μ is the fluid viscosity, ρ is the fluid density, $\nu = \mu/\rho$ is the fluid kinematic viscosity, ∇ is the gradient operator, and ∇^2 is the Laplacian operator.

2.2 Boundary conditions

At all solid surfaces of the cavity, the no slip condition requires that $\hat{\boldsymbol{u}} = 0$. For the purpose of the numerical calculations in the open-cavity arrangement (Fig. 1.3), the following boundary conditions are assumed:

- At the inlet section of the external flow (Fig. 1.3), a flat or a parabolic velocity profile have been used along the axial direction.
- At the outlet section shown in Fig. 1.3, the derivatives of the circumferential and axial velocity components in the radial direction are set to zero:

$$\frac{\partial \hat{u}_\theta}{\partial r} = \frac{\partial \hat{u}_z}{\partial r} = 0 \tag{2.3}$$

where $\hat{u}_\theta$ and $\hat{u}_z$ are the circumferential and axial velocity components in the θ and z cylindrical coordinate directions, respectively. The radial velocity component, $\hat{u}_r$, is computed so that the continuity equation (2.1) at this outlet section is accomplished.

For the LDC flow case shown in Fig 1.1(b), the radial velocity component is assumed inversely proportional with the radial distance,

$$\hat{u}_r(r) = \frac{C_1}{r} \tag{2.4}$$

In all three-dimensional calculations of both the open-cavity flow arrangement, Fig. 1.3, and the LDC flow case, Fig. 1.1(b), periodic boundary conditions are applied in circumferential direction, that is:

$$(\hat{\boldsymbol{u}}, \hat{p})_{\theta=0} = (\hat{\boldsymbol{u}}, \hat{p})_{\theta=\theta_{\max}} \tag{2.5}$$

where $\theta_{\max}$ is the angel of the circumferential sector in which the 3D calculation is performed. Obviously, when the calculations are performed over the whole circumferential domain, it is equal to $\theta_{\max} = 2\pi$.

2.3 Vorticity conservation equations

The vorticity vector, $\hat{\boldsymbol{\omega}}$, of a fluid motion is defined as:

$$\hat{\boldsymbol{\omega}} = \nabla \times \hat{\boldsymbol{u}} \tag{2.6}$$

and the vorticity conservation equation for incompressible flows is (Tritton, 1988):

$$\frac{\partial \hat{\boldsymbol{\omega}}}{\partial t} + (\hat{\boldsymbol{u}} \cdot \nabla)\hat{\boldsymbol{\omega}} = (\hat{\boldsymbol{\omega}} \cdot \nabla)\hat{\boldsymbol{u}} + \nu(\nabla^2 \hat{\boldsymbol{\omega}}) \tag{2.7}$$

In the above equation, the term $(\hat{\boldsymbol{u}} \cdot \nabla)\hat{\boldsymbol{\omega}}$ represents the rate of change of $\hat{\boldsymbol{\omega}}$ due to convection of vorticity. The term $(\hat{\boldsymbol{\omega}} \cdot \nabla)\hat{\boldsymbol{u}}$ represents the action of velocity gradients on $\hat{\boldsymbol{\omega}}$ (the rate of change of vorticity due stretching and tilting of the vortex lines). This term is absent in 2D flows because $\hat{\boldsymbol{\omega}}$ is perpendicular to the plane of flow. In three-dimensional flows, in contrast, there are vorticity-changing processes associated with the vortex stretching and tilting term $(\hat{\boldsymbol{\omega}} \cdot \nabla)\hat{\boldsymbol{u}}$. The last term of Eq. (2.7) represents the diffusion of $\hat{\boldsymbol{\omega}}$ down a vorticity gradient, in the same way that the term $\nu(\nabla^2 \hat{\boldsymbol{u}})$ in the Navier-Stokes equation (2.2) represents the diffusion of momentum down a momentum gradient.

2.4 Scaling of variables

For the purpose of better understanding the physics of the flow and presenting the results consistently, the following non-dimensional variables are defined (Humphrey and Phinney, 1996):

$$Z = \frac{z}{D},\ R = \frac{r}{D}\ \tau = \frac{t}{D/U_{average}},$$

$$\boldsymbol{u} = \frac{\hat{\boldsymbol{u}}}{U_{average}},\ \text{and}\ p = \frac{\hat{p}}{\rho U^2_{average}} \tag{2.8}$$

Based on the above non-dimensional variables, the non-dimensional stream-function is defined as:

$$\psi = \frac{\hat{\psi}}{U_{average} d R_c} \tag{2.9}$$

and the non-dimensional vorticity vector is scaled as:

$$\boldsymbol{\omega} = \frac{\hat{\boldsymbol{\omega}} D}{U_{average}} \tag{2.10}$$

where D is the width of the toroid cross-section, $R_c = (R_i + R_o)/2$ is the radius of curvature of the toroid, and $U_{average}$ is velocity characteristic of the toroidal cavity. For open-cavity arrangement sketched in Fig. 1.3, preliminary 2D flow calculations have shown that the plane-average value of the radial velocity in the external channel equals approximately to channel-width average velocity at $r = R_c$. Thus, the latter has been used to define $U_{average}$ which can be estimated by applying the mass balance between the feed tube region and the mid cross-section of the channel:

$$U_{average} = \frac{d^2 U_{tube}}{8hR_c} \tag{2.11}$$

where d is the feeding tube diameter and U_{tube} is the averaged velocity in the feeding tube. For the LDC type of flow, $U_{average}$ denotes the radially-averaged radial velocity corresponds to the top wall of the toroid and is given by:

$$U_{average} = \frac{C_2}{D} \ln\left(\frac{R_c + D/2}{R_c - D/2}\right) \tag{2.12}$$

By using the above scaled variables defined by Eqns. (2.8-2.12), the continuity equation (2.1), the Navier-Stokes equation (2.2), and the vorticity conservation equation (2.7) can be written in a nondimensional form as:

Continuity equation:

$$\nabla \cdot \boldsymbol{u} = 0 \tag{2.13}$$

Navier-Stokes equation:

$$\frac{\partial \boldsymbol{u}}{\partial \tau} + (\boldsymbol{u} \cdot \nabla)\boldsymbol{u} = -\nabla p + \frac{1}{\mathrm{Re}} \nabla^2 \boldsymbol{u} \tag{2.14}$$

Vorticity conservation equation:

$$\frac{\partial \boldsymbol{\omega}}{\partial \tau} + (\boldsymbol{u} \cdot \nabla)\boldsymbol{\omega} = (\boldsymbol{\omega} \cdot \nabla)\boldsymbol{u} + \frac{1}{\mathrm{Re}} (\nabla^2 \boldsymbol{\omega}) \tag{2.15}$$

where the Reynolds number characteristic of the cavity is defined as:

$$\mathrm{Re} = \frac{\rho U_{average} D}{\mu} \tag{2.16}$$

The dimensionless continuity equation, the radial, circumferential and axial momentum conservation equations, and the vorticity conservation equations in a cylindrical coordinate system are presented in Appendix A.

2.5 Fluctuation kinetic energy and vorticity budgets

It is useful to decompose the flow field into a mean and fluctuating flow in order to gain more physical understanding of three-dimensional flow mechanisms (Tennekes and Lumley 1972). The dimensionless velocity vector, the vorticity vector, and the pressure are decomposed as follows:

$$\boldsymbol{u} = \boldsymbol{U}' + \boldsymbol{u}' \,, p = P' + p' \tag{2.17}$$

$$\boldsymbol{\omega} = \boldsymbol{\Omega}' + \boldsymbol{\omega}' \tag{2.18}$$

The vector variables $\boldsymbol{U}'$ and $\boldsymbol{\Omega}'$ and the scalar variable P' are defined as the time average of the velocity vector, the vorticity vector, and the pressure, respectively,

$$\boldsymbol{U}' = \frac{1}{(t_f - t_i)}\int_{t_i}^{t_f} \boldsymbol{u}dt \,,\ \boldsymbol{\Omega}' = \frac{1}{(t_f - t_i)}\int_{t_i}^{t_f} \boldsymbol{\omega}dt \,, P' = \frac{1}{(t_f - t_i)}\int_{t_i}^{t_f} pdt \tag{2.19}$$

and they should be independent of t_i and t_f for the decomposition to make sense. Substituting Eqns. (2.17) into the Navier-Stokes equation, Eq. (2.14), gives:

$$\begin{aligned} &\frac{\partial \boldsymbol{u}'}{\partial \tau} + (\boldsymbol{U}' \cdot \nabla)\boldsymbol{U}' + (\boldsymbol{u}' \cdot \nabla)\boldsymbol{U}' + (\boldsymbol{U}' \cdot \nabla)\boldsymbol{u}' + (\boldsymbol{u}' \cdot \nabla)\boldsymbol{u}' = \\ &-\nabla p' - \nabla P' + \frac{1}{\mathrm{Re}}\nabla^2 \boldsymbol{U}' + \frac{1}{\mathrm{Re}}\nabla^2 \boldsymbol{u}' \end{aligned} \tag{2.20}$$

Taking the time-average of all terms of Eq. (2.20) and assuming that the mean value of a fluctuating quantity itself is zero gives:

$$(\boldsymbol{U}' \cdot \nabla)\boldsymbol{U}' + \overline{(\boldsymbol{u}' \cdot \nabla)\boldsymbol{u}'} = -\nabla P' + \frac{1}{\mathrm{Re}}\nabla^2 \boldsymbol{U}' \tag{2.21}$$

The conservation equations of the velocity fluctuations are obtained now by subtracting Eq. (2.21) from Eq. (2.20),

$$\frac{\partial \boldsymbol{u}'}{\partial \tau} + (\boldsymbol{u}' \cdot \nabla)\boldsymbol{U}' + (\boldsymbol{U}' \cdot \nabla)\boldsymbol{u}' + (\boldsymbol{u}' \cdot \nabla)\boldsymbol{u}' - \overline{(\boldsymbol{u}' \cdot \nabla)\boldsymbol{u}'} = -\nabla p' + \frac{1}{\mathrm{Re}}\nabla^2 \boldsymbol{u}' \tag{2.22}$$

The perturbed vorticity equation is obtained by a similar procedure. The final fluctuating vorticity conservation equation is:

$$\begin{aligned} &\frac{\partial \boldsymbol{\omega}'}{\partial \tau} + (\boldsymbol{u}' \cdot \nabla)\boldsymbol{\Omega}' + (\boldsymbol{U}' \cdot \nabla)\boldsymbol{\omega}' + (\boldsymbol{u}' \cdot \nabla)\boldsymbol{\omega}' - \overline{(\boldsymbol{u}' \cdot \nabla)\boldsymbol{\omega}'} = \\ &+ (\boldsymbol{\omega}' \cdot \nabla)\boldsymbol{U}' + (\boldsymbol{\Omega}' \cdot \nabla)\boldsymbol{u}' + (\boldsymbol{\omega}' \cdot \nabla)\boldsymbol{u}' - \overline{(\boldsymbol{\omega}' \cdot \nabla)\boldsymbol{u}'} + \frac{1}{\mathrm{Re}}\nabla^2 \boldsymbol{\omega}' \end{aligned} \tag{2.23}$$

On the other hand, the equation governing the time-averaged fluctuating kinetic energy, $\frac{1}{2}\overline{\boldsymbol{u}'.\boldsymbol{u}'}$, is obtained by multiplying Eq. (2.22) by the fluctuation velocity vector, $\boldsymbol{u}'$, and taking the time average of all terms. Thus, the fluctuation kinetic energy budget is written in a scalar form as:

$$\begin{aligned} U'_j \frac{\partial}{\partial X_j}\left(\frac{1}{2}\overline{u'_i u'_i}\right) = -\frac{\partial}{\partial X_j}\left(\overline{u'_j p'} + \overline{u'_i u'_i u'_j} - \frac{2}{\mathrm{Re}}\overline{u'_i s'_{ij}}\right) \\ - \overline{u'_i u'_j} S'_{ij} - \frac{2}{\mathrm{Re}}\overline{s'_{ij} s'_{ij}} \end{aligned} \tag{2.24}$$

where S'_{ij} is the mean rate of strain defined by:

$$S'_{ij} = \frac{1}{2}\left(\frac{\partial U'_i}{\partial X_j} + \frac{\partial U'_j}{\partial X_i}\right) \tag{2.25}$$

and s'_{ij} is the fluctuation rate of strain defined by:

$$s'_{ij} = \frac{1}{2}\left(\frac{\partial u'_i}{\partial X_j} + \frac{\partial u'_j}{\partial X_i}\right) \tag{2.26}$$

The equation for the mean-square vorticity fluctuations, $\frac{1}{2}\overline{\boldsymbol{\omega}'.\boldsymbol{\omega}'}$, is also obtained by multiplying Eq. (2.23) by the fluctuation vorticity vector, $\boldsymbol{\omega}'$, and taking the time average of all terms. The final equation is written in a scalar form as:

$$\begin{aligned} U'_j \frac{\partial}{\partial X_j}\left(\frac{1}{2}\overline{\omega'_i \omega'_i}\right) = -\overline{u'_j \omega'_i}\frac{\partial \Omega'_i}{\partial X_j} - \frac{1}{2}\frac{\partial}{\partial X_j}\left(\overline{u'_j \omega'_i \omega'_i}\right) + \overline{\omega'_i \omega'_j s'_{ij}} + \overline{\omega'_i \omega'_j} S'_{ij} \\ + \Omega'_j \overline{\omega'_i s_{ij}} + \frac{1}{\mathrm{Re}}\frac{\partial^2}{\partial X_j \partial X_j}\left(\frac{1}{2}\overline{\omega'_i \omega'_i}\right) - \frac{1}{\mathrm{Re}}\overline{\frac{\partial \omega'_i}{\partial X_j}\frac{\partial \omega'_i}{\partial X_j}} \end{aligned} \tag{2.27}$$

To understand how the circumferential fluctuations can destabilize the mean flow for the cases where the 3D-flow is stationary and is periodic in the circumferential direction, the dimensionless velocity vector, the vorticity vector, and the pressure are decomposed into a circumferentially-averaged and a circumferentially-fluctuating quantity as follows:

$$u_i = U''_i + u''_i\,,\ \omega_i = \Omega''_i + \omega''_i\,,\ p = P'' + p'' \tag{2.28}$$

where u''_i, ω''_i, and p'' are fluctuating quantities and U''_i, Ω''_i, and P'' are circumferentially-averaged quantities defined as:

$$U_i = \frac{1}{2\pi}\int_0^{2\pi} u_i d\theta\,,\ \Omega''_i = \frac{1}{2\pi}\int_0^{2\pi} \omega_i d\theta\,,\ P'' = \frac{1}{2\pi}\int_0^{2\pi} p d\theta \tag{2.29}$$

By using the decomposition of Eq. (2.28), the governing equation for the circumferentially-averaged kinetic energy, $\frac{1}{2}\overline{\boldsymbol{u}''\cdot\boldsymbol{u}''}$, is:

$$\begin{aligned} U''_j \frac{\partial}{\partial X_j}\left(\frac{1}{2}\overline{u''_i u''_i}\right) &= -\frac{\partial}{\partial X_j}\left(\overline{u''_j p''} + \overline{u''_i u''_i u''_j} - \frac{2}{\mathrm{Re}}\overline{u''_i s''_{ij}}\right) \\ &\quad - \overline{u''_i u''_j} S''_{ij} - \frac{2}{\mathrm{Re}}\overline{\frac{\partial u''_i}{\partial X_j}\frac{\partial u''_i}{\partial X_j}} \end{aligned} \tag{2.30}$$

and the equation for the circumferentially-averaged vorticity fluctuations $\frac{1}{2}\overline{\boldsymbol{\omega}''.\boldsymbol{\omega}''}$ is:

$$\begin{aligned} U''_j \frac{\partial}{\partial X_j}\left(\frac{1}{2}\overline{\omega''_i \omega''_i}\right) &= -\overline{u''_j \omega''_i}\frac{\partial \Omega''_i}{\partial X_j} - \frac{1}{2}\frac{\partial}{\partial X_j}\left(\overline{u''_j \omega''_i \omega''_i}\right) + \overline{\omega''_i \omega''_j s''_{ij}} + \overline{\omega''_i \omega''_j} S''_{ij} \\ &\quad + \Omega''_j \overline{\omega''_i s''_{ij}} + \frac{1}{\mathrm{Re}}\frac{\partial^2}{\partial X_j \partial X_j}\left(\frac{1}{2}\overline{\omega''_i \omega''_i}\right) - \frac{1}{\mathrm{Re}}\overline{\frac{\partial \omega''_i}{\partial X_j}\frac{\partial \omega''_i}{\partial X_j}} \end{aligned} \tag{2.31}$$

The over bar stands now for averaging the terms over the circumferential direction. The circumferentially-averaged and -fluctuating rates, S''_{ij} and s''_{ij}, of strain are:

$$S''_{ij} = \frac{1}{2}\left(\frac{\partial U''_i}{\partial X_j} + \frac{\partial U''_j}{\partial X_i}\right) \tag{2.32}$$

$$s''_{ij} = \frac{1}{2}\left(\frac{\partial u''_i}{\partial X_j} + \frac{\partial u''_j}{\partial X_i}\right) \tag{2.33}$$

2.6 Taylor-Görtler phenomena in the LDC flow problem

The inviscid centrifugal instability mechanism was firstly investigated by Rayleigh (1916). He considered the revolving motion of inviscid fluid with a basic-state velocity $u_\theta(r)$, an arbitrary function of the radial distance r from the rotation axis. Rayleigh derived his criterion of stability that characterized by the following discriminant:

$$\Phi = \frac{d(\Gamma)^2}{r^3 dr} \tag{2.34}$$

where Γ is the circulation defined by:

$$\Gamma = ru_\theta \tag{2.35}$$

and he showed that the necessary and sufficient condition for the existence of inviscid axisymmetric instability is the appearance of any negative value of the discriminant, Φ, in the flow field. This criterion is known as the Rayleigh's circulation criterion. Drazin and Reid (1981) demonstrated that this Rayleigh's criterion is a sufficient condition for the instability of Couette flow, the flow between two rotating coaxial cylinders, of an inviscid fluid. Bayly (1988) proposed the extension of the Rayleigh's centrifugal instability theory to general inviscid 2D flows. He found that the sufficient condition for centrifugal instability is that the streamlines be convex closed curves in some region of the flow. Rayleigh's inviscid theory was extended by Taylor (1923) to study experimentally and theoretically the stability of viscous circular Couette flow. Taylor found that Rayleigh's circulation criterion is only a necessary condition for a centrifugal instability. This is attributed to the stabilizing effect of the viscosity, and thus, the instability is described in term of Rayleigh's discriminant and another new parameter (Taylor number) to consider the viscous effect. The flow in a curved channel (Dean instability problem) and the flow in a boundary layer on a concave surface (Görtler Problem) are other examples of viscous flow that exhibit centrifugal instability (Drazin and Reid, 1981).

Lid-driven cavity flow instability is referred to as Taylor-Görtler instability since it is due to the development of a boundary layer on a concave surface (Görtler) and the flow is characterized by closed streamlines (Taylor). The Görtler number is defined by (Freitas and Street, 1988):

$$G = \frac{U_\infty}{\nu}\sqrt{\frac{\delta_m}{\Re}} \tag{2.36}$$

where δ_m is the momentum boundary layer thickness, $\Re$ is the radius of curvature of the streamlines, and U_∞ is the characteristic velocity out of the boundary layer. The Görtler number is approximated here using the following assumptions (Freitas and Street, 1988): $\delta_m \approx$ the larger size of the resulting Taylor-Görtler vortices, $\Re = D/2 - \delta$, and U_θ is approximately equal to the tangential velocity corresponds to the loop of the radius $\Re$ just next to the momentum boundary layer.

2.7 Energy conservation equation

The present study has considered the forced convection-heat transfer process accompanying the toroidal LDC flow. It is assumed that no new flow phenomena arise because the velocity field is unaffected by the temperature variations. After calculating the velocity field, the temperature distributions can be determined by solving the following differential equation that describes the conservation of energy (Bird et al., 1960):

$$\frac{\partial T^*}{\partial \tau} + \boldsymbol{u} \cdot \nabla T^* = \frac{1}{\mathbf{RePr}} \nabla^2 T^* \tag{2.37}$$

where $T^* = (T - T_c)/(T_h - T_c)$ is the dimensionless temperature, T_c and T_h are the temperatures at the bottom wall (Z = 0) and at the top wall(Z = 1), respectively, and Pr is the Prandtl number defined as:

$$\Pr = \frac{C_P \mu}{k} \tag{2.38}$$

Here, C_P is the fluid heat capacity and k is the fluid thermal conductivity and they are assumed as constant.

The boundary conditions of Eq. (3.37) are defined as follows. The (inner-radius) and (outer-radius) walls are adiabatic, which implies:

$$\left.\frac{\partial T^*}{\partial R}\right|_{R=R_i} = \left.\frac{\partial T^*}{\partial R}\right|_{R=R_o} = 0 \tag{2.39}$$

One of the following boundary conditions are used at the top and the bottom walls:

- Constant wall temperature: $\left.T^*\right|_{z=0} = 0, \left.T^*\right|_{z=1} = 1$ (2.40)

- Constant heat flux: $\left.\frac{\partial T^*}{\partial Z}\right|_{z=0} = \left.\frac{\partial T^*}{\partial Z}\right|_{z=1} = C$ (2.41)

Periodic boundary conditions are assumed in the circumferential direction, that is:

$$\left.T^*\right|_{\theta=0} = \left.T^*\right|_{\theta=\theta_{\max}} \tag{2.42}$$

Since the (inner-radius) and the (outer-radius) walls are assumed adiabatic, the global heat balance requires that:

$$\hbar\left(\left.T^*\right|_{z=1} - \left.T^*\right|_{z=0}\right) = -\frac{k}{D}\left.\frac{\partial T^*}{\partial Z}\right|_{z=1} = -\frac{k}{D}\left.\frac{\partial T^*}{\partial Z}\right|_{z=0} \tag{2.43}$$

where $\hbar$ is the local heat transfer coefficient. A surface-average value for $\hbar$ is given by:

$$\bar{\hbar} = \frac{-D}{\left(T^*\big|_{Z=1} - T^*\big|_{Z=0}\right)} \frac{\int_{R_i}^{R_o}\int_0^{2\pi} k \frac{\partial T^*(R,0,\theta)}{\partial Z} R d\theta dR}{\pi(R_o^2 - R_i^2)} \tag{2.44}$$

The performance of the forced-convection heat-transfer is expressed in term of the average Nusselt number, $\overline{\mathrm{Nu}}$, defined as:

$$\overline{\mathrm{Nu}} = \frac{D\bar{\hbar}}{k} \tag{2.45}$$

3. METHODOLOGY

This chapter describes two experimental facilities mounted as a part of the present research to realize the shear-driven flow of liquid water in an open-cavity of square cross-section and of curvature ratio $\delta = 0.25$ and 0.51. The chapter explains also the experimental and the numerical methodologies utilized to visualize and to simulate the flow.

3.1 Experimental description of the toroidal cavity flow apparatuses

Shear-driven flows of liquid water have been realized experimentally in two toroidal cavities under isothermal conditions. One cavity has been designed in the present study and its curvature ratio is $\delta = D/R_c = 0.51$. The other designed by Cushner (2000) with $\delta = 0.25$, allows to examine the effect of toroid curvature on the flow behavior. Figure 3.1 shows the dimensions of these two cavities.

3.1.1 The experimental apparatus for the toroidal cavity with d= 0.51

The apparatus corresponds to the test section of $\delta = 0.51$ has been mounted at the Laboratory of Hydrodynamic Tunnel of Chemical Engineering Department, Rovira i Virgili University. Figure 3.2 shows a front view of the toroidal cavity apparatus in its assembled form. Liquid water has been pumped from a circular tank (500.0 mm in diameter) into an another one (600.0 mm in diameter) to stabilize the flow and to absorb the disturbances caused by the centrifugal pump. The pump has a constant volumetric flow rate of 1000 L/hr. A recirculating line has been used to adjust the flow rate to the desired Reynolds number. Water flows up through a

Plexiglas feeding tube, 300.0 mm in length and 100.0 mm in diameter. This feeding tube has been connected to the circular mouth of the elliptical mould which has been made of Polyurethane resin, see Fig. 3.1(a), and it has been painted in a black color to reduce the light reflection. Within the mould, the water goes up within a tubular space (85.0 mm vertical length), then it flows through a trumpet-shaped space. The purpose of this trumpet-shaped curvature is to reduce the disturbances of the external flow entering the cavity. Water enters the cavity through a circular channel of width h = 4.0 mm (gap-to-width ratio, $\gamma = h/D$ =0.04). The lid rests on the toroid at three points where three 4.0 mm drill bits, 120 degrees apart, are placed on the upper surface of the outlet section. Three C-clamps have been used to resist any possible vibration caused by the external flow and to hold the lid in position. The external channel flow causes the motion of fluid in the cavity and then leaves through the outlet channel section. The existing water falls down into a collector of square cross-section (800x800x150 mm), and then it has been re-circulated to the circular tank (500.0 mm in diameter) using a centrifugal pump. The outlet section is 55.0 mm long and has the same vertical gap as in the inlet channel section. The external cylinder of the cavity has been made from a 5.0 mm thick transparent Plexiglas tube. The Plexiglas base, the mould, and the external cylinder joints have been perfectly sealed so that no leakage of water has been noticed.

3.1.2 The experimental apparatus for the toroidal cavity with d= 0.25

This apparatus has been assembled at the Aerospace Research Laboratory of Mechanical and Aerospace Engineering Department, University of Virginia. All parts of the test section shown in Fig. 3.1(b) have been made from Plexiglas. The lid has a cusp at its center to stabilize the stagnation location of the fluid. A circular gutter has been implemented in the lid and a circular wall has been built around the outer perimeter of the outlet channel section. This is to have an overflow of water into a gutter instead of water running down the walls of the test section. For further details on the toroid test-section ($\delta = 0.25$), see Cushner (2000). Figure 3.3 show a front view of the toroidal cavity apparatus with $\delta = 0.25$. The cavity sits on three 6" long, ½" diameter rubber-capped bolts distributed 120 degrees apart to provide leveling mechanism for the test section.

Water liquid flows down from 38 L head tank. The height for the head tank is set to 2.5 m to achieve the maximum desired Reynolds number. Then, water passes vertically upward through the rotameter and flow conditioning section, which consists of 20.0 mm in diameter and 400.0 mm long feeding tube. A stainless steel screen has been put at the inlet section of the tube. The first 200.0 mm long of the tube has been filled with a bundle of drinking straws and a second screen is placed at the end of these straws. The next 200.0 mm long has been left to be unobstructed and then the water passes through a third screen which is located at the outlet section of the tube where the trumpet-shaped space of the toroid has been reached. Cushner (2000) has found that the flow in the trumpet-shaped space first decelerates and then it accelerates once it passes 60.0 mm radial distance. Thus, two relatively fine cylindrically-shaped screens have been used to reduce significantly the size and the intensity of the separation bubble. All screen used in the experiments consist of 0.508 mm thick stainless steel wire with 0.2954 mm^2 spaces. The lid sits on three points where three UNC 10-32 fine-thread screws placed 120 degrees apart have been used to determine the vertical distance between the lid and the cavity. Water enters the cavity through a gap of 2.0 mm ($\gamma = 0.04$), it induces the motion of fluid in the cavity and then it leaves through the outlet channel section. After the outlet channel section, water has been driven to the gutter of the lid through an overflow process. Peristaltic pump has been used to recirculate the water from the gutter to the head tank. It has been noticed that the outflow stream of the pump is a mixture of air and water. Hence, a slight vacuum, $P \approx 0.9$ atm, has been applied in the head tank to blow out air from the recirculating water.

3.2 Flow visualization techniques

The open-cavity flow has been visualized using two experimental techniques. Particle Image Velocimetry (Raffel, 1998) has been used for velocity measurements of the flow in the toroidal cavity of δ = 0.51. In the toroidal cavity of δ = 0.25, a rheoscopic fluid (light-reflecting microscopic particles suspended in water) has been used to obtain a qualitative visualization of the flow.

3.2.1 Particle Image Velocimetry (PIV) technique

Particle Image Velocimetry (PIV) has been used to measure the velocity vectors in the (R-Z) plane with θ = 0 and in a nearly square part of (R-θ) mid-plane. The present arrangement of the experimental apparatus with δ = 0.51 has not allowed us to measure the velocities in a vertical planes at specific values of R since the side views of the toroid have been obstructed by the dropping-down water.

Pliolite spherical micro-particles have been used in PIV experiments. These particles are characterized by a high reflectivity and a density of about 1004 Kg/m^3. They range in diameter from 75 to 150 μm. The light sheets used to illuminate planes in the cavity has been provided using a 150 W lamp projector. The light is shone through a thin slit made in a darkness slide and the lens of the lamp projector has be adjusted so that a light sheet of about 1.0 mm thickness has been obtained. The light sheet has directed vertically through the toroid lid to illuminate the (R-Z) plane. It has been oriented horizontally through the side of the cavity to illuminate the (R-θ) planes that seen through the top of the cavity. An electronic RS-170 CCD video camera with a resolution of (640x480) pixels has been used to take a sequence of frames with a sampling frequency of about 18 Hz. The two-frame cross correlation algorithm of Microsoft TSI INSIGHT has been used to determine the particle displacement between two selected frames.

In measuring the velocity vectors in a vertical (*R*-*Z*) plane, the camera should be ideally mounted in the normal PIV system arrangement, e.g., with the camera axis perpendicular to both radial and axial directions. However, the image observed in doing so is distorted in both directions. This is due to the presence of the cylindrical Plexiglas wall between the camera and the illuminated plane. To minimize the distortion problem, the camera has been positioned instead above the lid of the cavity so that it is perpendicular to the radial axis and inclined about the axial axis by around I_1 = 68 degrees; see Fig. 3.4. With this arrangement, only axial distortion of the image appears because of the light refraction among air, Plexiglas cavity lid, and water.

For the purpose of correcting the axial distortion, it has been assumed in the sketch of Fig. 3.4 that the rays of the light, originating at different axial positions, z_{real} , and crossing the Plexiglas cover at different horizontal positions, travel towards the camera with a constant angle $I_{1.}$ The above assumption leads to a linear model, which correlates the real position, z_{real} to the corresponding image one, z_{image} by:

$$z_{real} = a\,z_{image} + b \tag{3.1}$$

The justification for Eq. (3.1) may be obtained as follows. Applying Snell's law (Klein, 1970) between air and glass gives:

$$I_2 = \sin^{-1}\left(\frac{N_{air}\sin(I_1)}{N_{Plexiglas}}\right) \tag{3.2}$$

where, as shown in Fig. 3.4, I_2 is the angle between the light ray in Plexiglas medium and the normal to the horizontal surface. N_{air}, and $N_{Plexiglas}$ are the refraction indexes of air and Plexiglas with values of 1.00 and 1.50, respectively. Applying Snell's law between glass and water gives:

$$I_3 = \sin^{-1}\left(\frac{N_{Plexiglas}\sin(I_2)}{N_{water}}\right) \tag{3.3}$$

where I_3 is the angle between the light ray in the water medium and the normal to the Plexiglas surface and N_{water} is the refraction index of water with a value of 1.33. It is clear from the figure that:

$$\Delta x = thick_{cover}\tan(I_2) \tag{3.4}$$

and,

$$x = \frac{z_{real}}{\tan(90 - I_3)} \tag{3.5}$$

The linear treatment developed here assumes that the extension of the light ray, traveling through the air medium towards the camera, will reach the corresponding image location, z_{image} in Fig. 3.4. Thus,

$$z_{image} + thick_{cover} = (x + \Delta x)\tan(90 - I_1) \tag{3.6}$$

By substituting the results of x and Δx , Eqns. (3.4) and (3.5), into Eq. (3.6):

$$z_{real} = \frac{\tan(90 - I_3)}{\tan(90 - I_1)}\, z_{image} + thick_{cover}\tan(90 - I_3)\left(\frac{1.0}{\tan(90 - I_1)} - \tan(I_2)\right) \tag{3.7}$$

Comparing Eqns. (3.1) and (3.7) gives:

$$a = \frac{\tan(90 - I_3)}{\tan(90 - I_1)} \tag{3.8}$$

and,

$$b = thick_{cover} \tan(90 - I_3)\left(\frac{1.0}{\tan(90 - I_1)} - \tan(I_2)\right) \tag{3.9}$$

Based on this approximated linear model, the axial velocity component will be corrected as:

$$u_z^{real} = \frac{\Delta z_{real}}{\Delta t} = a\,\frac{\Delta z_{image}}{\Delta t} = a\, u_z^{image} \tag{3.10}$$

The linear model of Eq. (3.7) has been verified experimentally for three camera angles, $I_1 = 68^o$, 60^o, and 52^o. Figure 3.5 shows the measured image locations for several values of z_{real}. It is clear in the figure that the linear model agrees with the experimental results for $I_1 = 68^o$. When I_1 is reduced to 60^o and 52^o, the linear approximation does not work well. Hence, the camera has been positioned and inclined about the axial axis by around $I_1 = 68$ degrees.

3.2.2 Rheoscopic fluid flow visualizations

Rheoscopic fluid has been used to provide a qualitative flow visualization in the open-cavity with δ = 0.25. The fluid used is Kalliroscope Corp. AQ-1000 rheoscopic concentrate, which consists of suspensions of 6x30x0.07 μm crystalline platelets in water. When the suspended platelets are put into motion, they orient to align their larger dimension with local shear stress direction thereby making flow patterns visible. In the presence of incident light, rheoscopic platelets will reflect differing intensities light areas such that a striking white floodlight image is produced. The rheoscopic suspension has been added progressively, in 10.0 ml increments, to the gutter of the lid until the concentration is enough to easily view the flow structure. It has been found that a concentration of around 1% by volume is high enough to produce an adequate flow visualization.

A green light beam is generated using a Coherent Innova 70 5-w Argon ion laser and a TSI COLORBURST Multicolor Beam Separator. The beam coming from a TSI fiberoptic probe (Model 9833) is used to produce a light sheet of around 4 mm thickness by passing the beam through a cylindrical lens. The light sheets have been oriented vertically through the toroid lid to view the flow at the vertical planes with R = 3.6, 3.8, 4, 4.2, and 4.4. They are oriented horizontally through the side of the cavity to visualize the flow in the horizontal (R-q) planes with Z = 0.1, 0.3, and 0.5, and 0.7. The 3D-flow behaviors corresponding to these planes have been recorded over a period of about 2 minutes using a commercial video camera. This is in order to observe any time-dependent phenomenon of the vortex flow and instantaneous still images have been acquired from the video records.

3.3 Estimation of uncertainties in the experiment

The sources of uncertainty associated with the experiments arise from experimental and instrumentation errors. Most importantly, the uncertainty of the Reynolds number must be estimated. Equation (2.16) shows that Re is a combination of the channel-width average velocity, $U_{average}$ at $r = R_c$ (see Fig. 1.3), the width of the toroid cross-section, D, the density, r , and the viscosity, m, of the operating fluid. The variations in density and viscosity have been reduced to negligible amounts due to the following reasons. Firstly, in the flow visualization experiments in the cavity with $\delta = 0.25$, a small quantity of rheoscopic fluid (1% by volume) have been mixed with the liquid water. For the PIV experiments in the cavity with $\delta = 0.51$, small amounts (around 2 g) of the Pliolite particles (its density is around 1004 Kg/m^3) have been added to a relatively big quantity (it is around 250 Kg) of liquid water. Secondly, the temperature of the operating fluid has been continuously measured using a Mercury glass-thermometer (the reading uncertainty is ±0.5 ^{o}C). The temperature was nearly constant during the time of running the experiment. Thus, the changes in density and viscosity of water due to temperature variation are considered negligible.

The channel-width average velocity, $U_{average}$, is a function of the radially-averaged axial velocity in the feeding tube, U_{tube}, the feeding tube diameter, d, the radius of curvature of the toroid, R_c, and the gap of the external flow region, h; see Eq. (2.11). The design errors in the toroid test-section and the feeding tube of both cavities ($\delta = 0.25$ and 0.51) do not exceed ±0.3% of the cavity width, and thus the uncertainties in D, d, and R_c, have been considered negligible. Furthermore, the gap of the external flow region has been measured using a dial caliper; the uncertainty of the reading is ±0.005 mm which can be also considered negligible.

The radially-averaged axial velocity in the feeding tube, U_{tube} is calculated from the corresponding volumetric flow rate of liquid water. The flow meters used in the apparatus of δ = 0.25 and 0.51 are graduated in increments of 0.1 gpm and 20.0 L/h, respectively. By estimating the reading uncertainty as half of the smallest graduated increment, the uncertainty in the reading is ±0.05 gpm and ±10.0 L/h for the apparatus of δ = 0.25 and 0.51, respectively. For gap-to-width ratio, $\gamma = 0.04$, the error in the experimental Re is ±6.3% and ±5.7% for the facility of δ = 0.25 and 0.51, respectively.

On the other hand, a possible misalignment of the toroid lid leading to a non-axisymmetric gap width of the external channel will give a significant source of uncertainty in experiments. This source of error has been minimized as follows. The gap width has been measured using the dial caliper at six different circumferential positions. The toroid test section has been leveled carefully by a digital level accurate to 1/10th of a degree. Then, the C-clamps, used to hold the lid in position have been tightened gently.

3.4 Numerical procedure

Calculations have been performed using the CUTEFLOWS-II program, which is a recent evolution of the original CUTEFLOWS code (Humphrey et al., 1995). The acronym CUTEFLOWS stands for Computing Unsteady Three-dimensional Elliptic Flows. The CUTEFLOWS code calculates unsteady incompressible flows in Cartesian or cylindrical coordinates. The original code, developed in the late eighties by the group of J. A. C. Humphrey at UC Berkeley, is globally second order accurate in space and time. It has been successfully tested and applied to many flows geometries, including LDC flow (Humphrey and Phinney, 1996) and flow between corotating disks (Schuler et al., 1990; Humphrey et al., 1992; Humphrey et al., 1995; Iglesias and Humphrey, 1998; and Herrero et al., 1999a, b). The code uses a staggered grid control-volume arrangement to discretize the conservation equations in terms of the primitive variables. Details of the staggered control-volume arrangement may be found in the book of Patankar (1980). The diffusion terms are discretized by central difference approximations. The convection terms are interpolated at the faces of the respective control volumes by means of the QUICK (Quadratic Upstream Interpolation for Convective Kinematics) upwind scheme (Leonard, 1979). A Poisson equation, resulting from the imposition of the mass conservation equation in the scalar control volume, is solved by means of the conjugate gradient method to obtain the pressure field at each time step. A solution procedure akin to the SIMPLE method described by Patankar is used to obtain the velocity corrections that will fulfill the mass and momentum conservation laws simultaneously. A second order explicit Euler method is used to integrate the system of ordinary differential equations resulting from the spatial discretization of the conservation equations in the calculation grids.

The evolution of the code, CUTEFLOWS-II, has been recently developed at the Transport Phenomena research group of the Universitat Rovira i Virgili. The new features of the CUTEFLOWS-II program are the following:

(a) A higher accuracy in the schemes of spatial discretization. CUTEFLOWS-II features a fourth-order accurate centered, and a fifth-order accurate upwind scheme in the diffusion and convection terms, respectively (Rai and Moin, 1991). A pseudo-spectral (Fourier) approximation is also available for flows that feature periodic boundary conditions in one coordinate direction.

(b) Two new Runge-Kutta algorithms, second- and fourth-order accurate, respectively, have been added for the explicit time integration of the discrete conservation equations.

(c) The Poisson equation for pressure is solved more efficiently by means of a refined version of the conjugate gradient method which includes a pre-conditioning of the matrix of coefficients (Golub, 1996).

(d) The code is completely written in Fortran 90. This makes it more flexible. For example, it is not necessary to recompile the whole package each time that the size of the grid, or a particular boundary condition is changed. Also, pre-compiler directives are no longer needed. This makes the new code portable to any operating system with the only requirement of a Fortran-90 compiler that complies with the standards.

(e) The interaction of the user with the code is quite straightforward. It is easy for the user to select between several available options at the input file and to define a new problem from scratch, that is, to specify what are the boundary conditions, the calculations grids, etc.

3.4.1 Code testing

The original CUTEFLOWS code has been used to calculate flows between corotating disks by Schuler et al. (1990), Humphrey et al. (1992, 1995), Iglesias and Humphrey (1998), and Herrero et al. (1999a, b). This type of flow will therefore be employed to test the performance of CUTEFLOWS-II before using it to predict the toroidal flows that are the subject of the present investigation. The test geometry is sketched in Fig. 3.6. It corresponds to the configuration previously used by Herrero et al. (1999a, b) to analyze the constant-property laminar flow and heat transfer in the space between coaxial disks corotating in a cylindrically enclosure. Zero width of the gap between the rim of each disk and the curved enclosure (A = 0) has been assumed in their study. These authors have assessed the performance of CUTEFLOWS program in axisymmetric flow calculations for the configuration shown in Fig. 3.6 at a Reynolds number of $\mathrm{Re} = \rho \Xi R_2{}^2 / \mu = 20565$ (this value of Re corresponds to an angular velocity of $\Xi = 300$ rpm for air at 25 ^{o}C). Calculations have been performed using two grid node distributions: one with (N_RxN_z) = (74x40) nodes and a much finer one with (200x100) nodes in order to check the effect of grid refinement on the calculated results.

Figures 3.7, 3.8, 3.9, and 3.10 show the time records of the axial velocity component at two mid-plane (z/H = 0.5) points located at $R = r/R_2$ = 0.81 and 0.90. These time records correspond to calculations performed with the original CUTEFLOWS (Herrero et. al, 1999a) and with the CUTEFLOWS-II code with both the QUICK and the fifth-order upwind schemes for the convection terms. The calculation on the finer (200x100) calculation grid has been also obtained with CUTEFLOWS-II and the fifth-order accurate scheme. Qualitatively, it is apparent that the periodic behavior of the axial velocity component predicted by CUTEFLOWS is reproduced by CUTEFLOWS-II. Quantitatively, Table 3.1 shows the values of the dimensionless oscillation frequencies and the root-mean-square (rms) values of the axial velocity component obtained from each calculation at the two mid-plane monitoring locations. The dimensionless frequency of the axial velocity predicted by the CUTEFLOWS-II/5th order algorithm in the finest 200x100 grid is $F^{*}= 0.060$ (see Fig. 3.10). This value has been considered as a reference in evaluating the performance of the three algorithms on the (74x40) grid. The original CUTEFLOWS code with the (74x40) grid yields $F^{*} = 0.071$ with a 18% departure from the reference value; see Fig. 3.7. The oscillation frequencies calculated by CUTEFLOWS-II/QUICK and CUTEFLOWS-II/5th order with the (74x40) grid over-predict the reference value by 10% and 6.7%, respectively (see Figs. 3.8 and 3.9). The rms values are not comparable with a reference value for the (200x100) grid because the location of the monitoring points in the two grids do not coincide. Only slight differences have been observed between the rms values predicted by the three algorithms on the (74x40) grid for the mid-plane location $R = 0.81$. In contrast, the percent rms values at the location with $R = 0.90$ are 0.468, 0.248, and 0.277, which have been obtained using CUTEFLOWS, CUTEFLOWS-II/QUICK, and CUTEFLOWS-II/5th, respectively. This means that predictions at the monitoring location with $R = 0.90$ obtained with both CUTEFLOWS-II schemes are similar, so what differs is CUTEFLOWS. In CUTEFLOWS-II/QUICK, the diffusion terms in Eqns. (A.1.2–A.1.4) have been discretized using a fourth-order centered scheme whereas CUTEFLOWS uses second order approximation in the diffusion as well as in the source curvature terms. Such a difference in the discretization schemes is the most probable cause for the discrepancies in the predicted rms velocity values shown in Table 3.1. The use of

QUICK or the fifth-order accurate scheme in the convection terms does however produce only slight differences between the respective results.

Recently, Al-Shannag et al. (2002) have considered the effect of the gap on the corotating disk flow in a fixed cylindrical enclosure. The dimensions of the test geometry are given in Fig. 3.6 but with $A/R_2 = 0.0064$, 0.013, 0.026, 0.052 and 0.077. At $A/R_2 = 0.026$, the 3D numerical results obtained using CUTEFLOWS-II program faithfully reproduce, for the first time, the experimental variations of the mean and rms circumferential velocities measured by Schuler et al. (1990); see Fig. 7 in Appendix B.

Further tests of the code have been performed by comparing our results obtained using CUTEFLOW-II for the LDC flow problem with the corresponding numerical results reported by Albensoeder et al. (2001a) and Spassov (2001); see Sec. 4.2.1.

3.4.2 Calculation grid in the toroidal cavity

The calculation grid of the open-cavity arrangement has been constructed in the (*R*-*Z*) plane as follows. As shown in Fig. 3.11, the grid nodes in the *Z*-direction have been distributed uniformly in the external flow region ($Z > 1.0$). Within the body of the cavity, the spacing between the nodes in the *Z*-direction increases linearly by an expansion factor not larger than 1.2. A uniform grid has been also used in the *R*-direction within the cavity. The radial grid spacing also increases linearly in the outflow region by a factor below 1.2. The grid independence of the calculated results has been examined first. For each Re, a coarse grid has been first used and then it has been gradually refined until the numerical results with the two finest grids coincide.

Two-dimensional (axisymmetric) flow calculations have been performed for the toroidal cavity with δ = 0.51 at Re = 500 and 1000. The numerical study of Spassov (2001) of the LDC flow in a toroidally shaped geometry has reported a steady 2D flow behavior for Re = 500 and for curvature ratios in the range $0 \leq \delta \leq 1.0$. Depending on the toroid curvature ratio, three-dimensionality in the flow appears at critical Reynolds number in the range 500<Re<1000. Therefore, the values Re = 500 and 1000 have been selected to examine the grid independence of the numerical results. Table 3.2 shows the number of grid nodes prescribed in both the axial and the radial directions. The calculations have been initiated from zero values of all variables within the flow domain and the boundary conditions are those described in Sec. 2.2. The results calculated on the different grids have been presented and compared in terms of the centerline velocity profiles.

Figures 3.12 and 3.13 show the centerline velocity profiles obtained in the three grids at Re = 500 and 1000, respectively. It is clear that the velocity profiles obtained with the (32x42) and the (72x72) grids do not agree, while the latter basically coincide with the profiles obtained with the finest (127x127) grid. Therefore, the calculation grids consisting of (N_RxN_z) = (72x72) nodes have been chosen as the optimal one for performing unsteady 3D calculations with Re = 500 and 1000.

For the LDC flow arrangement shown in Fig. 1.1b, a uniform grid consisting of (N_RxN_z) = (72x72) nodes has been used in the *(R-Z)* plane. This grid is 1.75 more refined than the one used in the 3D flow calculations of Spassov (2001). In the LDC flow calculations, the dimensionless integration time step was set as $\Delta\tau \leq 0.01$ to guarantee a stable convergence and to rule out its influence on the results. In the open-cavity flow calculations, the time step was reduced even more $\Delta\tau \leq 0.004$. This is due to the dependence of the integration time step on the minimum spacing of the calculation grid.

In the 3D flow calculations, a periodic boundary condition has been prescribed in the *q*-direction. The same optimal ($N_R x N_Z$) calculation grids used in the 2D flow calculations have been used in the *(R-Z)* plane to perform the 3D ones. The *q*-grid calculation nodes have been distributed uniformly in the circumferential direction. 3D calculations have been firstly performed over the entire domain of the toroid. When few 3D-flow structures have been produced, the *q*-grid has been refined to capture these structures correctly. For the calculation cases in which many 3D-flow structures are obtained, the *q*-grid refinement is of very high cost of calculation. The periodicity of the flow in the θ-direction permits us to re-make these calculations over a sector of angle θ_{max}, which contains at least two full 3D-flow structures. Figure 3.14 summarizes the 3D flow calculation cases performed as a part of the present work.

Re = 20 565, Grid nodes: (N_RxN_z) = (74x40)			
Numerical Algorithm	Dimensionless frequency	RMS x 100	
		R = 0.81	R = 0.90
CUTEFLOWS	0.071	1.070	0.468
CUTFLOWS-II/QUICK	0.066	1.099	0.248
CUTEFLOW-II/5th Order	0.064	1.096	0.277
Re = 20 565, Grid nodes: (N_RxN_z) = (200x100)			
Numerical Algorithm	Dimensionless frequency		
CUTEFLOWS-II/5th Order	0.060		

Table 3.1. Performance of the original CUTEFLOWS and the new code CUTEFLOWS-II.

Re	N_{cavity}	N_{channel}	$N_{\text{total}} = N_{\text{cavity}} + N_{\text{channel}} - 1$
500, 1000	34	9	42
500, 1000	64	9	72
500, 1000	117	11	127

(a)

Re	N_{cavity}	$N_{\text{outlet flow region}}$	$N_{\text{total}} = N_{\text{cavity}} + N_{\text{outlet flow region}} - 1$
500, 1000	21	12	32
500, 1000	51	22	72
500,1000	101	27	127

(b)

Table 3.2. Grid node distributions used in 2D-cavity flow calculations (open-cavity flow arrangement). (a) in the *Z*-direction; (b) in the *R*-direction.

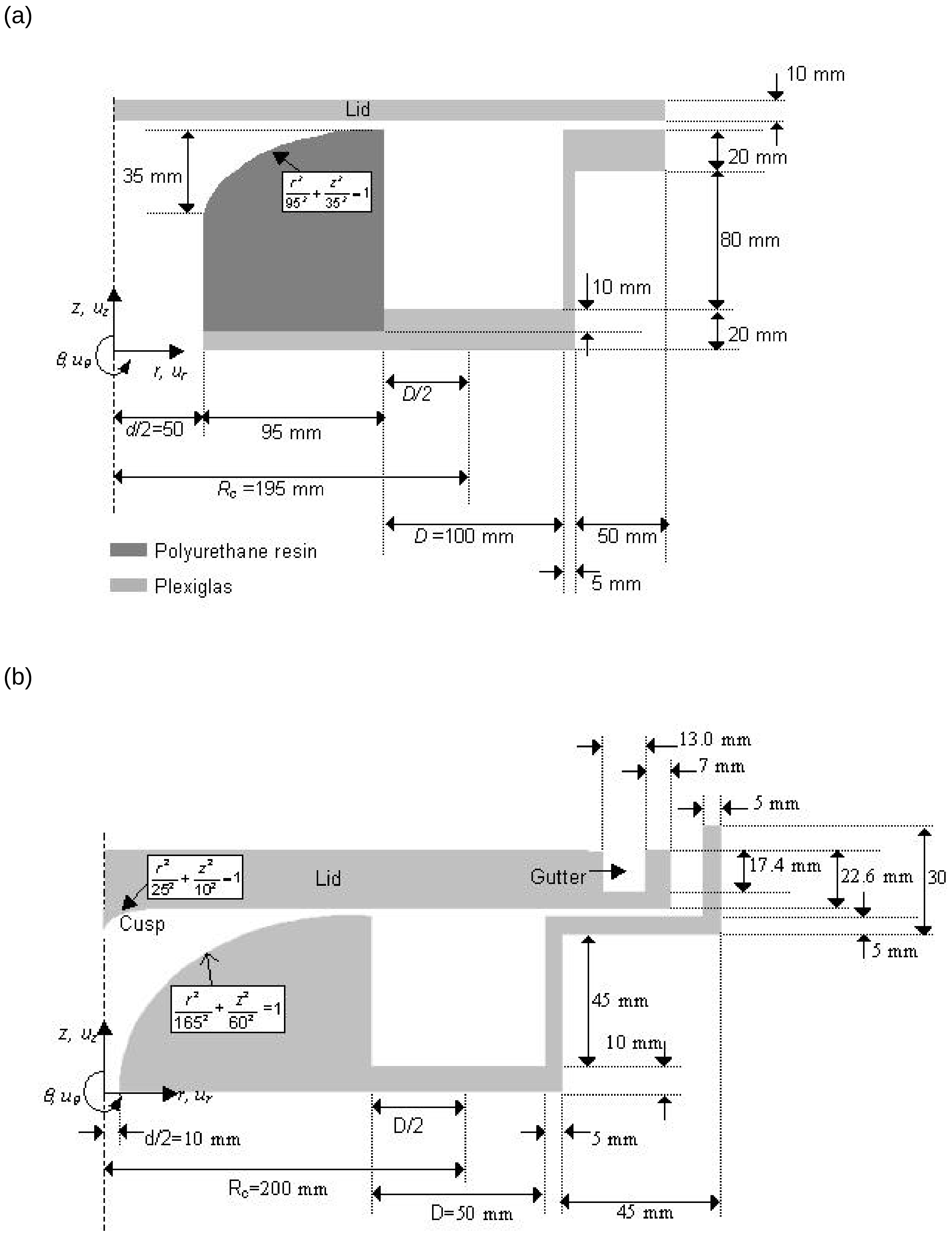

Figure 3.1. Toroidal cavity dimensions with curvature ratio δ = 0.51(a) and 0.25(b).

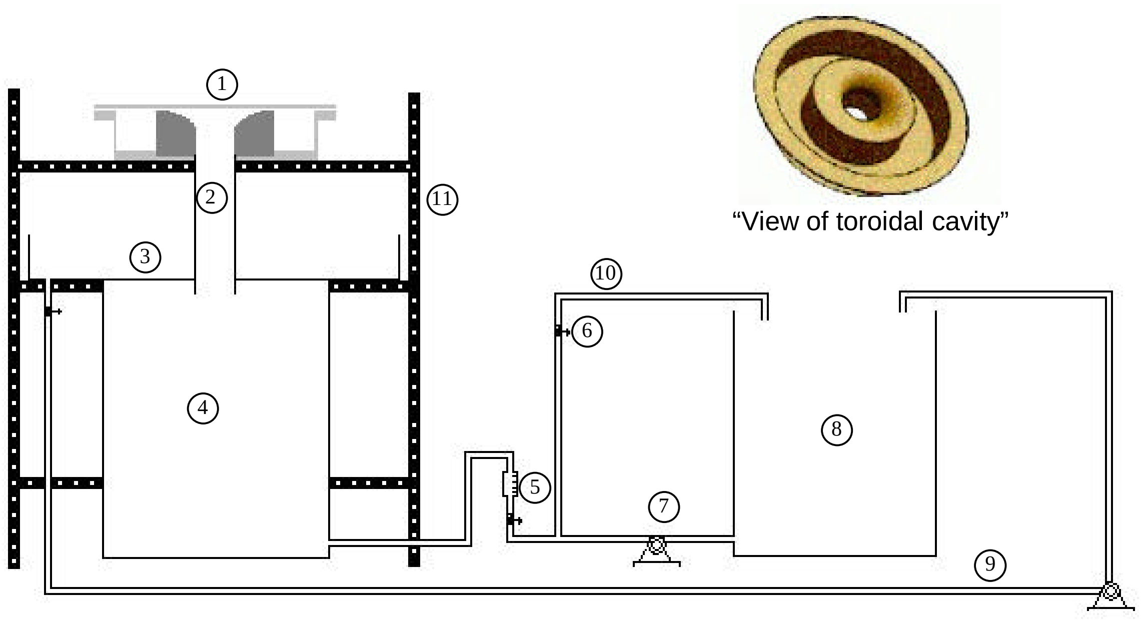

Figure 3.2. Front view of the toroidal cavity apparatus with curvature ratio, δ = 0.51. 1) Cavity, 2) Feeding tube, 3) Dropping water collector of square cross-section (800 x 800 x 150 mm), 4) Circular tank 600 mm in diameter, 5) Rotameter, 6) Regulating valve, 7) Centrifugal pump, 8) Circular tank 500 mm in diameter, 9) PEBD tube, 25 mm in diameter, 10) Recirculating line pump, and 11) Truss structure.

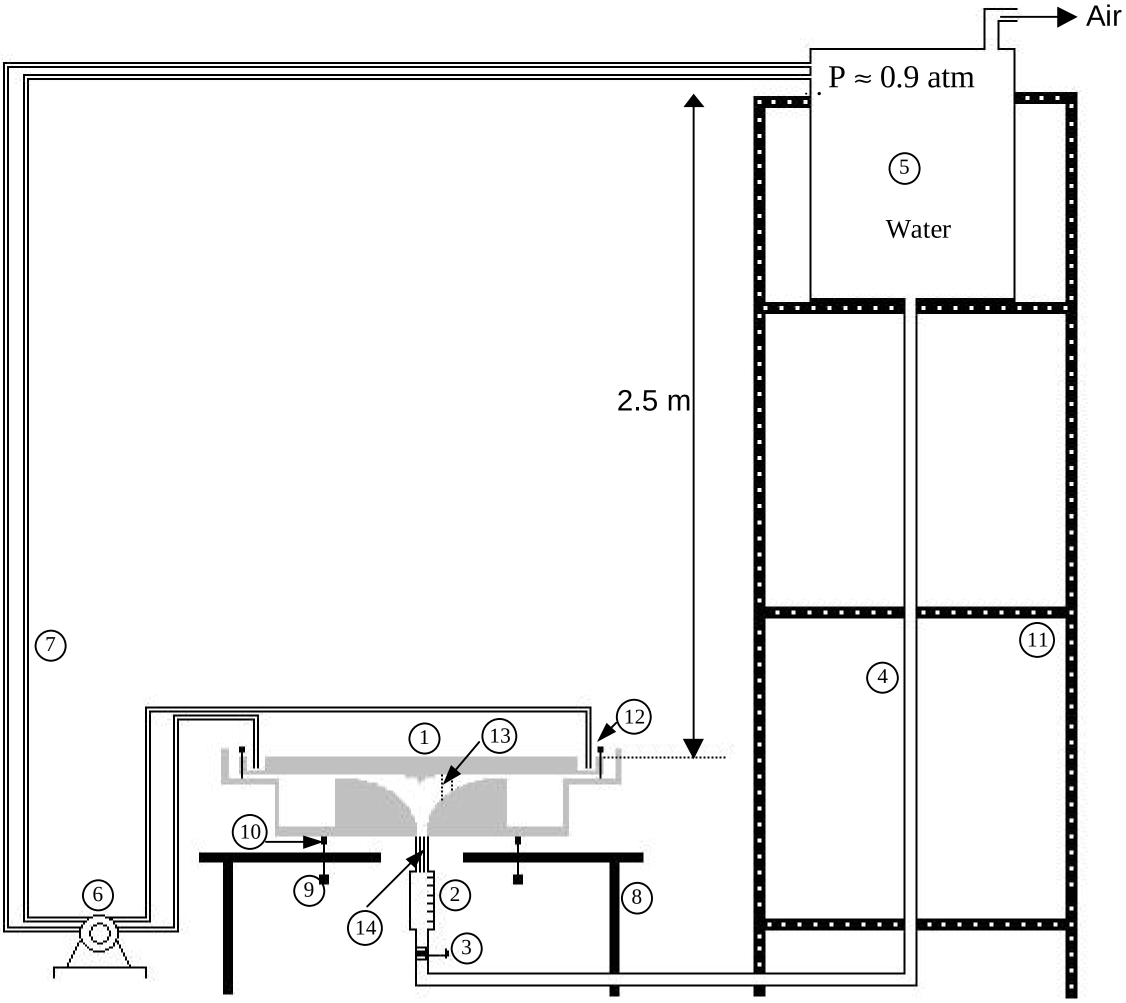

Figure 3.3. Front view of the toroidal cavity apparatus with curvature ratio, δ = 0.25. 1) Cavity, 2) Rotameter, 3) Regulating valve, 4) Tygon tubes 25 mm in diameter, 5) Head tank, 6) Peristaltic pump, and 7) Tygon tubes 8 mm in diameter, 8) Mount table, 9) Bolt (6” long ½ diameter), 10) Rubber doorstop cap, and 11) Truss structure, 12) UNC 10-32 fine-thread screws. 13) Flow stabilizing screens (0.508 mm wire with 0.2954 mm^2 spaces, 14) 20 cm long drinking straws.

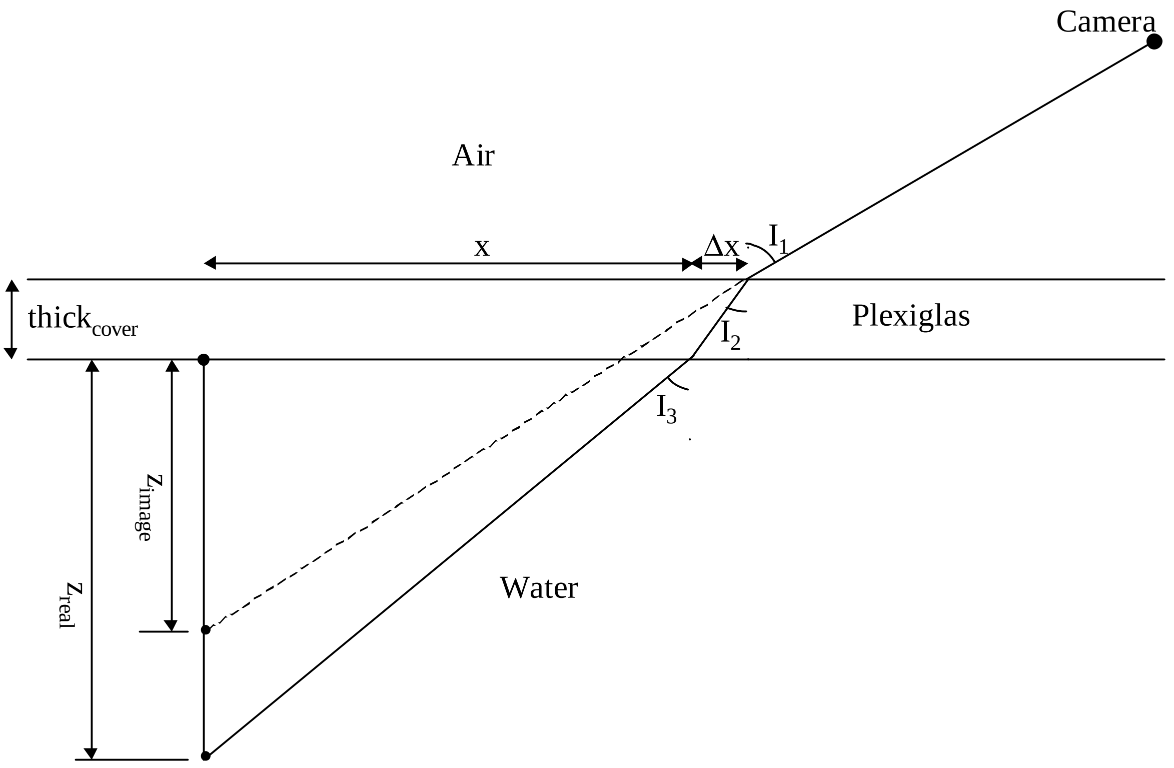

Figure 3.4. Sketch of the refraction of the light from a point at the base of the cavity to the camera lens.

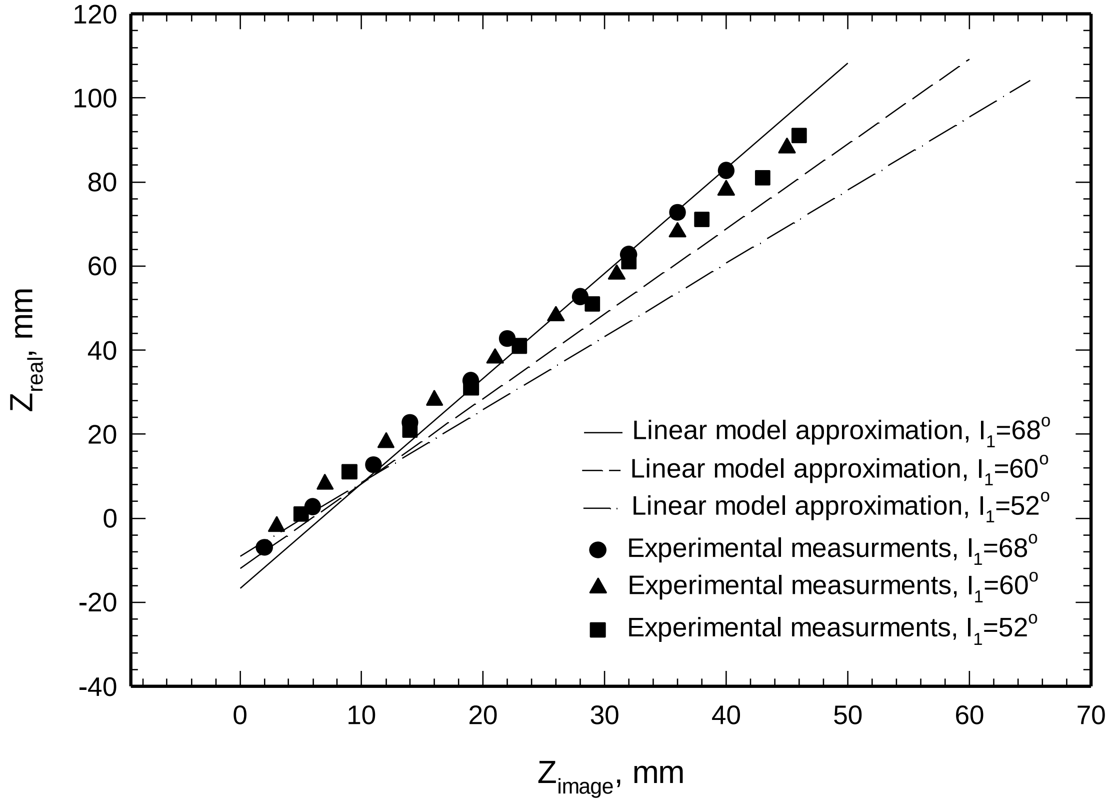

Figure 3.5. Variation of the real axial locations with their corresponding values in the distorted image.

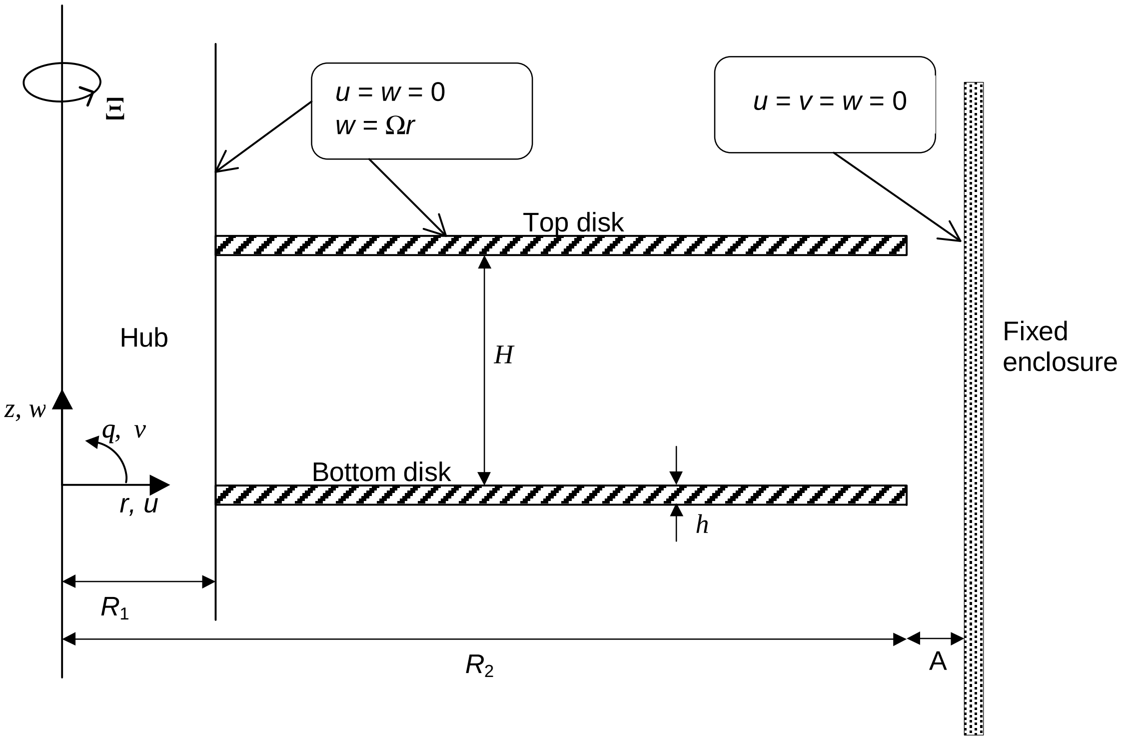

Figure 3.6. Schematic of the test section configuration for the air flow in the unobstructed space between a pair of the disks. In the present study, R_1 = 56.4 mm, R_2 = 105 mm H = 9.53 mm, h = 1.91 mm, A = 0 mm.

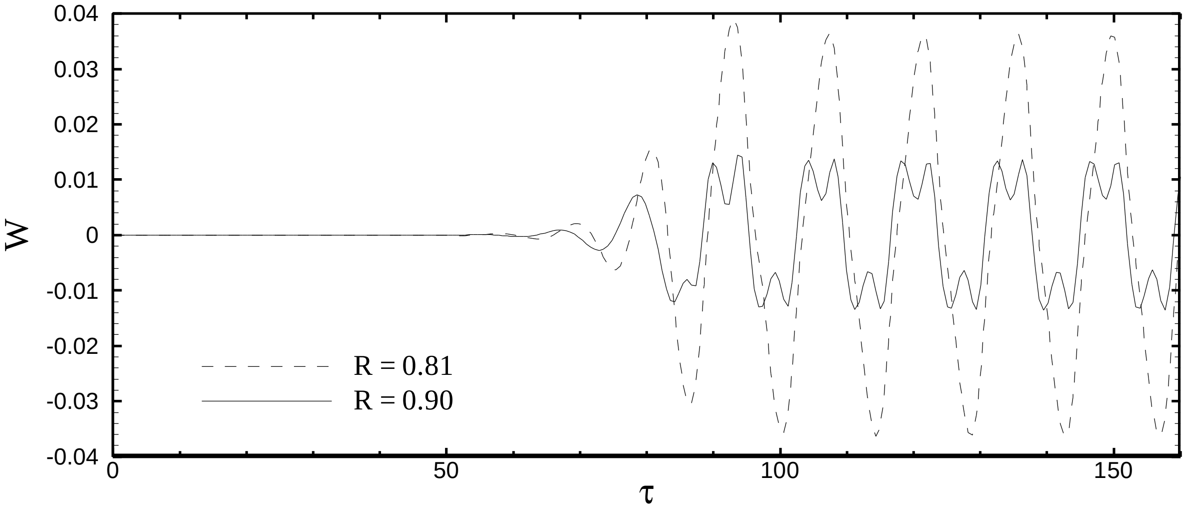

Figure 3.7. Time variation of the axial velocity component at two mid-plane locations with R = 0.81 and R = 0.90, obtained from two-dimensional calculations with Re = 20565, and (N_RxN_z) = (74x40) nodes, using CUTEFLOWS (Herrero et al., 1998a).

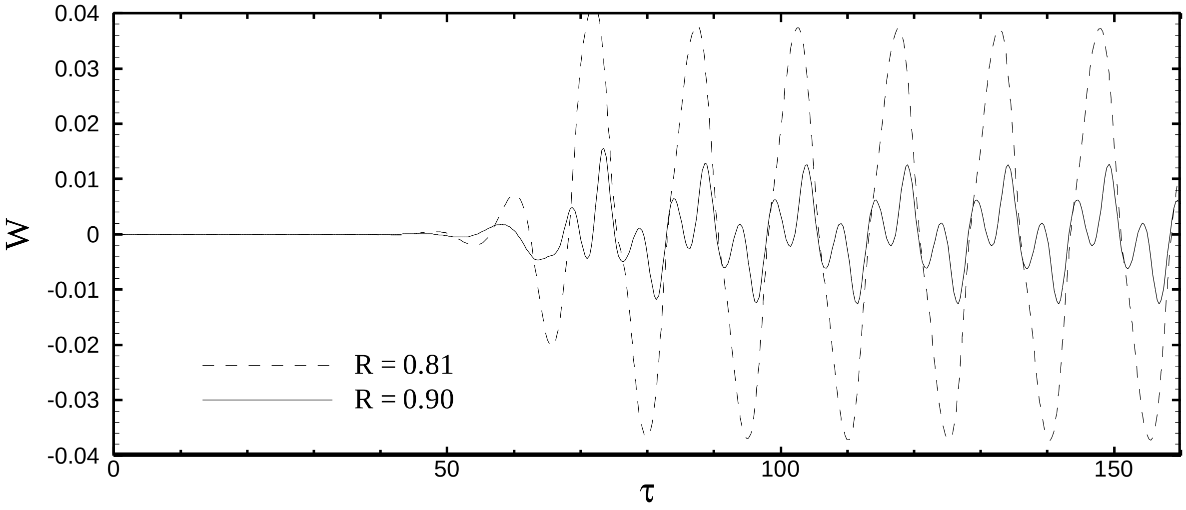

Figure 3.8. Time variation of the axial velocity component at two mid-plane locations with R = 0.81 and R = 0.90, obtained from two-dimensional calculations with Re = 20565, and (N_RxN_z) = 74x40 nodes, using CUTEFLOWS-II/QUICK.

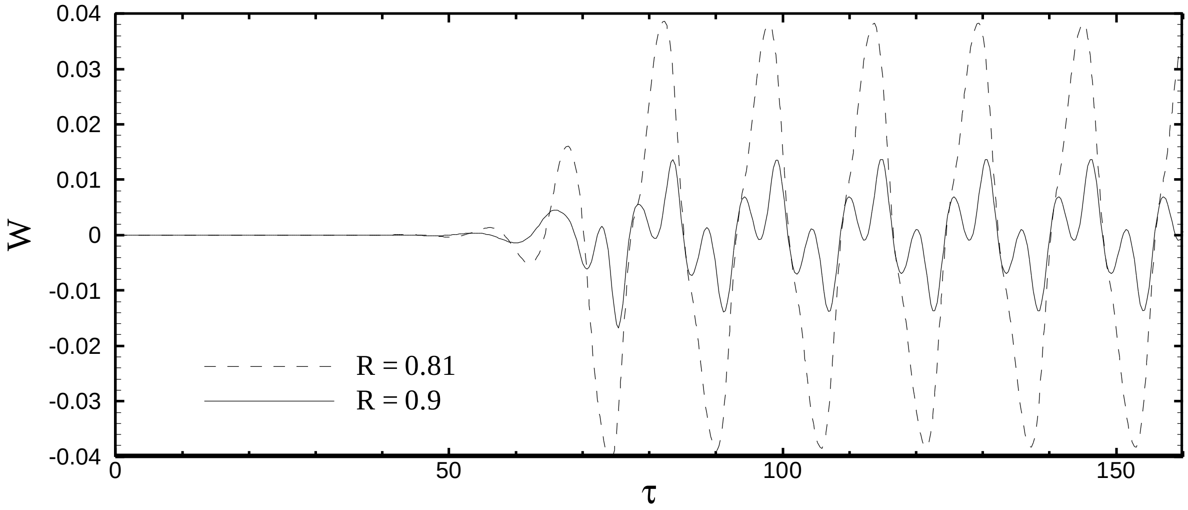

Figure 3.9. Time variation of the axial velocity component at two mid-plane locations with *R* = 0.81 and *R* = 0.90, obtained from two-dimensional calculations with Re = 20565, and (N_RxN_z) = 74x40 nodes, using CUTEFLOWS–II/5th order.

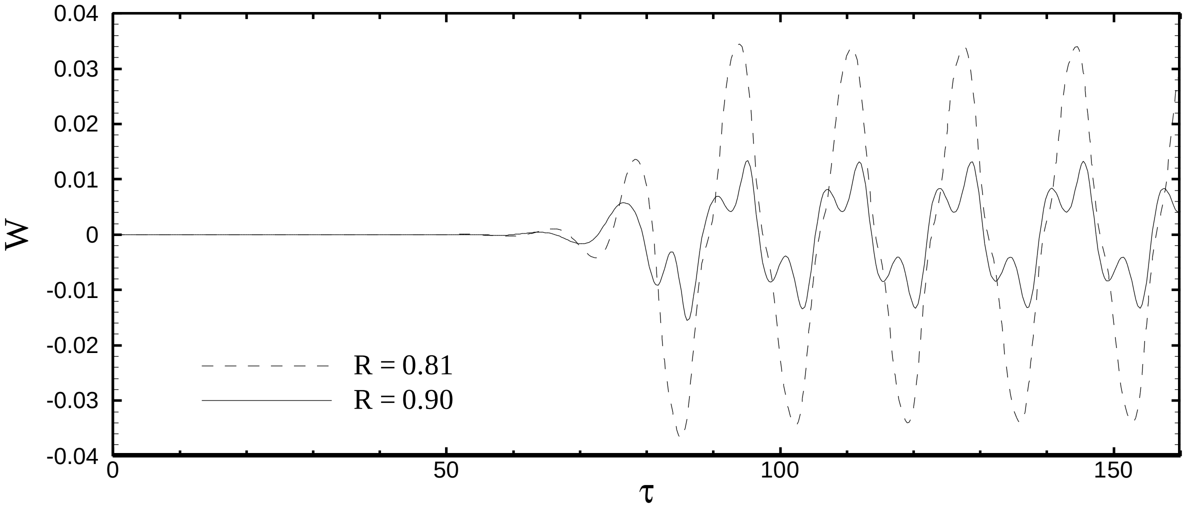

Figure 3.10. Time variation of the axial velocity component at two mid-plane locations with *R* = 0.81 and *R* = 0.90, obtained from two-dimensional calculations with Re = 20565, and (N_RxN_z) = 200x100 nodes, using fourth-order CUTEFLOWS – II/5th order.

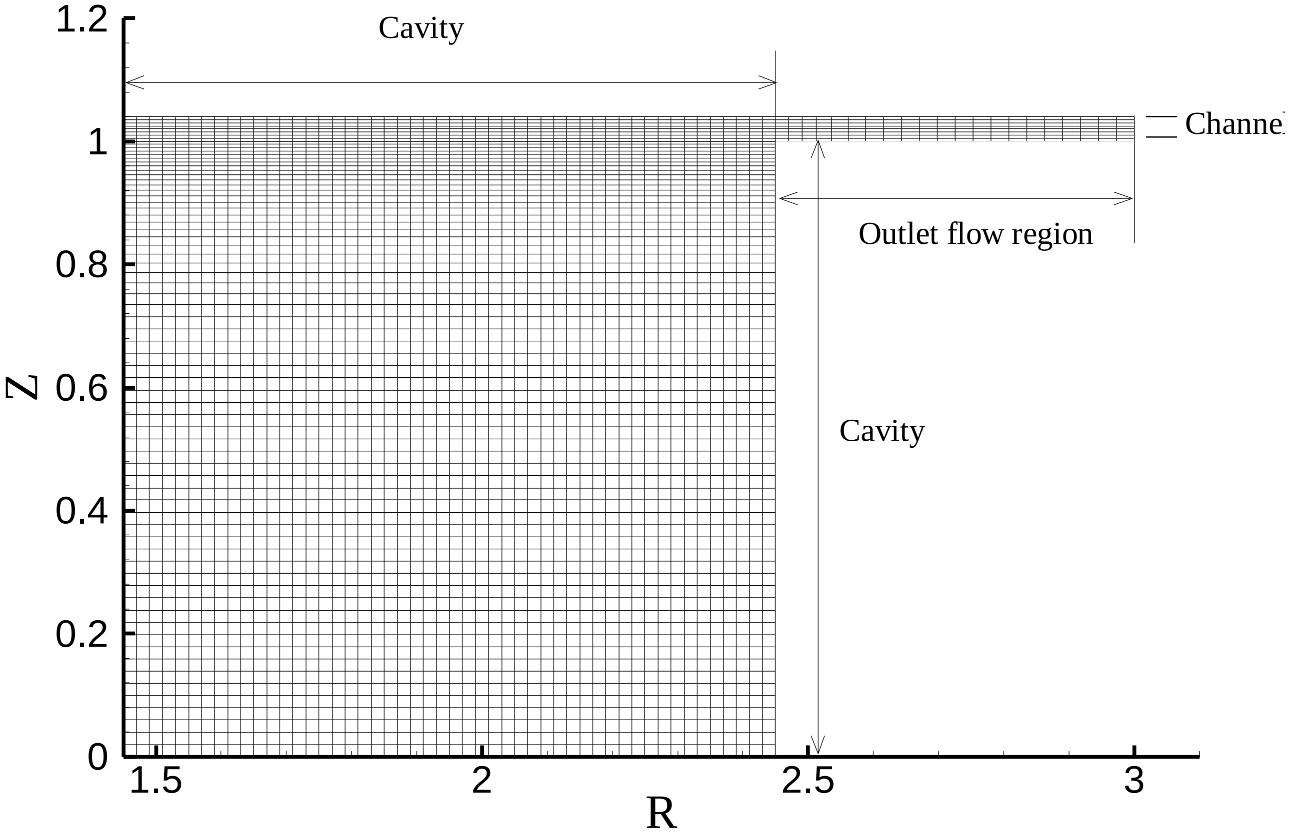

Figure 3.11. Schematic of the calculation grid in the (*R*-*Z*) plane of the open-cavity arrangement.

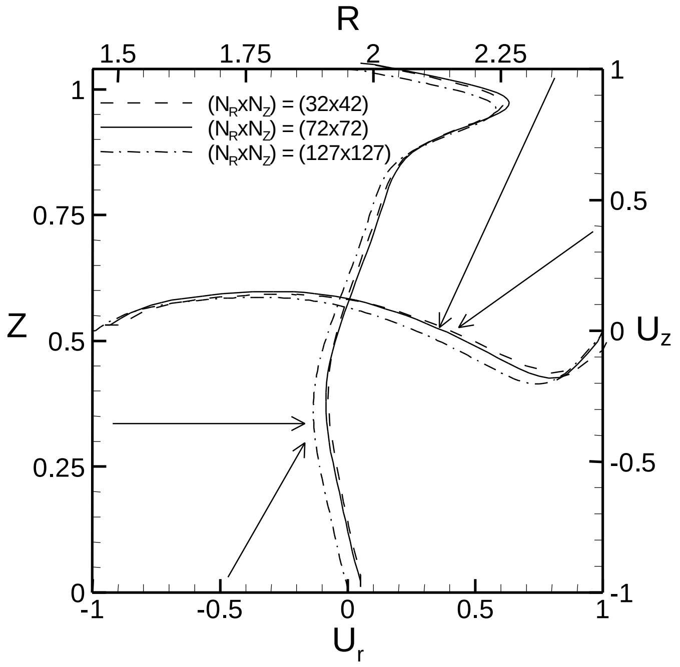

Figure 3.12. Velocity profiles along the horizontal and vertical centerlines, obtained from 2D calculations for Re = 500 with three different grids.

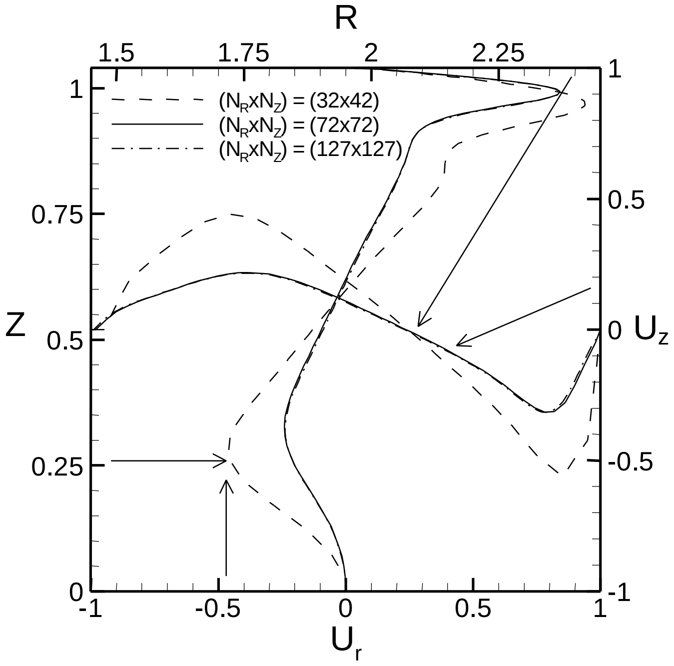

Figure 3.13. Velocity profiles along the horizontal and vertical centerlines, obtained from 2D calculations for Re = 1000 with three different grids.

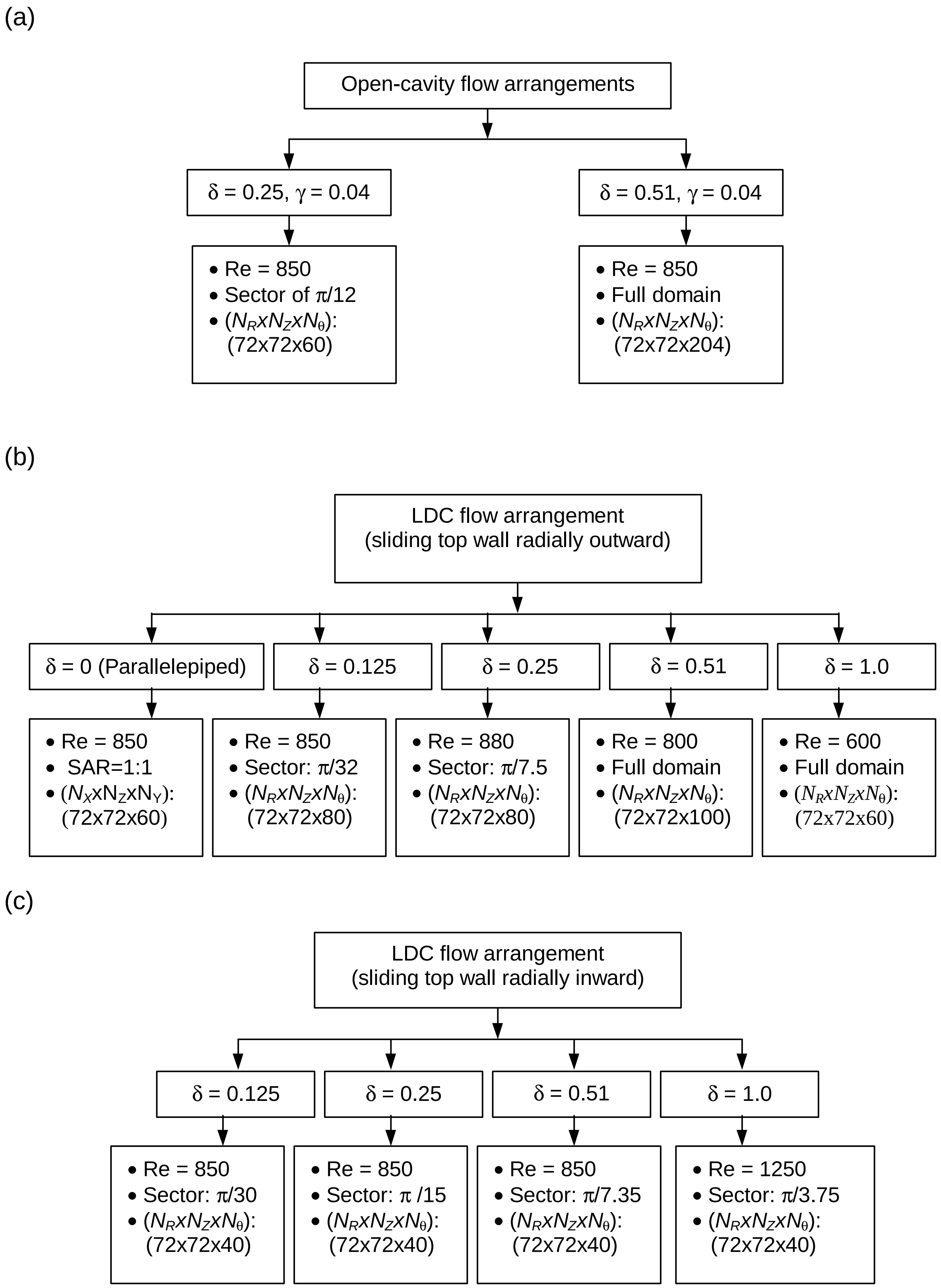

Figure 3.14. Summary of the 3D flow calculations performed as a part of the investigation. (a) Open-cavity flow arrangement, (b) LDC flow arrangement (sliding top wall radially outward), and (c) LDC flow arrangement (sliding top wall radially inward).

4. RESULTS AND DISCUSSION

4.1 Experimental results

The experiments have focused on the 3D-flow features in the open-cavity shown in Fig. 1.3. The flow has been viewed through the top and the downstream (outer-radius) walls of the toroid using a light sheet. During the beginning of the experiment, the fluid is allowed to stabilize and remove transients for a period of about 10 minutes. When the experiment has been run at low Reynolds numbers, the fluid in the external channel region penetrates largely into the cavity. Unfortunately, it was not possible to realize 2D LDC flow expected at low Reynolds numbers. The external flow penetration has been reduced by increasing the gap-to-width ratio to the maximum possible value γ = 0.04 and by running the experiment at higher Reynolds numbers.

Flow visualizations using a rheoscopic fluid have been performed for the flow with δ = 0.25, γ = 0.04, and Re = 1000±63. Figure 4.1(a)-(c) provide instantaneous snapshots, of the flow in the (R-θ) planes with Z = 0.1, 0.3, and 0.5, respectively. As shown in Fig. 4.1(a), at Z = 0.1, the counter rotating Taylor-Görtler pairs aligned in radial direction separate the flow into 3D structures near the bottom of toroid. These structures have the same shape and size. Each one of them is related to one vortex pair. It has been observed that the 3D structures are distributed periodically over the whole circumferential domain. Three of these structures are contained in a sector of about 21 degrees. Thus, the total number of the vortex pairs in the entire domain has been approximated as N = 51±1. For toroidal cavity flows, the wavenumber, κ, is defined as $\kappa = 2\pi/(\lambda/D) = ND/R_c = \delta N$; where λ is the dimensional wavelength. Based on this definition, the flow in the toroid with δ = 0.25 and γ = 0.04 is characterized by an experimental wavenumber, $\kappa = 12.75 \pm 0.25$. At larger axial location (Z = 0.3 and 0.5), the circumferentially periodic vortices are aligned near the upstream (inner-radius) wall and orient themselves in the axial direction (normal to the paper); see Fig. 4.1(b) and (c). As can be seen in Figs. 4.2(a)-(e), the 3D flow structures in the vertical planes with R = 3.6, 3.8, 4.0, 4.2, and 4.4 are located near the bottom wall. Close to the downstream (outer-radius) wall at R = 4.2 and 4.4, other 3D flow structures appear near the external channel region. During the real-time observation of the flow, it is noticed that the vortices disappear and reappear alternatively over a period on the order of one minute. This unsteady flow regime is similar to the one observed in the same toroid with $\gamma = 0.015$ and $\mathrm{Re} = 5000$ (Cushner, 2000; Humphrey et al., 2001, 2002(appendix C)).

The particle image velocimetry (PIV) technique has been used to measure the flow of liquid water in the toroidal cavity shown in Fig. 1.3 with δ = 0.51 and γ = 0.04 at Re = 1000±57. Figure 4.3(a) shows the experimental velocity vectors in the (R-Z) plane with θ = 0. In the PIV flow visualizations, the statistical cross-correlation algorithm deploys a uniform grid on the measurement section. The height and the width of each grid cell must be greater than the displacement of the tracer particles. As shown in the figure, the PIV system is unable to capture the velocity vectors at the upper part of the vertical plane, where the velocity is highest. A primary flow cell appears to occupy the bulk of the toroid cross-section. Null values of the velocity vectors appear also in the lower part of the plane because of the too low velocity values. The measured velocity vectors in a nearly square part of the (R-θ) mid-plane are shown in Fig. 4.3(b). They demonstrate the presence of three-dimensional structures in the toroidal cavity flow at the experimental Reynolds number Re = 1000±57. One pair of TGV appears in the (R-θ) plane of the figure, which corresponds, to a sector of a round 23 degrees. The total number of three-dimensional flow structures in the toroid is about $N = 16 \pm 1$ and thus, the flow is characterized by a wavenumber $\kappa = 8.16 \pm 0.51$.

4.2 Numerical results

Unsteady three-dimensional calculations have been performed for the shear-driven cavity of both LDC and open-cavity flow arrangements sketched in Fig 1.1(b) and Fig. 1.3, respectively. Calculations have been realized using a Kernel PC machine with a 900 MHz Intel processor and 1.0 Gbytes of RAM and a AT/AT compatible PC machine which has two 1800 MHz AMD processors and 2.0 Gbytes of RAM. All 3D-flow calculation cases and their corresponded grids have been described in Sec. 3.4.2. The 3D calculation grid, for example, of the open-cavity flow arrangement consists of (N_RxN_zxN_θ) = (72x72x204) nodes and occupies around 410 Mbytes of RAM. The calculation CPU-times are found to be 8.9 hours, using the 900 MHz Intel processor, and 4.0 hours, using the 1800 MHz AMD processor, for a dimensionless integration time of τ = 10.

4.2.1 Toroidal lid-driven cavity flow (sliding the top wall radially outward)

The LDC flow arrangement in which the motion is induced by sliding the top flat wall radially outward, see Fig. 1.1(b), has been considered first in order to investigate the flow instability cleanly, that is, excluding the effect of the external channel flow. The effect of the curvature ratio of the toroid has been studied by performing unsteady 3D calculations for δ = 0 (parallelepiped), 0.125, 0.25, 0.51, and 1.0. For the parallelepiped lid-driven cavity, a steady mode of $\kappa = 15.7$ has been obtained at Re = 850. This result is in excellent agreement with the corresponding result reported by Albensoeder et al. (2001a) and by Spassov (2001). The numerical results presented in this subsection are in excellent agreement with the corresponding results found by Spassov (2001).

Toroid with δ = 0.125. A steady mode with $\kappa = 16.0$ has been found at Re = 850. The toroidal cavity of small curvature has the same flow behavior of the parallelepiped cavity. The velocity vector plots in the (R-θ) mid-plane, Fig 4.4(a), and in the (Z-θ) mid-plane, Fig 4.4(b), present counter-rotating TGV near the upstream (inner-radius) wall and near the bottom of the toroid, respectively.

The three-dimensional structures of TGV have been visualized in the entire field of the toroid by plotting isosurfaces of helicity, $\Pi = \boldsymbol{u} \cdot \boldsymbol{\omega}$, the dot product of velocity and vorticity. Note that the axisymmetric flow has zero helicity. The velocity vector plots shown in Figs. 4.4(a) and (b) and the isosurfaces of helicity shown in Fig. 4.4(c) indicate the presence of the 3D-vortex flow in a region between the upstream wall and the bottom of the cavity.

Toroid with δ = 0.25. A time-dependent 3D flow has been obtained at Re = 880. Figure 4.5 displays the time-variations of the three velocity components at $(R,Z,\theta) = (4,0.25,0.06\pi)$. The time records show time-periodic behavior with a dimensionless oscillation frequency $F^* = 2\pi/\Lambda^* = 0.556$, where $\Lambda^* = \Lambda U_{average} / D$ is the dimensionless period of oscillation. The three-dimensional flow is also periodic in the θ-direction with a wavenumber $\kappa = 7.5$.

The dynamics of the TGV has been examined next; movies of the velocity vectors in a vertical and horizontal planes of the toroid have been obtained over the period of oscillation to watch the evolution of the flow. The instantaneous velocity vectors of Figs. 4.6(a) and (b) clearly show that the counter-rotating vortices appear to alternate between two identical but spatially displaced states of motion during half cycle of oscillation ($\Lambda^*/2$). The sizes, shapes, and the number of TGV at the times $\tau_1 = 2720$ and $\tau = \tau_1 + \Lambda^*/2 = 2725.65$ are exactly the same. Relative to a fixed reference point, the projection of the two pairs of TGV shown in Figs. 4.6(a) and (b) undergo a circumferential displacement of half wavelength ($\lambda/2$). Owing to this circumferential displacement, the structures of the fluctuating flow appear to alternate the sense of rotation periodically with time; see Figs. 4.7(a) and (b). In addition to that, the number of the structures of the time-averaged flow has been doubled and thus, the average wavelength is reduced to the half; see Fig. 4.8. Indeed, from Eulerian viewpoint, movie would shows time-periodic alternation in the sense of rotation of TGV every $\Lambda^*/2$.

A time sequence of isosurfaces of helicity has been obtained over the period of oscillation Λ^* with dimensionless time steps of $\Lambda^*/32$ (beginning with $\tau_1 = 2720$). The circumferential domain consists of two wavelengths. Figures 4.9(a)-(f) show the evolution of TGV structures in the form of isosurfaces plots of helicity every $\Lambda^*/6$. As shown in Fig. 4.9(a), the isosurfaces indicate that the 3D structures of TGV are aligned between the bottom and the upstream wall of the toroid. During the first half of the period of oscillation, Figs. 4.9(a)-(d) show that the two pairs of TGV are decaying and other two pairs are appearing in new positions with a circumferential displacement of $\lambda/2$. The new pair will decay during the second half of Λ^* and the old pairs will be reproduced, see Figs. 4.9(d), (e), (f), and (a).

Toroids with δ = 0.51 and 1.0. A steady mode has been found at $Re = 800$ for $\delta = 0.51$ and at $Re = 600$ for $\delta = 1.0$. Figures 4.10(a) and (b) present the velocity vectors for $\delta = 0.51$ in the (Z,θ) and (R,θ) mid-planes, respectively. Five pairs of TGV are seen in the entire circumferential domain. Figures 4.11(a) and (b) show that for $\delta = 1.0$, three pairs of TGV appear in the (Z,θ) and (R,θ) mid-planes. Thus, the 3D flow is characterized by a steady mode of long wavelength, $\kappa = 2.0 - 3.0$, at large curvature ratios.

In addition, the 3D flow structures have been visualized by the helicity isosurfaces plotted in Fig. 4.11(c) for $\delta = 1.0$. The axially aligned structures near the upstream (inner-radius) wall depict the region for the presence of TGV. Other circumferentially aligned 3D structures appear near the core of the toroid.

4.2.2 Toroidal lid-driven cavity flow (sliding the top wall radially inward)

Unlike the flow in the parallelepiped LDC, the effect of the curvature of the toroidal cavity is to accelerate/decelerate the fluid of the main circulation cell. The present study has examined numerically the effect of this acceleration/deceleration process on the flow behavior. Three-dimensional calculations have been performed for the LDC flow arrangement, in which the fluid motion is generated by sliding the top wall of the toroid radially inward. The numerical solutions show that the toroidal cavity 3D-flow in this arrangement is steady for all discrete values of the curvature ratios (δ = 0.125, 0.25,0.51, and 1.0) considered. For δ = 0.125, 0.25, and 0.51, a three-dimensional flow has been obtained at Re = 850. When the curvature of the toroid has been increased to $\delta = 1.0$, a higher value of Reynolds number, Re = 1250, has been required to generate a steady 3D flow.

Figures 4.12 (a)-(d) present one pair of the counter-rotating TGV in a sector of $\pi/60$, $\pi/30$, $\pi/14.7$, and $\pi/7.5$ for δ = 0.125, 0.25, 0.51, and 1.0, respectively. As the curvature ratio increases, the total number of TGV in the toroid increases in a way such that the wavenumber, $\kappa = \delta N$, will remain constant and equal to $\kappa = 15$. Therefore, this LDC flow is characterized exactly by the same type of mode predicted in the present study and reported by Albensoeder et al. (2001) and Spassov (2001) for the rectangular LDC flow case. The isosurfaces of helicity in Fig. 4.13 show three-dimensional flow structures distributed uniformly near the upstream (outer-radius) wall and the bottom of the toroid.

4.2.3 Toroidal shear-driven cavity flow (open-cavity arrangement)

Unsteady 3D calculations have been performed for the open-cavity sketched in Fig. 1.3 for curvature ratios δ = 0.25 and 0.51 and a gap-to-width ratio of γ = 0.04. They have been firstly performed over a sector of the toroid where periodic boundary conditions have been prescribed in the θ-direction. These 3D calculations have yielded steady axisymmetric solutions for Reynolds numbers below Re = 850 in the toroid with δ = 0.51 and for Re < 1000 in the toroid with δ = 0.51.

Figures 4.14(a) and (b) show isocontours of dimensionless stream-function at Re = 800 for the toroids with δ = 0.25 and 0.51, respectively. The streamlines show some encroachment of the external flow into the cavity. These plots give an overall picture of the steady axisymmetric flow pattern. The flow structure is characterized, as in the LDC flow problem, by a primary vortex near the geometric center of the toroid and a pair of secondary weaker eddies develop in the lower corners of the cavity. For the two cases investigated, the curvature of the cavity has little effect on the axisymmetric flow structure which is similar to the steady 2D rectangular LDC flow structure discussed in Sec. 1.1.1.

Three-dimensional calculations have been performed over the entire circumferential domain of toroid. The 3D solutions corresponding to δ = 0.25 and 0.51

have shown a similar 3D flow behavior. Thus, only numerical results obtained for $\delta = 0.51$ have been presented and discussed in this section.

Figures 4.15(a)-(c) show the calculated time records of the axial, radial, and circumferential velocity components, respectively, at location with $(R,Z,\theta) = (1.95,0.25,0.22\pi)$. In contrast to the corresponding LDC case with $\delta = 0.51$, the three-dimensional flow is time-periodic with a dimensionless frequency of $F^* = 0.154$. This value is 3.61 times smaller than the dimensionless frequency of the LDC flow with $\delta = 0.25$. It is clear that the external channel flow affects the 3D-flow behavior of the toroidal cavity.

The instantaneous distribution of the circumferential velocity component in the horizontal (R-θ) planes ($Z = 0.1$) is shown in Fig. 4.16. As can be seen, seventeen flow structures are distributed uniformly along the circumferential direction. Thus, the calculated 3D flow in a toroid with $\delta = 0.51$ and $\gamma = 0.04$ has a wavenumber $\kappa = 8.67$ at Re = 850. An identical wavenumber has been obtained in a toroid with $\delta = 0.25$ and $\gamma = 0.04$ at Re = 1000. This wavenumber value is in a good agreement with the experimental wavenumber, $\kappa = 8.16 \pm 0.51$ obtained from the PIV measurements for the open-cavity case of $\delta = 0.51$ and $\gamma = 0.04$. Although 3D calculations predict the same wavenumber for the two toroids investigated, the experimental one corresponding to $\kappa = 13.0 \pm 0.25$ for $\delta = 0.25$ deviates from the calculated one.

Figure 4.17 displays the instantaneous velocity vectors in the horizontal (R-θ) plane with Z = 0.62 at the instant $\tau = 3440$. The figure shows the pairs of counter-rotating TGV distributed near the upstream (inner-radius) wall and oriented in the axial direction (normal to the paper). The instantaneous velocity-vector plots in the vertical (Z-θ) mid-plane show the pairs of counter-rotating TGV near the bottom of the cavity oriented in the radial direction; see Figs. 4.18(a) and (b). The dynamic behavior of TGV explained in Sec. 4.2.1 for the LDC flow case (δ = 0.25) has been reproduced in this open-cavity arrangement.

Figure 4.19 presents instantaneous isosurfaces with dimensionless helicity $\Pi = \pm 0.04$ in one-quarter of the toroid. The isosurfaces of helicity suggest that the counter-rotating vortex tubes occupy banana-like regions near the upstream (inner-radius) wall. Smaller structures with non-zero helicity are also observed near the external flow region and near the downstream (outer-radius) wall.

4.2.4 Kinetic energy and vorticity analysis

The kinetic energy and vorticity transfer rates corresponding to circumferential fluctuations have been calculated for the flows of steady modes. When the flow is time-dependent, the transfer rates corresponding to time-fluctuations have been estimated.

4.2.4.1 Circumferentially-fluctuating kinetic energy and vorticity budgets

Equation (2.30) has been used to estimate the rates of the dissipation and the production of the circumferentially-fluctuating kinetic energy. All terms of Eq. (2.30) have been firstly calculated. For all 3D steady modes, the second and the third terms on the right-hand side of the equation dominate the kinetic energy balance and the other terms are negligible. Hence, the equation is reduced to:

$$0 = \mathrm{P}''_E + D''_E \tag{4.1}$$

where $\mathrm{P}''_E = -\overline{u''_i u''_j} S''_{ij}$ and $D''_E = -\frac{2}{\mathrm{Re}} \overline{s''_{ij} s''_{ij}}$ are the mean rates of production and dissipation of the fluctuating kinetic energy, E'', respectively.

Figure 4.20 shows isocontours of the mean quantities of the production, P''_E, and the dissipation, D''_E of the fluctuating energy in the (R-Z) plane for the LDC flow case (sliding the top wall radially outward) with δ = 0.125. The isocontours of P''_E presented in Fig. 4.20(a) demonstrate the production of TGV in the same region visualized by the isosurfaces of helicity; see Fig. 4.4(c). As shown in Fig. 4.20(b), the TGV are dissipated in the region near the upstream wall.

In this context, it is even more interesting to analyze the production and the dissipation rates of the fluctuating vorticity; see Eq. (2.31). On calculating all terms of the equation, it is found that the spatial variations of all mean quantities except Ω''_i and U''_i, the production $\overline{\omega''_i \omega''_j s''_{ij}}$, and the mixed production $\Omega''_j \overline{\omega''_i s''_{ij}}$ are negligible. Thus, Eq. (2.31) is reduced to:

$$0 = \mathrm{P}''_1 + \mathrm{P}''_2 + D''_\omega \tag{4.2}$$

where $\mathrm{P}''_1 = -\overline{u''_j \omega''_i} \dfrac{\partial \Omega''_i}{\partial X_j}$, and $\mathrm{P}''_2 = \overline{\omega''_i \omega''_j} S''_{ij}$ represent the production terms of $\dfrac{1}{2}\overline{\boldsymbol{\omega}''.\boldsymbol{\omega}''}$ and $D''_\omega = -\dfrac{1}{\mathrm{Re}} \overline{\dfrac{\partial \omega''_i}{\partial X_j} \dfrac{\partial \omega''_i}{\partial X_j}}$ represents the corresponding dissipation term.

Figure 4.21 shows the distributions of the mean quantities of the production and the dissipation of the fluctuating vorticity in the (*R*-*Z*) plane for the same LDC flow case with δ = 0.125. Their corresponding spatial distributions are shown in Fig 4.22. As shown in Figs. 4.21(a) and 4.22(a), the production P''_1 occurs mostly near the upper upstream corner of the toroid. The production P''_2 concentrates in regions between the upstream (inner-radius) wall and the bottom of the toroid; see Figs. 4.21(b) and 4.22 (b). Figures 4.21(c) and 4.22(c) show the dissipation of the fluctuating vorticity near the shear layers of the top and the upstream walls. The integration of the mean terms P''_1 and P''_2 over the (*R*-*Z*) plane indicates that about 75% of the three-dimensional vortex flow is produced by P''_2. This means that most of the production has been caused mostly by the stretching/tilting of vorticity fluctuations by the mean rate of strain S''_{ij}. The rest of the production comes through a vorticity exchange between $\frac{1}{2}\overline{\boldsymbol{\omega}''.\boldsymbol{\omega}''}$ and $\frac{1}{2}\overline{\boldsymbol{\Omega}''.\boldsymbol{\Omega}''}$, which is represented by P''_1.

At a larger curvature ratio (δ = 1.0), about 75% of the fluctuation vorticity comes through P''_1 instead. As shown in Fig. 4.23(a), the P''_1 foci are localized near the upper part of the downstream (outer-radius) wall. The term P''_2 has about 25% of the production, which occurs near the top wall of the toroid; see Fig 4.23(b). This suggests that the circumferentially-aligned 3D structures, see Fig. 4.11(c), are produced through an energy exchange between the fluctuating vortex flow ($\frac{1}{2}\overline{\boldsymbol{\omega}''.\boldsymbol{\omega}''}$) and the mean vorticity ($\frac{1}{2}\overline{\boldsymbol{\Omega}''.\boldsymbol{\Omega}''}$). Figure 4.23(c) shows that the dissipation of the fluctuation vorticity occurs near the viscous boundary layer of both the downstream (outer-radius) and top walls. The vorticity production and dissipation regions are also confirmed by the energy budget analysis shown in Figs. 4.24(a) and (b).

When the fluid motion in the toroid is induced by sliding the top wall radially inward, the production and the dissipation of fluctuating energy, not shown here, are predicted near the upstream (outer-radius) wall for the toroids with δ = 0.125, 0.25, and 0.51. For a larger curvature ratio (δ = 1.0), the fluctuating energy is produced near the dividing streamlines between the core vortex and the downstream eddy; see Fig. 4.25(a). This local field information suggests that Taylor-Görtler vortices originate near the concave separation surface of downstream eddy. As can be seen in Fig 4.25(a), another part of the kinetic energy is also produced near the upper part of the downstream (inner-radius) wall. Figure 4.25(b) shows that the dissipation is primarily in the same regions of the kinetic energy production.

4.2.4.2 Time-fluctuating vorticity budget

The numerical analysis of the time-fluctuating vorticity, Eq. (2.27), shows that the production $\mathrm{P}_1' = -\overline{u_j'\omega_i'}\dfrac{\partial \Omega_i'}{\partial X_j}$ and $\mathrm{P}_2' = \overline{\omega_i'\omega_j'}S_{ij}'$, and the dissipation $D_\omega' = -\dfrac{1}{\mathrm{Re}}\overline{\dfrac{\partial \omega_i'}{\partial X_j}\dfrac{\partial \omega_i'}{\partial X_j}}$ are the dominant terms in the equation. The equation governs the fluctuating vorticity transfer is therefore approximated by:

$$0 = \mathrm{P}_1' + \mathrm{P}_2' + D_\omega' \tag{4.3}$$

Figures 4.26(a) and (b) show isocontours of P_1' and P_2' in the (*R*-*Z*) plane, respectively, for the flow case with δ = 0.25. As can be seen, the fluctuating vortex is produced mainly in the region between the upstream and the bottom walls. The isocontours of the corresponding D_ω', shown in Fig 4.26(c), demonstrate the dissipation of TGV near the upstream and the top walls. Note that the isocontours of P_1', P_2', and D_ω' presented in Fig 4.26 as a circumferentially-averaged quantities in the (*R*-*Z*) plane. The integration of these terms over the (*R*-*Z*) plane gives about 30% of the production through P_1' and about 70% through P_2'. Like the circumferential fluctuation of the steady mode at δ = 0.125, most of the production is caused by the stretching/tilting of the time vorticity fluctuations by the mean rate of strain S_{ij}'.

The fluctuating vorticity equation has been also analyzed for the open-cavity flow with δ = 0.51. Figure 4.27 shows the mean streamlines together with the isocontours of P_1', P_2', and D_ω' in the (*R*-*Z*) plane. It is seen in Figs. 4.27(a) and (b) that the production and the dissipation of fluctuating vorticity is highly concentrated near the dividing streamlines between the core vortex and the external flow region and near the upper upstream corner where the fluid leaves the toroid. Notwithstanding, TGV are still produced through P_2' that peak in banana-like foci near the upstream (inner-radius) wall; see Fig 4.28 (Here, P_2' denotes local quantities of the production and not circumferentially averaged ones).

4.2.5 Forced-convection heat transfer in the toroidal lid-driven cavity

The presents study has also assessed the role of Taylor-Görtler vortices in improving the mixing process of the toroidal LDC flows. The heat transfer rates accompanying the toroidal cavity flow (sliding top wall radially outward) have been calculated using the boundary conditions of Eq. (2.40) or Eq. (2.41). The initial condition used to solve the energy transport equation (Eq. (2.37)) is that the temperature is constant over the entire flow domain. Prandtl numbers, Pr = 0.71(air) and 7.1(water) have been chosen in carrying out the numerical simulations. The heat transfer rates have been presented in terms of the average Nusselt number, $\overline{\mathrm{Nu}}$, defined by Eq. (2.45).

Figure 4.29(a) shows the dependence of heat transfer rate on the curvature of the toroid obtained from both 2D and 3D calculations at Re = 880 and Pr = 7.1. Note that for all discrete values of δ considered, a three-dimensional flow is obtained in the 3D calculation. The top and the bottom walls have constant temperatures. As shown in Fig. 4.29(a), the heat transfer rates of the 3D flow solutions are higher than the corresponding rates of the 2D flow solutions for any discrete value of δ considered. This is due to the fact that the counter-rotating TGV begin to interact with the main circulation cell exchanging heat between the bulk and the near-wall regions, and therefore enhancing the mixing process; see Fig. 4.30. The same trend shown in Fig. 4.29(b) has been obtained when the boundary conditions of constant heat flux have been applied at both the top and the bottom walls of the cavity.

When the Prandtl number is decreased, the Peclet number (Pe = RePr) is also decreased, thereby increasing the viscous transport term of the energy conservation equation, Eq. (4.37). This leads to an increase in the thermal boundary layer and, thus, the heat transfer coefficient is reduced. Due to this fact, the heat transfer rates at Pr = 0.71 are lower than the corresponding rates at Pr = 7.1; see Fig. 4.31.

Figure 4.32 presents the variations of heat transfer rate with Reynolds number in a toroid with $\delta = 0.125$ and at Pr = 7.1. In the 2D flow region, it can be seen that the average Nusselt number varies with the Reynolds number according to the linear relation: $\overline{\mathrm{Nu}} = 3.77 + 0.010\mathrm{Re}$; ($200 \le \mathrm{Re} \le 800$). At Re = 200, the streamlines shown in Fig. 4.33(a) demonstrate that the stronger primary vortex occupies the bulk of the toroid. This primary vortex starts to transfer heat from the top to the bottom of the toroid. While the secondary corner eddies grow slightly in size by increasing Reynolds number from Re = 200 to 800, the primary vortex still occupies the bulk of the toroid; see Fig. 4.33(b). The streamlines of the primary vortex shown in Fig. 4.33(b) have now higher circulation velocities that lead to a notable increase in the heat transfer rate. Although the flow becomes three-dimensional at Re = 850, the heat transfer rate only increases slightly since the incipient TGV are still very week. Indeed, in the 3D flow region, the linear relationship ($\overline{\mathrm{Nu}} = -16.53 + 0.035\mathrm{Re}$) has been obtained for Re in the range $850 \le \mathrm{Re} \le 1000$. The larger slope value of this linear relation compared to 0.010 for the 2D flow indicates the positive role of TGV in increasing the transfer rates.

At a larger curvature ratio (δ = 1.0), Fig. 4.34 shows that the heat transfer rate is not practically affected by Reynolds number variation in the 2D flow region ($200 \le \mathrm{Re} \le 550$). In contrast to case with δ = 0.125, the averaged Nusselt number has a nearly constant value of about $\overline{\mathrm{Nu}} = 3.7$. Although the bulk of the toroid is occupied by the primary vortex cell at Re = 200, see Fig. 4.35(a), a low transfer rate is obtained due to the low circulation velocities at this Reynolds numbers. As can be observed in Fig. 4.35(b), as the Reynolds number increases from Re = 200 to 550 the primary vortex becomes smaller in size and it migrates toward the upper downstream corner of the toroid. The lower part of the toroid is occupied by a weaker counter rotating vortex, which transfers small amounts of heat from the bulk to the bottom of the toroid. At the same time that 2D-3D transition occurs at Re = 600, the circumferentially-averaged streamlines presented in Fig. 4.36 above show that the mean primary vortex returns has expanded in size. Indeed, the weaker cell occupying the lower part of the toroid at Re = 550 is damped and the more usual secondary vortices are developed in the lower corners of the cavity. This leads to the drastic increase, noticed in Fig 4.34, in the average Nusselt number ($\overline{\mathrm{Nu}} = 7.9$). In the 3D flow region, the average Nusselt number varies with Re according to the linear relation: $\overline{\mathrm{Nu}} = 1.44 + 0.010\mathrm{Re}$ for Reynolds numbers in the range $600 \le \mathrm{Re} \le 1000$. Since slope value of this relation is smaller than the corresponding value for the case of δ = 0.125, it can be concluded that the heat transfer rate is less sensitive to Re variations when the toroid radius of curvature is large.

(a)

(b)

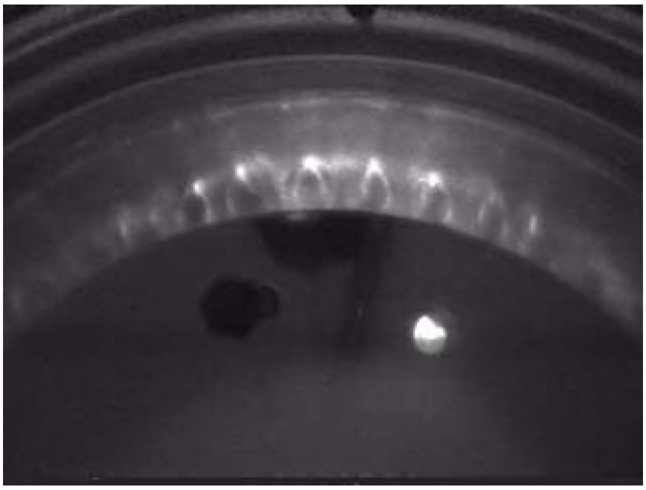

(c)

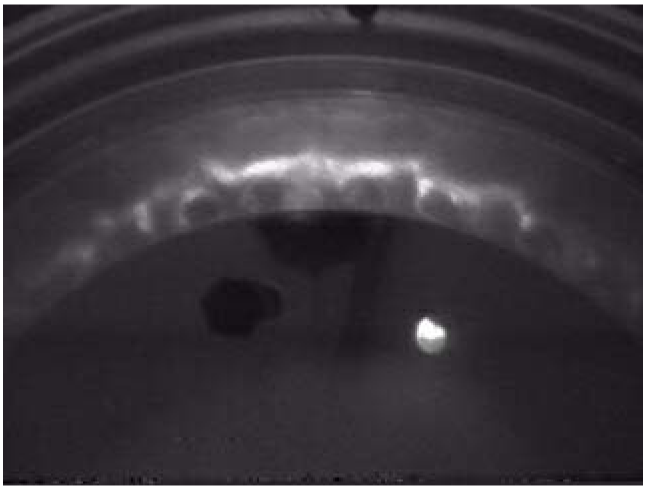

Figure 4.1. Experimental visualization of the instantaneous open-cavity flow in a toroid with $\delta = 0.25$ and $\gamma = 0.04$ and at Re = 1000±63. Pictures show views of (R-θ) plane with $Z = 0.1$ (a), 0.3 (b), and 0.5 (c).

(a)

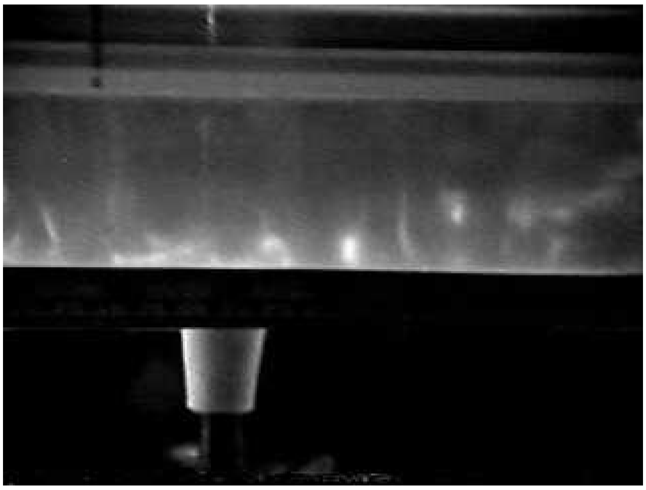

(b)

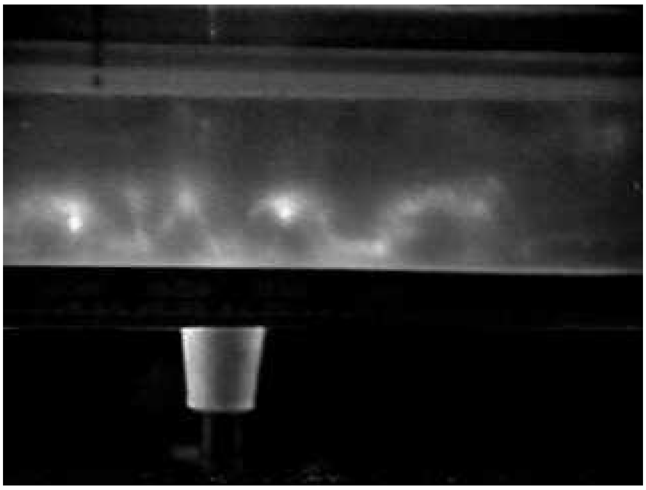

(c)

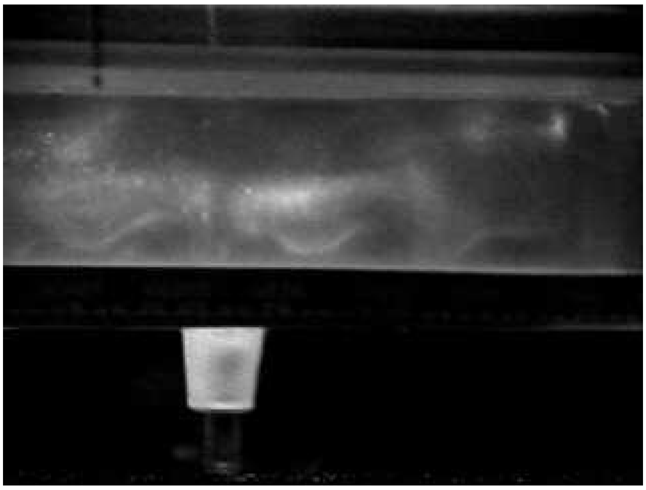

(d)

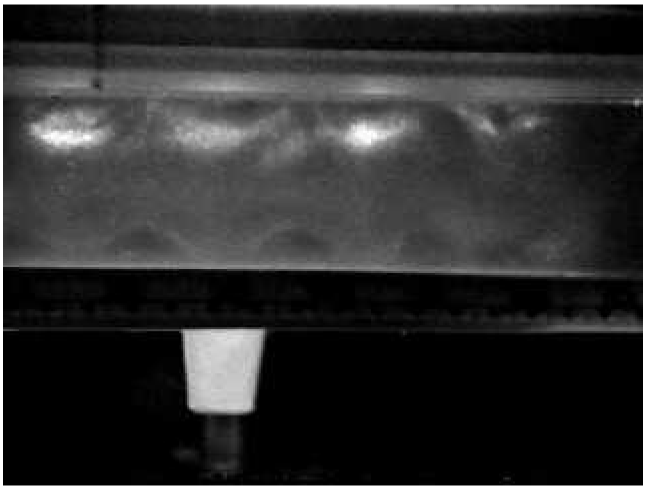

(e)

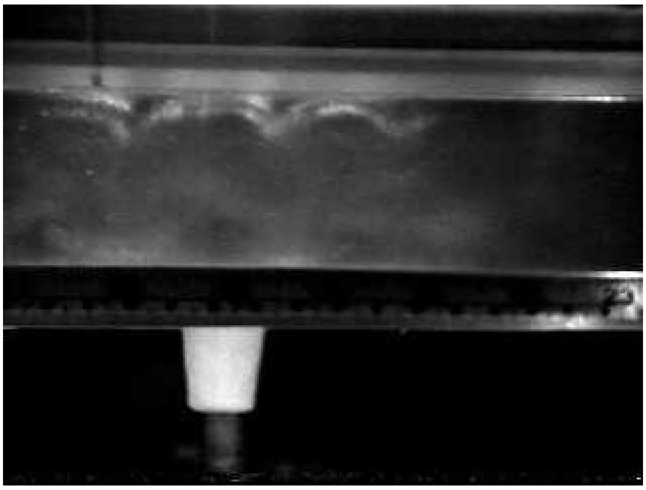

Figure 4.2. Experimental visualization of the instantaneous open-cavity flow for the conditions of Fig. 4.1. Pictures show views of the flow in the vertical plane with R = 3.6 (a), 3.8 (b), 4.0 (mid-plane) (c), 4.2 (d), and 4.4 (e).

(a)

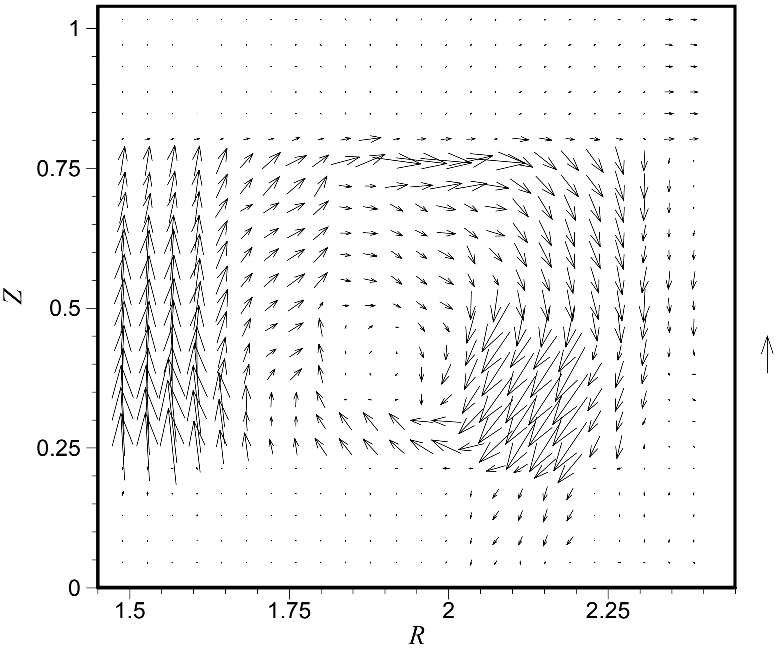

(b)

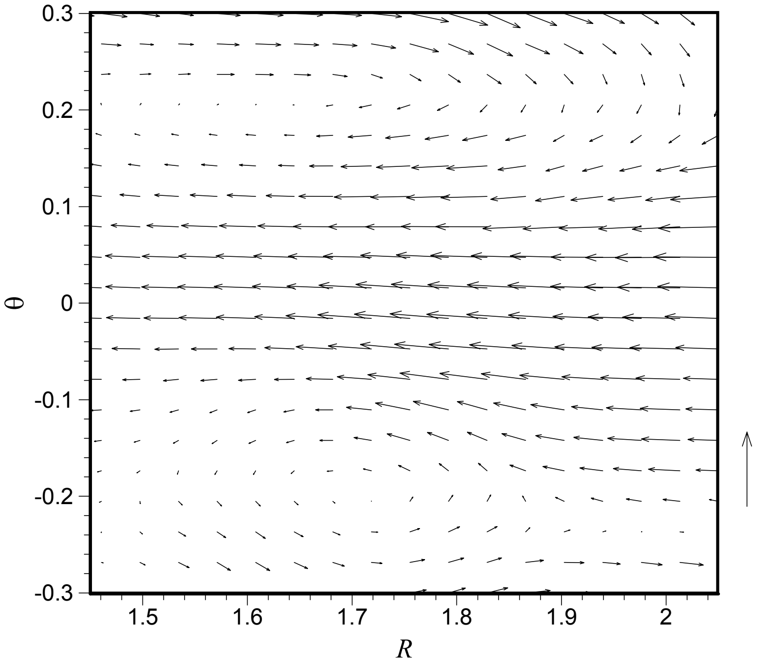

Figure 4.3. Experimental velocity vectors obtained using PIV velocity measurements for the open-cavity flow with δ = 0.51 and γ = 0.04 and at Re = 1000±57. (a) Velocity vectors in the (*R*-*Z*) plane with θ = 0 and (b) Velocity vectors in a section of the (*R*-θ) mid-plane. The arrows in the right of the figures correspond to a dimensionless velocity of 0.1.

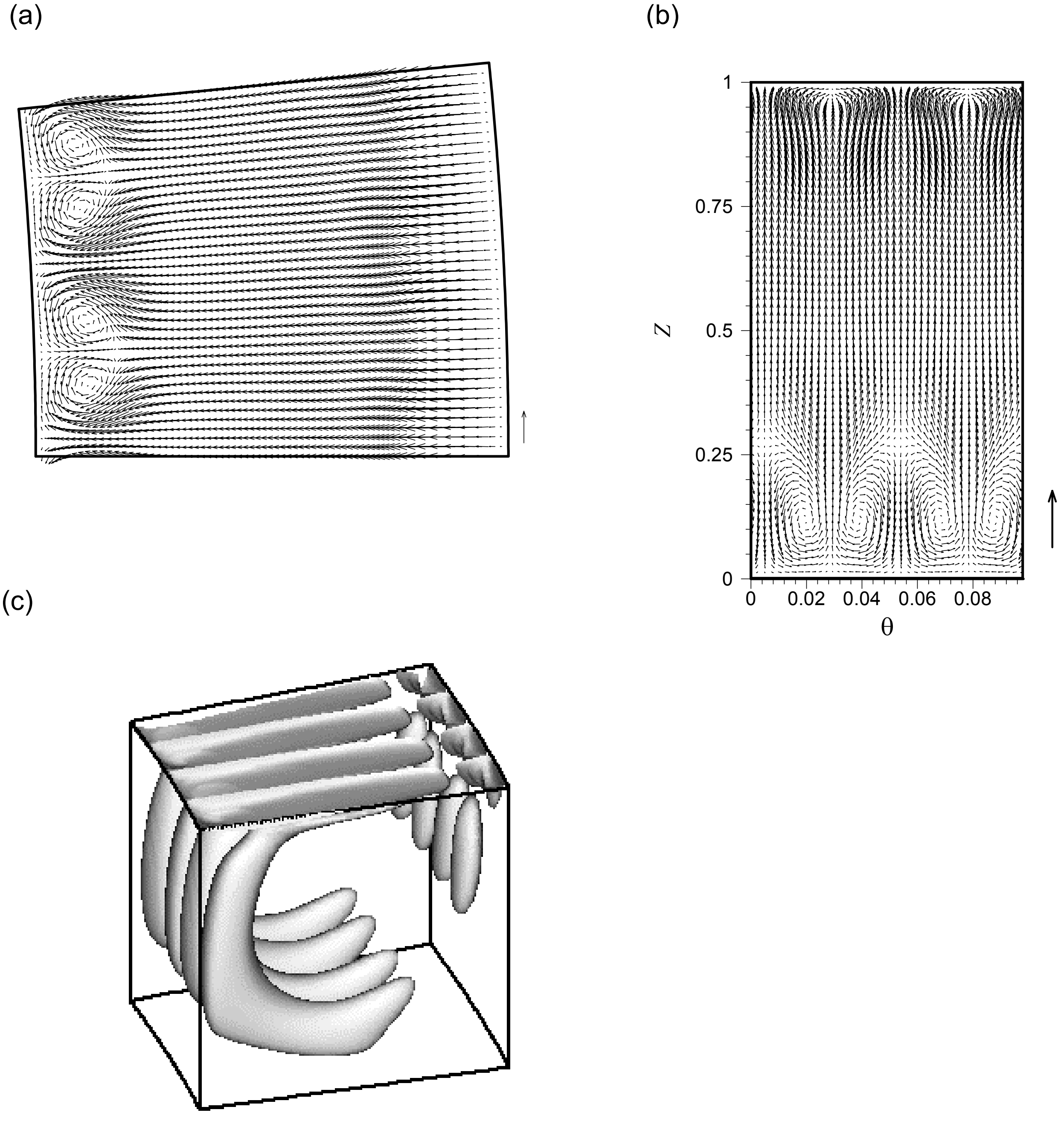

Figure 4.4. Plots of (a) Velocity vectors in (R-θ) mid-plane; (b) Velocity vectors in (Z-θ) mid-plane, and (c) Isosurfaces of the dimensionless helicity (levels = ±0.10) for the LDC flow (sliding wall radially outward) with $\delta = 0.125$ and Re = 850.

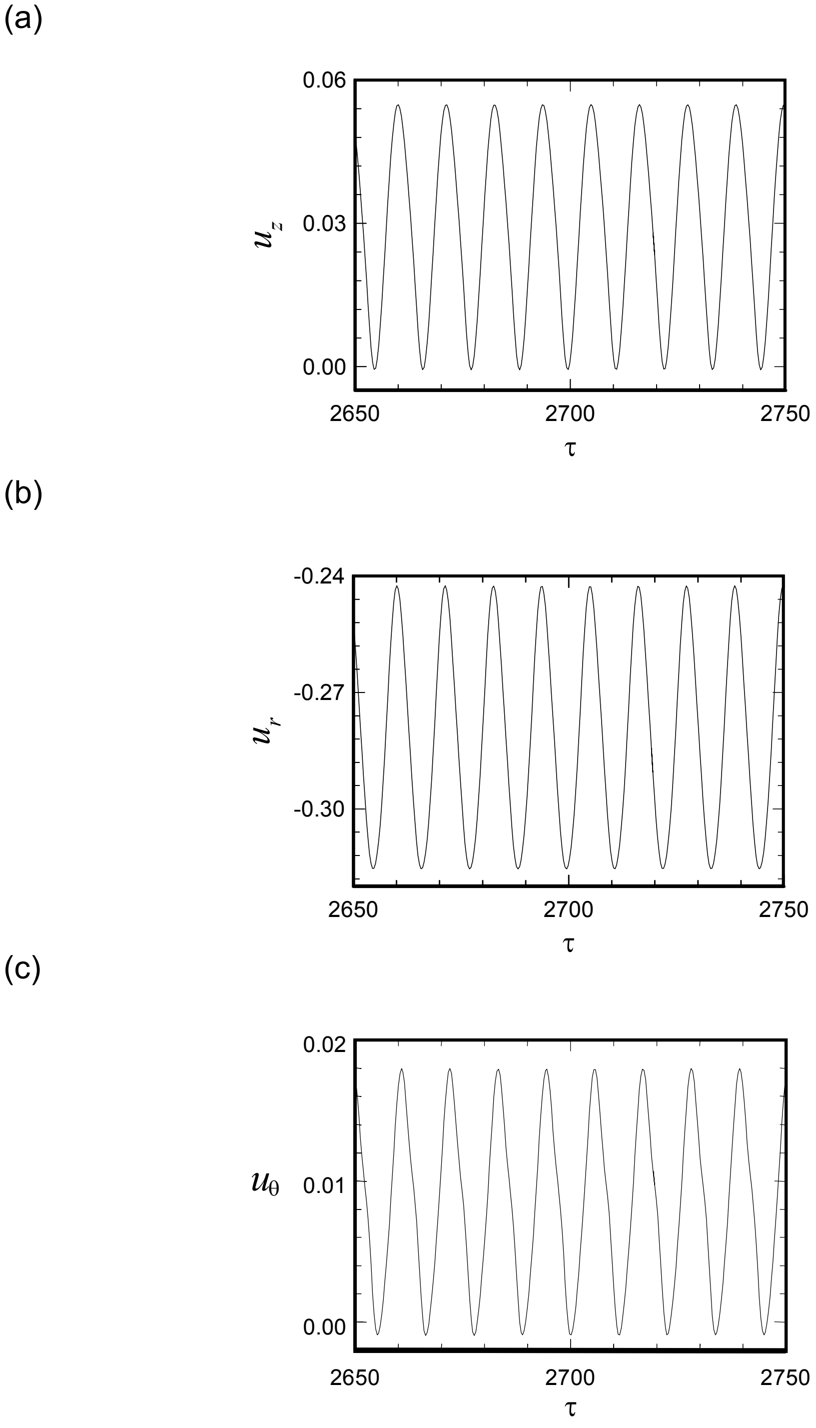

Figure 4.5. Time variations of the dimensionless velocity components for the LDC flow (sliding wall radially outward) with δ = 0.25 and at Re = 880: (a) Axial velocity component; (b) Radial velocity component; and (c) Circumferential velocity component. The plots correspond to the location (R,Z,θ) = (4.0,0.25,0.06π).

(a)

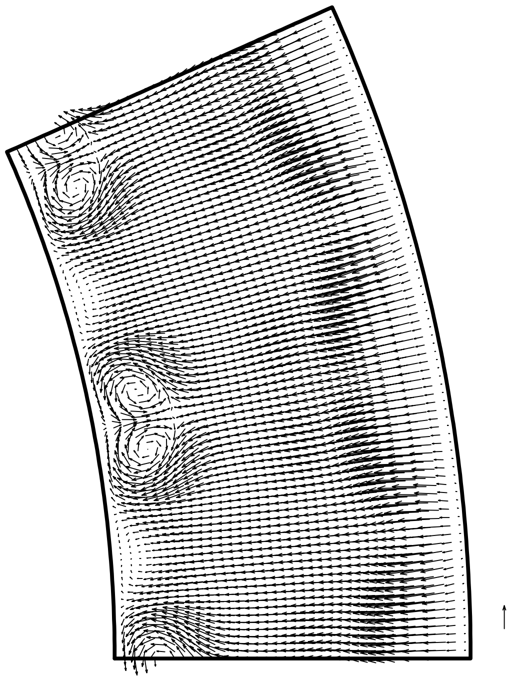

(b)

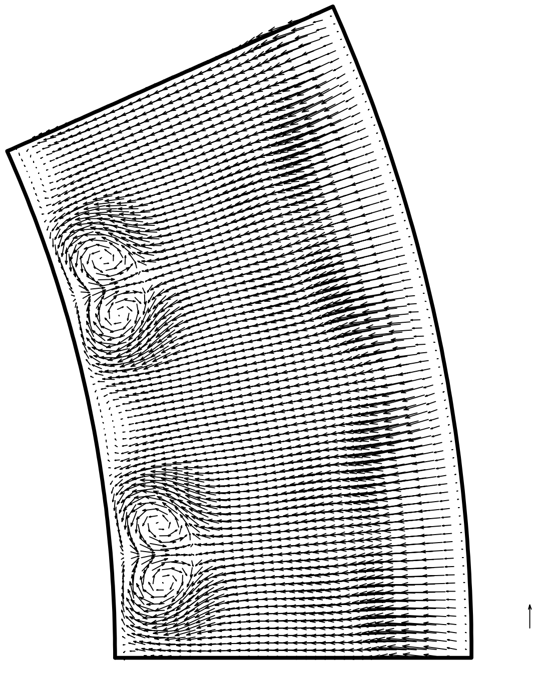

Figure 4.6. Instantaneous velocity vectors in the (R-θ) mid-plane at τ = 2720 (a) and 2725.65 (b) and for the conditions of Fig. 4.5. The arrows in the right of the figures correspond to a dimensionless velocity of 0.1.

(a)

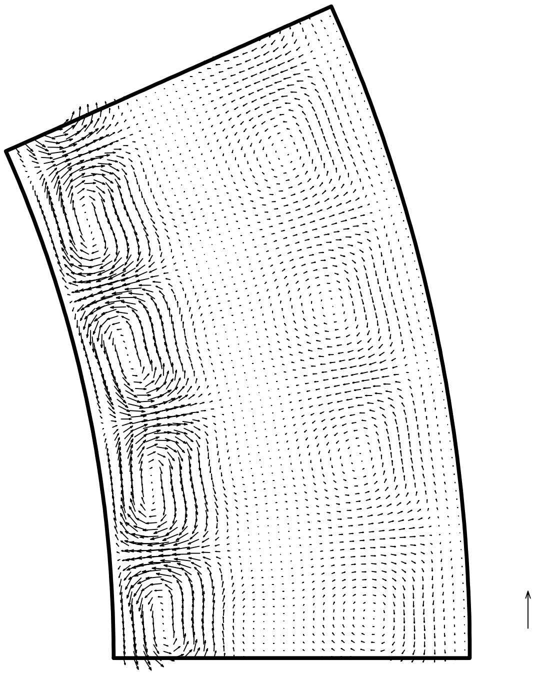

(b)

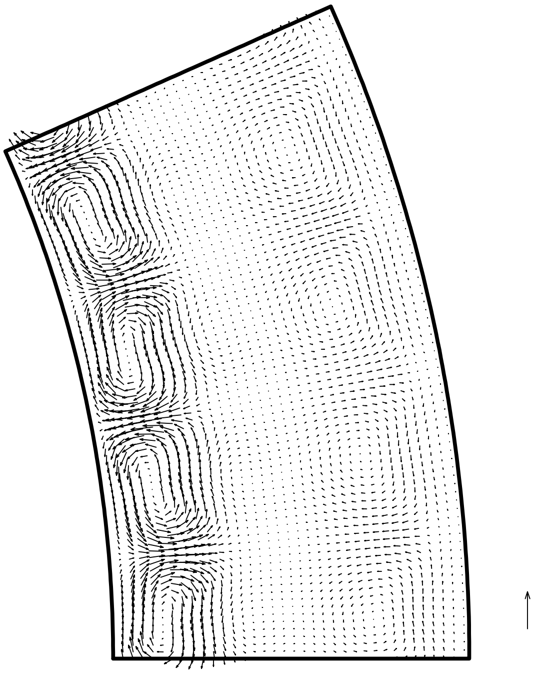

Figure 4.7. Fluctuating velocity vectors in the (R-θ) mid-plane at τ = 2720 (a) and 2725.65 (b) and for the conditions of Fig. 4.5. The arrows in the right of the figures correspond to a dimensionless velocity of 0.1.

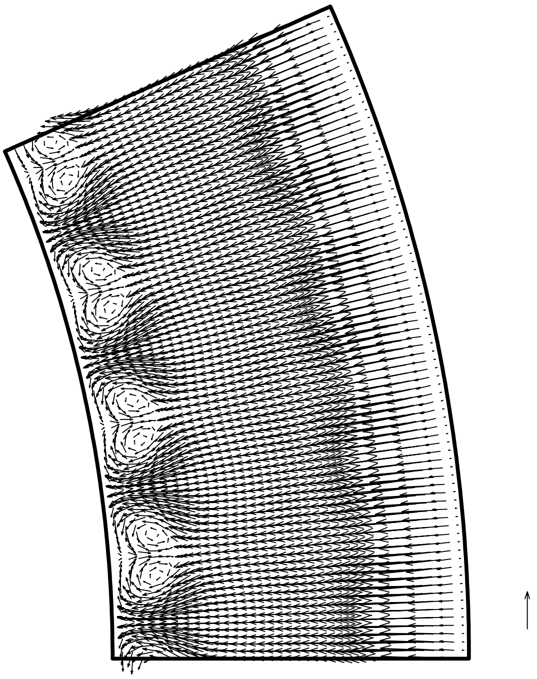

Figure 4.8. Mean velocity vectors in the (R-θ) mid-plane for the conditions of Fig. 4.5. The arrow in the right of the figure corresponds to a dimensionless velocity of 0.1.

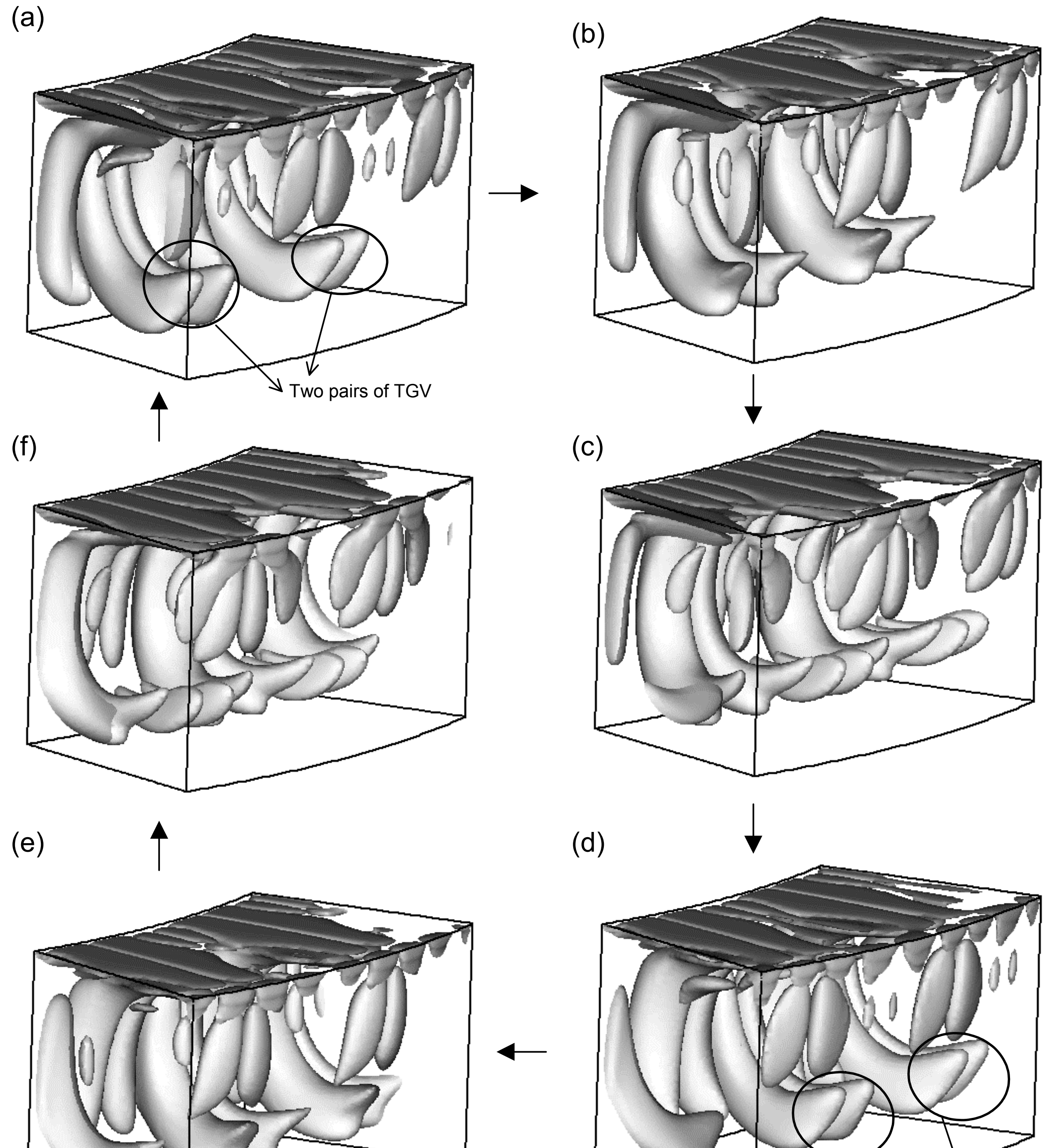

Figure 4.9. Temporal variation of isosurfaces of helicity (dimensionless levels = ± 0.1) over the dimensionless period of oscillation Λ^* for the conditions of Fig. 4.5. $\tau = \tau_1 = 2720$ (a), $\tau_1+0.1667\,\Lambda^*$ (b), $\tau_1+0.3333\,\Lambda^*$ (c), $\tau_1+0.5\,\Lambda^*$ (d), $\tau_1+0.6667\,\Lambda^*$ (e), and $\tau_1+0.8335\,\Lambda^*$ (f).

(a)

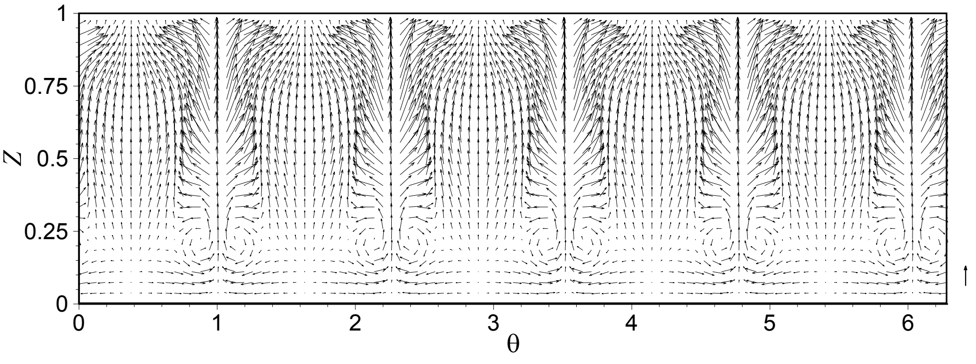

(b)

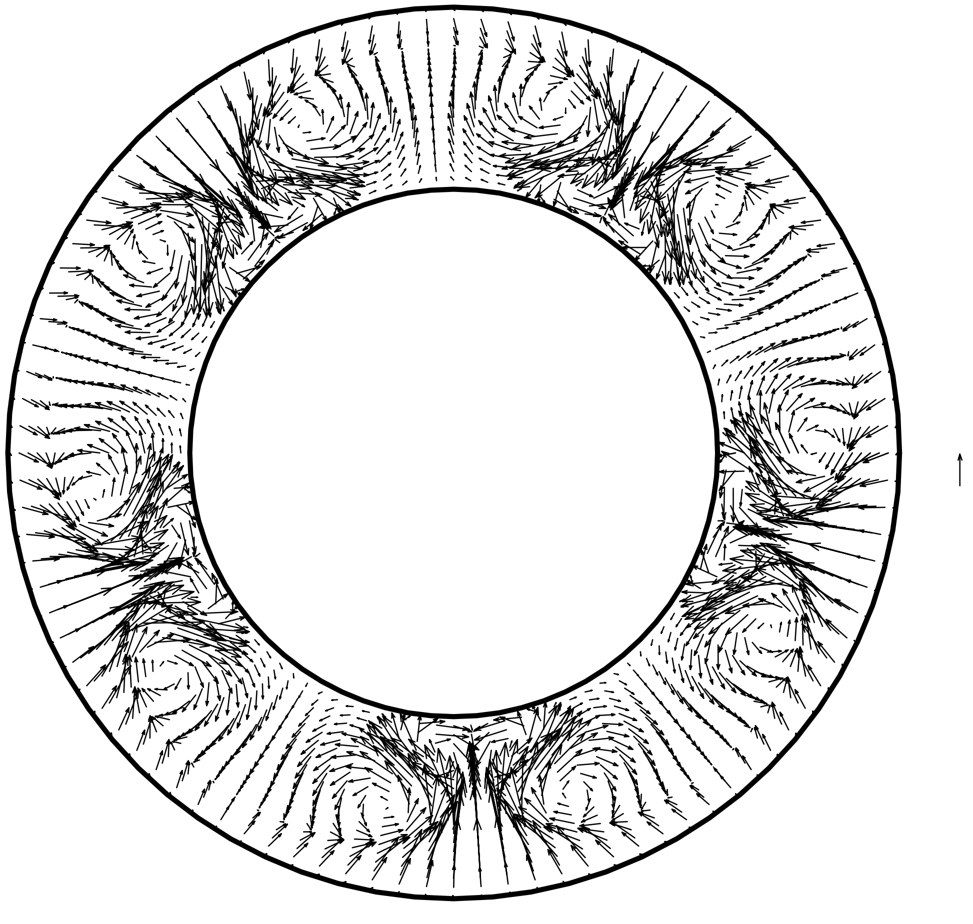

Figure 4.10. Plots of (a) Velocity vectors in (*Z*-θ) mid-plane and (b) Velocity vectors in (*R*-θ) plane with $Z = 0.6$ for the LDC flow (sliding wall radially outward) with $\delta = 0.51$ and at $\mathrm{Re} = 800$. The arrows in the right of the figures correspond to a dimensionless velocity of 0.1.

(a)

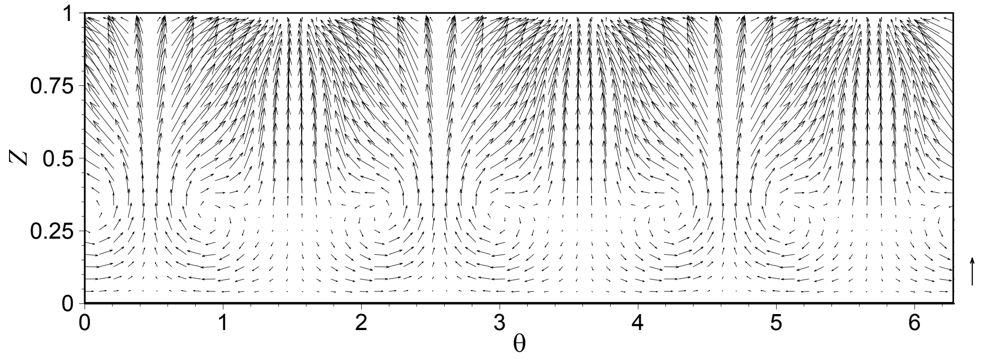

(b)

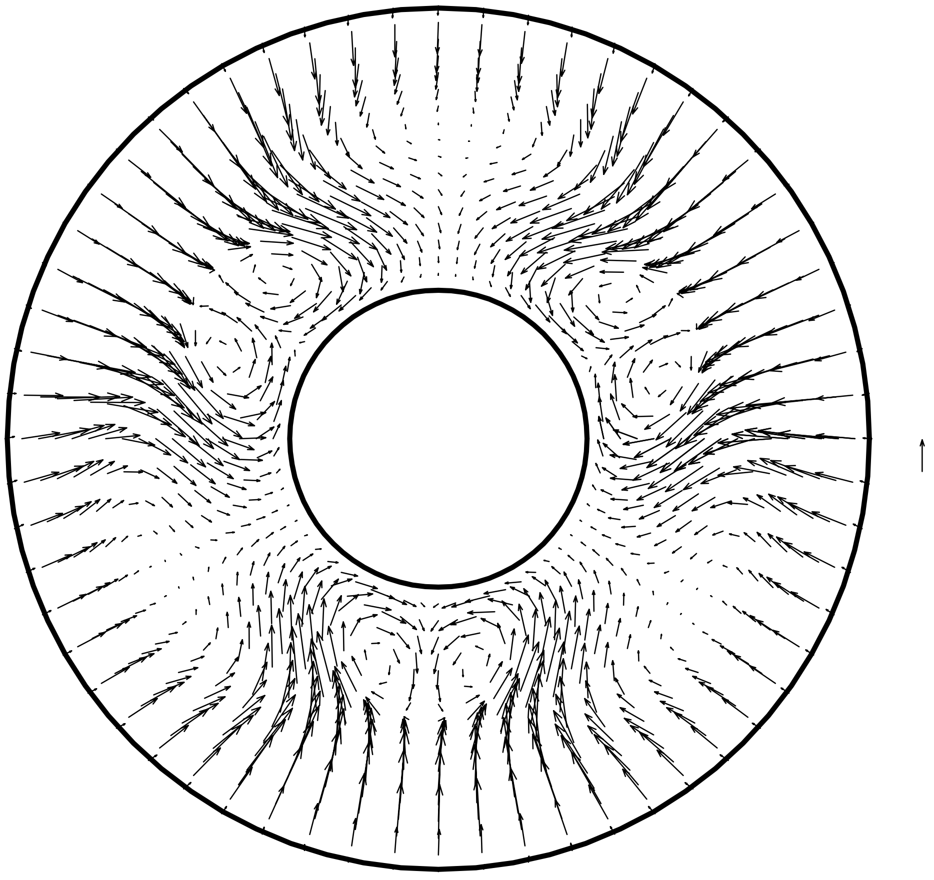

(c)

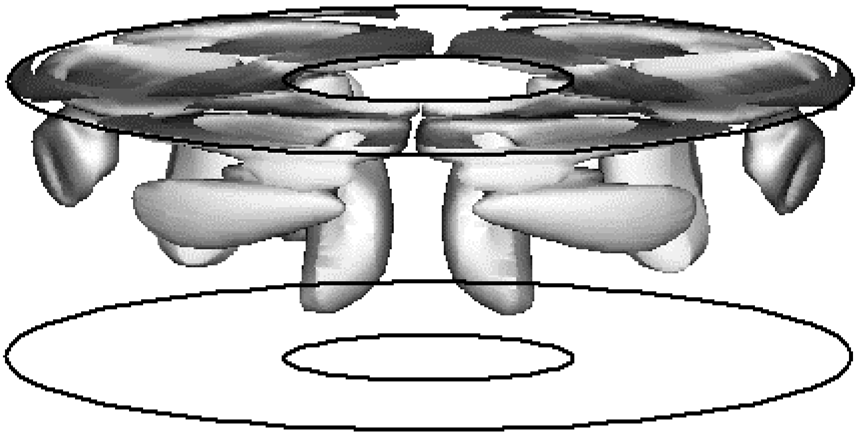

Figure 4.11. Plots of (a) Velocity vectors in (Z-θ) mid-plane; (b) Velocity vectors in (R-θ) plane with Z = 0.6; and (c) Isosurfaces of the dimensionless helicity (levels = ±0.10) for the LDC flow arrangement (sliding wall radially outward) with δ = 1.0 and at Re = 600. The arrows in the right of the figures (a) and (b) correspond to a dimensionless velocity of 0.1.

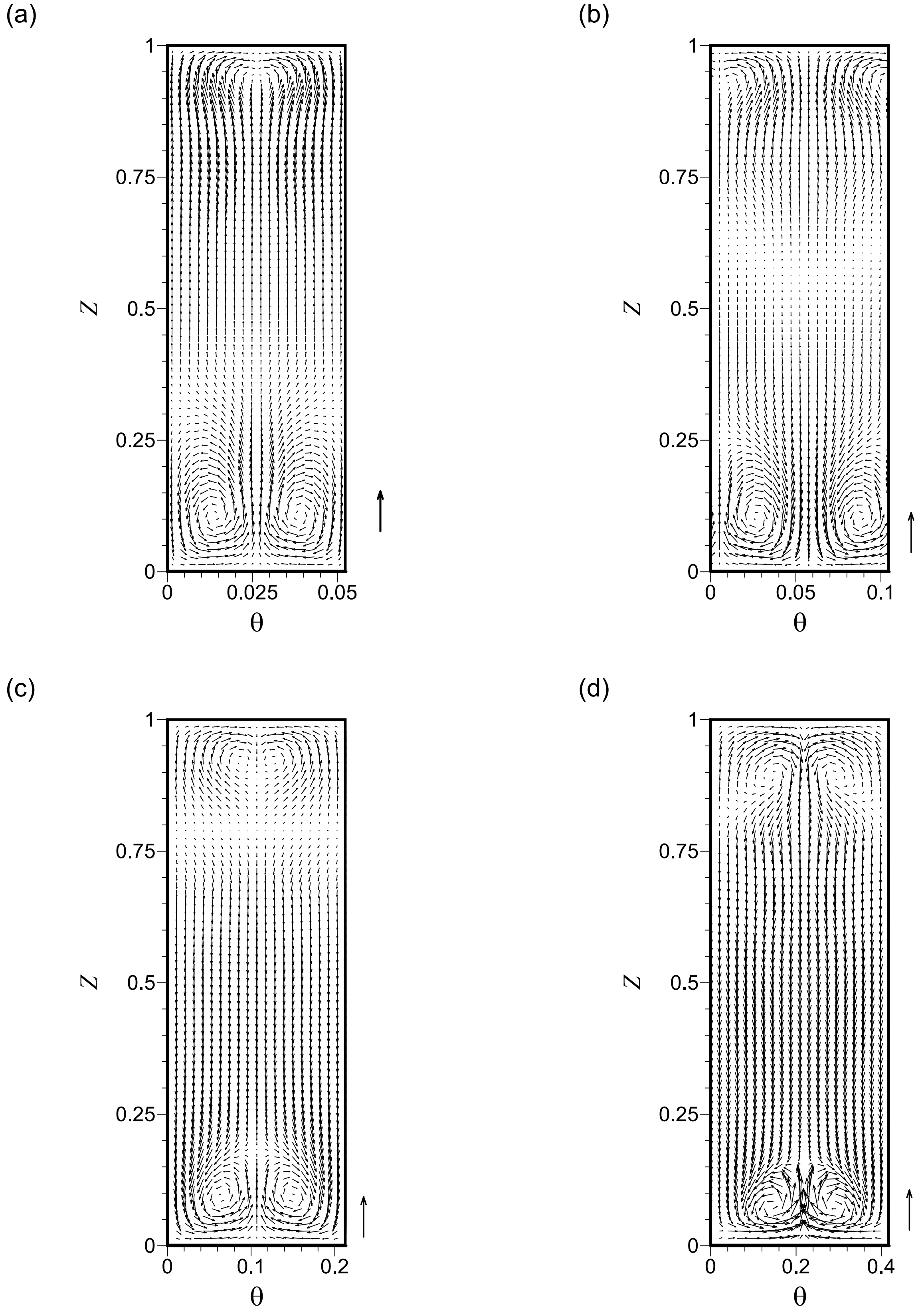

Figure 4.12. Velocity vectors in the vertical (Z-θ) mid-planes for the LDC flow arrangement (sliding wall radially inward) with: (a) $\delta = 0.125$, Re = 850; (b) $\delta = 0.25$, Re = 850; (c) $\delta = 0.51$, Re = 850; and (d) $\delta = 1.0$, Re = 1250. The arrows in the right of the figures correspond to dimensionless velocity of 0.1.

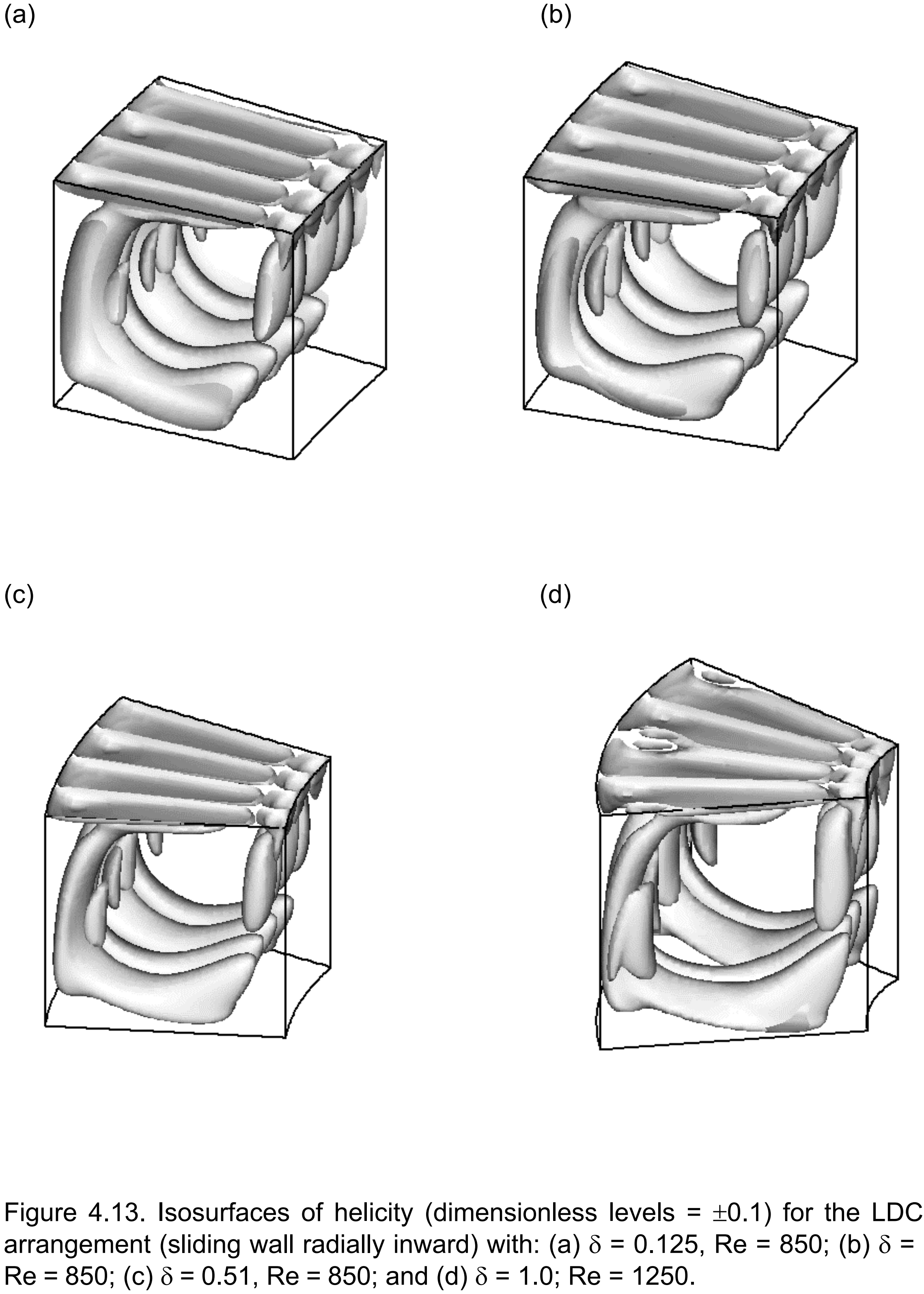

Figure 4.13. Isosurfaces of helicity (dimensionless levels = ±0.1) for the LDC flow arrangement (sliding wall radially inward) with: (a) $\delta = 0.125$, Re = 850; (b) $\delta = 0.25$, Re = 850; (c) $\delta = 0.51$, Re = 850; and (d) $\delta = 1.0$; Re = 1250.

(a)

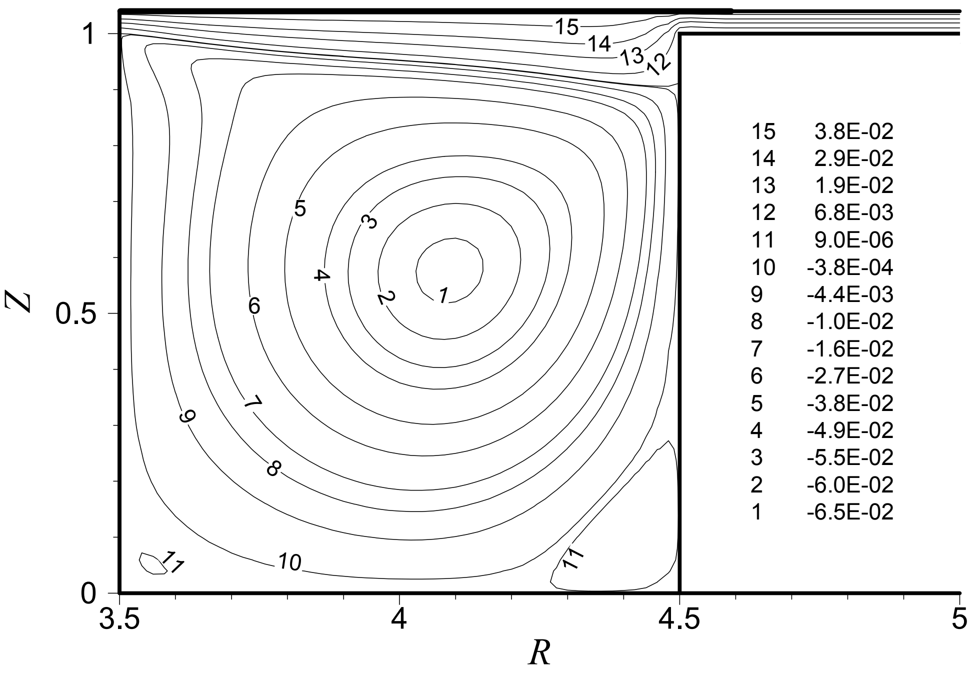

(b)

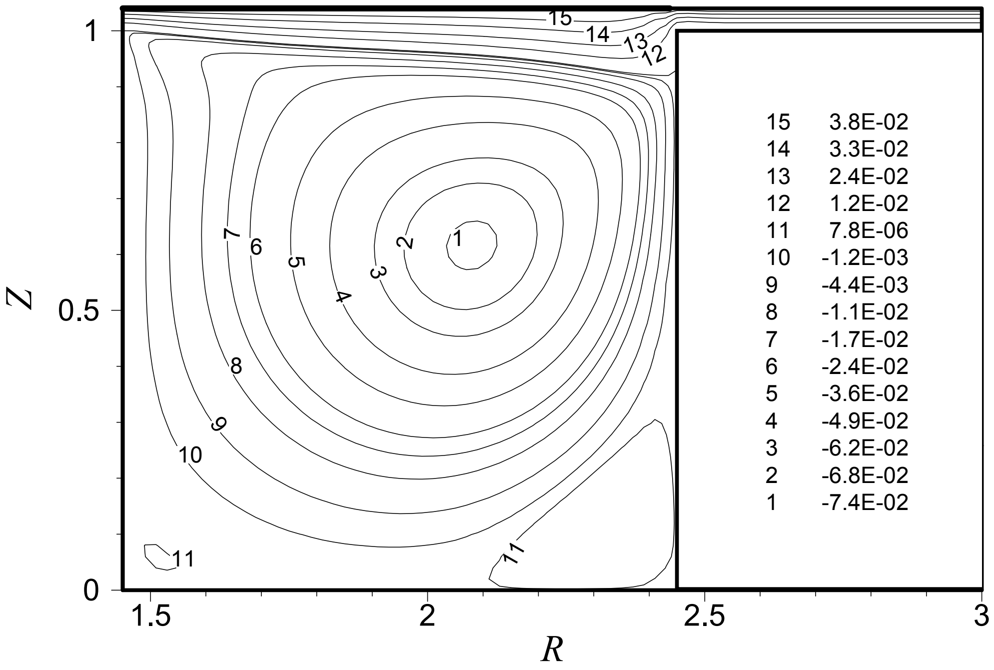

Figure 4.14. Isocontours of the dimensionless stream-function of the axisymmetric flows obtained from unsteady 3D calculations at Re = 800 for the open-cavity flow arrangement with γ = 0.04 and δ = 0.25 (a) and 0.51 (b).

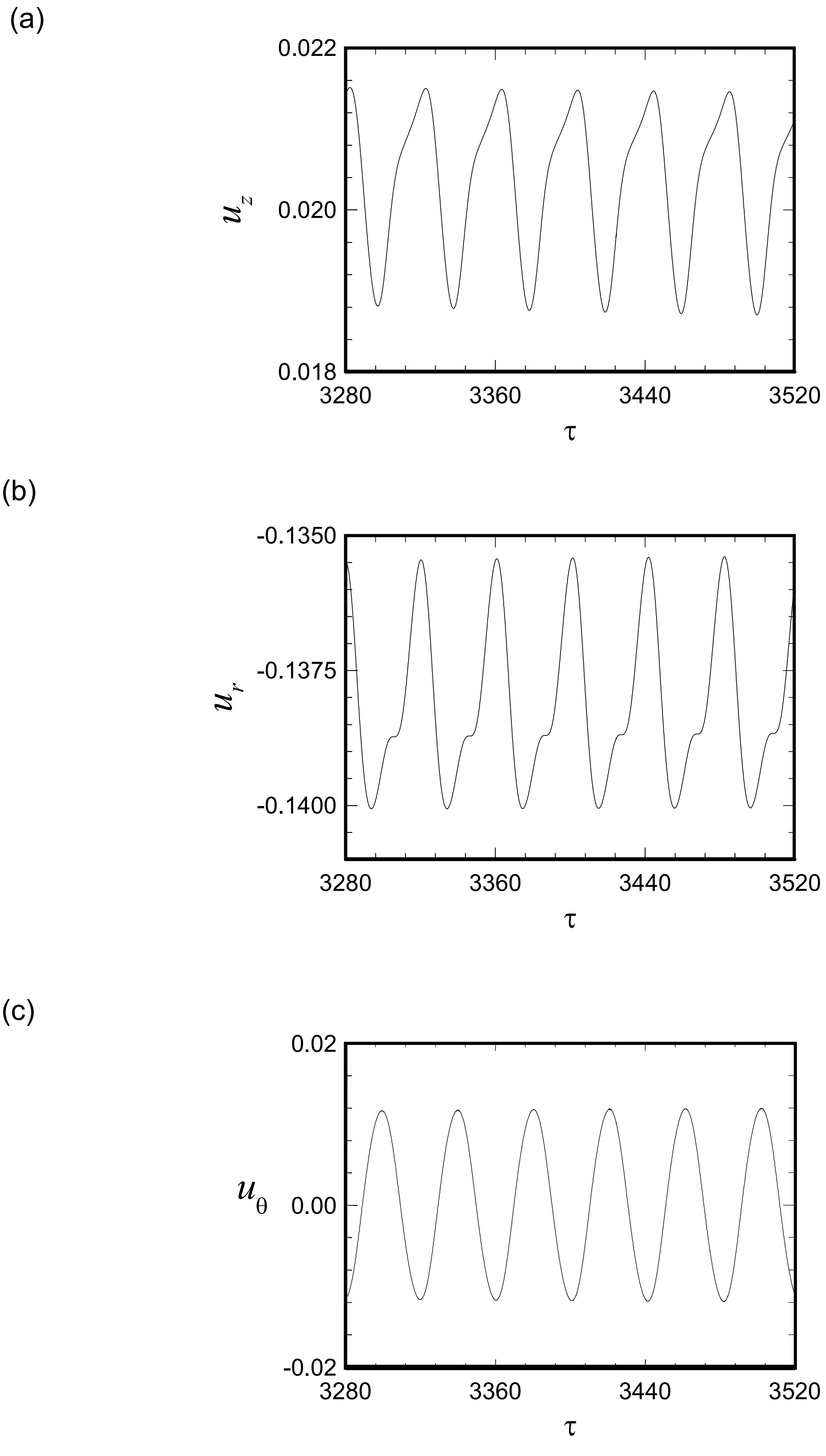

Figure 4.15. Time variations of the dimensionless velocity components for the open-cavity flow arrangement with $\delta = 0.51$ and $\gamma = 0.04$ and at Re = 850. (a) Axial velocity component; (b) Radial velocity component; and (c) Circumferential velocity component. The plots correspond to the location $(R,Z,\theta) = (1.95,0.25,0.22\pi)$.

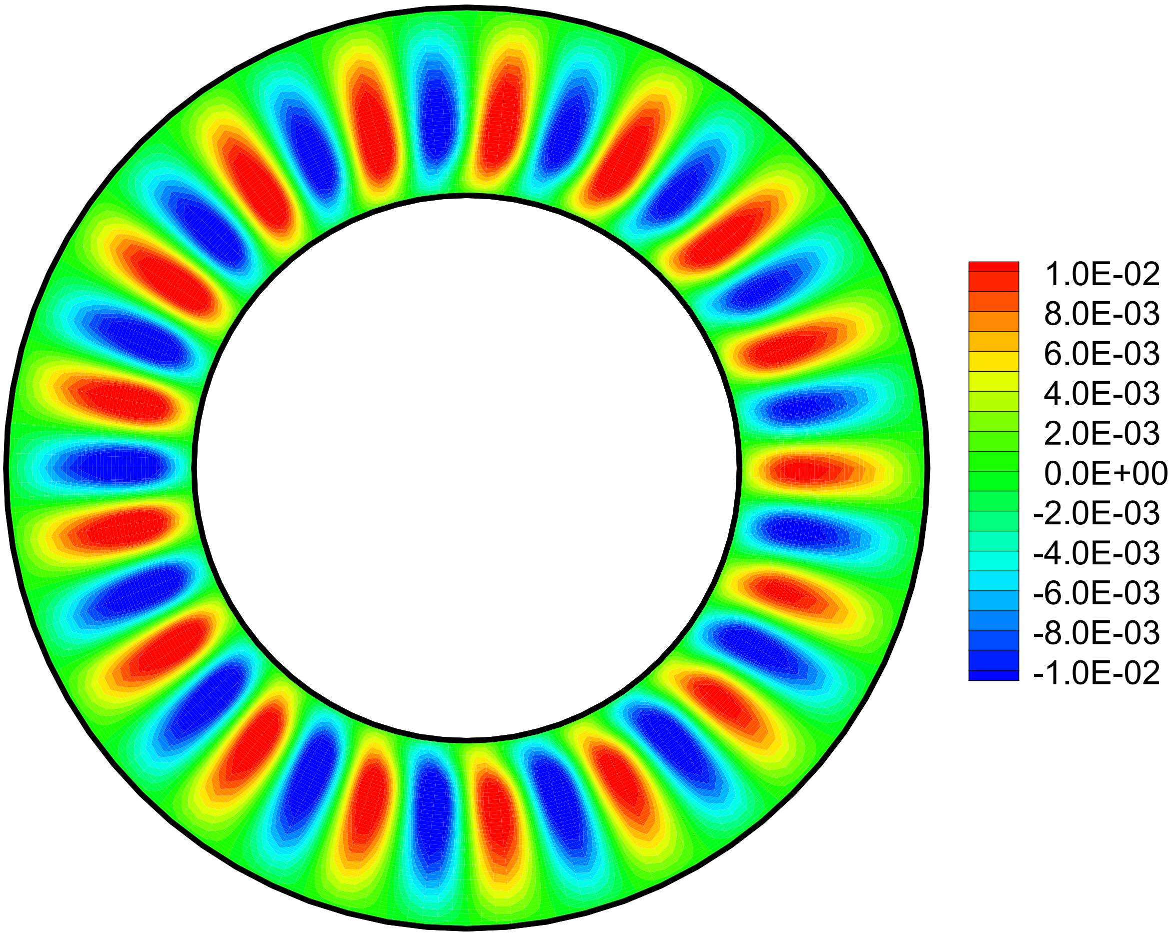

Figure 4.16. Instantaneous distribution of the dimensionless circumferential velocity component in the (R-θ) plane with Z = 0.1 at τ = 3440 and for the conditions of Fig. 4.15.

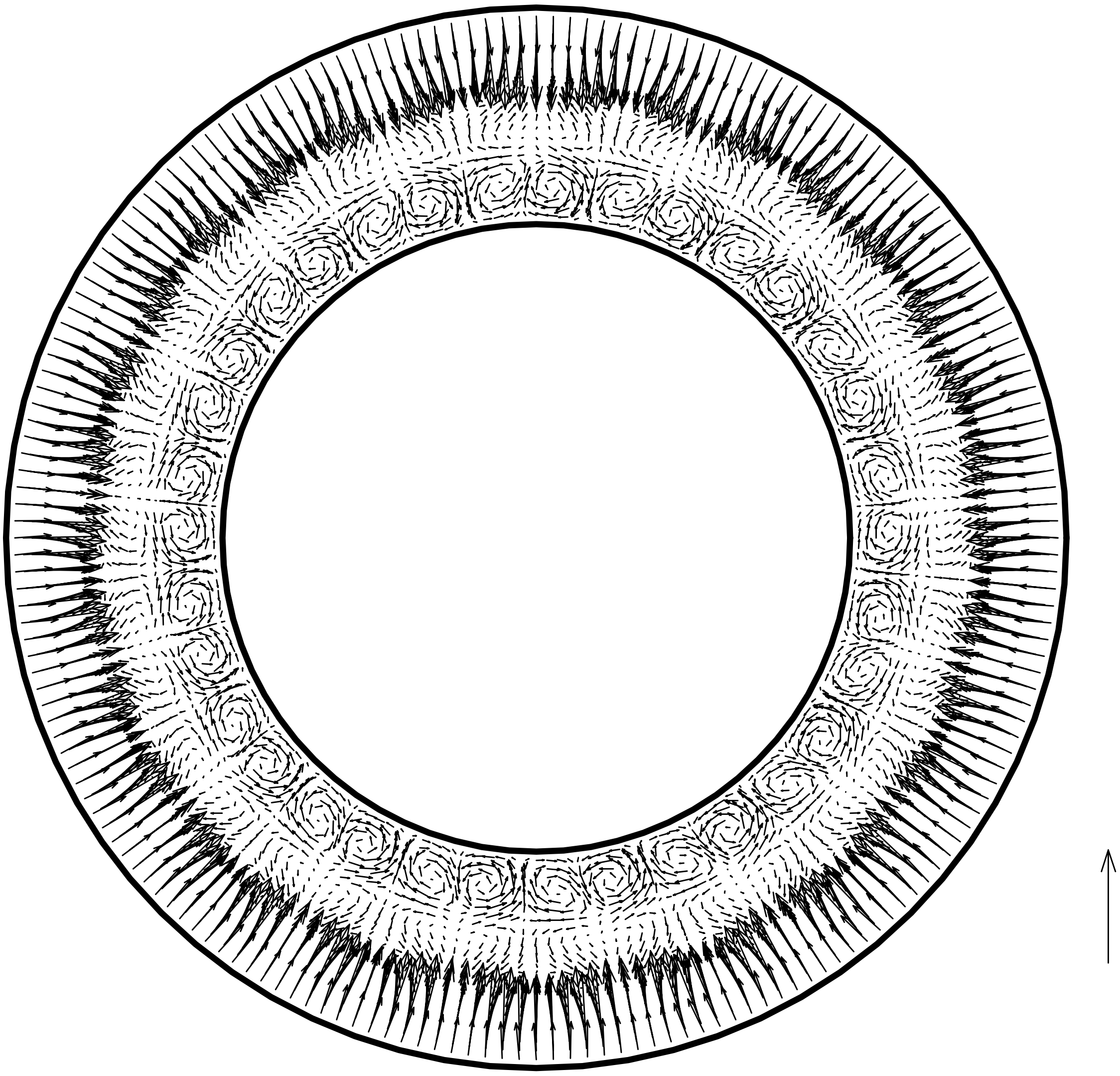

Figure 4.17. Instantaneous velocity vectors in the (R-θ) plane with Z = 0.62 at $\tau = 3440$ and for the conditions of Fig. 4.15. The arrow in the right of the figure corresponds to a dimensionless velocity of 0.1.

(a)

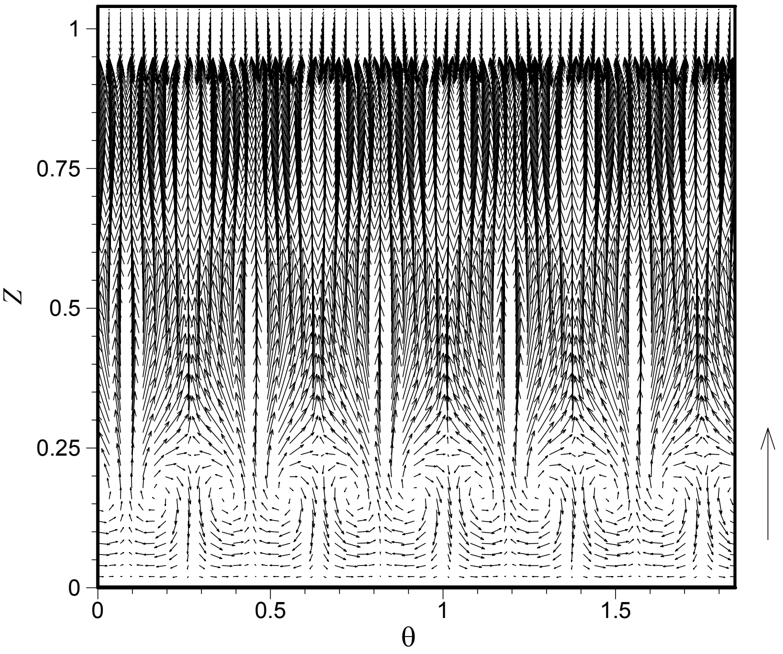

(b)

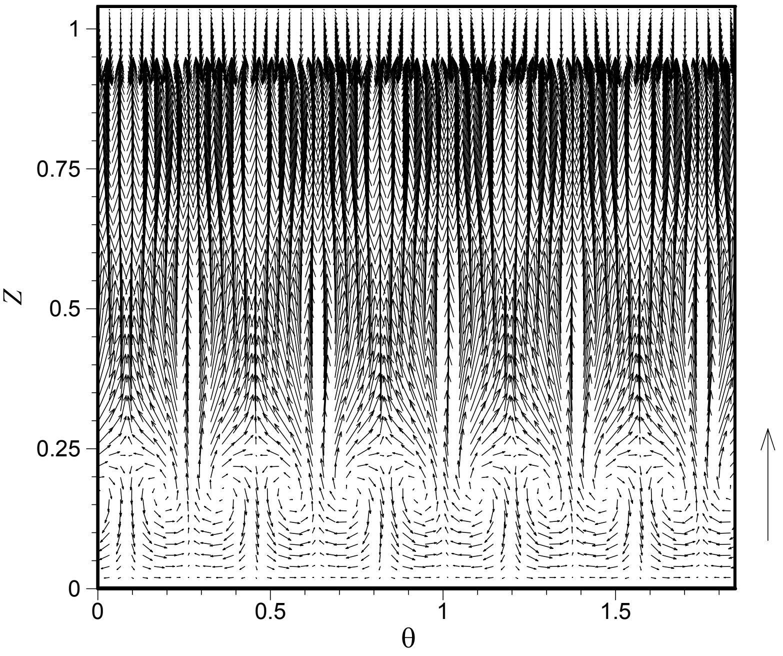

Figure 4.18. Instantaneous velocity vectors at times: τ = 3440 (a) and 3460 (b) in the (Z-θ) mid-plane for the conditions of Fig. 4.15. The arrows in the right of the figures correspond to a dimensionless velocity of 0.1.

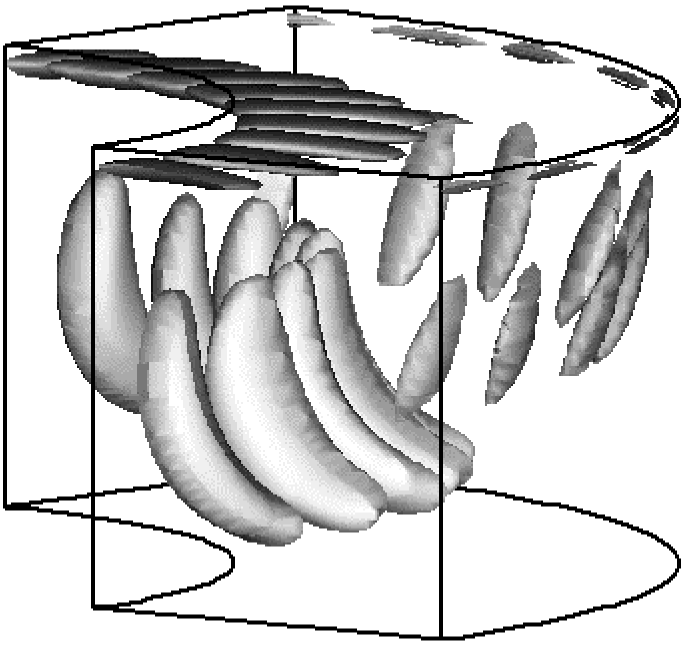

Figure 4.19. Instantaneous isosurfaces of the dimensionless helicity, Π, presented in one quarter of the toroid at τ = 3440 for the conditions of Fig. 4.15. The dimensionless levels of helicity = ±0.04.

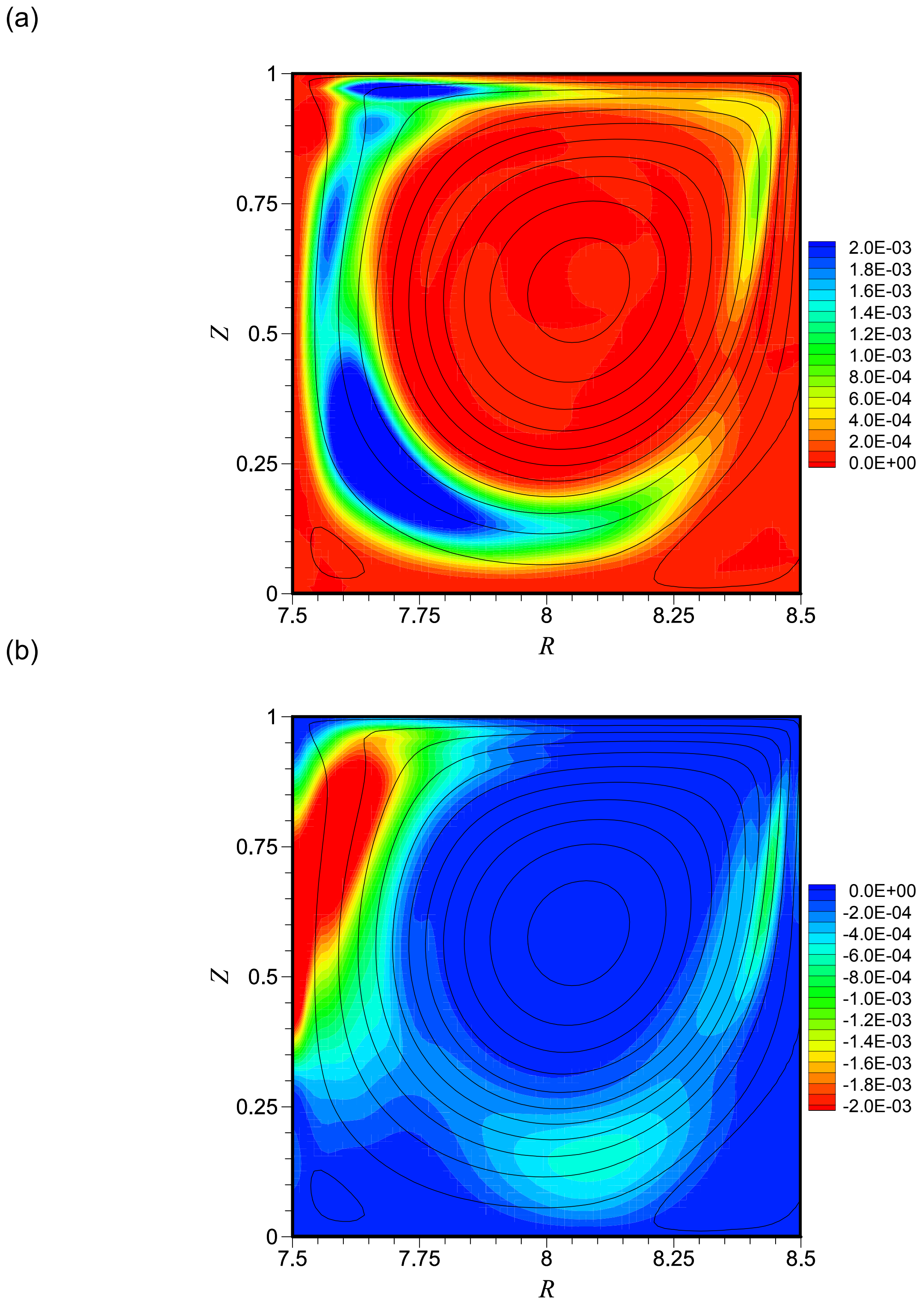

Figure 4.20. Circumferentially averaged streamlines together with the distributions of the production and dissipation of the fluctuating energy in the (*R*-*Z*) plane for the LDC flow arrangement (sliding wall radially outward) with δ = 0.125 and at Re = 850. (a) The energy production P''_E and (b) The energy dissipation D''_E .

(a)

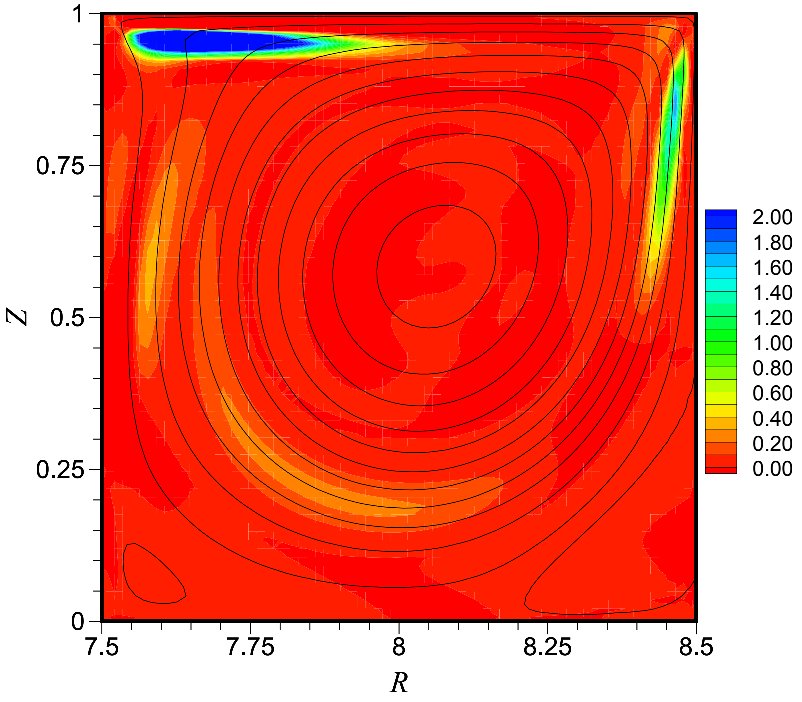
1
0.75
0.5
0.25
0
Z
7.5
7.75
8
8.25
8.5
R
2.00
1.80
1.60
1.40
1.20
1.00
0.80
0.60
0.40
0.20
0.00

(b)

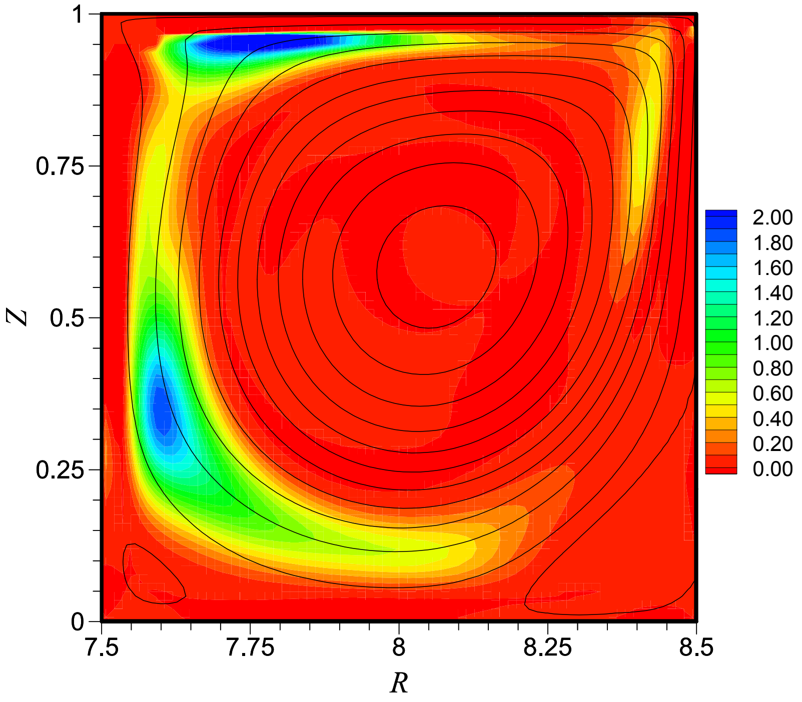
1
0.75
0.5
0.25
0
Z
7.5
7.75
8
8.25
8.5
R
2.00
1.80
1.60
1.40
1.20
1.00
0.80
0.60
0.40
0.20
0.00

(c)

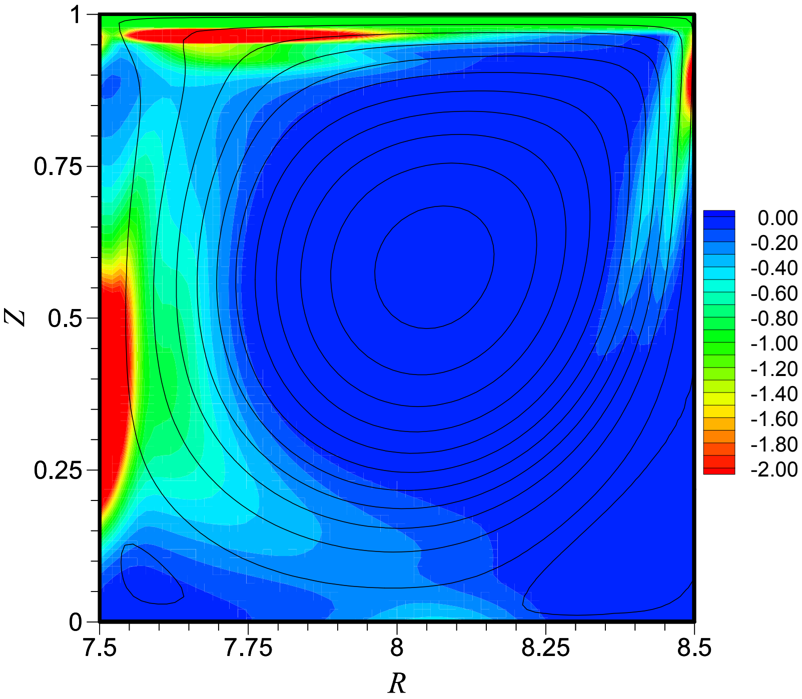

Figure 4.21. Circumferentially averaged streamlines together with the distributions of the production and dissipation of the fluctuating vorticity in the (*R*-*Z*) plane for LDC flow arrangement (sliding wall radially outward) with δ = 0.125 and at Re = 850. (a) Vorticity production P_1''; (b) Vorticity production P_2''; and (c) Vorticity dissipation D_ω''.

(a)

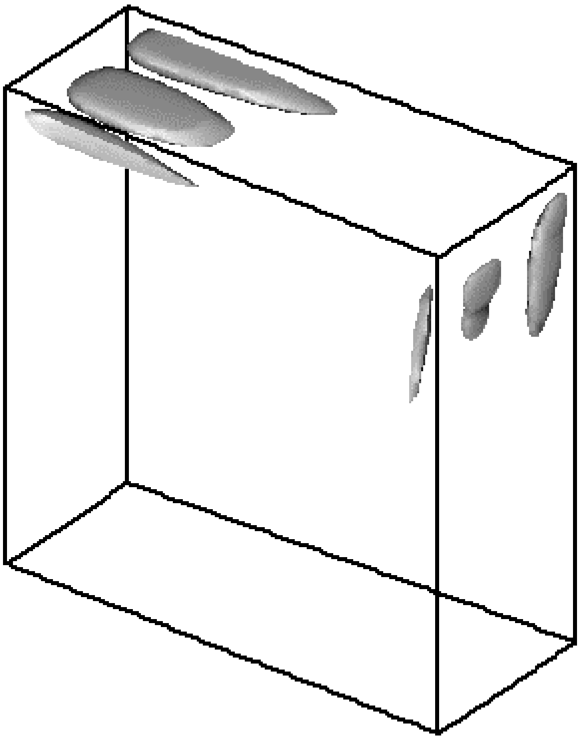

(b)

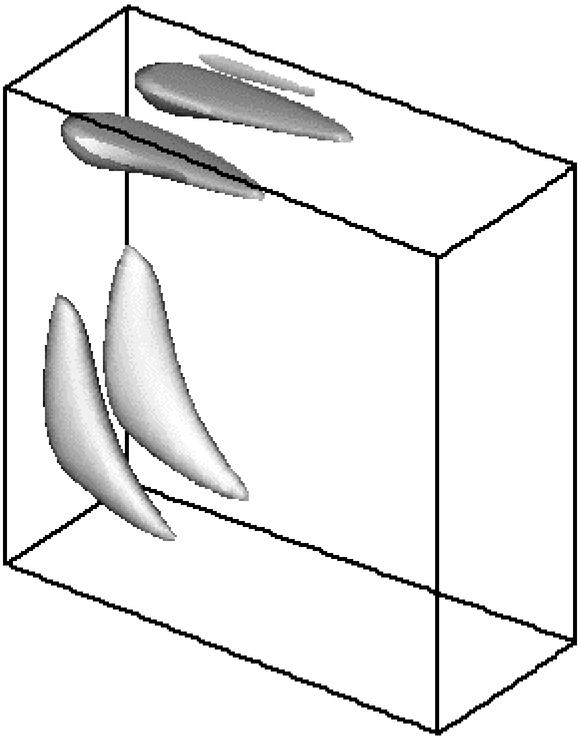

(c)

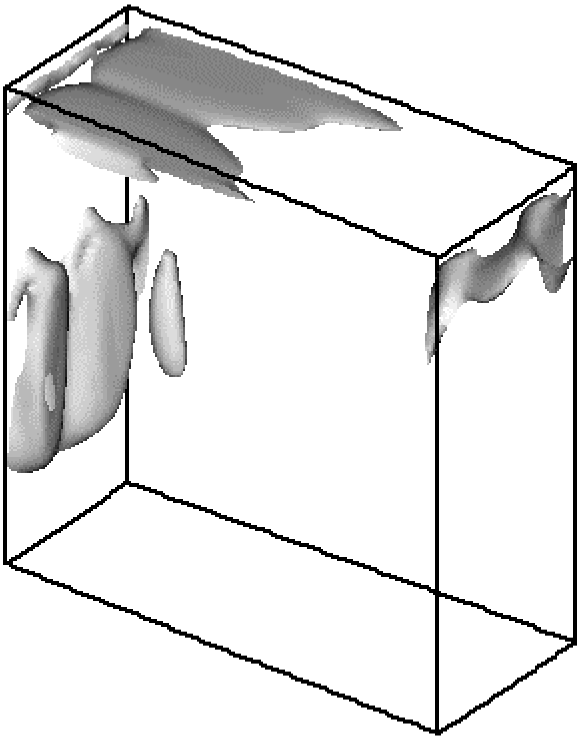

Figure 4.22. Local distributions of the production and the dissipation of fluctuating vorticity over one wavelength for the LDC flow arrangement (sliding wall radially outward) with $\delta = 0.125$ and at Re = 850. (a) Isosurface of the vorticity production P_1''; (b) Isosurface of the vorticity production P_2''; and (c) Isosurface of vorticity dissipation D_ω''. The dimensionless level of the isosurface = 1.5 (Production) and –1.5 (Dissipation).

(a)

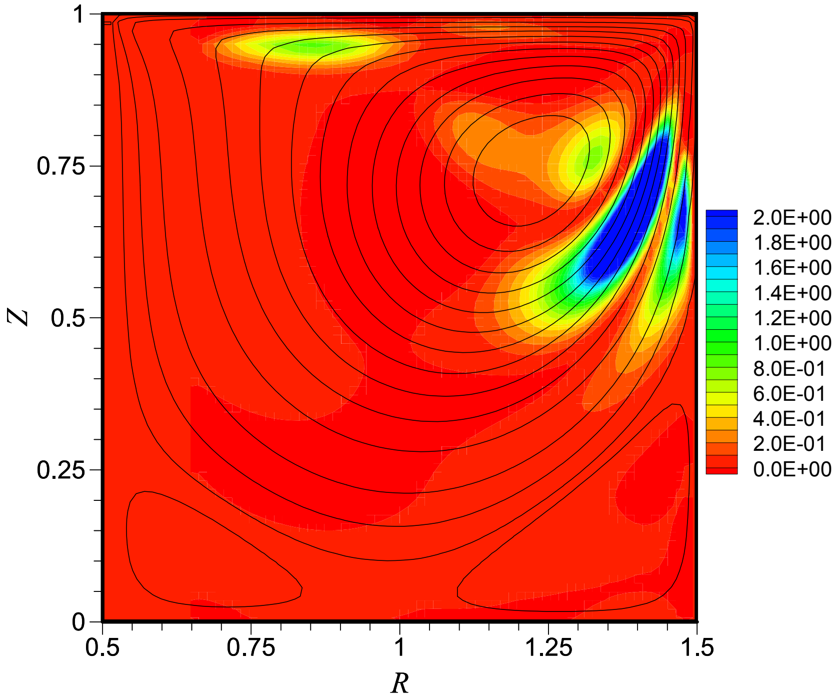
1
0.75
0.5
0.25
0
Z
0.5
0.75
1
1.25
1.5
R
2.0E+00
1.8E+00
1.6E+00
1.4E+00
1.2E+00
1.0E+00
8.0E-01
6.0E-01
4.0E-01
2.0E-01
0.0E+00

(b)

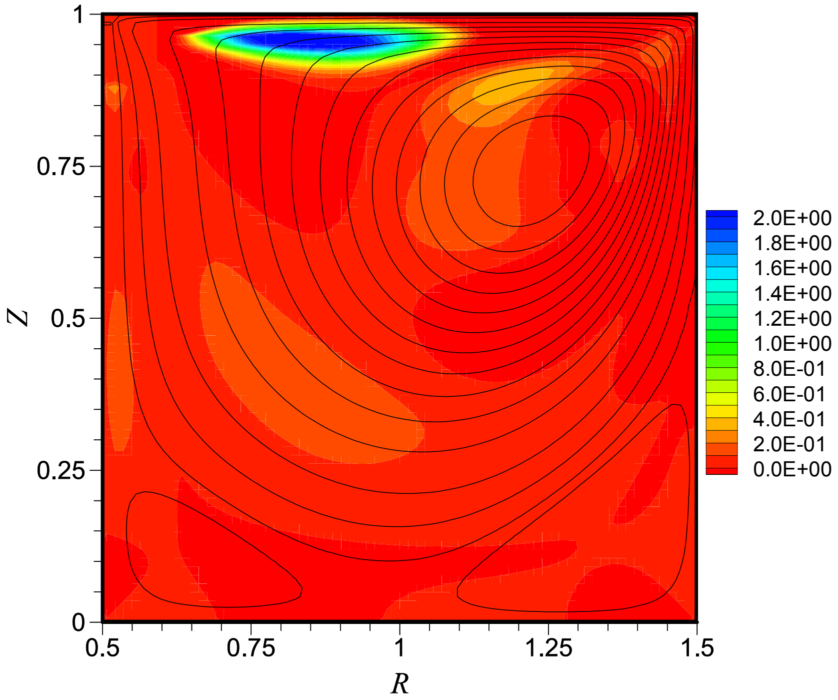
1
0.75
0.5
0.25
0
Z
0.5
0.75
1
1.25
1.5
R
2.0E+00
1.8E+00
1.6E+00
1.4E+00
1.2E+00
1.0E+00
8.0E-01
6.0E-01
4.0E-01
2.0E-01
0.0E+00

(c)

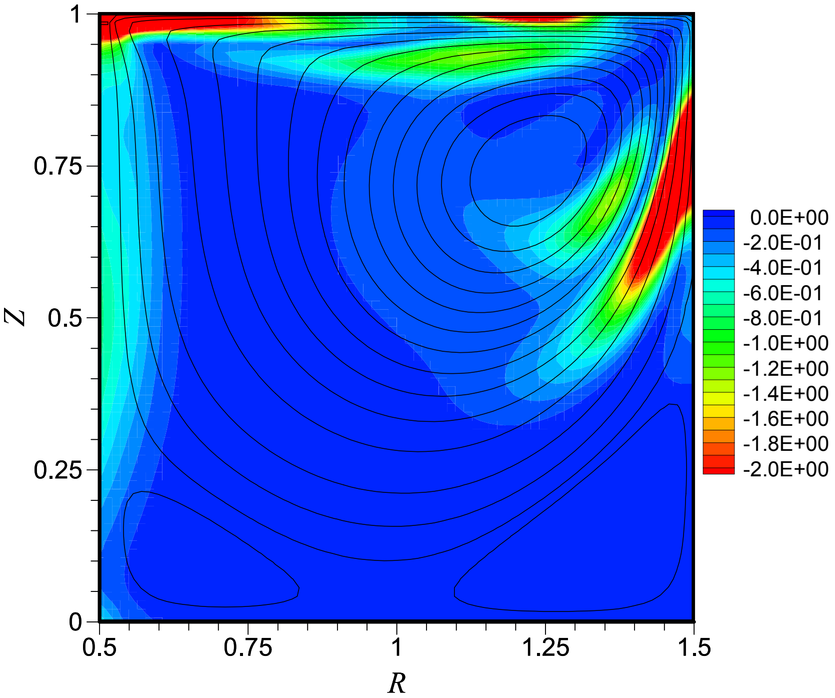

Figure 4.23. Circumferentially-averaged streamlines together with the distributions of the production and dissipation of the fluctuating vorticity in the (*R*-*Z*) plane for the LDC flow arrangement (sliding wall radially outward) with δ = 1.0 and at Re = 600. (a) The vorticity production P_1'' (b) The vorticity production P_2''; and (c) The vorticity dissipation D_ω''.

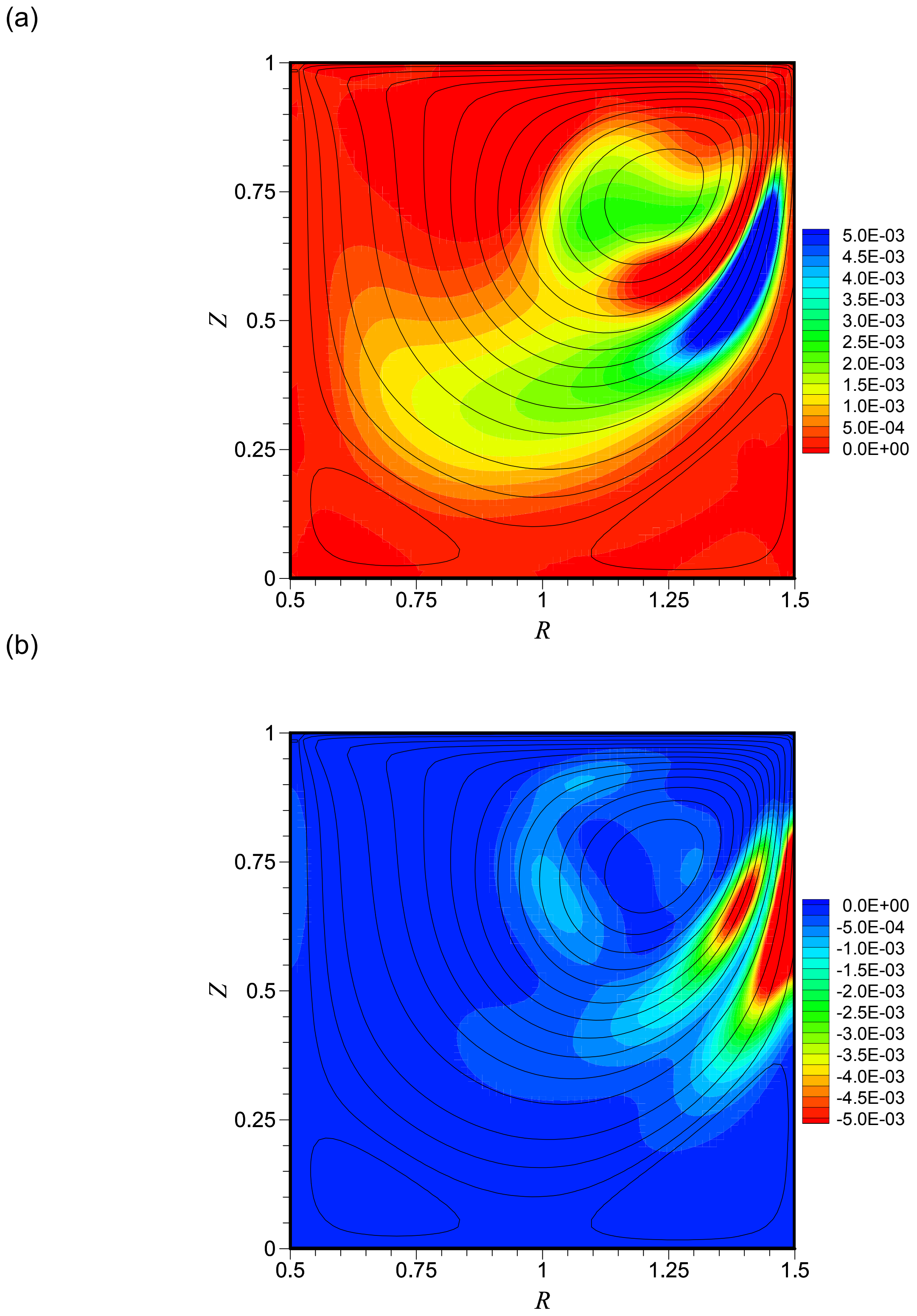

Figure 4.24. Circumferentially averaged streamlines together with the distributions of the production and dissipation of the fluctuating kinetic energy in the (*R*-*Z*) plane for the LDC flow arrangement (sliding wall radially outward) with δ = 1.0 and at Re = 600. (a) The energy production P_E'' and (b) The energy dissipation D_E''.

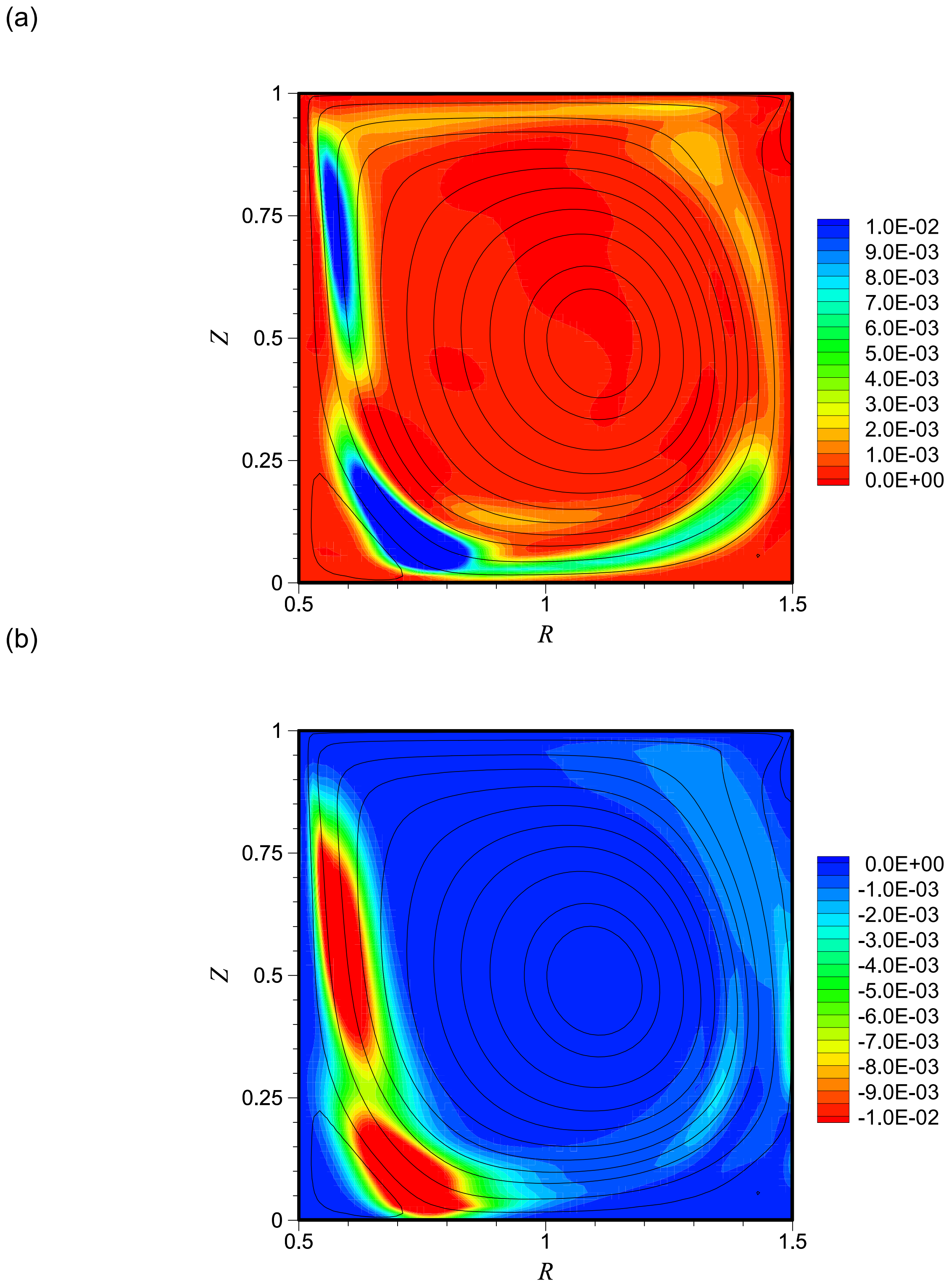

Figure 4.25. Circumferentially-averaged streamlines together with the distributions of the production and dissipation of the fluctuating kinetic energy in the (*R*-*Z*) plane for the LDC flow arrangement (sliding wall radially inward) with $\delta = 1.0$ and at Re = 1250. (a) The energy production P''_E and (b) The energy dissipation D''_E .

(a)

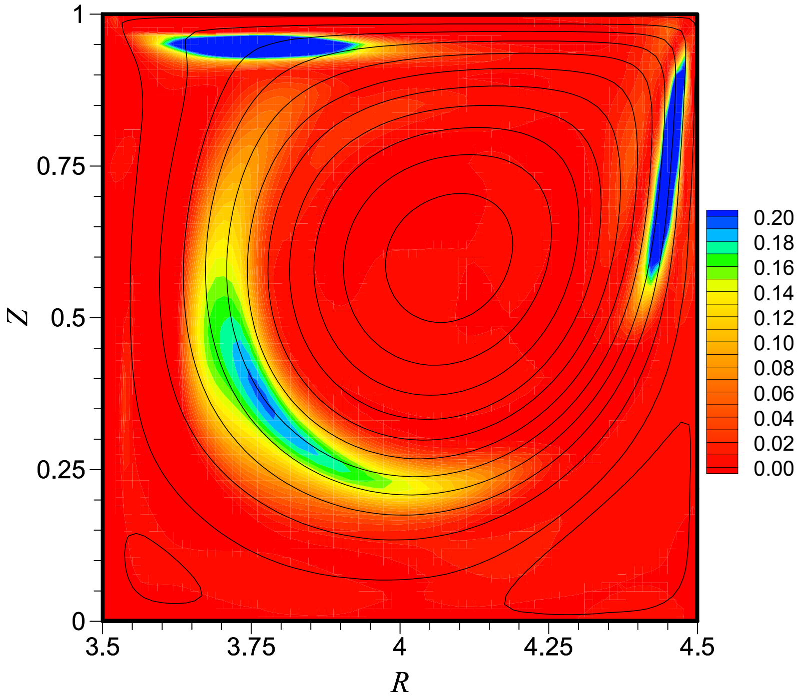
1
0.75
Z 0.5
0.25
0
3.5
3.75
4
4.25
4.5
R
0.20
0.18
0.16
0.14
0.12
0.10
0.08
0.06
0.04
0.02
0.00

(b)

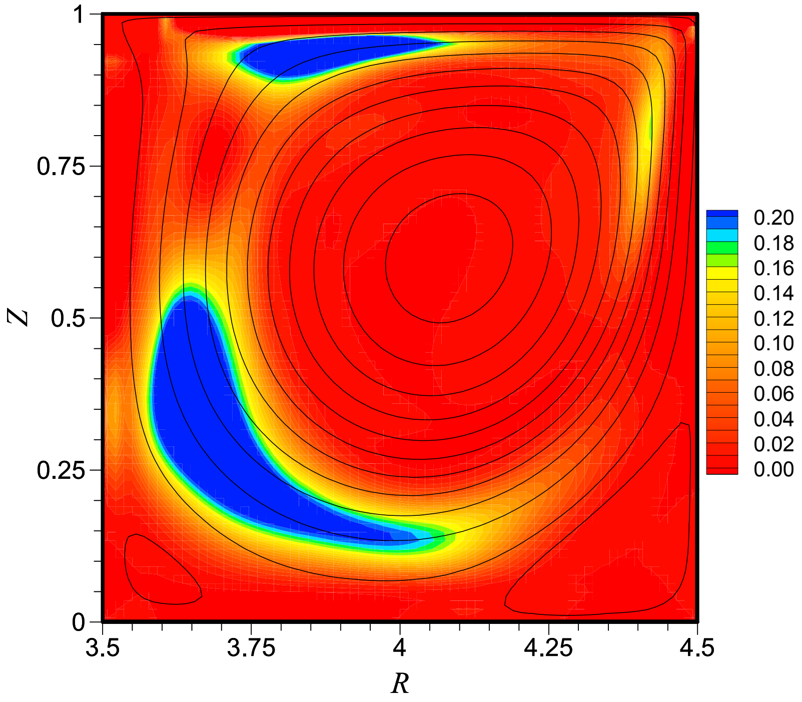
1
0.75
Z 0.5
0.25
0
3.5
3.75
4
4.25
4.5
R
0.20
0.18
0.16
0.14
0.12
0.10
0.08
0.06
0.04
0.02
0.00

(c)

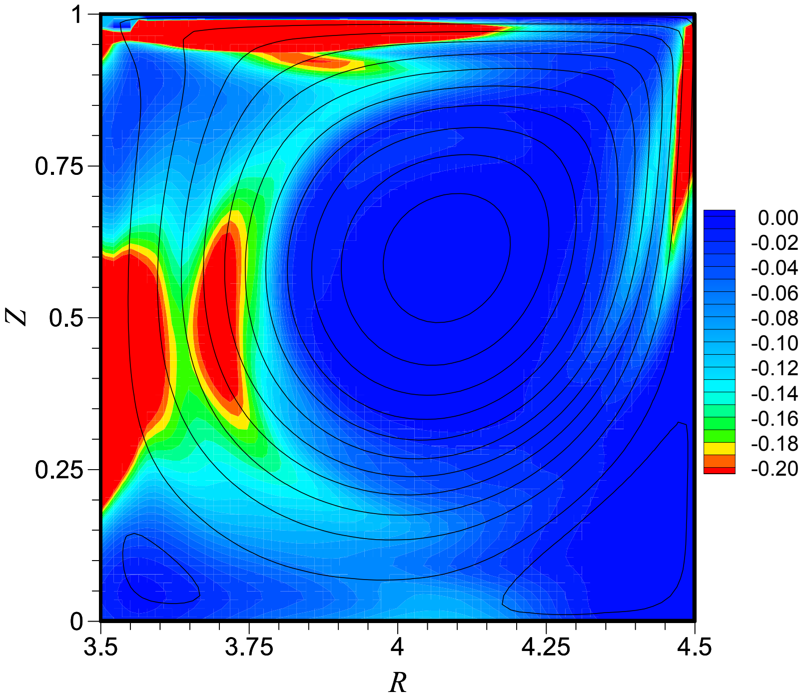

Figure 4.26. Circumferentially- and time-averaged streamlines together with the distributions of the production and dissipation of the fluctuating vorticity in the (*R*-*Z*) plane for the LDC flow arrangement (sliding wall radially outward) with δ = 0.25 and at Re = 880. (a) The vorticity production P_1' and (b) The vorticity production P_2'; and (c) The vorticity dissipation D_ω'.

(a)

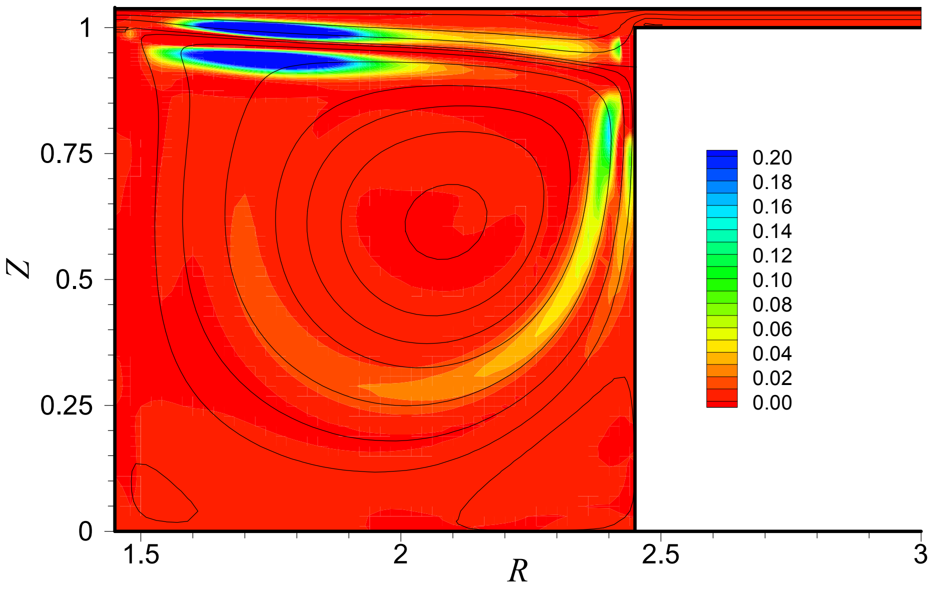
1
0.75
0.5
0.25
0
Z
1.5
2
2.5
3
R
0.20
0.18
0.16
0.14
0.12
0.10
0.08
0.06
0.04
0.02
0.00

(b)

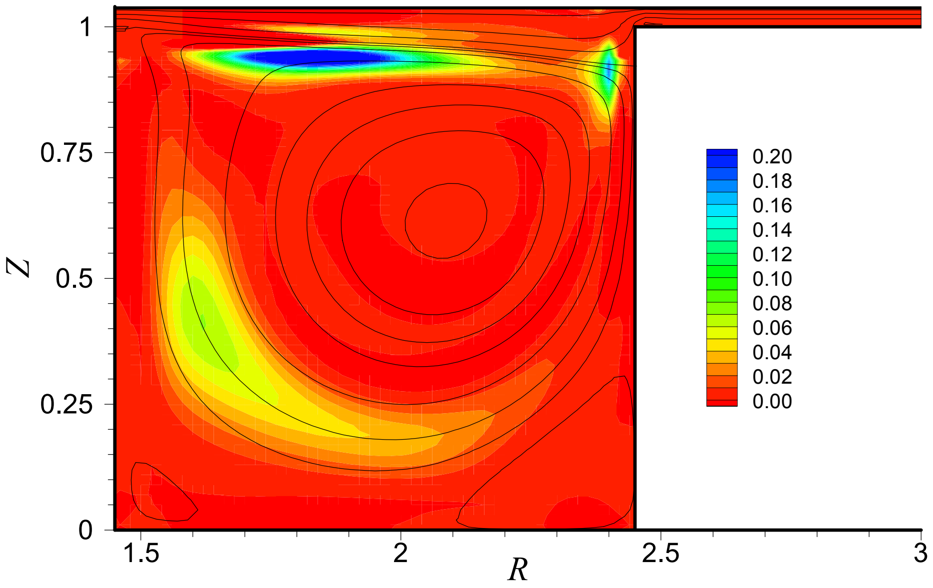
1
0.75
0.5
0.25
0
Z
1.5
2
2.5
3
R
0.20
0.18
0.16
0.14
0.12
0.10
0.08
0.06
0.04
0.02
0.00

(c)

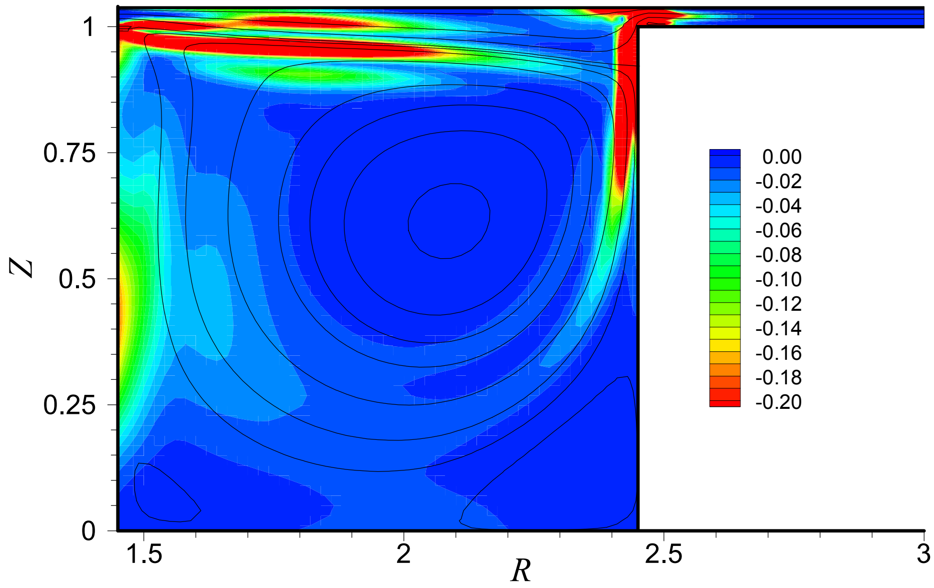

Figure 4.27. Circumferentially- and time-averaged streamlines together with the distributions of the production and dissipation of the fluctuating vorticity in the (*R*-*Z*) plane for open-cavity flow arrangement with $\delta = 0.51$ and $\gamma = 0.04$ and at $\mathrm{Re} = 850$. (a) The vorticity production P_1' and (b) The vorticity production P_2'; and (c) The vorticity dissipation D_ω'.

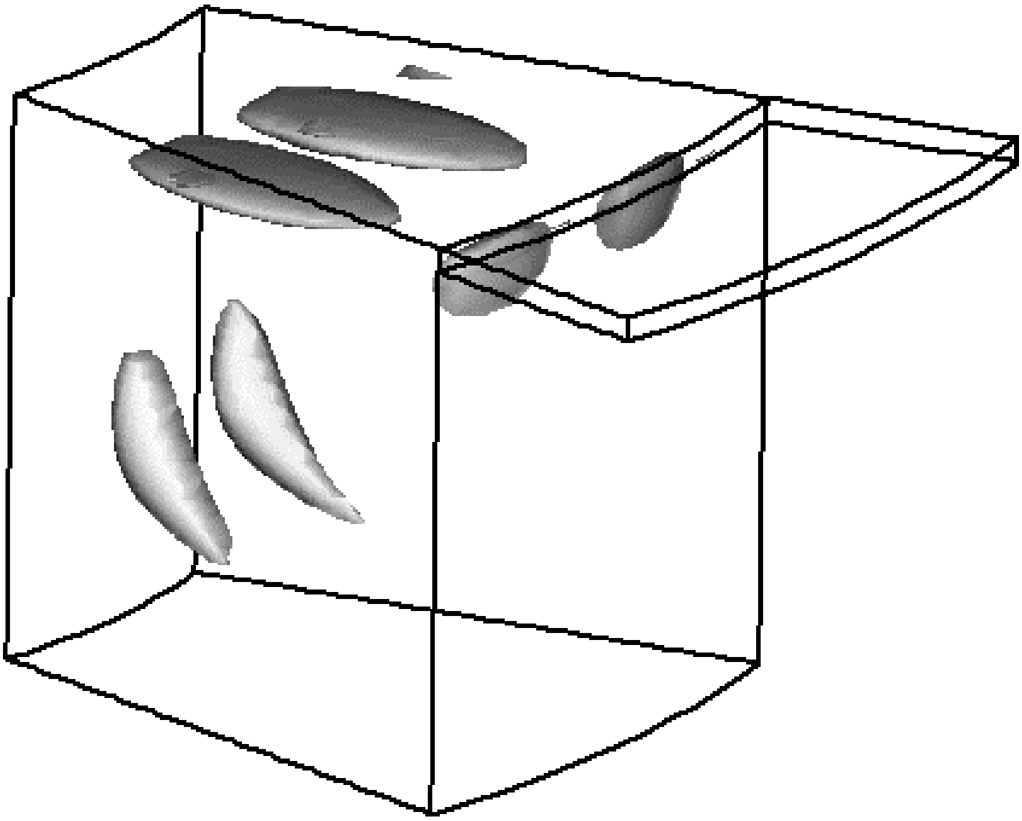

Figure 4.28. Local distributions of the fluctuating vorticity production P_2' over one wavelength for the conditions of Fig. 4.27. The dimensionless level of the isosurface = 0.1.

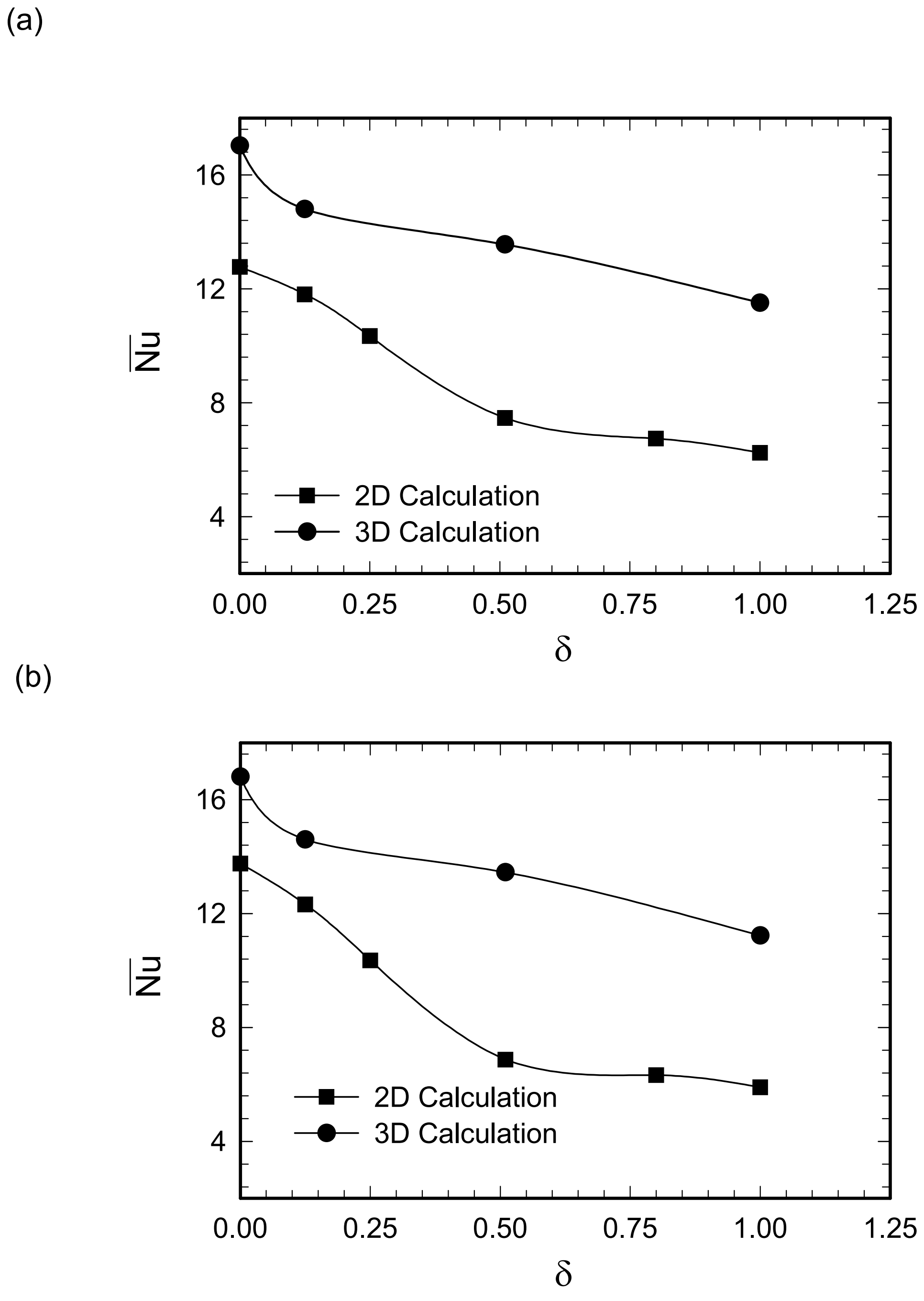

Figure 4.29. Variations of average Nusselt number as a function of the toroid curvature obtained from the 2D and 3D calculations for the LDC flow arrangement (sliding wall radially outward) at Re = 880 and Pr = 7.1(water). Boundary condition of (a) Constant temperature and (b) Constant heat flux have been used at the top wall and bottom walls.

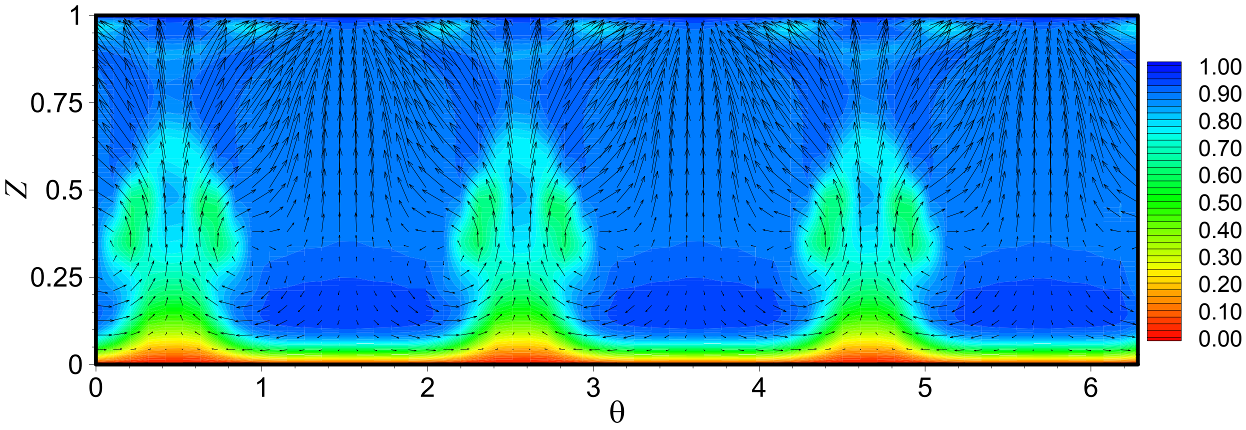

Figure 4.30. Velocity vectors together with isocontours of the dimensionless temperatures in the (Z-θ) mid-plane for the LDC flow arrangement (sliding wall radially outward) with $\delta = 1.0$, Re = 600, and Pr = 7.1(water). Boundary conditions of constant temperature have been applied at the top and bottom walls.

(a)

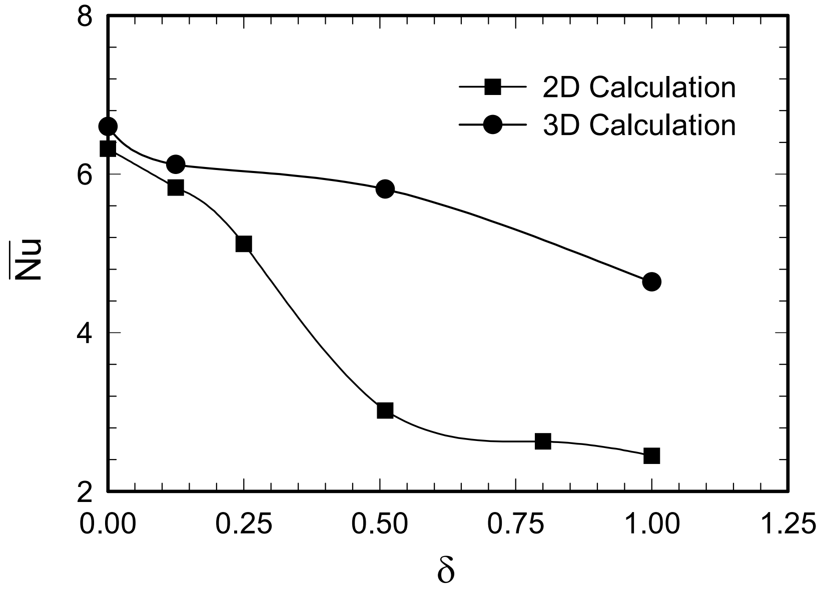

(b)

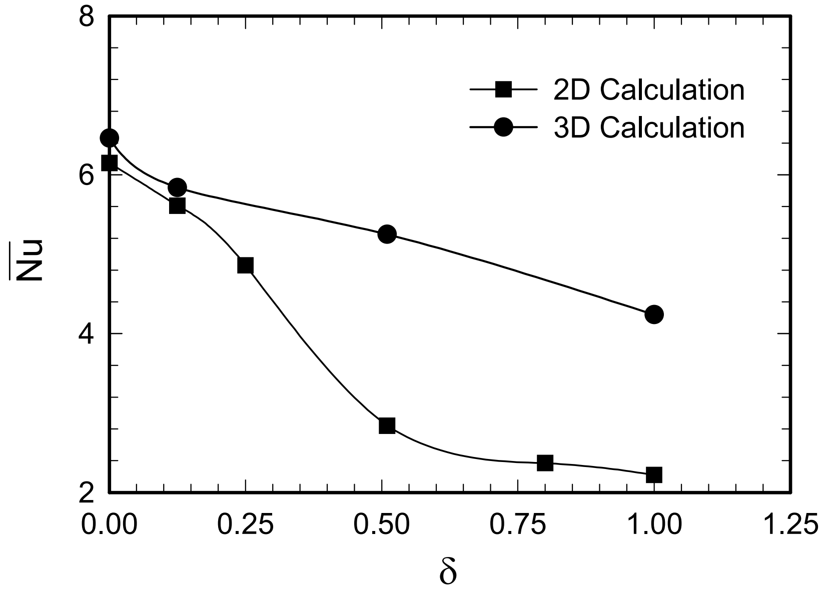

Figure 4.31. Variations of average Nusselt number as a function of the toroid curvature obtained from the 2D and 3D calculations for the LDC flow arrangement (sliding wall radially outward) at Re = 880 and Pr = 0.71(air). Boundary conditions of (a) Constant temperature and (b) Constant heat flux have been used at the top and bottom walls.

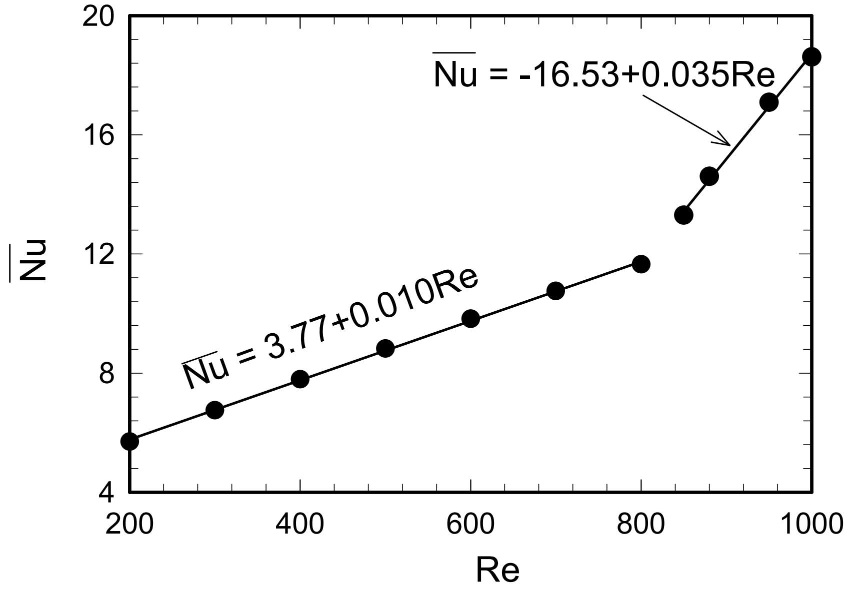

Figure 4.32. Variations of average Nusselt number as a function of Reynolds number for the LDC flow arrangement (sliding wall radially outward) with δ = 0.125 and Pr = 7.1 (water). Boundary conditions of constant temperature have been applied at the top and bottom walls.

(a)

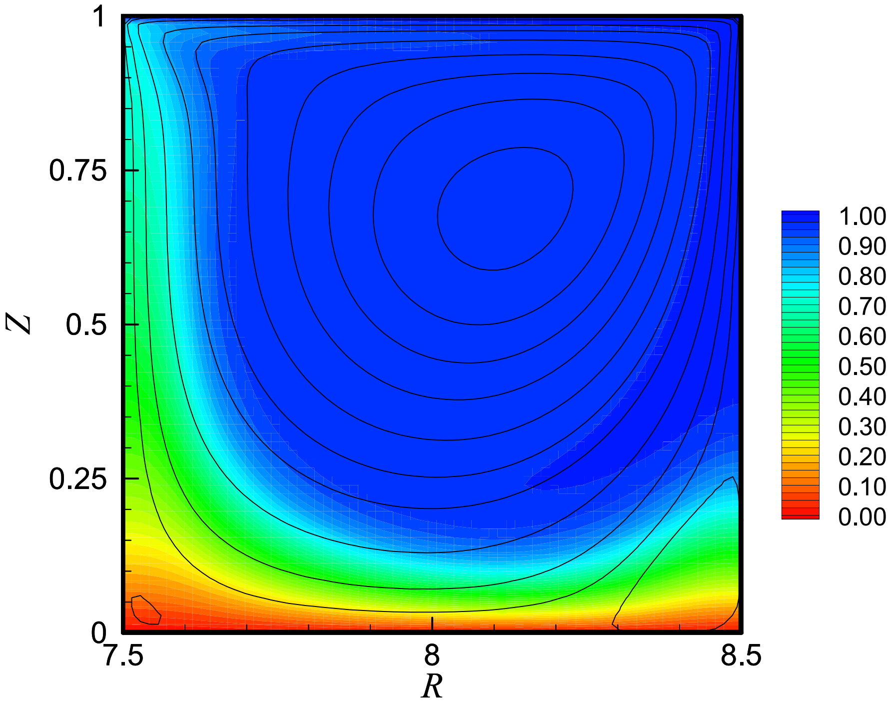

(b)

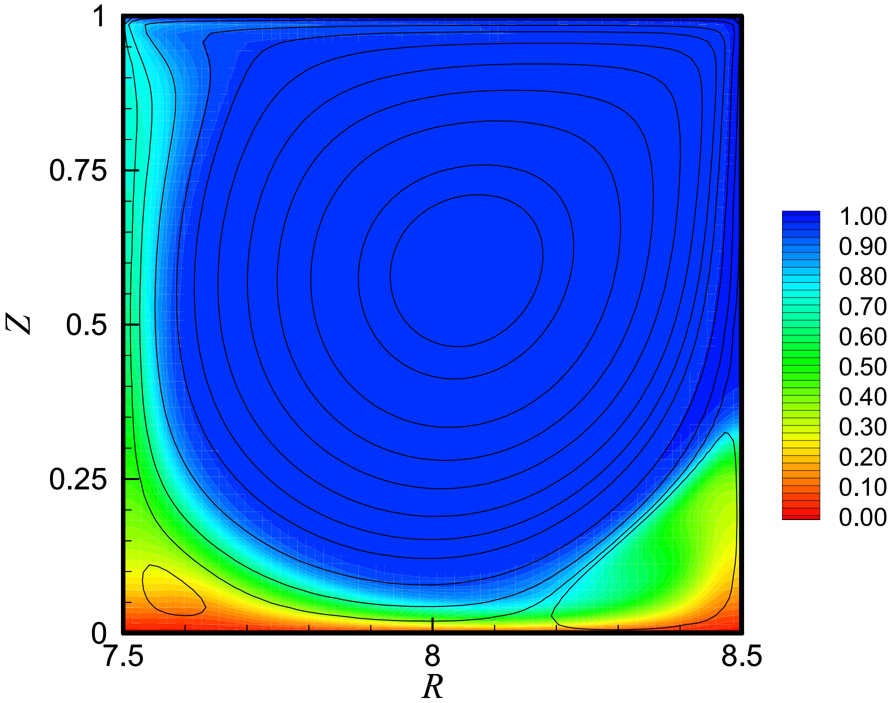

Figure 4.33. Streamlines together with isocontours of the dimensionless temperatures in the (*R*-*Z*) plane for the LDC flow arrangement (sliding wall radially outward) with δ = 0.125, Pr = 7.1 (water), and Re = 200 (a) 800 (b). Boundary conditions of constant temperature have been applied at the top and bottom walls.

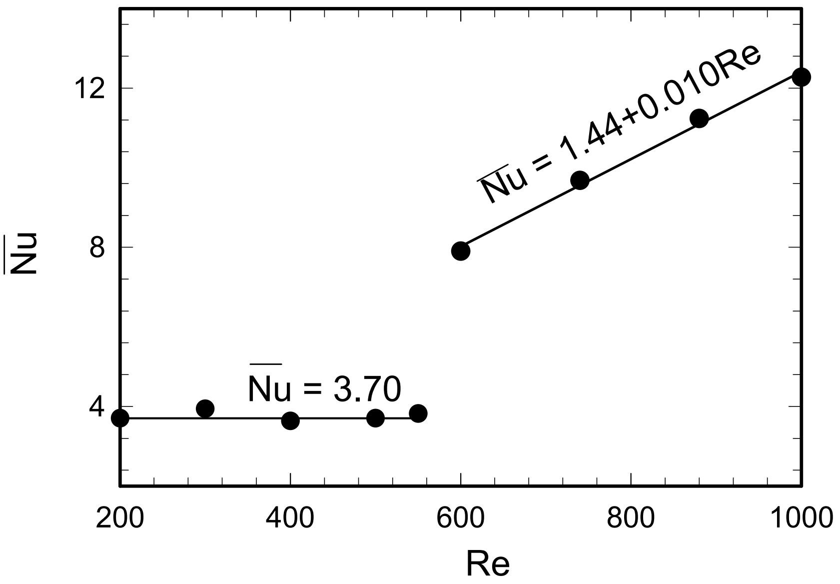

Figure 4.34. Variations of average Nusselt number as a function of Reynolds number for the LDC flow arrangement (sliding wall radially outward) with $\delta = 1.0$ and $Pr = 7.1$ (water). Boundary conditions of constant temperature have been applied at the top and bottom walls.

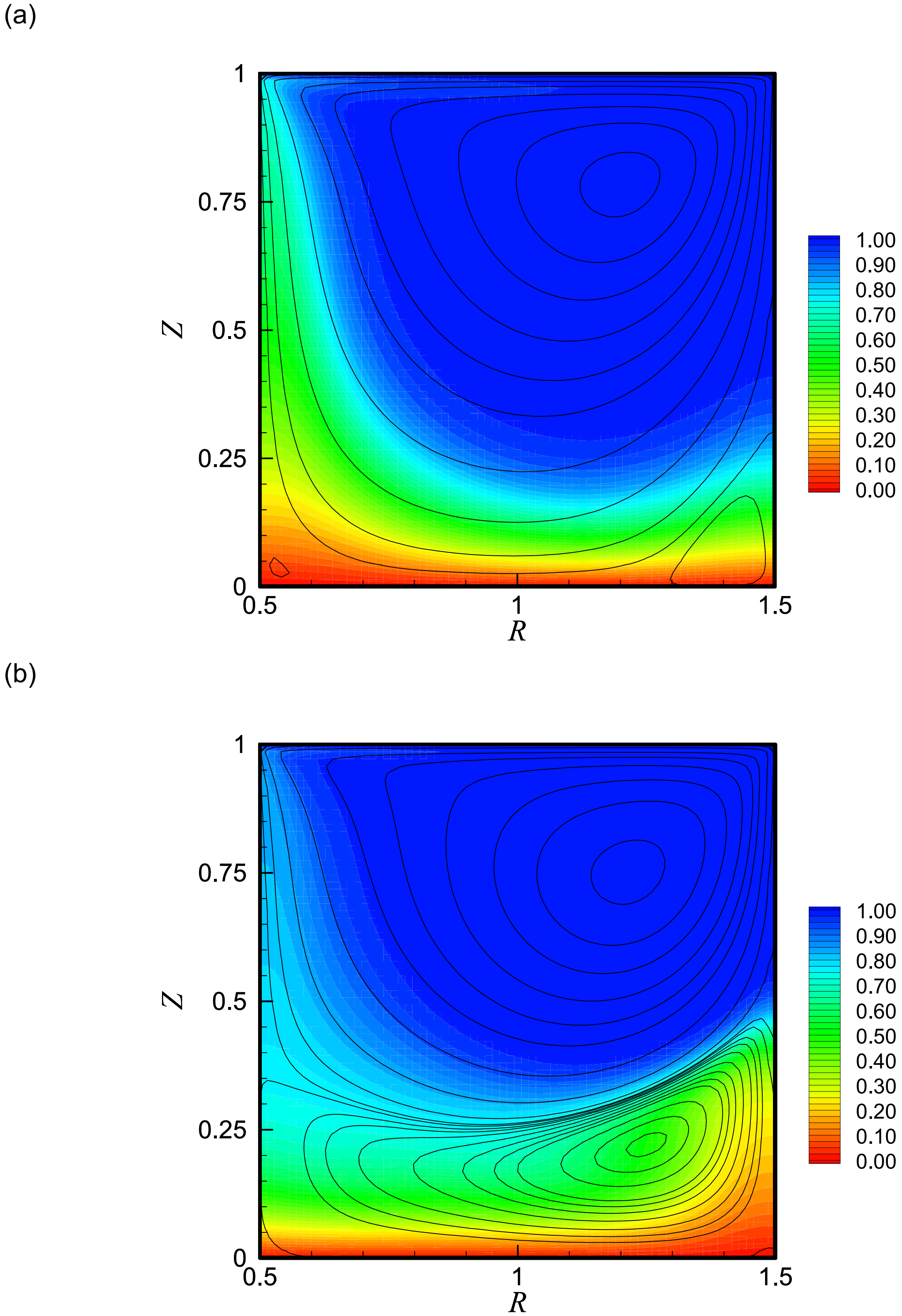

Figure 4.35. Streamlines together with isocontours of the dimensionless temperatures in the (*R*-*Z*) plane for LDC flow arrangement (sliding wall radial outward) with δ = 1.0, Pr = 7.1 (water), and Re = 200 (a) and 550 (b). Boundary conditions of constant temperature have been applied at the top and bottom walls.

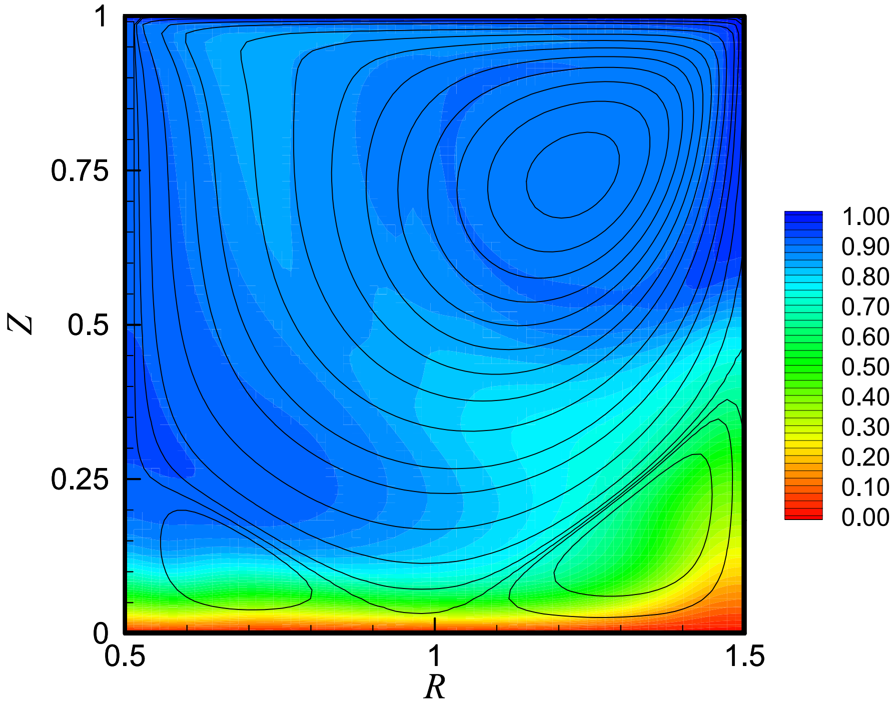

Figure 4.36. Circumferentially-averaged streamlines together with isocontours of the circumferentially-averaged temperatures in the (R-Z) plane for the LDC flow arrangement (sliding wall radially outward) with $\delta = 1.0$, Pr = 7.1 (water), and Re = 600. Boundary conditions of constant temperature have been applied at the top and bottom walls.

5. CONCLUSIONS AND FUTURE WORK

Direct Numerical Simulations (DNS) and flow visualization experiments have been used to study the flow structure in a toroidal cavity of square cross-section. The calculated Görtler numbers, Eq. (2.36), of the toroidal LDC and open-cavity flow arrangements considered are greater than ten. This satisfies the stability criterion for the appearance of Taylor-Görtler vortices (TGV), due to the curvature of the streamlines of recirculating core flow and not because of the geometrical curvature of the toroid (Freitas and Street,1988).

The centrifugal-type instabilities of LDC flow (sliding top wall radially outward) are characterized by three different types of modes: i) steady modes of short wavelength at low curvature, ii) unsteady modes of long wavelength at $\delta = 0.25$, and iii) steady modes of even longer wavelength at high curvature.

The 3D open-cavity flows with curvature ratios $\delta = 0.25$ and 0.51 have a time-periodic regimes with the same wavenumber for both curvatures. Comparison of the numerical results of the LDC and open-cavity flow arrangements shows that the external channel flow affects the 3D-flow behavior. The dynamic behavior of TGV is as follows. From Eulerian viewpoint, the vortices alternate the sense of rotation periodically every half period of oscillation. Relative to a fixed reference point, the vortices disappear and reappear with a circumferential shift of half wavelength every half period of oscillation.

Flow visualizations have allowed for the first time to capture TGV in the toroidal cavities (Humphrey et al., 2001 ; 2002(see appendix C)). At $\delta = 0.25$, the real-time observations have shown unsteady flow regime characterized by disappearance and reappearance of the vortices alternatively over a period of order of one minute. Moreover, the PIV measurements of the flow in the open-cavity with $\delta = 0.51$ have given a wavenumber in agreement with the calculated one.

Like the circumferentially-fluctuating vorticity budget of the steady LDC flow at low curvature, the TGV of the unsteady flow regimes are caused mostly by stretching/tilting of the time vorticity fluctuations by the mean rate of strain. The rest of the production comes through an exchange between the time-fluctuating and the mean vorticity fields.

When the LDC motion is induced by sliding the top wall radially inward, steady modes of short wavelength will dominate the 2D-3D transition process for any δ value. For small curvatures of the inward LDC, the vortices are produced mostly near the upstream wall. By increasing the curvature ratio to $\delta = 1.0$, higher Reynolds number (Re = 1250) is required to produce the TGV near the concave separation surface of downstream eddy and near the upper part of the downstream wall.

While the spatial distributions of the 3D vortex production and dissipation depend on the toroidal cavity flow configuration and its curvature, TGV are always aligned in banana-like structures between the upstream wall and the bottom of the cavity for all toroidal flow arrangements.

Comparison of the heat-transfer rates corresponding to two- and three-dimensional flows shows the important role of TGV in enhancing the transport process in the toroidal cavity. In particular, Taylor-Görtler modes of longer wavelength are preferred to improve the mixing process.

On the other hand, it is worthy to measure, in a future research, the time variations of velocity at certain points of the flow domain using, for example, Laser-Doppler velocimetry (LDV), thereby allowing the experimental verification of the time-periodic flow behavior. Numerical analysis of the complex dynamic of TGV during the earlier stages of 3D flow development would be helpful to obtain a complete explanation of the periodic alternation in the sense of rotation of vortices. In addition, it would be interesting to investigate the breakdown of the Taylor-Görtler vortex flow and the transition to turbulence.

For rectangular LDC flows ($\delta = 0$), Albensoeder et al. (2001a) have reported three different types of modes that depending on the aspect ratio of cavity cross-section. It is recommended to study the dependency of 2D-3D flow transition on the aspect ratio at different curvatures.

From practical engineering point of view, toroidal cavity flow configuration provides an interesting geometry for industrial fermentation processes where high level of mixing are required at moderate levels of the mechanical stresses exert upon the microorganisms.

REFERENCES

Aidun, C. K., Triantafillopoulos, N. G., and Benson, J. D., “Global Stability of a Lid-Driven Cavity with Throughflow: Flow Visualization Studies”, *Physics of Fluids*, vol. 3, no. 9, pp. 2081-2091, 1991.

Albensoeder, S., Kuhlmann, H. C., and Rath, H. J., “Three-dimensional centrifugal-flow instabilities in the lid-driven-cavity problem”, *Physics of Fluids*, vol. 13, no. 1, pp. 121-135, 2001.

Albensoeder, S., Kuhlmann, H. C., and Rath, H. J., “Multiplicity of steady two-dimensional flows in two-sided lid-driven cavities*”, Theoretical and Computational Fluid Dynamics Fluids*, vol. 14, pp. 223-241, 2001.

Alleborn, N., Raszillier, H., and Durst, F., “Lid-driven cavity with heat and mass transport”, *International Journal of Heat and Mass Transfer*, vol. 42, pp. 833-853, 1999.

Al-Shannag, M., Herrero, J., Humphrey, J. A. C., and Giralt, F., “Effect of radial clearance on the flow between corotating disks in fixed cylindrical enclosures”, *Journal of fluid Engineering*, 2002 (Accepted).

Bayly, B. J., ”Three-dimensional centrifugal-type instabilities in inviscid two-dimensional flows”, *Physics of Fluids*, vol. 31, pp. 56-64, 1988.

Benjamin, A. S., and Denny, V.E., ”On the Convergence of Numerical Solutions for 2-D Flow in a Cavity at Large Re”, *Journal of Computational Physics*, vol. 33, pp. 340-358, 1979.

Benson, J. D., and Aidun, C. K., “Transition to unsteady nonperiodic state in a through-flow lid-driven cavity”, *Physics of Fluids* A, vol. 4, pp. 2316-2319, 1992.

Bird, R. B., Stewart, W. E., and Lightfoot, E. N., *Transport Phenomena*, John Wiley & Sons, New York, 1960.

Blohm, CH., and Kuhlmann H. C., “The two-sided lid-driven cavity: experiments on stationary and time-dependent flows”, *Journal of Fluid Mechanics*, vol. 450, pp. 67-95, 2002.

Burggraf, O. R., “Analytical and numerical studies of the structure of steady separated flow”, *Journal of Fluid Mechanics*, vol. 24, pp. 113-151, 1966.

Cuesta, I., Grau, F. X., Giralt, F., and Cohen, Y., “Air-water mass transfer of organics from shallow ponds under laminar circulation”, *International Journal of Heat and Mass Transfer*, vol. 42, pp. 165-179, 1999.

Cushner, J., ”Experimental visualization of a shear-driven-cavity problem”, M.Sc. Thesis, College of Engineering, Bucknell University, Lewisburg, Pennsylvania, 2000.

Deshpande, M. D., and Milton, S. G, “Kolmogorov scales in a driven cavity”, *Physics of Fluid Dynamics Research*, vol. 22, pp. 359-381, 1998.

Ding, Y., and Kawahara, M., “Linear Stability of Incompressible Flow Using a Mixing Finite Element Methods”, *Journal of Computational Physics*, vol. 139, pp. 243-273, 1998.

Drazin, P. G., and Reid, W. H., *Hydrodynamic Stability*, Cambridge University Press, Cambridge, 1981.

Freitas, C. J. and Street, R. L., “Nonlinear transient phenomena in complex recirculating flow: A numerical investigation,” *International Journal for Numerical Methods in Fluids*, vol. 8, pp. 769-802, 1988.

Freitas, C. J., Street, R. L., Findikakis, A. N. and Koseff, J. R., “Numerical simulation of three dimensional flow in a cavity,” *International Journal for Numerical Methods in Fluids*, vol. 5, pp. 561-575, 1985.

Ghia,U., Ghia, K. N., and Shin, C.T., ”High-Re Solutions for Incompressible Flow Using the Navier-Stokes Equations and Multigrid Methods in Fluids”,*. Journal of Computational Physics*, vol. 48, pp. 387-411, 1982.

Golub, G. H. and Van Loan, Ch. F., *Matrix Computations*, 3rd ed., Johns Hopkins University Press, Baltimore, 1996.

Goodrich, J. W., Gustafson, K., and Halasi, K., “Hopf Bifurcation in the Driven Cavity”, *Journal of Computational Physics*, vol. 90, 219-261, 1990.

Herrero, J., Giralt, F., and Humphrey, J. A. C.,” Influence of the geometry on the structure of the flow between a pair of corotating disks”, *Physics of Fluids*, vol. 11, no. 1, pp. 88-96, 1999.

Herrero, J., Giralt, F., and Humphrey, J. A. C.,” Non-isothermal laminar flow and heat transfer between disks corotating in a fixed enclosure”, *International Journal of Heat and Mass Transfer,* vol. 42, pp. 3291-3306, 1999.

Humphrey, J. A. C., Cushner, R., Al-Shannag, M., Herrero, J., and Giralt, F. “Shear-driven flow in a toroid of square cross-section”, *Journal of fluid Engineering*, 2002, (Accepted).

Humphrey, J. A. C., Cushner, J., Sudarsan, R., Al-Shannag, M., Herrero, J., and Giralt, F. “Experimental and numerical investigation of the shear-driven flow in a toroid of square cross-section”, 2nd International Symposium on Turbulence and Shear Flow Phenomena, Royal Institute of Technology (KTN), Stockholm, Sweden, 27-29, June 2001.

Humphrey, J. A. C., and Phinney, L. M., “Extension of the Wall-Driven Enclosure Flow Problem to Toroidally Shaped Geometries of Square cross-section”, *Journal of Fluid Engineering*, vol. 118, pp. 779-786, 1996.

Humphrey, J. A. C., Schuler, C. A., and Iglesias, I.,” Analysis of viscous dissipation in disk storage systems and similar flow configurations”, *Physics of Fluids A*, vol. 4, no. 7, pp. 1415-1426, 1992.

Humphrey, J. A. C., Schuler, C. A., and Webster, D. R.,” Unsteady laminar flow between a pair of disks corotating in a fixed cylindrical enclosure”, *Physics of Fluids*, vol. 7, no. 6, pp. 1225-1240, 1995.

Iglesias, I. and Humphrey, J. A. C.,” Two- and three-dimensional laminar flows between disks co-rotating in a fixed cylindrical enclosure”, *International Journal for Numerical Methods in Fluids*, vol. 26, pp. 581-603, 1998.

Iwatsu, R., Ishii, K., Kawamura, T., Kuwahara, K., and Hyun, J. M., “ Numerical Simulation of Three-Dimensional Flow structure in a Driven Cavity”, *Fluid Dynamics Research*, vol. 5, pp. 173-189, 1989.

Jana, S. C., Metcalfe, G., and Ottino, J. M.,” Experimental and numerical studies of mixing in complex Stokes flows: the vortex mixing flow and multicellular cavity flows”, *Journal of Fluid Mechanics*, vol. 269, pp. 199-246, 1994.

Jeje, A. A., and Zimmerman, M. H., “Resistance to Water Flow in Xylem Vessels”, *Journal of Experimental Botany*, vol. 30, pp. 817-823, 1979.

Jordan, S. A., and Ragab, S. A., “On the Unsteady and Turbulent Characteristics of the Three-Dimensional Shear-Driven Cavity Flow”, *Journal of Fluid Engineering*, vol. 116, pp. 439-449, 1994.

Klein, M. V., *Optics*, John Wiley & Sons, New York, 1970.

Koseff, J. R., and Street, R. L., “Visualization studies of a shear driven three-dimensional recirculation flow”, *Journal of Fluid Engineering*, vol. 106, pp. 21-29, 1984a.

Koseff, J. R., and Street, R. L., “On end wall effects in a lid-driven cavity flow”, *Journal of Fluid Engineering*, vol. 106, pp. 385-389, 1984b

Koseff, J. R., and Street, R. L., “The lid-driven cavity flow: a synthesis of qualitative and quantitative observations”, *Journal of Fluid Engineering*, vol. 106, pp. 390-398, 1984c.

Koseff, J. R., Street, R. L., and ASCE, M., “Circulation Structure in a Stratified Cavity Flow”, *Journal of Hydraulic Engineering*, vol. 111, pp. 334-354, 1985.

Koseff, J. R., Street, R. L., Gresho, P. M., Upson, C. D., Humphrey, J. A. C., and To, W. M., “A three-dimensional lid-driven cavity flow: experiment and simulation”, *3rd*

International Conference On Numerical Methods in Laminar and Turbulent Flow (ed. C. Taylor), pp. 564-581, 1983.

Ku, H. C., Hirsh, R. S., and Taylor, T. D., “A Pseudospectoral method for solution of the three-dimensional incompressible Navier-Stokes equations”, *Journal of Computational Physics*, vol. 70, pp. 439-462, 1987.

Kuhlmann H. C., Wanschura, M., and Rath, H. J., “Flow in two-sided lid-driven cavities: non-uniqueness, instabilities, and cellular structures”, *Journal of Fluid Mechanics*, vol. 336, pp. 267-299, 1997.

Kuhlmann H. C., Wanschura, M., and Rath, H. J., “Elliptic instability in two-sided lid-driven cavity flow”, *European Journal of Mechanics*- B/FLUID, vol. 17, no. 4, pp. 561-569, 1998.

Leonard, B. P., “A Stable and Accurate Convective Modeling Procedure Based on Quadratic Upstream Interpolation”, *Computer Methods in Applied Mechanics and Engineering*, vol. 19, 59-98, 1979.

Leriche, E., and Gavrilakis, S., “ Direct numerical simulation of the flow in a lid-driven cubical cavity”, *Physics of Fluids*, vol. 12, no. 6, pp. 1363-1376, 1999.

Luchini, P., “A Deferred-Correction Multigrid Algorithm Based on a New Smoother for the Navier-Stokes Equations”, *Journal of Computational Physics,* vol. 92, pp. 349-368, 1991.

Miles, K. C., Nagarajan, B., and Zumbrunnen, D. A.,” Three-dimensional chaotic mixing of fluids in a cylindrical cavity”, *Journal of Fluid Engineering*, vol. 117, pp. 582-588, 1995.

Nishida, H., and Satufoka, N., “Higher-Order Solutions of Square Driven Cavity Flow Using a Variable-Order Multi Grid Methods*”, International Journal for Numerical Methods in Engineering*, vol. 19, pp. 637-653, 1992.

Osswald, G. A., Ghia, K. N., and Ghia, U., “ A Direct Algorithm for Solution of Incompressible Three-Dimensional Unsteady Navier-Stokes Equations”, *AIAA pape*r, pp. 87-1139, 1987.

Ottino, J. M., *The kinematics of Mixing: Stretching, Chaos, and Transport*, Cambridge University Press, Cambridge, 1989.

Pan, F., and Acrivos, A., “Steady flow in rectangular cavity”, *Journal of fluid mechanics*, vol. 28, pp. 643-655, 1967.

Patankar, S. V., *Numerical Heat Transfer and Fluid Flow*, McGraw-Hill, New York, 1980.

Poliashenko, M., and Aidun, C. K.,“A Direct Method for Computation of Simple Bifurcations”, *Journal of Computational Physics*, vol. 121, pp. 246-260, 1995.

Prasad, A. K., and Koseff, J. R., “Reynolds Number and End-Wall Effects on a Lid-Driven Cavity Flow”, Physics of Fluid A, vol. 92, pp. 208-218, 1989.

Prasad, A. K., Perng, C. Y., and Koseff, J. R., “Some Observations on the Influence of Longitudinal Vortices in a Lid-Driven Cavity Flow”, AIAA paper, no. 88-3654CP, pp. 288-295, 1988.

Raffel, M, Willert C. E., and Kompenhans, J., *Particle image velocimetry a practical guide*, Springer, Berlin, 1998.

Rai, M. M. and Moin, P. “Direct Simulations of Turbulent Flow Using Finite-Difference Schemes”, *Journal of Computational Physics*, vol. 96, pp. 15-53, 1991.

Ramanan, R., and Homsy, G. M., “Linear Stability of Lid-Driven Cavity Flow”, *Physics of Fluids*, vol. 6, no. 8, pp. 2690-2701, 1994.

Rayleigh, “ On the dynamic of revolving fluids”, *Proc. Roy. Soc.*, A 93, pp. 148-154, 1916.

Rhee, H. S., Koseff, J. R., and Street, R. L., “Flow visualization of recirculating flow by rheoscopic liquid and liquid crystal”, *Experiments in fluids*, vol. 2, pp. 57-64, 1984.
Sand, I. O., “On unsteady reacting flow in a channel with a cavity”, *Journal of Fluid Mechanics*, vol. 229, pp. 339-364, 1991.

Schreiber, R., and Keller, H. B., “Driven Cavity Flows by Efficient Numerical Techniques”, *Journal of Computational Physics,* vol. 49, pp. 310-333, 1983.

Schuler, C. A, Usry, W., Weber, B., Humphrey, J. A. C., and Grief, R., “On the flow in unobstructed space between shrouded corotating disks”, *Physics of Fluids A,* vol. 2, no. 10, pp. 1760-1770, 1990.

Shankar, P. N., and Deshpande, M. D.,” Fluid mechanics in the driven cavity”, *Annual Review of Fluid Mechanics*, vol. 32, pp. 93-136, 2000.

Shen, J., “Hopf Bifurcation of the unsteady regularized driven cavity flow*”, Journal of Computational Physics*, vol. 95, pp. 228-245, 1991.

Spassov, U. D., ”Estudio de la instabilidad de flujos incompresibles. Analisis lineal de estabilidad y simulacion numerica directa”, Ph.D. Thesis, Department of Mechanical Engineering, ETSEQ, Rovira i Virgili University, Catalunya, 2001.

Sudarsan, R., Humphrey, J. A. C., and Heinrich, J., “Three-dimensional unsteady wall-driven flow in a toroid of square cross-section: a new CFD paradigm,” Proceedings of the ASME FED Summer Meeting: Forum on Industrial and Environmental Applications of Fluid Mechanics, FEDSM98-5314, June 21-25, Washington, D.C. (1998).

Takami, H., and Keller, H. B.,”Numerical study of three-dimensional flow within a cubic cavity”, *Journal of the Physical Society of Japan*, vol. 37, pp. 1695-1698, 1974.

Taylor, G. I., ”Stability of a viscous liquid contained between rotating cylinders”, *Phil. Trans. R. Soc.*, *A* 223, pp. 289-343, 1923.

Tennekes, H., and Lumley, J. L., *A First Course in Turbulence*, MIT Press, Cambridge, 1972.

APPENDICES

APPENDIX A:

A.1 Equations of motion in cylindrical coordinates:

Continuity equation:

$$\frac{1}{R}\frac{\partial(Ru_R)}{\partial R}+\frac{1}{R}\frac{\partial u_\theta}{\partial\theta}+\frac{\partial u_Z}{\partial Z}=0 \tag{A.1.1}$$

R-momentum:

$$\begin{aligned}&\frac{\partial u_R}{\partial\tau}+u_R\frac{\partial u_R}{\partial R}+\frac{u_\theta}{R}\frac{\partial u_R}{\partial\theta}+u_Z\frac{\partial u_R}{\partial Z}-\frac{{u_\theta}^2}{R}=-\frac{\partial p}{\partial R}+\\&\frac{1}{\mathrm{Re}}\left(\frac{1}{R}\frac{\partial}{\partial R}\left(R\frac{\partial u_R}{\partial R}\right)+\frac{1}{R^2}\frac{\partial^2 u_R}{\partial\theta^2}+\frac{\partial^2 u_R}{\partial Z^2}-\frac{2}{R^2}\frac{\partial u_\theta}{\partial\theta}-\frac{u_R}{R^2}\right)\end{aligned} \tag{A.1.2}$$

θ-momentum:

$$\begin{aligned}&\frac{\partial u_\theta}{\partial\tau}+u_R\frac{\partial u_\theta}{\partial R}+\frac{u_\theta}{R}\frac{\partial u_\theta}{\partial\theta}+u_Z\frac{\partial u_\theta}{\partial z}+\frac{u_R u_\theta}{R}=-\frac{\partial p}{R\partial\theta}+\\&\frac{1}{\mathrm{Re}}\left(\frac{1}{R}\frac{\partial}{\partial R}\left(R\frac{\partial u_\theta}{\partial R}\right)+\frac{1}{R^2}\frac{\partial^2 u_\theta}{\partial\theta^2}+\frac{\partial^2 u_\theta}{\partial Z^2}+\frac{2}{R^2}\frac{\partial u_R}{\partial\theta}-\frac{u_\theta}{R^2}\right)\end{aligned} \tag{A.1.3}$$

Z-momentum:

$$\begin{aligned}&\frac{\partial u_Z}{\partial\tau}+u_R\frac{\partial u_Z}{\partial R}+\frac{u_\theta}{R}\frac{\partial u_Z}{\partial\theta}+u_Z\frac{\partial u_Z}{\partial Z}=-\frac{\partial p}{\partial Z}+\\&\frac{1}{\mathrm{Re}}\left(\frac{1}{R}\frac{\partial}{\partial R}\left(R\frac{\partial u_Z}{\partial R}\right)+\frac{1}{R^2}\frac{\partial^2 u_Z}{\partial\theta^2}+\frac{\partial^2 u_Z}{\partial Z^2}\right)\end{aligned} \tag{A.1.4}$$

A.2 Equations of vorticity in cylindrical coordinates:

$$\omega_R=\frac{1}{R}\frac{\partial u_Z}{\partial\theta}-\frac{\partial u_\theta}{\partial Z} \tag{A.2.1}$$

$$\omega_\theta=\frac{\partial u_R}{\partial Z}-\frac{\partial u_Z}{\partial R} \tag{A.2.2}$$

$$\omega_Z=\frac{1}{R}\frac{\partial(Ru_\theta)}{\partial R}-\frac{1}{R}\frac{\partial u_R}{\partial\theta} \tag{A.2.3}$$

R-component vorticity equation:

$$\begin{aligned}
&\frac{\partial \omega_R}{\partial \tau} + u_R \frac{\partial \omega_R}{\partial R} + \frac{u_\theta}{R}\left(\frac{\partial \omega_R}{\partial \theta} - \omega_\theta\right) + u_Z \frac{\partial \omega_R}{\partial Z} = \\
&\omega_R \frac{\partial u_R}{\partial R} + \frac{\omega_\theta}{R}\left(\frac{\partial u_R}{\partial \theta} - u_\theta\right) + \omega_Z \frac{\partial u_R}{\partial z} + \\
&\frac{1}{\mathrm{Re}}\left(\frac{1}{R}\frac{\partial}{\partial R}\left(R\frac{\partial \omega_R}{\partial R}\right) + \frac{1}{R^2}\frac{\partial^2 \omega_R}{\partial \theta^2} + \frac{\partial^2 \omega_R}{\partial Z^2} - \frac{2}{R^2}\frac{\partial \omega_\theta}{\partial \theta} - \frac{\omega_R}{R^2}\right)
\end{aligned} \qquad (\mathrm{A.2.4})$$

θ-component vorticity equation:

$$\begin{aligned}
&\frac{\partial \omega_\theta}{\partial \tau} + u_R \frac{\partial \omega_\theta}{\partial R} + \frac{u_\theta}{R}\left(\frac{\partial \omega_\theta}{\partial \theta} + \omega_R\right) + u_Z \frac{\partial \omega_\theta}{\partial z} = \omega_R \frac{\partial u_\theta}{\partial R} + \frac{\omega_\theta}{R}\left(\frac{\partial u_\theta}{\partial \theta} + u_R\right) + \omega_Z \frac{\partial u_\theta}{\partial Z} + \\
&\frac{1}{\mathrm{Re}}\left(\frac{1}{R}\frac{\partial}{\partial R}\left(R\frac{\partial \omega_\theta}{\partial R}\right) + \frac{1}{R^2}\frac{\partial^2 \omega_\theta}{\partial \theta^2} + \frac{\partial^2 \omega_\theta}{\partial Z^2} + \frac{2}{R^2}\frac{\partial \omega_R}{\partial \theta} - \frac{\omega_\theta}{R^2}\right)
\end{aligned} \qquad (\mathrm{A.2.5})$$

Z-component vorticity equation:

$$\begin{aligned}
&\frac{\partial \omega_Z}{\partial \tau} + u_R \frac{\partial \omega_Z}{\partial R} + u_\theta \frac{\partial \omega_Z}{R\partial \theta} + u_Z \frac{\partial \omega_Z}{\partial Z} = \omega_R \frac{\partial u_Z}{\partial r} + \omega_\theta \frac{\partial u_Z}{r\partial \theta} + \omega_Z \frac{\partial u_Z}{\partial z} + \\
&\frac{1}{\mathrm{Re}}\left(\frac{1}{R}\frac{\partial}{\partial R}\left(R\frac{\partial \omega_Z}{\partial R}\right) + \frac{1}{R^2}\frac{\partial^2 \omega_Z}{\partial \theta^2} + \frac{\partial^2 \omega_Z}{\partial z^2}\right)
\end{aligned} \qquad (\mathrm{A.2.6})$$

A.3 Energy conservation equation in cylindrical coordinates:

$$\frac{\partial T^*}{\partial \tau} + u_R \frac{\partial T^*}{\partial R} + u_\theta \frac{\partial T^*}{R\partial \theta} + u_Z \frac{\partial T^*}{\partial Z} = \frac{1}{\mathrm{Re}\,\mathrm{Pr}}\left(\frac{1}{R}\frac{\partial}{\partial R}\left(R\frac{\partial T^*}{\partial R}\right) + \frac{1}{R^2}\frac{\partial^2 T^*}{\partial \theta^2} + \frac{\partial^2 T^*}{\partial z^2}\right) \qquad (\mathrm{A.3.1})$$

APPENDIX B:

EFFECT OF RADIAL CLEARANCE ON THE FLOW BETWEEN COROTATING DISKS IN FIXED CYLINDRICAL ENCLOSURES

by

Mohammad Al-Shannag[1], Joan Herrero[1], Joseph A. C. Humphrey[2], and Francesc Giralt[1]

(Accepted in Journal of Fluid Engineering)

---

[1] Universitat Rovira i Virgili, Department of Chemical Engineering, 43006 Tarragona, Catalonia, Spain

[2] Department of Mechanical and Aerospace Engineering, University of Virginia, Charlottesville, Virginia 22904-4746 (author to whom correspondence should be addressed)

ABSTRACT

Numerical results are obtained for the isothermal laminar flow of air between a pair of disks attached to and rotating with a hub in a fixed cylindrical enclosure. The presence of radial clearances or “gaps” between the rims of the disks and the curved enclosure wall, and the finite thickness of the disks, are considered in the calculations. The gaps allow time- and circumferentially-dependent axially-directed air flow exchanges between the contiguous inter-disk spaces. As a consequence, axisymmetric calculations of the flow, whether using boundary conditions in the gaps or extended to include the entire flow domain, fail to faithfully reproduce the experimentally measured radial variations of the mean and rms circumferential velocity components in the inter-disk space. Likewise, three-dimensional calculations using the symmetry-plane boundary condition in the gaps also fail to reproduce these variations. In contrast, computationally intensive three-dimensional calculations of the entire flow domain, including the gaps, yield results in very good agreement with the measured mean and rms velocities. These three-dimensional calculations reveal large velocity fluctuations in the gap regions accompanied by corresponding large fluctuations of the inter-disk flow, reflecting a destabilization of the structure and dynamics of the latter by the former. The axisymmetric calculations as well as those using the symmetry-plane condition in the gap are included in this study principally to elucidate their shortcomings in simulating the three-dimensional flows considered; they are not the main goal of the study. Notwithstanding, the physically approximate, full domain axisymmetric calculations yield useful qualitative results. They show that increasing gap size decreases disk surface shear and the associated disk torque coefficient, but at the cost of destabilizing the inter-disk flow. This observation is in agreement with earlier findings and is better understood as the result of the present study.

INTRODUCTION

Problem Statement

The unobstructed motion of a fluid driven by a pair of coaxial disks corotating in a fixed cylindrical enclosure is of fundamental interest and has interesting mixing applications. This configuration has also been proposed as a first approximation for modeling the bulk flow of air in disk drives; see Schuler et al. [1], Abrahamson et al. [2], and Humphrey et al. [3] for early reviews and Herrero et al. [4.5] for more recent references. Of interest here is the case shown in Fig.1 which includes the two end spaces defined by the outer surface of each disk and the flat (top or bottom) fixed enclosure wall facing it. The disks are attached to a hub and rotate at constant angular velocity, W, such that the Reynolds number is $Re = W R_2^2/n$, where R_2 is the radius of the disks and ν is the kinematic viscosity of the fluid. The presence of a small gap of width A between the rim of each disk and the curved enclosure wall allows axial flow exchanges between the contiguous inter-disk and disk/end-wall spaces. Notwithstanding, earlier work relating to disk drives has mostly ignored, assumed negligible, or oversimplified the effect of the gaps on the inter-disk and disk/end-wall flows. This investigation is concerned with quantifying the effect of the gaps on the structure and dynamics of the flows in these regions as well as on the torque required to rotate the disks.

Background

Many recent experimental fluid mechanics studies of coaxial disks corotating in cylindrical enclosures have typically involved several disks in a stack and have focused on visualizing and measuring the velocity field. Although necessary to allow disk rotation, in these studies the effects of the gaps on the flow have not been systematically investigated. An exception is the work by Hudson and Eibeck [6] who measured the total torque required to corotate a stack of N disks (N =1, 3 and 5) as a function of the Reynolds number, Re, the dimensionless inter-disk spacing, H/R_2, and the dimensionless gap width, A/R_2. (Abrahamson et al. [2], Hudson and Eibeck [6], Humphrey et al. [7] and others have also investigated the influence of an obstruction on the inter-disk flow but that effect is not considered here.) Hudson and Eibeck [6] found a weak dependence of the torque on the gap width for values $A/R_2 < 0.08$ and $H/R_2 < 0.2$ when $8 \times 10^4 < Re < 2.8 \times 10^5$. Analytical investigations by Schuler et al. [1] and Humphrey et al. [7], and numerical studies by Humphrey et al. [8], Iglesias and Humphrey [9] and Herrero et al. [4,5] have assumed $A = 0$, or have imposed a symmetry-plane or a periodic-plane boundary condition in the gap regions. In spite of these simplifications, these studies have quantified the nature and characteristics of the unsteady, 3D, vortical flow between a pair of corotating disks as a function of H/R_2 and Re. In particular, Iglesias and Humphrey [9] show that the presence of gaps lowers the threshold value of Re required for transition from a steady axisymmetric flow to the corresponding unsteady axisymmetric flow. Similarly, Herrero et al. [4] show that, for fixed H/R_2, the flow between a pair of corotating disks evolves from a steady axisymmetric state to an unsteady 3D state with increasing Re. (Henceforth, in this communication all references to “axisymmetric” flow imply a 2D flow that is circumferentially symmetric.)

The assumption of a symmetry-plane boundary condition in the gaps precludes axial flow through them. This limitation is somewhat relieved by resorting to a periodic-plane boundary condition but, to be applied in a logically consistent manner, such a condition requires the assumption of axisymmetric flow. The result is a flow across the gaps that may change its axial sense of motion with time but which, instantaneously, is everywhere (circumferentially) directed in the same (axial) direction. It is clear that the imposition of a symmetry-plane or periodic-plane boundary condition in the gaps leads to unrealistic constraints on fluid motion and, in particular, that such conditions do not apply to the gaps associated with the two end disks in an enclosure.

The calculations performed by Tzeng and Fromm [10] and by Humphrey et al. [7] apply to a stack of disks where the gap regions are part of the calculation domain. While limited to axisymmetric flows, the results point to the importance of avoiding artificial gap boundary conditions by including the gap regions in the calculation domain. The problem then becomes one of ensuring sufficient grid refinement to obtain accurate results throughout the entire flow field, but especially in the gap regions which affect the accuracy of the calculations elsewhere in the domain.

Purpose of this Study

As will be shown, the presence of gaps between the rims of the corotating disks and the fixed curved enclosure wall in the geometry of Fig. 1 significantly affects the structure and dynamics of the flow in the inter-disk space. Earlier attempts to match measurements and calculations of the mean and rms circumferential velocity components in the inter-disk space have met with mixed success. For example, Fig. 4 (discussed below) provides a comparison between measurements and calculations of these two quantities along the mid-plane, $Z = 0$, of the center pair of disks in a stack of N disks. The measurements are obtained in a stack with $N = 4$ disks while all the calculations have been made in a stack with $N = 2$ disks; otherwise, the measured and calculated flow conditions correspond exactly. The measurements are from Schuler et al. [1] for a geometry with the dimensions given in Fig. 1 and a disk speed of rotation of 300 rpm corresponding to $Re = 2.1 \times 10^4$. Of immediate interest here is the comparison between these measurements and the 3D calculations of Humphrey et al. [8], performed for a pair of disks of zero thickness using a symmetry-plane boundary condition in the gaps. (In this and the following figures, $R = r/R_2$, $Z = z/H$, $U = \langle u\rangle/\Omega R_2$, $U_{rms} = u_{rms}/\Omega R_2$, $V = \langle v\rangle/\Omega R_2$, $V_{rms} = v_{rms}/\Omega R_2$, $W = \langle w\rangle/\Omega R_2$, and $W_{rms} = w_{rms}/\Omega R_2$, where "< >" and the subscript "*rms*" denote the mean and rms values of the velocity components.) Both the calculated mean and rms circumferential velocities show qualitative agreement with the experimental data but significant discrepancies arise, particularly for the rms velocity. The rms measurements (and calculations) peak markedly at three distinct radial locations where flow unsteadiness contributes to the velocity fluctuations. The large experimental values of the rms at $R \leq 0.75$ contrast with the results obtained from both theoretical and numerical analyses performed to date which predict solid body rotation conditions for the flow in this region.

The purpose of this study is to accurately assess the effects of the gaps on the flow in a fixed cylindrical enclosure containing a pair of corotating disks. The geometry of interest is that of Fig.1, where the linear dimensions correspond to the experiment of Schuler et al. [1] assuming two disks, as opposed to four, in the enclosure. The structure and dynamics of the flow, as well as the variation of the disk torque coefficient, C_M, are analyzed numerically as a function of A/R_2 for a fixed value of $Re = 2.1 \times 10^4$. Both axisymmetric and 3D calculations are performed and the effects on the flow of imposing symmetry-plane or periodic-plane boundary conditions in the gaps are examined. The axisymmetric calculations as well as those using the symmetry-plane condition in the gap are included in this study for completeness. They elucidate the shortcomings in simulating the three-dimensional flows considered; they are not the main goal of the study. Notwithstanding, as will be shown, the physically approximate, full domain axisymmetric calculations yield useful qualitative results.

CONSERVATION EQUATIONS

The constant property, unsteady, axisymmetric or 3D, laminar flow of air is assumed. The corresponding mass and momentum conservation equations expressed relative to a fixed cylindrical coordinate system (see Fig. 1) are:

mass:

$$\frac{\partial w}{\partial z} + \frac{\partial u}{\partial r} + \frac{u}{r} + \frac{1}{r}\frac{\partial v}{\partial \theta} = 0 \tag{1}$$

r-momentum:

$$\frac{Du}{Dt} = -\frac{1}{\rho}\frac{\partial p}{\partial r} + \nu\left\{\frac{\partial}{\partial r}\left(\frac{1}{r}\frac{\partial}{\partial r}[ru]\right) + \frac{1}{r^2}\frac{\partial^2 u}{\partial \theta^2} - \frac{2}{r^2}\frac{\partial v}{\partial \theta} + \frac{\partial^2 u}{\partial z^2}\right\} + v^2/r \tag{2}$$

θ-momentum:

$$\frac{Dv}{Dt} = -\frac{1}{\rho r}\frac{\partial p}{\partial \theta} + \nu\left\{\frac{\partial}{\partial r}\left(\frac{1}{r}\frac{\partial}{\partial r}[rv]\right) + \frac{1}{r^2}\frac{\partial^2 v}{\partial \theta^2} + \frac{2}{r^2}\frac{\partial u}{\partial \theta} + \frac{\partial^2 v}{\partial z^2}\right\} - uv/r \tag{3}$$

z-momentum:

$$\frac{Dw}{Dt} = -\frac{1}{\rho}\frac{\partial p}{\partial z} + \nu\left\{\frac{1}{r}\frac{\partial}{\partial r}\left(r\frac{\partial w}{\partial r}\right) + \frac{1}{r^2}\frac{\partial^2 w}{\partial \theta^2} + \frac{\partial^2 w}{\partial z^2}\right\} \tag{4}$$

In Eqns. (2-4), u, v, w are the velocity components in the r, θ and z coordinate directions, p is pressure, and t is time. D/Dt denotes the operator $[\partial/\partial t + w(\partial/\partial z) + u(\partial/\partial r) + v/r(\partial/\partial\theta)]$, not to be confused with the substantial derivative since the base vector variation terms have been placed on the right-hand side of these equations.

For both axisymmetric and 3D flows, Eqns. (1-4) are solved subject to the following boundary conditions,

$u = w = 0;\ v = \Omega\, r$ on all rotating surfaces (hub and disks) (5a)

$u = v = w = 0$ on all fixed surfaces (curved, top and bottom walls of the enclosure) (5b)

The conditions for the 3D flows investigated in this work lead to aperiodic, modulated motions corresponding to “Region II” type flows in the study by Herrero et al. [4]. Therefore, it is necessary to resolve the entire flow field in the circumferential coordinate direction; that is, over a 360 degree θ domain. For this, circumferentially-periodic boundary conditions are imposed for the three velocity components in the θ-coordinate direction.

For those flow calculations restricted to the inter-disk space, one of the following two boundary conditions is implemented in the gap, $R_2 < r < R_2+A$:

a) Symmetry-plane:

$$\frac{\partial u}{\partial z} = \frac{\partial v}{\partial z} = w = 0 \ \text{ at } z = \pm (H+h)/2 \tag{6}$$

b) Periodic-plane:

$$(u,v,w,p)_{z=-(H+h)/2} = (u,v,w,p)_{z=(H+h)/2} \tag{7}$$

NUMERICAL ALGORITHM

The calculations have been performed using an upgraded version of the CUTEFLOWS numerical algorithm developed for unsteady, constant property, 2D and 3D flows. CUTEFLOWS (Computing Unsteady Three-dimensional Elliptic Flows) is second-order accurate in both space and time and has been extensively tested and used for a wide variety of problems; see Humphrey et al. [8], Iglesias and Humphrey [9], Herrero et al. [4,5] and the references therein. The upgraded algorithm is fourth-order accurate in both space and time. Both algorithms are based on a staggered-grid, control-volume discretization approach for deriving finite difference forms of the conservation equations in terms of their primitive variables. Mass conservation yields a discrete Poisson equation that is solved for pressure using the conjugate gradient method. The upgraded algorithm uses an upstream-biased differencing scheme (Rai and Moin [11]) for the convection terms. The spatially discretized momentum conservation equations are explicitly integrated in time by means of a fourth-order Runge-Kutta scheme. Like the original CUTEFLOWS code, the upgraded algorithm is capable of reproducing all known features of the unsteady, 3D, vortical flow between a pair of corotating disks. For further details see the references cited above.

Effect of grid refinement

The grid independence of the calculated results is established first for the case of axisymmetric flow. For this, the case with a gap ratio A/R_2 = 0.026 is investigated for the conditions shown in Fig. 1, corresponding to the experiment of Schuler et al. [1]. This case is solved using increasingly refined (*R*-*Z*) grids until the numerical results for the two finest grids essentially coincide. (Meaning that maximum discrepancies between calculated velocity components on the finest two grids are less than 5%, the average being 2%.) These are full domain calculations with no boundary conditions imposed in the gaps. We comment below on the results obtained for this case on three grids referred to as "coarse," "medium" and "fine."

In all cases the grids are non-uniform in the R and Z directions. They are constructed as in Herrero et al. [4] who calculated the flow between a pair of disks with the dimensions of Fig. 1 but with $A = 0$. As in that work, current near-wall node densities allow for the presence of at least five nodes in the disk Ekman layers and the curved wall boundary layer. In the inter-disk space and in each of the disk/end-wall spaces, the spacing between nodes increases linearly from each wall by a grid expansion factor not larger than 1.2. In addition, the grid spacing is not allowed to exceed 5% of the total distance covered by the grid in the radial and axial directions. Table 1 summarizes the minimum and maximum spacings and expansion factors used in the tests conducted for $A/R_2 = 0.026$. In the gap regions the grid is distributed uniformly in the radial and axial directions, with a spacing equal to the minimum spacing listed in Table 1. All calculations are performed using a dimensionless integration time step, $Dt = W\ Dt$, set to $Dt \leq 0.003$. This time step corresponds to a physical displacement equal to or less than 5.4 degrees for a disk rotating at 300 rpm ($W = 10\pi$ rad/s) and guarantees stable and accurate convergence.

Figures 2(a)-(c) and 3(a)-(c) show the axisymmetric flow results obtained for the case with $A/R_2 = 0.026$ on the three grids. Profiles of the mean and rms velocity components are compared in Figs. 2(a)-(c). It is clear from these two figures, particularly in the gap regions shown in Fig. 2(c), that the results of the coarse grid (90 x 132) and the medium grid (118 x 164) do not agree. However, the results of the medium grid essentially coincide with those obtained with the fine grid (182 x 240). Time records of the dimensionless axial velocity component corresponding to two mid-plane locations with $R = 0.9$ and $R = 1.0$ are shown in Figs. 3(a)-(c). While the coarse grid does not accurately resolve the velocity oscillations and amplitudes, the records obtained on the medium and fine grids are in very good agreement. From these tests we conclude that a non-uniform grid consisting of 118 x 164 (R-Z) nodes is sufficiently accurate for axisymmetric calculations of the flow with $A/R_2 = 0.026$. Table 2 shows the values of the (R-Z) grids used for each of the axisymmetric cases investigated.

For the 3D calculations, tests are performed for the case with $A/R_2 = 0.026$ using the above 118 x 164 (R-Z) grid in combination with 64 or 128 equally spaced grid nodes in the q direction. The differences between the results obtained with these two grids are sufficiently small (on average, less than 2% for the mean and less than 4% for the rms) to allow calculations of the cases with $A/R_2 = 0.026$ and $A/R_2 = 0.013$ using 64 nodes in the q direction. (Note that setting 64 nodes in the q direction yields a circumferential grid refinement that is more than twice that employed by Humphrey et al. [8].) The adequacy of the final 3D grids used is further confirmed by the goodness of the mean and rms velocity results obtained for the case with $A/R_2 = 0.026$ (Fig. 7, discussed below) relative to the experimental measurements.

RESULTS

The dimensions of the geometry shown in Fig. 1 match those of the experiment performed by Schuler et al. [1] for which $A/R_2 = 0.026$. In addition to this case, detailed calculations are performed for the case with $A/R_2 = 0.013$ to further elucidate the effects of the gap on the flow. Cases with other values of A/R_2 (0.0064, 0.013, 0.026, 0.052 and 0.077) are also examined for their effects on the disk torque coefficient. In order to vary A/R_2 for these cases, the quantity A is changed by varying the inside radius of the cylindrical enclosure. Each calculation case, corresponding to a particular value of A/R_2, is started from a fluid at rest and extended over a time period long enough to ensure a statistically stationary flow. A single disk angular velocity is considered corresponding to the experimental value of 300 rpm ($Re = 2.1 \times 10^4$).

Effect of the Gaps on the Flow Structure and Dynamics

The structure and dynamics of the flow are investigated in detail for two gap ratios ($A/R_2 = 0.026$ and 0.013). The geometry with $A/R_2 = 0.026$ is solved first, by restricting attention to the inter-disk space and imposing symmetry-plane or periodic-plane boundary conditions in the gaps. For this: i) axisymmetric and 3D calculations are performed with the symmetry-plane condition (Eq. 6); and, ii) axisymmetric calculations are performed with the periodic-plane condition (Eq. 7). Radial profiles of the mean and rms circumferential velocity components calculated along the mid-plane ($Z = 0$) are plotted in Figs. 4(a) and (b). The best overall calculation of the mean is obtained assuming axisymmetric flow and using the periodic-plane boundary condition. Both the axisymmetric and 3D results using the symmetry-plane boundary condition significantly overpredict the mean. The best near-wall calculations of the rms are obtained with the symmetry-plane condition, but neither set of boundary conditions yields accurate predictions of the rms for $R < 0.98$. Notwithstanding, it is clear that by allowing axisymmetric flow reversals in the gaps the periodic-plane boundary condition better reproduces the trend for the large rms values arising at $R < 0.94$. In contrast, with the symmetry-plane condition imposed it makes little difference to the calculation of the mean velocity whether the inter-disk flow is treated as axisymmetric or 3D, the differences between these two sets of results being almost indistinguishable.

In spite of the somewhat better results obtained for the flow in the inter-disk space, especially the mean velocity, when computed with a periodic-plane boundary condition applied in the gaps, the axisymmetric flow assumption is highly constraining. Similarly, irrespective of whether the inter-disk flow is calculated as axisymmetric or 3D, the imposition of a symmetry-plane boundary condition in the gaps is also very limiting. As shown below, these shortcomings are removed in two steps, first by extending the axisymmetric calculation to encompass the entire flow domain, thus removing the need to specify a gap boundary condition, and then by removing the axisymmetric constraint and performing a 3D calculation.

Figures 5(a)-(c) present time-averages of the cross-stream flow streamlines and of the mean and rms circumferential velocity components for an axisymmetric calculation of the entire flow domain. Figures 6(a)-(c) show the same quantities for the corresponding 3D calculation, where the quantities plotted have been averaged both with respect to time and along the circumferential coordinate direction. Although these axisymmetric and 3D calculations yield unsteady flows (with the 3D results showing relatively strong departures from time-periodicity), the mean velocity plots are fairly similar with the main cross-stream flows in the inter-disk and disk-end wall spaces being determined by the strong radial outflows along the disk Ekman layers. These radial outflows are also responsible for the additional pair of much smaller cross-stream flows arising in the gap regions. In contrast, distributions of the rms, shown in Figs. 5(c) and 6(c), reveal larger levels of this quantity in the inter-disk space for the 3D calculation case compared to the axisymmetric. In particular, the 3D results show stronger radial and axial penetrations, driven by the cross-stream flows between the disks and in the gaps, of fluid with low circumferential velocity and high rms. Such penetrations induce a small departure of the mean flow from the condition of solid body rotation for $R < 0.8$. Both the axisymmetric and 3D calculations yield rms levels larger than 10% near the curved enclosure wall and as high as 20% in the gaps. Although not shown here, the intensity of the strongly sheared flow in and around the gaps varies significantly with time.

Radial profiles of full domain mean and rms circumferential velocities obtained along the inter-disk mid-plane are compared in Fig. 7(a) and (b) with corresponding experimental results. (Also shown are the results obtained in a 3D calculation with $A/R_2 = 0.013$, discussed below.) It is clear that removing the specification of a gap boundary condition *and* extending the calculation dimensionality to predict a fully unconstrained 3D flow leads to significantly improved results for *both* the mean and rms velocities for *all* values of R. The circumferential dependence of the full domain 3D flow is illustrated in Figs. 8(a)-(d). These plots show cross-stream flow streamlines (derived from the cross-stream velocity components) for the same instant in time at four q–planes. The plots reveal a main cross-stream flow that oscillates strongly about the inter-disk mid-plane and which is accompanied by significant axial displacements of fluid in the gaps. The circumferentially-dependent axial flows in the gaps induce large non-axisymmetric variations in the cellular structures of the cross-stream flow in the inter-disk space and, to a smaller extent, in the end-wall spaces. The depth of penetration towards the hub of the oscillatory mid-plane flow varies with time and from plane to plane, leading to the large values of the rms observed in the inter-disk space. Such variations in the inter-disk space are not predicted assuming axisymmetric flow (regardless of whether gap boundary conditions are imposed or not), nor are they predicted by a 3D flow calculation using the symmetry-plane boundary condition.

Axisymmetric and 3D full domain calculations of the case with $A/R_2 = 0.013$ both yield time varying flows but their respectively averaged velocity fields are practically indistinguishable. Time- and q-averaged values of cross-stream flow streamlines, and of the mean and rms circumferential velocities, are plotted in Fig. 9. A comparison between these results and those obtained for $A/R_2 = 0.026$, in Fig. 6(a)-(c), shows similar spatial distributions for the mean velocity but somewhat different ones for the rms. In particular, while both cases have equally high values of the rms in the gaps, the case with $A/R_2 = 0.013$ has significantly lower values of the rms in the bulk of the inter-disk space; see Fig. 7(b) also.

Effect of the Gaps on the Disk Torque Coefficient

The disk torque coefficient, C_M, is a dimensionless measure of the total torque required to rotate a disk and includes: a) the torques associated with each of the flat surfaces of a disk; b) the torque associated with the rim surface of a disk; and, c) the torques due to the sections of the hub associated with a disk.

In the present geometry each of the two disks has an "inner" surface (I) that faces the surface of the opposite corotating disk, and an "outer" surface (O) that faces a fixed flat enclosure wall. It makes sense to define the above three contributions to the torque coefficient for *each* of the two surfaces of a disk. Thus, call $C^{I}_{M,disk}$ the mean torque acting on the inner surface of a disk, $C^{I}_{M,rim}$ the mean torque acting on the peripheral half-surface of the rim associated with the inner surface of a disk, and $C^{I}_{M,hub}$ the mean torque acting on the peripheral half-surface of the hub associated with the inner surface of a disk. The corresponding quantities for the outer surface of a disk are $C^{O}_{M,disk}$, $C^{O}_{M,rim}$ and $C^{O}_{M,hub}$. These quantities are calculated from the following expressions:

$$C^{I,O}_{M,disk} = \frac{\int_0^{2p}\int_{R_1}^{R_2} m\left|\frac{\partial v}{\partial z}\right| r^2\,dr\,dq}{1/2\,r\Omega^2 R_2^5} \tag{8-a}$$

$$C^{I,O}_{M,rim} = \frac{\int_0^{2p}\int_{z_1}^{z_2} m\left|\frac{\partial v}{\partial r}\right| R_2^2\,dz\,dq}{1/2\,r\Omega^2 R_2^5} \tag{8-b}$$

$$C^{I,O}_{M,hub} = \frac{\int_0^{2p}\int_{z_1}^{z_2} m\left|\frac{\partial v}{\partial r}\right| R_1^2\,dz\,dq}{1/2\,r\Omega^2 R_2^5} \tag{8-c}$$

where the vertical bars denote time-averaged wall values of the velocity gradients indicated. In these expressions the superscript " *I* " denotes the disk, rim, or hub surfaces associated with the inner surface of a disk and the superscript " *O* " denotes the disk, rim, or hub surfaces associated with the outer surface of a disk. Thus, with reference to Fig.1, $C^{I}_{M,disk}$ is evaluated at $z = \pm H/2$ and $C^{O}_{M,disk}$ at $z = \pm (H/2 + h)$; $C^{I}_{M,rim}$ is evaluated from $z_1 = \pm H/2$ to $z_2 = \pm (H/2 + h/2)$ and $C^{O}_{M,rim}$ from $z_1 = \pm (H/2 + h/2)$ to $z_2 = \pm (H/2 + h)$; $C^{I}_{M,hub}$ is evaluated from $z_1 = 0$ to $z_2 = \pm H/2$ and $C^{O}_{M,hub}$ from $z_1 = \pm (H/2 + h)$ to $z_2 = \pm (3H/2 + h)$.

From the above equations it is possible to obtain the following quantities:
Mean torque coefficient for a disk near the middle of a stack of disks in a cylindrical enclosure

$$C_M^{MD} = 2(C^{I}_{M,disk} + C^{I}_{M,rim} + C^{I}_{M,hub}) \tag{9-a}$$

Mean torque coefficient for a single disk in a cylindrical enclosure

$$C_M^{SD} = 2(C^{O}_{M,disk} + C^{O}_{M,rim} + C^{O}_{M,hub}) \tag{9-b}$$

Mean torque coefficient for a disk at the end of a stack of disks in a cylindrical enclosure

$$C_M^{ED} = (C^{I}_{M,disk} + C^{O}_{M,disk} + C^{I}_{M,rim} + C^{O}_{M,rim} + C^{I}_{M,hub} + C^{O}_{M,hub}) = 1/2(C_M^{MD} + C_M^{SD}) \tag{9-c}$$

Mean torque coefficient for a stack of *N* disks in a cylindrical enclosure

$$C_M^{Stack} = (N-2)C_M^{MD} + 2C_M^{ED} = (N-1)C_M^{MD} + C_M^{SD} \tag{9-d}$$

Note that in the above four equations it is implied that the various contributions to the torque coefficient are additive and the results discussed below support this assumption.

Calculated values of C_M^{MD} and C_M^{SD} are given in Fig. 10 where they are plotted as a function of the gap ratio A/R_2. In all cases $Re = 2.1 \times 10^4$ and both full domain axisymmetric and 3D values are presented, the latter being limited to two gap sizes because of the long calculation times involved. As expected, the calculations show that $C_M^{SD} > C_M^{MD}$, by a factor as large as four at intermediate values of A/R_2. They also reveal an insensitivity of C_M^{SD} with respect to the gap size. In the A/R_2 range investigated we find $C_M^{SD} \approx 0.024$, in close agreement with the results obtained using the single disk correlations of Daily and Nece [12] ($C_M^{SD} = 0.020$), Hudson and Eibeck [6] ($C_M^{SD} = 0.021$), and Humphrey et al. [7] ($C_M^{SD} = 0.020$) by setting $Re = 2.1 \times 10^4$.

The figure also compares present calculations of C_M^{MD} with the correlation proposed by Hudson and Eibeck [6] for $Re > 8 \times 10^4$. The correlation is given by $C_M^{MD} = 0.46 Re^{-0.35} (H/R_2)^{0.5} (A/R_2)^{-0.07}$ and, as observed for C_M^{SD}, shows a very weak dependence on A/R_2. Agreement between the calculations and the experimental fit varies between 1% and 15% in the range $0.010 < A/R_2 < 0.060$. In contrast, the calculated value of C_M^{MD} for the largest gap explored, $A/R_2 = 0.077$, is significantly smaller than the value given by the fit. The discrepancy is partly due to the lower Re of the current study (large gaps in disk flows at high Re are expected to facilitate turbulent exchanges of momentum that can significantly increase the disk torque coefficient), but may also be attributed to the over-constraining assumption of axisymmetric flow. In this respect, while there is good agreement between the axisymmetric and 3D calculations of C_M^{MD} and C_M^{SD} for the case with $A/R_2 = 0.013$, a 12% discrepancy arises between the values for C_M^{MD} for the more critical case with $A/R_2 = 0.026$. As discussed further above, such a discrepancy is explained by the inability of the axisymmetric calculations to fully capture the physics of the inter-disk flow for $A/R_2 = 0.026$. Thus, while the axisymmetric calculations follow the empirical trend and predict decreasing C_M^{MD} with increasing A/R_2, they should only be used for qualitative guidance, especially for large values of A/R_2.

Increasing A/R_2 might be viewed as a convenient way to reduce the torque, and hence the power requirement of a stack of disks. However, the rms values in Fig. 7(b) show that such a reduction will come at the expense of a more unstable inter-disk flow. A related observation has been made by Humphrey et al. [7] who show that the inwards radial displacement of fluid with high circumferential momentum works to reduce total disk torque at the cost of destabilizing fluid motion in the inter-disk space. That study also supports the observation made here, that axial transport of circumferential momentum across the gaps can significantly alter the structure and dynamics of the inter-disk flow while not significantly affecting the flows in the disk-end wall spaces.

CONCLUDING REMARKS

Present numerical calculations show that the structure and dynamics of the flow in the space between a pair of disks corotating in a fixed cylindrical enclosure at $Re = 2.1 \times 10^4$ are sensitive to the size of the gaps between the rims of the disks and the curved enclosure wall. This is due to axial transport of circumferential momentum between the inter-disk spaces connected by the gaps. In this regard, regardless of the imposition or not of symmetry-plane or periodic-plane boundary conditions in the gaps, the assumption of axisymmetric flow yields results that, while numerically accurate, fail to faithfully reproduce measured variations of the mean and rms circumferential velocities. Likewise, a 3D calculation using the symmetry-plane boundary condition in the gaps also fails to reproduce the variations observed in the measurements. In contrast, a 3D calculation of the flow including the gaps and the inter-disk spaces as parts of an interconnected flow domain yields mean and rms velocities in very good agreement with the corresponding measurements.

At a qualitative level, present full domain axisymmetric calculations suggest that increasing A/R_2 works to significantly reduce the disk torque coefficient, but at the expense of increasing flow unsteadiness as revealed by the calculations of the rms circumferential velocity. This observation agrees with previous related findings and suggests that while disk torque may be significantly reduced by increasing gap size, the reduction may come at the expense of a significantly destabilized flow due to the enhanced axial exchanges of momentum through the gaps. However, it is important to keep in mind that, because of the differences in flow structure and dynamics predicted by axisymmetric and 3D calculations, respectively, axisymmetric values of the disk momentum coefficient are not reliable at a quantitative level, especially for large values of A/R_2. For accurate predictions of all flow behavior, computationally intensive full domain 3D calculations are required, even for integral quantities such as the disk momentum coefficient.

From a practical standpoint, present calculations suggest that equations 9(a)–(d) can be used together with previously reported empirical correlations, analytical equations or full domain 3D numerical results to predict the torque coefficients associated with one or more disks corotating in a cylindrical enclosure. However, because most previous results have been obtained for conditions corresponding to moderate and high values of the Reynolds numbers, as illustrated here, their use to predict torque at lower values of Reynolds than for which they were derived must be viewed with caution.

ACKNOWLEDGEMENTS

Financial support for this investigation was provided by the Spanish government to MS, JH and FG through projects DGES-PB96-1011 and DGESYC-PPQ2000-1339, and through a grant received by JACH from the National Storage Industry Consortium. MS gratefully acknowledges a research travel grant to conduct research at UVA provided by the Catalan government.

REFERENCES

[1] Schuler, C. A., Usry, W., Weber, B., Humphrey, J. A. C., and Greif, R., 1990, “On the flow in the unobstructed space between shrouded corotating disks,” *Phys. Fluids* A, **2**, pp. 1760-1770.

[2] Abrahamson, S.D., Chiang, C. and Eaton, J.K., 1991, “Flow Structure in Head Disk Assemblies and Implications for Design,” *Adv. Inf. Storage Syst.*, **1**, pp. 7111-132.

[3] Humphrey, J. A. C., Chang, C.-J., Li, H., and Schuler, C. A., 1991, “Unobstructed and obstructed rotating disk flows: A summary review relevant to information storage systems,” *Adv. Inf. Storage Syst.*, **1**, pp. 79-110.

[4] Herrero, J., Giralt, F., and Humphrey, J. A. C., 1999-a “Influence of the geometry on the structure of the flow between a pair of corotating disks”, *Phys. Fluids*, **110**, pp. 88-96.

[5] Herrero, J., Giralt, F., and Humphrey, J. A. C., 1999-b, “Non-isothermal laminar flow and heat transfer between disks corotating in a fixed enclosure,” *Int. J. Heat Mass Transfer*, **42**, pp. 3291-3306.

[6] Hudson, A. J. and Eibeck, P. A., 1991, “Torque measurements of corotating disks in an axisymmetric enclosure”, ASME J. Fluids Engr., **113**, pp. 648-653.

[7] Humphrey, J. A. C., Schuler, C. A., and Iglesias, I., 1992, “Analysis of viscous dissipation in disk storage systems and similar flow configurations”, *Phys. Fluids* A, **4**, pp. 1415-1427.

[8] Humphrey, J. A. C., Schuler, C. A., and Webster, D. R., 1995, “Unsteady laminar flow between a pair of disks corotating in a fixed cylindrical enclosure,” *Phys. Fluids*, **7**, pp. 1225-1240.
[9] Iglesias, I. and Humphrey, J. A. C., 1998, “Two- and three-dimensional laminar flows between disks co-rotating in a fixed cylindrical enclosure,” *Int. J. Numer. Meth. Fluids*, **26**, 581-603.
[10] Tzeng, H.-M. and Fromm, J. E., 1990, “Airflow study in a cylindrical enclosure containing multiple corotating disks”, IBM *Research Division*, Report RJ 7334 (68815).
[11] Rai, M. M. and Moin, P., 1991, “Direct Simulations of Turbulent Flows Using Finite-Difference Schemes”, *J. Comput. Phys.*, 96, pp. 15-53.
[12] Daily, J.W. and Nece, R.E., 1960, "Chamber dimension effects on induced flow and frictional resistance of enclosed rotating disks," J. Basic Eng., Trans.
ASME, pp. 217-232.

Coordinate	Grid (Nodes)	Minimum Spacing, mm	Maximum Spacing, mm	Expansion factor
R-direction	Coarse (90)	0.15000	0.88955	1.20
	Medium (118)	0.12273	0.68972	1.10
	Fine (182)	0.07500	0.49968	1.05
Z-direction	Coarse (132)	0.14690	0.47530	1.20
	Medium (164)	0.12273	0.25720	1.10
	Fine (240)	0.07346	0.24562	1.05

Table 1. Minimum and maximum spacing and expansion factors used in the axisymmetric flow calculations with A/R_2 = 0.026.

Coordinate	A/R_2				
	0.0064	0.013	0.026	0.052	0.077
R-direction (nodes)	104	108	118	140	162
Z-direction (nodes)	164	164	164	164	164

Table 2. Grid nodes used in the axisymmetric flow calculations of the various A/R_2 cases.

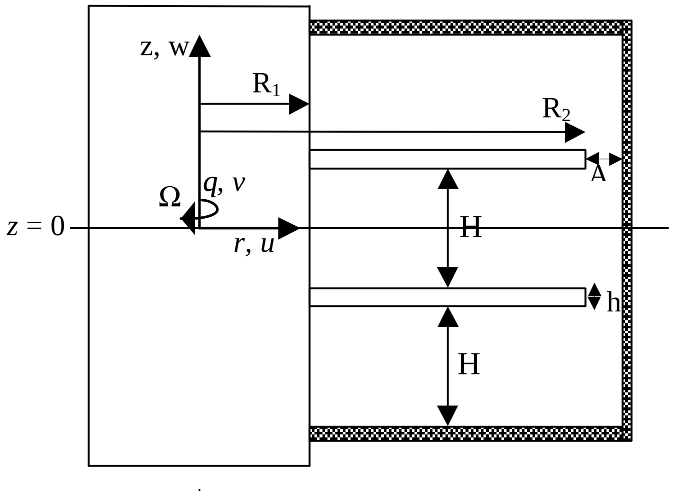

Figure 1. Sketch of the flow configuration investigated numerically. The geometrical parameters shown match those of the test section investigated experimentally by Schuler et al. [1] in which: R_1 = 56.4 mm, R_2 = 105 mm, H = 9.53 mm, h = 1.91 mm and A = 2.7 mm. In this study calculations are performed for five gap sizes (A/R_2 = 0.0064, 0.013, 0.026, 0.052 and 0.077) with Re = 2.1 x 10^4.

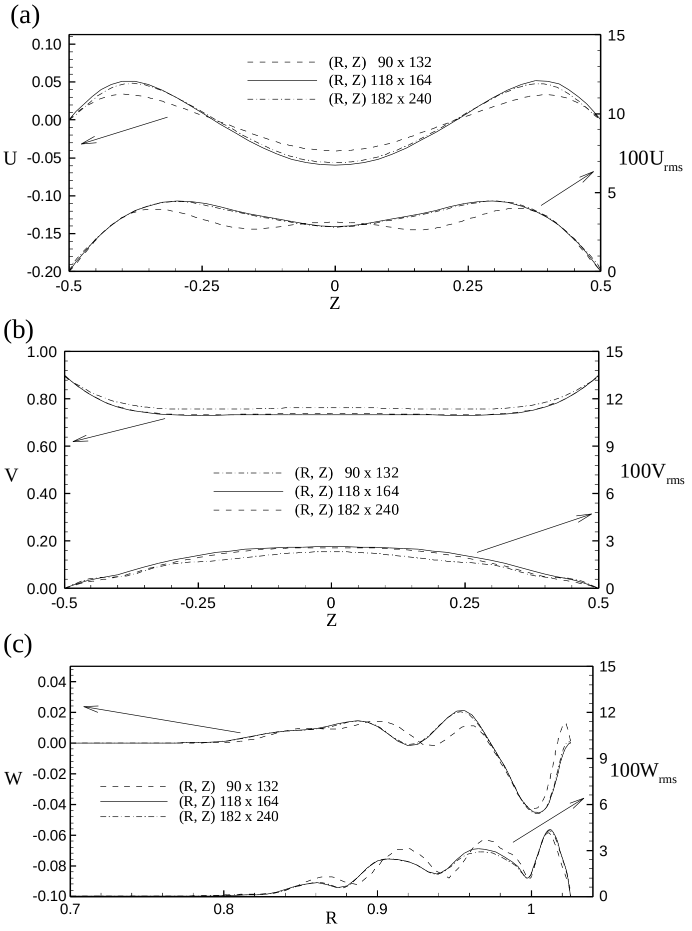

Figure 2. Effect of grid refinement on axisymmetric calculations of the mean and rms velocities for Re = 2.1 x 10^4 with A/R_2 = 0.026. (a) Axial profiles of radial velocity components at R=1.0. (b) Axial profiles of the circumferential velocity components at R=0.9. (c) Radial profiles of the axial velocity components at Z=0.25.

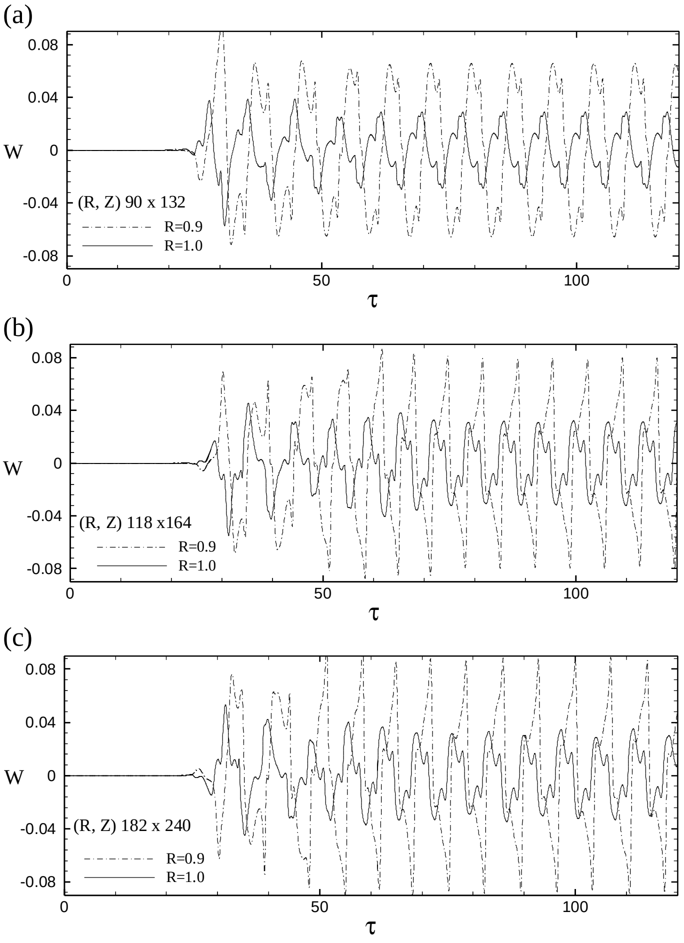

Figure 3. Effect of grid refinement on the time dependence of the axial velocity component at $Z = 0$ for $R = 0.90$ and 1.0. Calculation conditions correspond to Fig. 2.

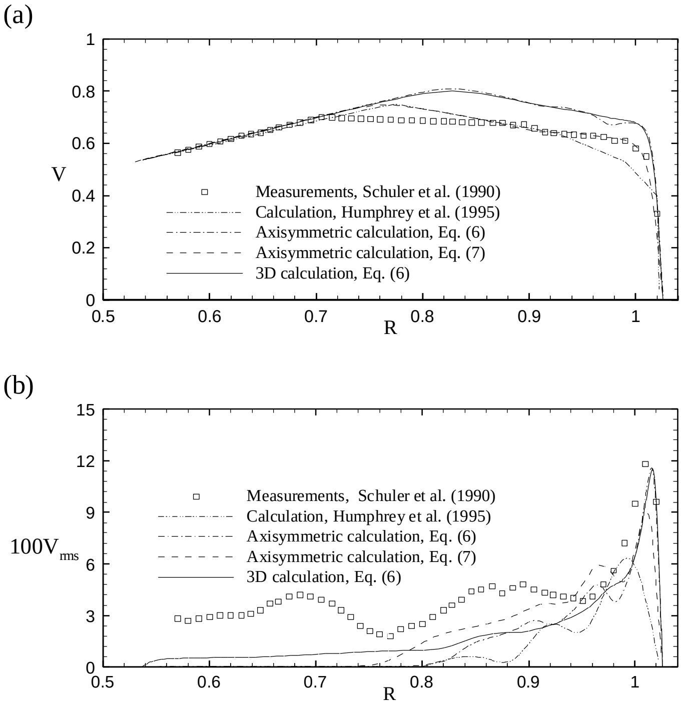

Figure 4. Measured and calculated radial profiles of the mean (a) and rms (b) circumferential velocities along the inter-disk mid-plane, $Z = 0$, for the case with $A/R_2 = 0.026$. Calculations are restricted to the inter-disk space of Fig. 1 using symmetry-plane (Eq. 6) or periodic-plane (Eq. 7) boundary conditions in the gaps. The axisymmetric results are averaged over time and the 3D results (and the measurements) are averaged over time and in the circumferential direction. The 3D calculations by Humphrey et al. [8] are for a pair of disks of zero thickness using symmetry-plane boundary conditions in the gaps.

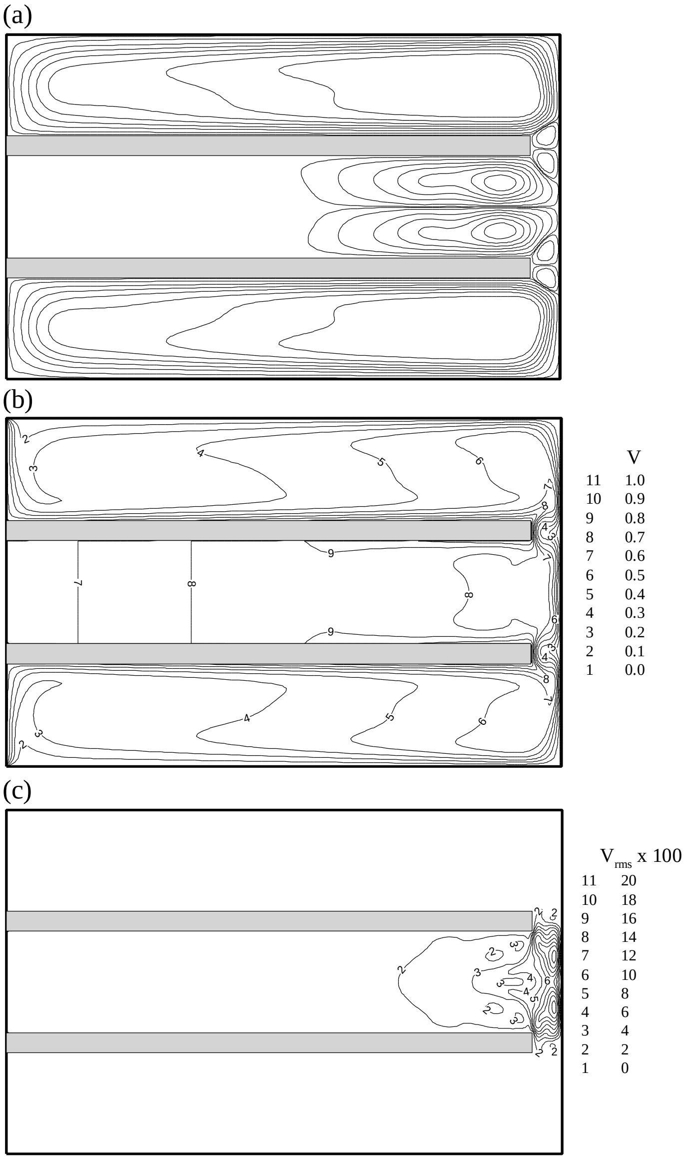

Figure 5. Cross-stream distributions of the time-averaged flow obtained in a full domain axisymmetric calculation for the geometry of Fig. 1 with A/R_2 = 0.026. (a) Cross-stream flow streamlines (unlabelled). (b) Contours of the mean circumferential velocity component. (c) Contours of the rms circumferential velocity component.

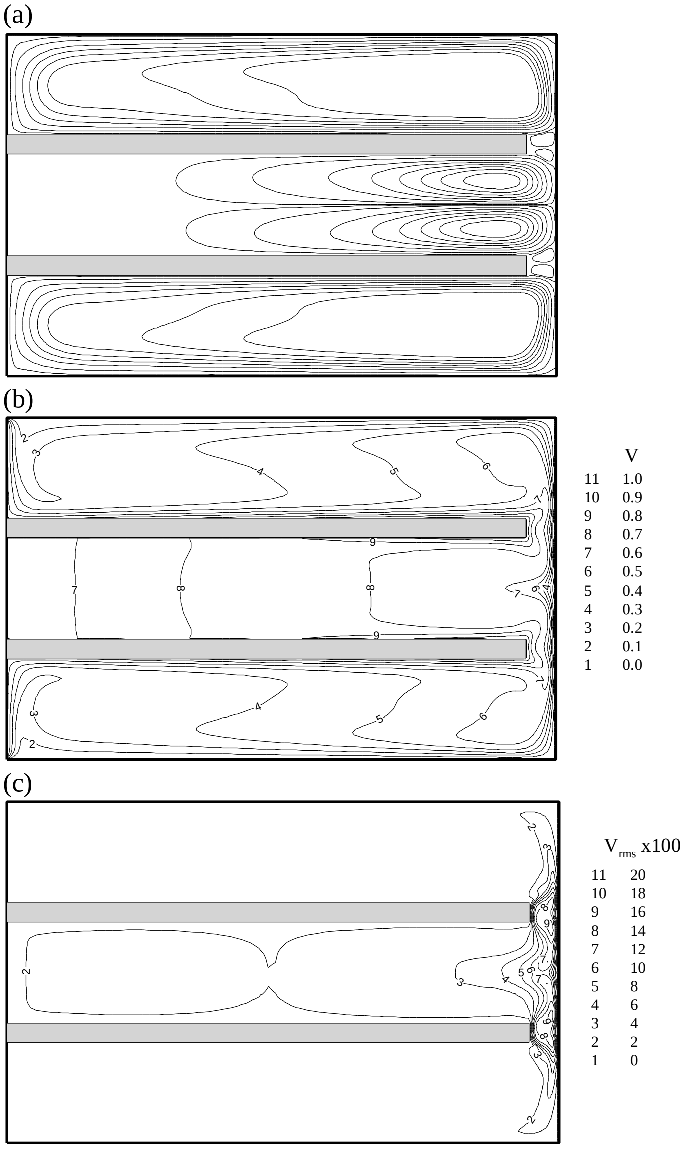

Figure 6. Cross-stream distributions of the time- and circumferentially-averaged flow obtained in a full domain 3D calculation for the geometry of Fig. 1 with A/R_2 = 0.026. (a) Cross-stream flow streamlines based on the axial and radial velocity components (unlabelled). (b) Contours of the mean circumferential velocity component. (c) Contours of the rms circumferential velocity component.

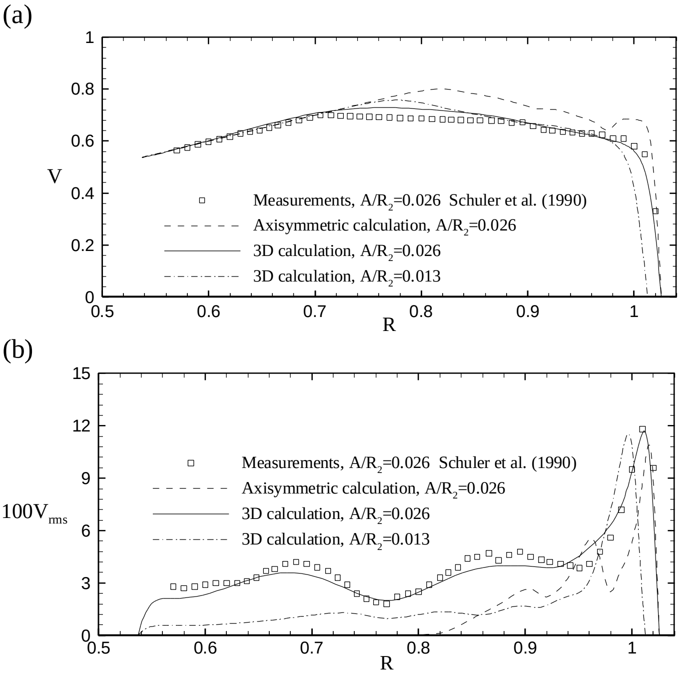

Figure 7. Measured and calculated radial profiles of the mean circumferential velocity (a) and rms (b) along the inter-disk mid-plane, $Z = 0$. These are full domain calculations corresponding to the geometry of Fig. 1 with $A/R_2 = 0.013$ and 0.026. The axisymmetric results are averaged over time and 3D results (and the measurements) are averaged over time and in the circumferential direction.

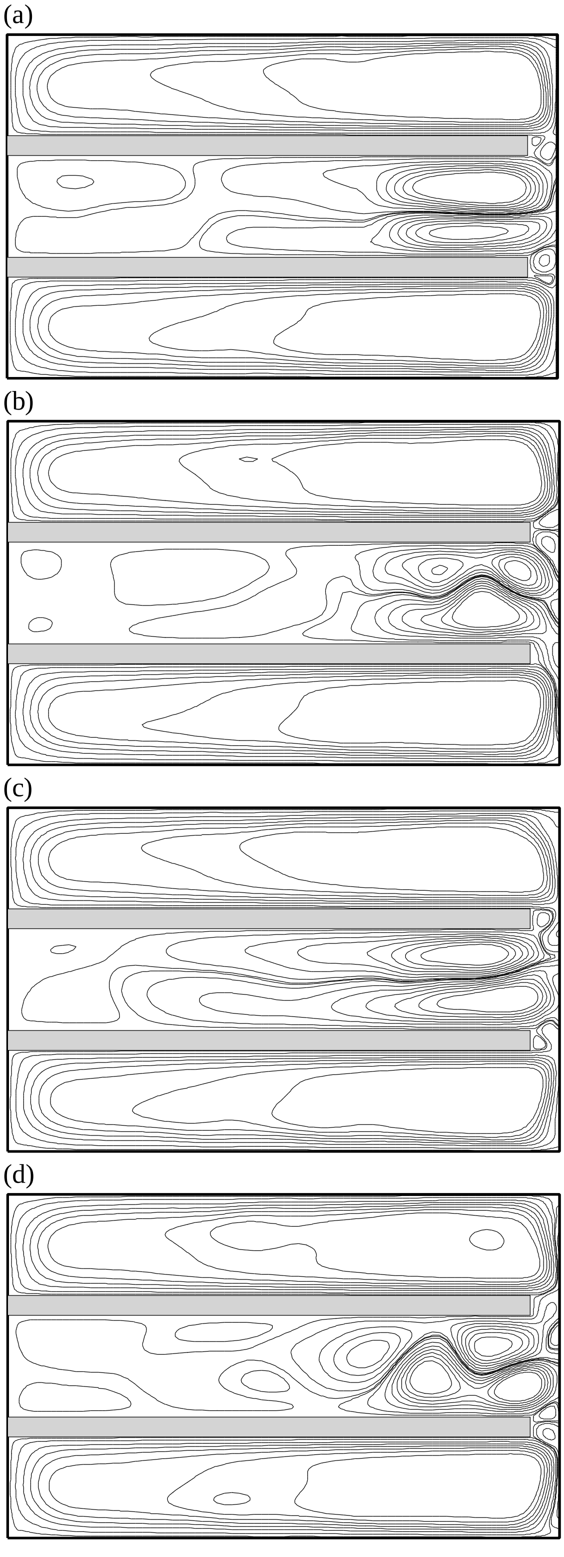

Figure 8. Instantaneous cross-stream flow streamlines (unlabelled) corresponding to the full domain 3D calculation conditions of Fig. 6 ($A/R_2 = 0.026$). Contours are plotted at selected (R-Z) planes corresponding to: (a) q = 0.72π; (b) 0.84π; (c) 1.03π; (d) 1.91π.

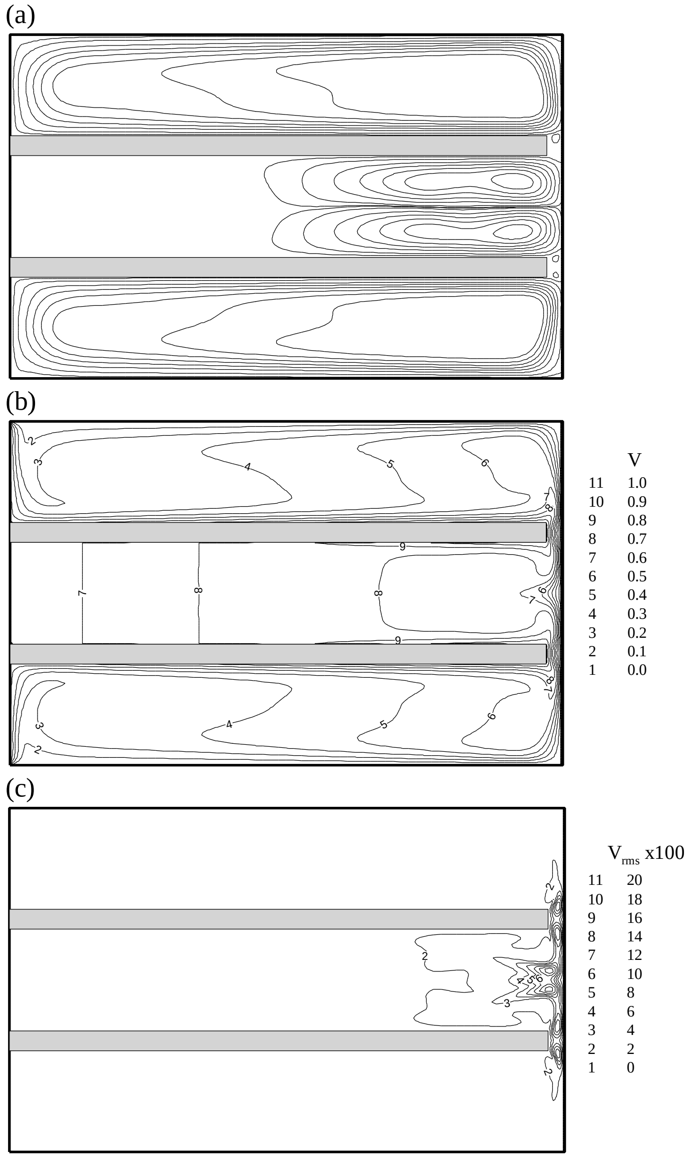

Figure 9. Cross-stream distributions of the time- and circumferentially-averaged flow obtained in a full domain 3D calculation for the geometry of Fig. 1 with A/R_2 = 0.013. (a) Cross-stream flow streamlines based on the axial and radial velocity components (unlabelled). (b) Contours of the mean circumferential velocity component. (c) Contours of the rms circumferential velocity component.

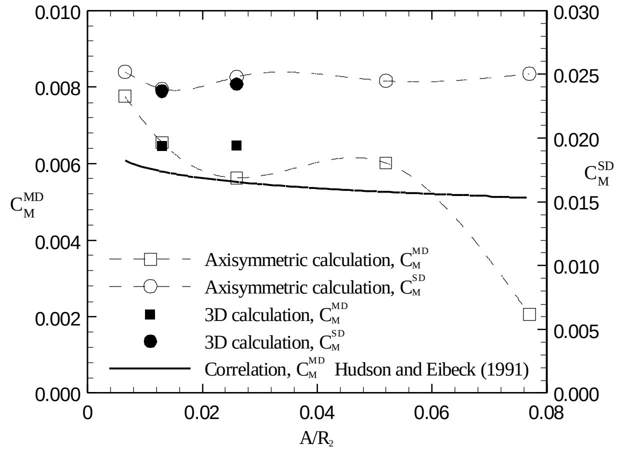

Figure 10. Variations of the disk torque coefficients C_M^{MD} and C_M^{SD} (defined in the text) as a function of A/R_2 for full domain axisymmetric and 3D calculations. Also shown is the experimental fit for C_M^{MD} obtained by Hudson and Eibeck [6]. The axisymmetric calculations are connected by dotted lines to help visualize the qualitative trends in the data but the lines are not to be interpreted as “best fits” to the numerical data.

APPENDIX C:

SHEAR-DRIVEN FLOW IN A TOROID OF SQUARE CROSS-SECTION

by

J. A.C. Humphrey[1], J. Cushner[2], M. Al-Shannag[3],
J. Herrero[3] and F. Giralt[3]

(Accepted in Journal of Fluid Engineering)

---

[1] Department of Mechanical and Aerospace Engineering, University of Virginia, Charlottesville, VA 22904, USA. Author for correspondence.

[2] Shen Milsom & Wilke, Inc., 417 Fifth Avenue, New York, NY10016, USA.

[3] Department of Chemical Engineering, University of Rovira i Virgili, 43006 Tarragona, Catalunya, Spain.

ABSTRACT

The two-dimensional wall-driven flow in a plane rectangular enclosure and the three-dimensional wall-driven flow in a parallelepiped of infinite length are limiting cases of the more general shear-driven flow that can be realized experimentally and modeled numerically in a toroid of rectangular cross-section. Present visualization observations and numerical calculations of the shear-driven flow in a toroid of square cross-section of characteristic side length D and radius of curvature R_c reveal many of the features displayed by sheared fluids in plane enclosures and in parallelepipeds of infinite as well as finite length. These include: the recirculating core flow and its associated counter-rotating corner eddies; above a critical value of the Reynolds (or corresponding Goertler) number, the appearance of Goertler vortices aligned with the recirculating core flow; at higher values of the Reynolds number, flow unsteadiness and vortex meandering as precursors to more disorganized forms of motion and eventual transition to turbulence. Present calculations also show that, for any fixed location in a toroid, the Goertler vortex passing through that location can alternate its sense of rotation periodically as a function of time, and that this alternation in sign of rotation occurs simultaneously for all the vortices in a toroid. This phenomenom has not been previously reported and, apparently, has not been observed for the wall-driven flow in a finite-length parallelepiped where the sense of rotation of the Goertler vortices is determined and stabilized by the end wall vortices. Unlike the wall-driven flow in a finite-length parallelepiped, the shear-driven flow in a toroid is devoid of contaminating end wall effects. For this reason, and because the toroid geometry allows a continuous variation of the curvature parameter, $d = D/R_c$, this flow configuration represents a more general paradigm for fluid mechanics research.

INTRODUCTION

The two-dimensional (2D) wall-driven flow in a plane rectangular enclosure, also referred to as the “lid- or wall-driven cavity flow,” has been a computational fluid dynamics paradigm of long-standing interest. Although such a flow cannot be realized experimentally, approximations have been obtained in enclosures shaped like parallelepipeds of rectangular cross-section and of finite length. In the parallelepiped geometry, fluid motion is induced by the in-plane sliding of one of the four longitudinal walls of the parallelepiped, in a direction normal to the parallelepiped’s longitudinal axis.

In the case of the plane square enclosure (Fig. 1-a), the flow is characterized by the Reynolds number $Re = D\,U/n$, where D is the enclosure cross-section length, U is the sliding wall velocity, and ν is the kinematic viscosity of the fluid. In the case of a parallelepiped of square cross-section (Fig. 1-b), in addition to Re it is necessary to specify the longitudinal to cross-section length ratio, L/D. In contrast to the 2D flow in the idealized plane square enclosure, that in a finite-length parallelepiped is 3D due to pressure gradient effects induced by the viscous action of the end walls. In addition, above a critical value of Re (or an equivalent Goertler number) centrifugal instabilities trigger the appearance of pairs of counter-rotating vortices with axes aligned along the recirculating core flow direction. The wavelength of these vortices scales with D and in a finite-length parallelepiped their sense of rotation is permanently fixed by the end wall vortices.

We propose a new geometrical configuration for the investigation of instabilities of shear-driven flows in enclosures that is realizable experimentally and numerically without incurring the end wall bias present in the finite-length parallelepiped configuration. This consists of the shear-driven flow in a toroid of square cross-section where, in the limit of low Re and large radius of curvature, R_c, fluid motion approaches that in the idealized plane square enclosure. As for the parallelepiped configuration, at a critical value of *Re* in a toroid centrifugal instabilities trigger the appearance of Goertler vortex pairs that, with increasing *Re*, become unsteady and ultimately transition to a turbulent state of motion. In addition to circumventing the end wall bias, the toroid configuration allows the investigation of the effect of the geometrical curvature parameter, $d = D/R_c$, on shear-driven flows. For these reasons, therefore, it represents a more general fundamental paradigm than its parallelepiped predecessors.

EARLIER WORK

Numerical calculations of the 2D wall-driven flow in a plane rectangular enclosure have been performed by, for example, Ghia et al. [1], Iwatsu et al. [2, 3] and Nishida and Satofuka [4]. Corresponding 3D calculations of the parallelepiped geometry have been performed by Koseff et al. [5], Freitas et al. [6], Kim and Moin [7], Freitas and Street [8], and Iwatsu et al. [2, 3]. Experimental investigations of the finite-length parallelepiped geometry include the pioneering studies performed by Koseff and Street [9 – 11], and later by Prasad and Koseff [12] and Aidun et al. [13]. The stability of the 2D base flow to longitudinal disturbances in an infinitely long parallelepiped has been investigated numerically by Ramanan and Homsy [14], Ding and Kawahara [15, 16] and Albensoeder et al. [17]. By means of linear stability analysis and experiments, Albensoeder et al. [17] demonstrate the dependence of the instabilities observed on the enclosure cross-section dimensions. For parallelepipeds of cross-section equal to or close to square, they conclude that the steady 2D flow destabilizes to a steady 3D flow of dimensionless wavenumber $k\,(\equiv 2p/(\,l/D))$ = 15.43 for a critical *Re* = 786.3. They also find from their experiments that end wall effects can suppress instabilities in finite-length parallelepipeds.

With reference to Fig. 1, the investigations performed in infinite- and finite-length parallelepipeds reveal significant (*u*, *w*) cross-stream motions in *x*-*z* planes perpendicular to the wall-driven recirculating core flow. These motions are induced by: a) pressure gradients arising at each of the two end walls in finite-length parallelepipeds; and, b) centrifugal instabilities responsible for the Goertler vortices that arise above a critical value of the Reynolds number (or an equivalent Goertler number) in both infinite- and finite-length parallelepipeds. The vortices appear as counter-rotating pairs periodically distributed in the longitudinal direction (*x*-direction in Fig. 1-b) and their axes are aligned with the recirculating core flow. They have been referred to as Taylor-Goertler-like vortices in the literature but, because of the manner of shearing, appear to have more in common with the centrifugal instability investigated by Goertler [18] in curved boundary layers than the centrifugal instability investigated by Taylor [19] in the space between concentric cylinders in relative rotation. In this regard, see Freitas and Street [8] for an application of the Goertler stability criterion to predict the onset of centrifugal instabilities in the wall-driven flow in a parallelepiped.

The end wall pressure gradients in finite-length parallelepipeds fix the sense of rotation of the first vortex next to each end wall. In turn, the end wall vortex fixes the sense of rotation of the Goertler vortex next to it and so on. Because the end wall pressure-gradient forces differ in magnitude from the centrifugal forces, and because of secondary instabilities, non-linear interactions among the vortices can induce time- and space-dependent variations among them as well as in their number. Although interesting in its own rigth, there is an unavoidable bias in the finite-length parallelepiped configuration that unnecessarily complicates both the physical understanding and the numerical calculation of 3D shear-driven enclosure flows.

A NEW SHEAR-DRIVEN ENCLOSURE FLOW PARADIGM

The end wall bias present in the finite-length parallelepiped geometry can be completely removed by converting the parallelepiped into a toroid. This is accomplished conceptually by curving the parallelepiped uniformly around a pair of parallel longitudinal walls and “dissolving” the end walls at the common plane where they meet to create a continuous, unobstructed toroid of square cross-section (Fig. 2-a). In this idealized configuration, one of the flat walls of the toroid (the top wall in Fig. 2-a) is made to slide radially outwards (or inwards) with an axisymmetric velocity distribution in order to drive the flow in the toroid by viscous shearing. In addition to *Re*, the new quantity $d = D/R_c$ (a geometrical curvature parameter) must be specified to characterize fluid motion. Clearly, for values of $d \rightarrow 0$, the effects of geometrical curvature are rendered negligible, resulting in a flow configuration which: i) at sufficiently low *Re* rigorously approximates the 2D wall-driven flow in a plane square enclosure; ii) at sufficiently high *Re* will display the Goertler vortices observed in finite-length parallelepipeds, but *devoid* of end wall bias; and, iii) at even higher *Re* will undergo transition to turbulence. In this sense then, the shear-driven flow in a toroid represents a more general fundamental fluid mechanics paradigm than its predecessors.

Using the second order accurate (space and time) explicit CUTEFLOWS Navier-Stokes solver of Humphrey et al. [20], Phinney and Humphrey [21] and Sudarsan et al. [22] have calculated the wall-driven flow in a toroid of square cross-section corresponding to Fig. 2-a to investigate the effects of varying d and *Re*. The bulk of this work is for 2D (axisymmetric) flow. However, time averages of 3D results calculated for $Re = 3200$ and $d = 0.005$ yield very good agreement with the Goertler vortices and time-averaged velocity profiles obtained by Koseff and Street [9, 11] in a finite-length parallelepiped with $Re = 3300$; see Sudarsan et al. [22]. For $Re = 3200$ and $d = 0.005$ as well as for $Re = 2400$ with $d = 0.25$, the instantaneous flow is unsteady and the Goertler vortices are observed to meander chaotically. Sudarsan et al. [22] conclude that above a critical value of *Re*, depending on the value of d, the flow in a toroid becomes 3D due to the appearance of Goertler vortex pairs distributed periodically in the circumferential coordinate direction. They also obtain evidence to suggest that the Goertler vortices in a toroid can simultaneously alternate their sense of rotation periodically as a function of time with characteristic dimensionless frequency $w = 2p/(TU/D)$.

The present study explores more carefully the 3D, unsteady, shear-driven flow in a toroid of square cross-section. The effort is part of an ongoing collaboration between the University of Virginia and the University of Rovira i Virgili. We are concerned with two basic flow configurations differing solely in the way fluid motion is induced. In one configuration, flow through a narrow gap, *g*, shown in Figs. 2-b and –c, is involved. With reference to Fig. 2-a, Configuration One (the idealized case) consists of a toroid with $g/D = 0$, the flow in the toroid being driven by the shearing action of the top wall sliding radially outwards with an axisymmetric, constant velocity *U*. With reference to Fig. 2-b, Configuration Two (the experimental case) consists of a toroid with $0 < g/D << 1$, the flow in the toroid being driven by the shearing action of the wall-jet that emerges from the gap, *g*, to expand radially outwards along the toroid top wall. For Configuration Two, the Reynolds number is defined as $Re_g = U_g D/n$, where U_g is the mean velocity of the fluid in the gap at the plane where it enters the toroid.

In this communication we present results for Configuration Two. For this configuration numerical calculations are performed for $Re_g = 1143$ and $g/D = 0.04$ in two toroids: one with $d = 0.25$ and another with $d = 0.51$. The main flow visualization results are obtained in a toroid with $Re_g = 5000$, $g/D = 0.015$ and $d = 0.25$. Following the procedure outlined by Freitas and Street [8], all three of these cases yield estimates of the Goertler number of order 10, exceeding the stability criterion for the appearance of Goertler vortices. In the calculations the upper limit on Re_g is imposed by grid refinement considerations. In the flow visualization experiments the lower limit on Re_g is imposed by the construction of the test section. Unfortunately, with the current apparatus it is not possible to obtain a large overlap in Re_g between the experiment and the calculations.

Experimental Apparatus

The experiments are performed in a flow apparatus that uses water as the working fluid. A toroid with $D = 0.05$ m and $R_c = 0.20$ m is accurately machined from a transparent Plexiglass block 24” x 24” x 8” using a CNC milling machine. With reference to Figs. 2-b and -c, the inlet flow passage to the toroid is defined by a trumpet-shaped surface (machined into the same Plexiglass block) and a separate, flat, circular, Plexiglass lid of diameter 0.50 m and thickness 2.26 cm. The curvature of the trumpet-shaped surface is geometrically defined by rotating a quarter-ellipse 360 degrees around the toroid axis of symmetry. The major and minor axes of this ellipse are $a = 0.165$ m and $b = 0.060$ m. The distance between the circular lid and the top of the toroid, defining the gap dimension g, is continuously adjustable between 0 and 5 mm using three UNC 10-32 fine-thread screws placed 120 degrees apart. The entire Plexiglass test section rests on a laboratory table where it is leveled by means of three 6” long, ½” diameter, rubber-capped bolts that pass through threaded bearings 120 degrees apart in the table to support the test section from below.

The test section is part of a recirculating flow system that redirects water leaving the toroid into a sump tank from where it is pumped into a constant head tank with an overflow line leading back to the sump tank. Tygon tubing is used for all flow connections and this serves to minimize the transmission of possible mechanical vibrations. A circular gutter built into the Plexiglass lid permits the continuous removal of water from the test section thus allowing unobstructed side and top views of the toroid. A globe valve controls the flow of water from the head tank into the test section, and the rate of flow is measured by means of a King flowmeter (0 - 1.5 gpm, ± 0.01 gpm). After the flowmeter the water passes vertically upwards through a flow conditioning section consisting of a glass tube of inner diameter 0.02 m and length 0.40 m. The inlet to this tube contains a bundle of tightly packed straws 0.20 m long located between a pair of stainless steel screens. This is followed by an unobstructed length of tube wherein the flow relaxes before passing through a third screen to finally connect with the inlet to the trumpet-shaped section, also of diameter 0.02 m. The flow in the trumpet-shaped section first decelerates slightly and then accelerates strongly as it approaches the toroid. A tendency of the flow to separate in the decelerating section is suppressed by the insertion of two relatively fine, cylindrically-shaped, concentric stainless steel screens. These additional screens further reduce any residual inhomogeneities in the flow approaching the toroid.

A rheoscopic fluid manufactured by Kalliroscope Corp. (AQ-1000 Rheoscopic Concentrate, consisting of micron-sized guanine platelets in suspension) is added to the water (1% by volume) for flow visualization purposes. The flow in the toroid is illuminated using a plane of light generated by passing the beam from a 5-mW He-Ne laser through a cylindrical lens. While it is possible to obtain images of the flow in planes normal to the r-, z- and q-coordinate directions, the highest quality and least optically-distorted images are obtained in r-q planes, normal to the z-coordinate direction. Photographs of the flow are taken with a Canon T90 camera using a 50 mm Canon Macrolens and Kodak Select B&W 200 ASA film.

Among the uncertainties affecting the experiment, those associated with geometrical dimensions during fabrication and assembly of the test section, water temperature variations, and mechanical vibrations are negligible, and those associated with optical distortion of images are small or correctable if necessary. Two sources of uncertainty affect the value of U_g in the Reynolds number, Re_g. One is due to the reading error (± 0.01 gpm) of the flowmeter scale, and the other is due to the positioning error (± 25 μm) of the circular lid which leads to an uncertainty in the gap width, *g*. The result is a final maximum percent rms uncertainty of ± 5% in Re_g. Of more concern is a possible misalignment of the lid leading to a non-axisymmetric gap width, *g*. Such a misalignment will induce uneven shearing of the flow in the toroid with corresponding distortions of the flow structures in it. However, with care this effect can be minimized. For further details on the experimental apparatus, procedure and uncertainties see Cushner [23].

Numerical Calculations

A fourth order (space and time) version of the CUTEFLOWS code referred to above is employed for the new calculations presented here, corresponding to Configuration Two. The code solves unsteady, 3D, constant property forms of the momentum and continuity equations in Cartesian or cylindrical coordinates. The numerical procedure is based on a staggered-grid, control-volume discretization approach for deriving finite difference forms of the conservation equations in terms of the primitive variables, velocity components and pressure. A fourth-order-accurate central differencing scheme is used to approximate the pressure and diffusion terms in the momentum equations. A quadratic upstream-weighted scheme is used for the convection terms. Continuity yields a discrete Poisson equation that is solved for pressure using the conjugate gradient method. The algorithm is explicit in time and uses a fourth-order Runge-Kutta solver. The dimensionless integration time-step is typically $t/(D/U) < 0.01$ and is small enough to guarantee both stable convergence and accuracy in the course of a calculation.

The calculation domain consists of the entire toroid (full 360 degrees) with the impermeable, no-slip condition imposed for velocity at all its internal surfaces. With reference to Fig. 2-c, the flow at the plane where it enters the toroid is taken as essentially fully developed Poiseuille flow. The flow leaving the toroid redevelops in an exit gap of the same height, g/D, as the inlet plane gap, and of length $l/D = 0.55$. Calculations are started from corresponding 2D (axisymmetric) solutions. Earlier linear stability analyses have shown that the 2D wall-driven flow in an infinitely long parallelepiped is unstable to infinitesimal disturbances. Using the present fourth order numerical scheme, the Goertler vortices appear spontaneously and it is unnecessary to seed disturbances. A typical run time for Configuration Two on a dual processor Dell workstation (PWS620) is about 10 hours for 100 seconds of numerical flow development.

Substantial grid refinement tests are first performed, culminating in the choice of a grid with ($N_r = 72$, $N_z = 72$, $N_q = 192$) nodes. The nodes in the *r-z* plane are unequally spaced while those in the *q* direction are equally spaced. Although not shown here, subsequent additional testing with this grid has yielded vortical flow structures with characteristics in excellent agreement with those obtained by Albensoeder et al. [17]. Namely, using periodic boundary conditions in the *x*-direction for the wall-driven flow in a parallelepiped of square cross-section corresponding to Fig. 1-b with $g/D = 0$ and $L/D = 2$, we find $k = 15.7$ and $w = 0$ at $Re = 850$ compared to the experimental values of $k = 15.43$ and $w = 0$ at $Re = 786.3$.

RESULTS AND DISCUSSION

A summary of some main findings follows below for Configuration Two.

Experimental Results

Flow visualization experiments have been performed in the range $10^3 \leq Re_g \leq 9 \times 10^3$ in a toroid with $d = 0.25$ for gap widths corresponding to $g/D = 0.015$, 0.030, 0.040 and 0.060; see Cushner [23]. Here we comment on the main observations made with a focus on the visualization results obtained for $Re_g = 5000$ with $g/D = 0.015$.

Because of the viscous action of the circular lid on the flow, there can be a significant penetration of the radially-expanding wall-jet into the toroid. For each gap width, g, a value of Re_g exists above which this penetration is minimal and for $g/D = 0.015$ this corresponds to $Re_g \approx 1600$. For $Re_g > 2000$, views of the flow in the r-z plane, made at an angle through the lid, clearly reveal the recirculating core flow and the two bottom corner eddies typical of 2D wall-driven flows in plane rectangular enclosures. (Note, however, with reference to Fig 1-a, that the eddy arising in the top left-hand corner of a wall-driven plane enclosure flow is not clearly visible in the experiment, and is not predicted numerically for the values of Re_g and g/D investigated.) The wall-jet penetration is discussed further below in relation to the numerical calculations performed.

Depending on the value of g/D, between $Re_g = 1000$ and 2000 a first instability leads to the appearance of Goertler vortices in the flow. (The exact value of Re_g cannot be determined in the current apparatus because of the wall-jet penetration limitation.) For the flow with $g/D = 0.015$ and $Re_g = 2000$ the dimensionless wavenumber of a vortex pair is $k \approx 6.3$, and between $Re_g = 3000$ and 4000, approximately, this doubles to $k \approx 12.6$. In the latter range of Re_g a slight meandering of the vortices (smaller in extent than half a wavelength) is observed over time periods of about 5 min. At $Re_g \approx 4100$ a second, marked instability, in the form of a Hopf bifurcation, is observed. This involves the continuous merging and splitting of the Goertler vortices. Beyond $Re_g \approx 6500$ the vortices are subjected to a strong wavy motion which, by $Re_g \approx 8000$, is disorganized and turbulent (although the intermittent presence of Goertler vortices is observed).

Flow visualization results corresponding to $Re_g = 5000$ with $g/D = 0.015$ are shown in Figs. 3 and 4. (In these and subsequent figures $r^* \equiv (r-r_i)/(r_o-r_i)$ and $z^* \equiv z/D$.) The results in Fig. 3 correspond to a snapshot of the flow in the z^*-q plane at $r^* = 0.90$. Those in Fig. 4 are obtained at different times at different r^*-q planes. Although the flow conditions correspond to an unsteady flow regime, it is not possible to extract a single characteristic frequency from the visualization observations. Notwithstanding, Goertler vortices of wavenumber $k \approx 12.5$ are clearly observed. At small values of z^* (near the toroid bottom wall), the vortices are aligned in the radial direction and fill the entire space between $r^* = 0$ and 1. With increasing z^* the vortices orient themselves axially, along the z^* coordinate direction, and are especially prominent along the inner curved half of the toroid, $r^* < 0.5$.

Numerical Results

Numerical calculations are performed for $Re_g = 1143$ and $g/D = 0.04$ in two toroids: one with $d = 0.25$ and another with $d = 0.51$. Because the details of these two flow are very similar, and because their Goertler vortices have essentially the same wavenumber, we focus on the results obtained for $d = 0.51$. Calculated values of the instantaneous circumferential velocity component, visualized using shades of gray ranging from white to black, are shown in Fig. 5. The results correspond to t^* ($\equiv tU_g/4D$) $= 856$ and are in excellent qualitative agreement with the experimental observations at higher Re_g and lower d in so far as the spatial structure, distribution, and orientation of the vortices are concerned. For the conditions calculated, the wavenumber of the vortices is $k = 8.7$ and the flow displays a time dependence of dimensionless frequency $w = 0.154$. (Note that in the toroid the dimensionless wavenumber $k\,(\equiv 2p/(l/D)) = (2pR_c/l)\,(D/R_c) = N\,d$, where N (= 17) is the total number of vortex pairs in the toroid.)

Figure 6 shows calculated time records of the dimensionless circumferential velocity component ($u^*_q = u_q/U_g$) at two axial locations $z^* = 0.25$ and $z^* = 0.50$ with $r^* = 0.5$ and $q = 0.22p$. The calculations correspond to the conditions of Fig. 5. Although the magnitudes of these monitor velocity components and their changes are small, and while the recirculating flow has experienced about 22 toroid periphery “turnovers” in the course of its development, it appears to still be evolving. Thus, we cannot state definitively whether the flow dynamics will continue to evolve towards a final, periodic state with $w = 0.154$, or will orbit, instead, within the basin of a strange attractor at some frequency close to $w = 0.154$.

Nevertheless, it is especially noteworthy for the numerical conditions explored that the entire flow field in the toroid alternates between two identical but spatially displaced states of motion as a function of time. This Hopf-like bifurcation is clearly illustrated by the velocity vector plots shown in Fig. 7 for two consecutive times of an oscillation cycle ($w = 0.154$) in the z^*-q plane located at $r^* = 0.5$. While the shape, size and number of the calculated structures are virtually the same at both times, their positions relative to a fixed reference point are displaced by half a wavelength in the q-coordinate direction. A movie of this flow reveals a sequentially alternating pattern of Goertler vortices in the main recirculating core flow direction. At any instant in a cycle, the two vortices in any vortex pair have a particular sense of rotation, the vortices in this pair counter-rotating with respect to each other. At a later time in the cycle, this vortex pair gives way to a new pair, displaced by half a wavelength in the q-coordinate direction, in which the vortices now rotate in the opposite sense to the original pair. At all times, however, the vortices remain equally spaced in the q-coordinate direction.

From an Eulerian viewpoint, the visual effect at a fixed location in the toroid is to observe *in situ* time-periodic alternations in sense of rotation of the vortices. This sign alternation in sense of rotation occurs simultaneously for all the vortices in a toroid, thus implying a phase shift in the recirculating core flow direction. We suggest that the periodic changes in sense of rotation of the vortices is due to a phase-shifted coupling between the tilting and stretching of circumferential, q- component of vorticity at the convex (inner-radius) wall and the tilting and stretching of the same component of vorticity at the concave (outer-radius) wall.

We referred earlier to a basic difference between the toroid flows corresponding to Configuration One (Fig. 2-a) and Configuration Two (Fig. 2-b and -c) that has to do with the way fluid motion is induced by shearing. In Configuration Two, a wall-jet expands radially outwards along the circular lid over the toroid. The viscous action of the lid on the wall-jet results in a penetration of the flow into the toroid and the formation of a stagnation line along the outer concavely-curved wall. This stagnation line falls below the exit gap by an amount p/D that depends on the values of Re_g and g/D. Figure 8 shows an instance of the calculated flow in the r^*-z^* plane corresponding to the maximum penetration depth of the wall-jet when $Re_g = 1143$, $g/D = 0.04$ and $d = 0.51$. (The corresponding plot for the minimum penetration depth in an oscillation cycle is virtually the same.) While the radially-decelerating expanding wall-jet and the flow in the vicinity of the stagnation line represent potential sources for additional instabilities in the toroid, these are not observed in the calculations. If they exist in the experiment it is not known how much they influence the centrifugal instability leading to the formation of the Goertler vortices.

CONCLUSIONS

Because of the absence of end wall effects, the shear-driven flow in a toroid of rectangular cross-section represents a more general fluid mechanics paradigm than its parallelepiped predecessors. In addition, radial accelerations and decelerations of fluid motion, induced by geometrical curvature, render this flow type especially rich in its physics.

Numerical calculations of the flow in a toroid can be performed assuming that a sliding wall shears the fluid. In contrast, an experimental realization of the flow requires the use of a wall-jet to shear the fluid. We refer to the former as Configuration One and to the latter as Configuration Two.

In the limit $d \rightarrow 0$ and at sufficiently low Reynolds number, the wall-driven flow in a toroid corresponding to Configuration One approximates the 2D flow in a plane enclosure. For $d = 0$ and above a critical value of *Re*, the same configuration represents the wall-driven flow in an infinitely long parallelepiped. Our 3D calculation approach yields results in excellent agreement with 2D plane square enclosure flows and with the 3D results of Albensoeder et al (2001) for the flow in a wall-driven parallelepiped of finite length (experiment) and infinite length (analysis). Thus, for the latter we obtain $k = 15.7$ and $w = 0$ at $Re = 850$ compared to $k = 15.43$ and$w = 0$ at $Re = 786.3$ for the resulting Goertler vortices. Earlier calculations in a finite-length parallelepiped for $Re = 3200$ and $d = 0.005$ have yielded results in very good agreement with the Goertler vortices and time-averaged velocity profiles obtained experimentally by Koseff and Street [9, 11] for $Re = 3300$;

Present calculations for Configuration Two with $d = 0.51$ (and $d = 0.25$), $g/D = 0.04$ and $Re_g = 1143$ reveal the same basic flow pattern as observed in Configuration One when the Goertler stability criterion is exceeded. This consists of a recirculating core flow and two smaller eddies at the bottom corners of the toroid, and centrifugally-induced Goertler vortex pairs of wavenumber $k = 8.7$ superimposed on and aligned with the recirculating core flow. Especially noteworthy, however, is the observation that for any fixed location in the toroid, the Goertler vortex passing through that location alternates in its sense of rotation periodically as a function of time, and that this sign alternation occurs simultaneously for all the other Goertler vortices in the toroid. From an Eulerian viewpoint, the visual effect is to observe *in situ*, simultaneous, time-periodic alternations in the sense of rotation of all the vortices in the toroid at frequency $w = 0.154$. Such behavior is precluded for the wall-driven flows in finite-length parallelepipeds where the sense of rotation of the Goertler vortices is determined and stabilized by the sense of rotation of the end wall vortices. A comparison between the calculated results with $d = 0.25$ and $d = 0.51$ suggests that vortex wavenumber is independent of curvature at this value of Reynolds.

Flow visualization observations in a toroid with $d = 0.25$, $g/D = 0.015$ and $Re_g = 5000$ reveal Goertler vortices of wavenumber $k \approx 12.5$ which appear to alternately merge and split around their average locations. The experimental results suggest that for a toroid with $d = 0.25$ vortex wavenumber increases with increasing Reynolds number.

While these are interesting and significant findings, further work is necessary to experimentally verify the periodic alternations in sense of rotation of the Goertler vortices. (In this regard, we have made new, encouraging observations in the existing experimental apparatus but the results are not definitive.) In addition, it is important to establish: a) the dependence on Re_g , $d$and g/D for transition from 2D to 3D flow and the appearance of flow unsteadiness; b) the conditions leading to, and a full understanding of, the time-dependent alternations in sense of rotation of the Goertler vortices; and, c) vortex structure breakdown and transition to turbulence as a function of the relevant geometrical and dynamical parameters.

In summary, while the physics of the shear-driven flow in a toroid has yet to be fully understood, this new configuration poses a number of significant questions related to centrifugally-driven flow instabilities while serving as a well-defined and challenging test case for computational fluid dynamic procedures aimed at solving complex, 3D, unsteady, laminar and turbulent flows.

ACKNOWLEDGMENTS

JACH gratefully acknowledges support received from NSF (grant CTS9504390) for this study. Thanks go to G. Waltman at Bucknell University for the construction of the toroid test section. MA, JH and FG thank the “Dirección General de Investigación Científica y Técnica” (Spain), DGICYT project no. PB96-1011, and the “Programa de Grups de Recerca

Consolidats de la Generalitat de Catalunya", CIRIT project no. 1998SGR-00102, for their support. We are sincerely grateful to R. Eichhorn (University of Houston) and J. Heinrich (University of Arizona) for enlightening discussions.

REFERENCES

1. Ghia,U., Ghia, K.N. and Shin, C.T. (1982) "High-Re solutions for incompressible flow using Navier-Stokes equations and a multigrid method'" *J. Comput. Phys.*, **48**, 387-411.
2. Iwatsu, R., Hyun, J.M. and Kuwahara, K. (1990) "Analyses of three dimensional flow calculations in a driven cavity," *Fluid Dynam. Research*, **6**, 91-102.
3. Iwatsu, R., Ishii, K., Kawamura, T., Kuwahara, K. and Hyun, J.M. (1989) "Numerical simulation of three-dimensional flow structure in a driven cavity," *Fluid Dynam. Research*, **5**, 173-189.
4. Nishida, H. and Satofuka, N. (1992) "Higher order solutions of square driven cavity flow using variable-order multigrid method," *Int. J. Numer. Methods Fluids*, **34**, 637-653. 5.
5. Koseff, J.R., Street, R.L., Gresho, P.M., Upson, C.D., Humphrey, J.A.C. and To, W.M. (1983) "A three dimensional lid driven cavity flow: experiment and simulation," Proceedings of the Third International Conference on Numerical Methods in Laminar and Turbulent Flow, Seattle, WA, 564-581.
6. Freitas, C.J., Street, R.L., Findikakis, A.N. and Koseff, J.R. (1985) "Numerical simulation of three dimensional flow in a cavity," *Int. J. Numer. Methods Fluids*, **5**, 561-575.
7. Kim, J. and Moin, P. (1985) "Application of fractional step method to incompressible Navier-Stokes equations," *J. Comput. Phys.*, **59**, 308-323.
8. Freitas, C.J. and Street, R.L. (1988) "Nonlinear transient phenomena in complex recirculating flow: A numerical investigation," *Int. J. Numer. Methods Fluids*, **8**, 769-802.
9. Koseff, J.R. and Street, R.L. (1984-a) "Visualization studies of a shear driven three dimensional recirculating flow," *J. Fluids Eng.* **106**, 21-29.
10. Koseff, J.R. and Street, R.L. (1984-b) "On end wall effects in lid driven cavity flow," *J.Fluids Eng.*, **106**, 385-389.
11. Koseff, J.R. and Street, R.L. (1984-c) "The lid driven cavity flow: a synthesis of qualitative and quantitative observations," *J. Fluids Eng.*, **106**, 390-398.
12. Prasad, A.K. and Koseff, J.R. (1989) "Reynolds number and end-wall effects on a lid driven cavity flow," *Phys. Fluids* A, **1**, 208-218.
13. Aidun, C.K., Triantafillopoulous, N.G. and Benson J.D (1991) "Global stability of lid driven cavity with throughflow: Flow visualization studies," *Phys. Fluids* A, **3**, 2081-2091.
14. Ramanan, N., and Homsy, G.M. (1994) "Linear stability of lid driven cavity flow," *Phys. Fluids*, **6**, 2960-2701.
15. Ding, Y. and Kawahara, M. (1998) "Linear stability of incompressible fluid flow in a cavity using finite element method," *Int. J. Numer. Methods. Fluids*, **27**, 139-157.
16. Ding, Y. and Kawahara, M. (1999) "Three-dimensional linear stability analysis of incompressible viscous flows using the finite element method," *Int. J. Numer. Methods. Fluids*, **31**, 451-.
17. Albensoeder, S., Kuhlmann, H.C. and Rath, H.J. (2001) "Three-dimensional centrifugal-flow instabi-lities in the lid-driven-cavity problem," *Phys. Fluids* A **13**, 121-135.
18. Goertler, H. (1951) "On the three-dimensional instability of laminar boundary layers on concave walls" NACA Technical Memorandum No. 1375.

19. Taylor, G.I. (1923) “Stability of a viscous liquid contained beween two rotating cylinders,” Phil. Trans. Roy. Soc., **45**, 289-343.
20. Humphrey, J.A.C., Schuler, C.A. and Webster, D.R. (1995) “Unsteady laminar flow between a pair of disks corotating in a fixed cylindrical enclosure,” *Phys. Fluids*, **7**, 1225-1240.
21. Phinney, L.M. and Humphrey, J.A.C. (1996) “Extension of the wall driven enclosure flow problem to toroidally shaped geometries of square cross-section,” *J. Fluids Eng.*, **118**, 779-786.
22. Sudarsan, R., Humphrey, J.A.C. and Heinrich, J. (1998) “Three-dimensional unsteady wall-driven flow in a toroid of square cross-section: a new CFD paradigm,” Proceedings of the ASME FED Summer Meeting: Forum on Industrial and Environmental Applications of Fluid Mechanics, FEDSM98-5314, June 21-25, Washington, D.C.
23. Cushner, J. (2000) “Experimental visualization of a shear-driven toroidal LDC flow,” M.Sc. Thesis, College of Engineering, Bucknell University, Lewisburg, Pennsylvania.

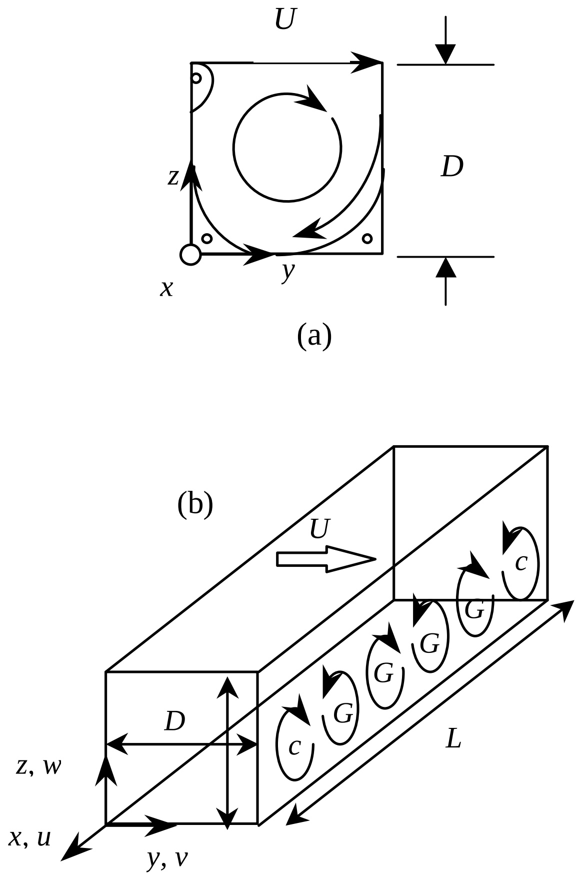

Figure 1. Wall-driven flows in enclosures of square cross-section. (a): 2D flow in a plane enclosure. (b): 3D flow in a parallelepiped. At sufficiently large *Re*, centrifugal instabilities trigger Goertler vortices in the parallelepiped where the two end walls fix the sense of rotation of the corner (“c”) vortices and, as a consequence, of the remaining (“G”) vortices. The sense of rotation of the vortices in the bottom half of the parallelepiped is shown projected on an *x*-*z* plane.

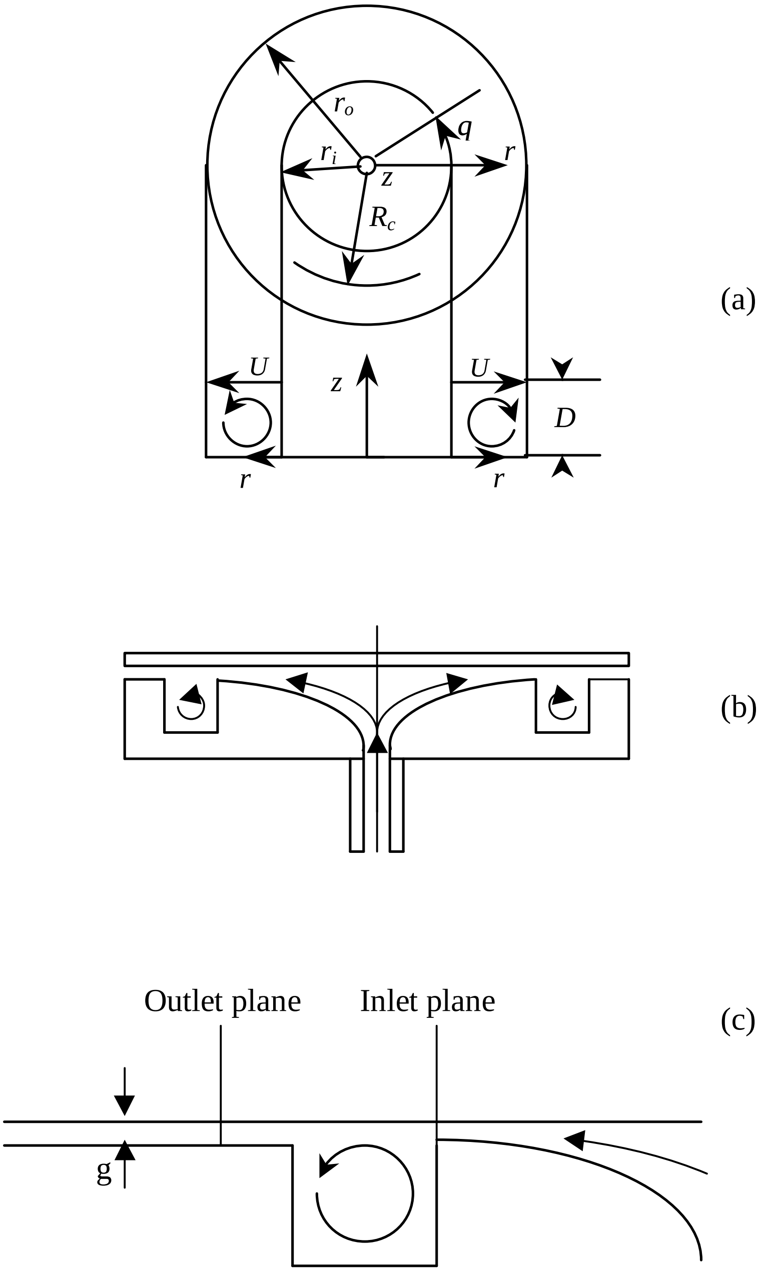

Figure 2. a) Top and side views of the idealized toroid (Configuration One); b) side view of the experimental configuration (Configuration Two); c) view showing one (r-z) plane of the 360 degree calculation domain corresponding to Configuration Two. Note that $g/D = 0$ for Configuration One and $g/D << 1$ for Configuration Two. The drawings are not to scale.

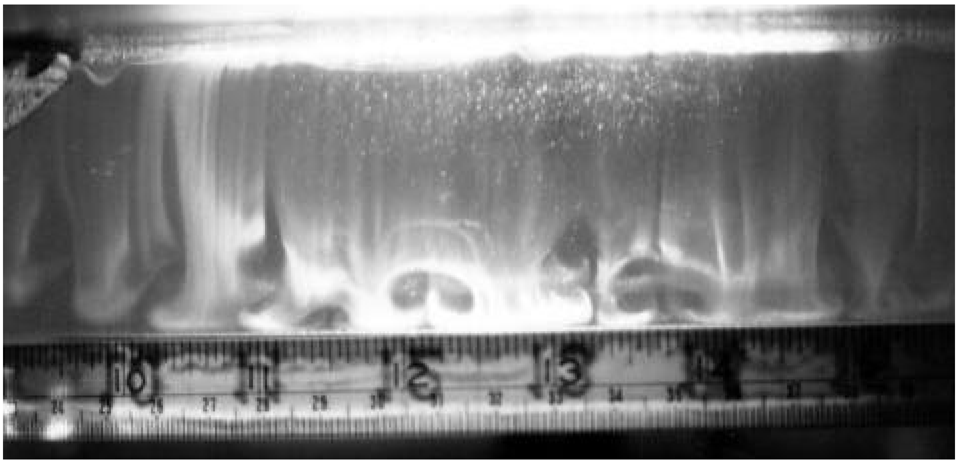

Figure 3. Visualization of the instantaneous flow in a toroid with $Re_g = 5000$, $d = 0.25$ and $g/D = 0.015$. Picture shows a z^*-q plane at $r^* = 0.90$ as seen through the curved outer side wall of the toroid.

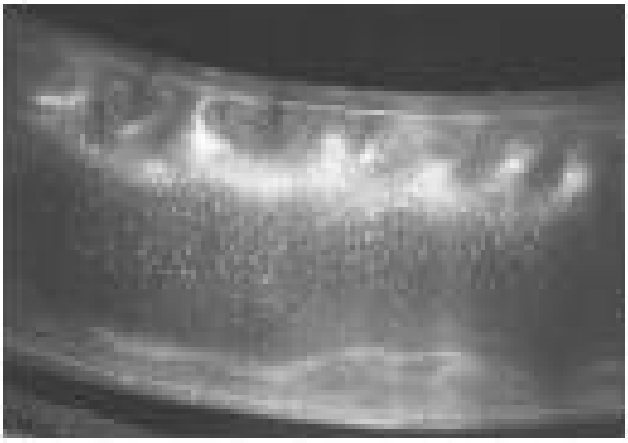

(a)

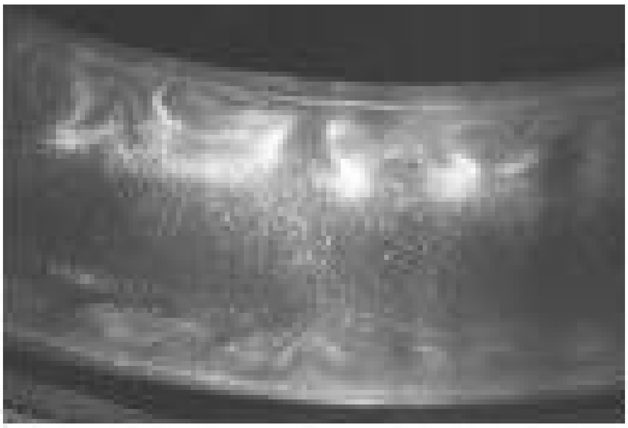

(b)

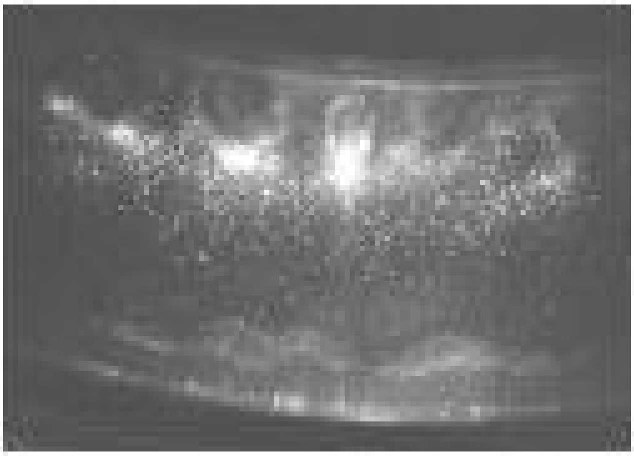

(c)

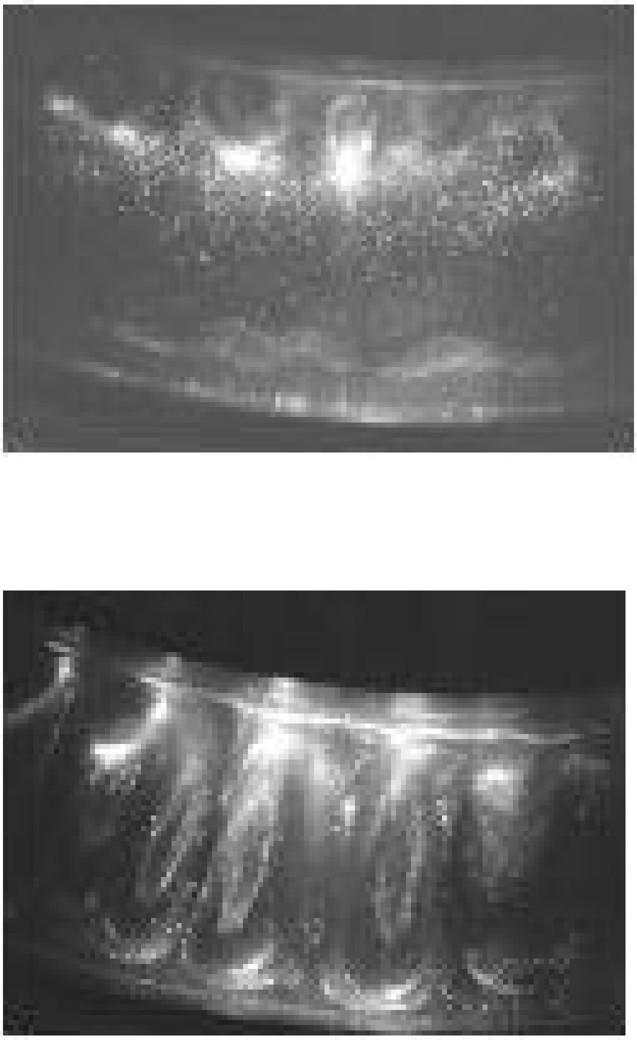

(d)

(e)

Figure 4. Visualization of the instantaneous flow in a toroid with Re_g = 5000, d = 0.25 and g/D = 0.015. Pictures show views of r^*-q planes as seen through the top wall of the toroid over a sector of 18 degrees: (a) z^* = 0.9; (b) 0.7; (c) 0.5; (d) 0.3; and (e) 0.1.

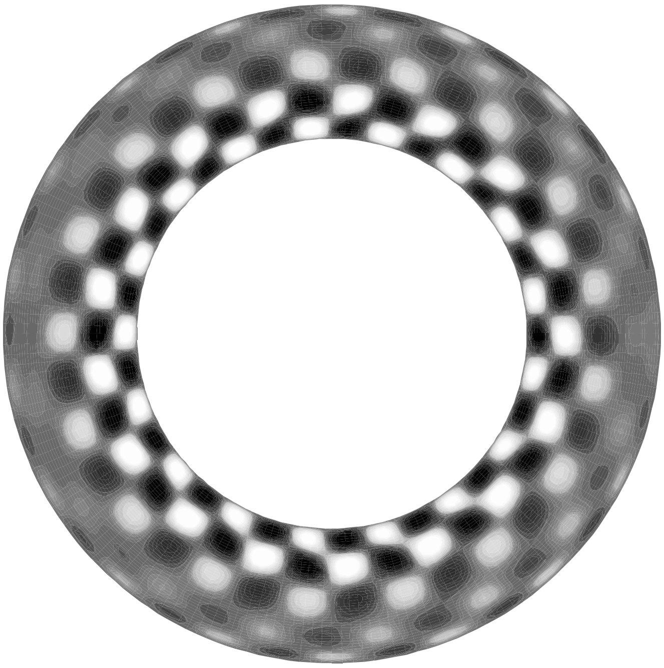

(a)

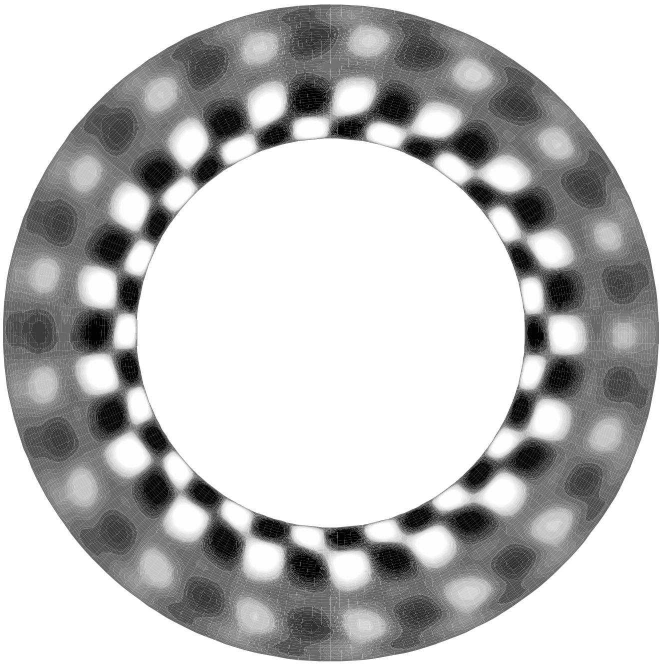

(b)

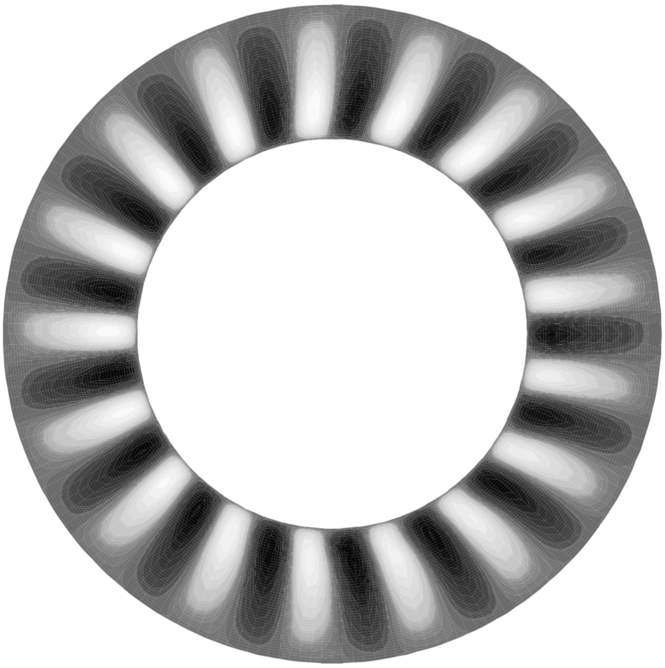

(c)

Figure 5. Instantaneous distributions of the calculated circumferential velocity component at t^* = 856 in r^*-q planes of a toroid with Re_g = 1143, d= 0.51 and g/D = 0.04: (a) z^*=0.7; (b) 0.5 and (c) 0.1. Black and white areas denote regions of opposite velocity.

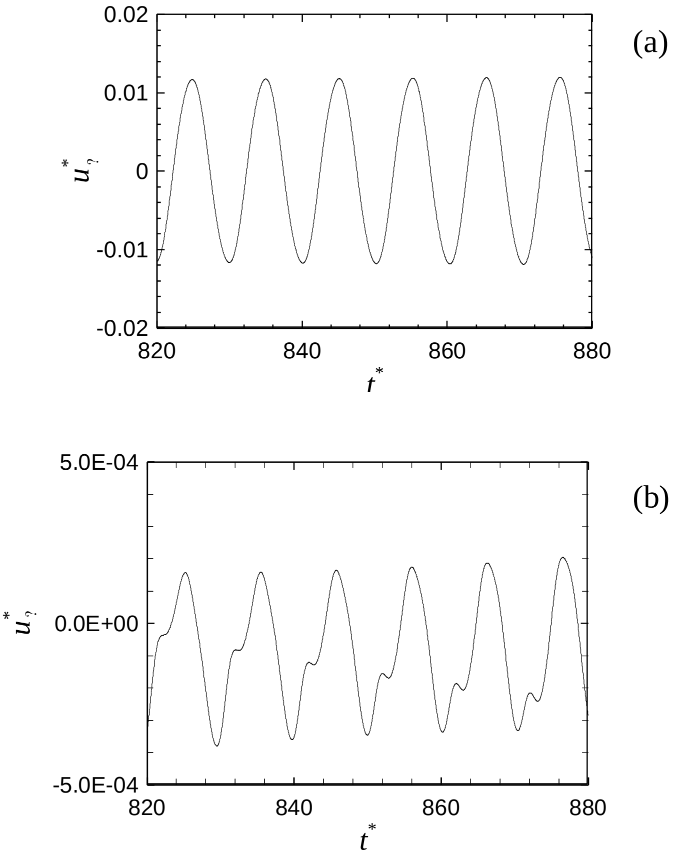

Figure 6. Time records of the dimensionless circumferential velocity component at (a) $z^* = 0.25$, $r^* = 0.5$ and $q = 0.22p$ (b) $z^* = 0.5$, $r^* = 0.5$ and $q = 0.22p$ for the conditions of Fig. 5.

(a)

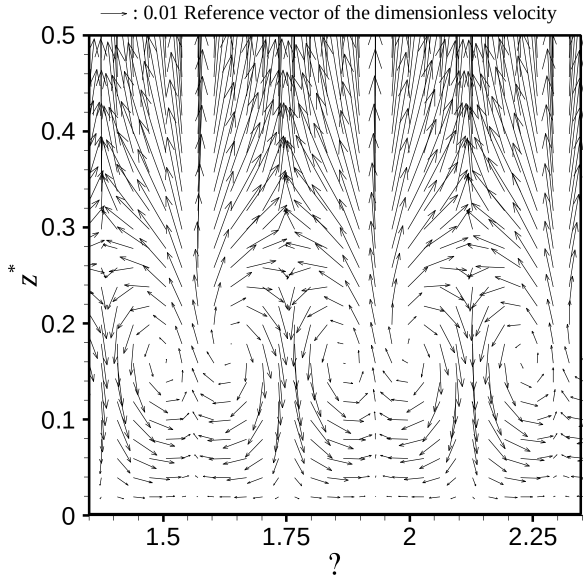

(b)

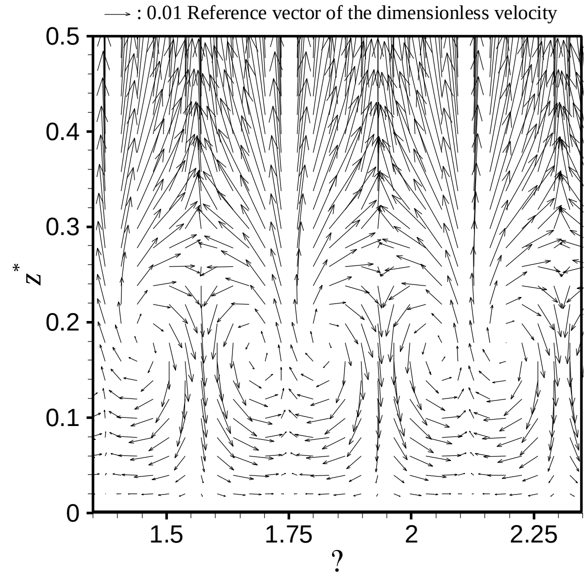

Figure 7. Instantaneous dimensionless velocity vectors at times t^* = 860 (a) and t^* = 865 (b) in the lower half of the z^*-q plane at r^* = 0.5 for the conditions of Fig. 5.

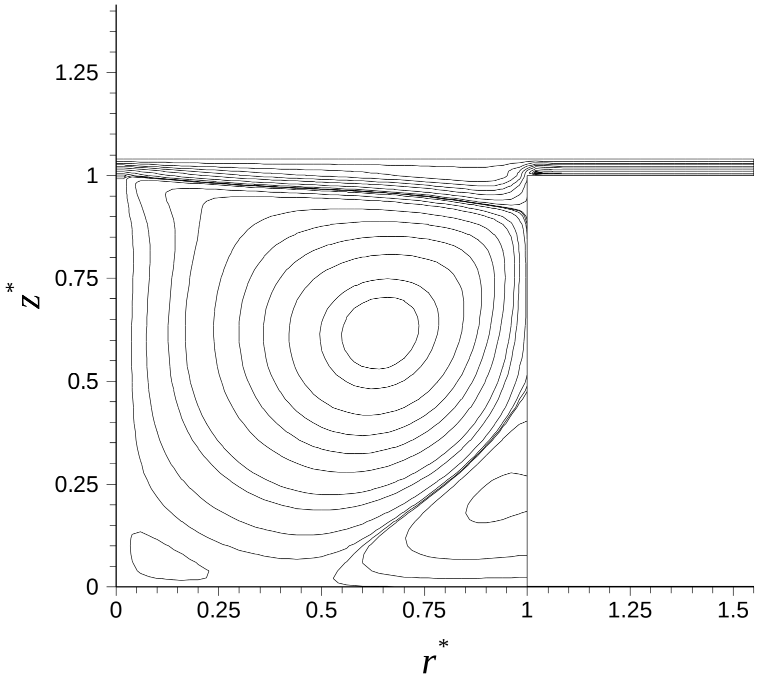

Figure 8. Instantaneous streamlines obtained from a full domain 3D flow calculation in a toroid with Re_g = 1143, d= 0.51 and g/D = 0.04. The wall jet flows from left to right at the top of the toroid thus inducing a clock-wise circulation of the core flow. Results shown correspond to the maximum penetration depth in an oscillation cycle. The maximum penetration depth is p/D = 0.079 and the minimum is p/D = 0.076.